Schriftenreihe des
Instituts für Mikrowellentechnik



12

Christina Knill

Novel MIMO OFDM Waveform Designs and High-Performance Signal Processing Methods for Digital Radars

Institut für Mikrowellentechnik
Universität Ulm

Novel MIMO OFDM Waveform Designs and High-Performance Signal Processing Methods for Digital Radars



universität ulm

Novel MIMO OFDM Waveform Designs and High-Performance Signal Processing Methods for Digital Radars

DISSERTATION

zur Erlangung des akademischen Grades eines

DOKTOR-INGENIEURS (Dr.-Ing.)

der Fakultät für Ingenieurwissenschaften,
Informatik und Psychologie der Universität Ulm

von

Christina Knill

aus Langenau

Gutachter: Prof. Dr.-Ing. Christian Waldschmidt
Prof. Dr.-Ing. Martin Vossiek
Amtierender Dekan: Prof. Dr.-Ing. Maurits Ortmanns

Ulm, 20. Dezember 2021

Bibliografische Information der Deutschen Nationalbibliothek
Die Deutsche Nationalbibliothek verzeichnet diese Publikation in der Deutschen Nationalbibliografie; detaillierte bibliografische Daten sind im Internet über http://dnb.dnb.de abrufbar.

Dissertation, Universität Ulm,
Fakultät für Ingenieurwissenschaften, Informatik und Psychologie, 2021

Impressum
Universität Ulm
Institut für Mikrowellentechnik
Prof. Dr.-Ing. Christian Waldschmidt
Albert-Einstein-Allee 41
89081 Ulm
https://www.uni-ulm.de/mwt

Eine Übersicht über alle Bände der Schriftenreihe finden Sie unter
https://www.uni-ulm.de/mwtschriften

Diese Veröffentlichung ist im Internet auf dem institutionellen Repositorium der Universität Ulm (https://oparu.uni-ulm.de) verfügbar und dort unter der Lizenz CC BY-NC-ND 4.0 publiziert.



Details zur Lizenz finden Sie unter
https://creativecommons.org/licenses/by-nc-nd/4.0/

ISBN 978-3-948303-25-9 ISBN 978-3-948303-26-6 (E-Book)

Abstract

Recent advances in digital hardware and processing power have enabled the realization of novel digital radars that are superior to radars commercially available today in flexibility and performance. This opens up new opportunities in radar waveform design, modulation, and high-performance signal processing that were previously unfeasible. Probably the most known digital radar modulation concept is orthogonal frequency-division multiplexing (OFDM), which has attracted much interest in radar research in the last two decades.

The goal of this thesis is to explore new possibilities for OFDM radar waveform design and high-performance digital processing to make future digital radars even more powerful and robust. To this end, the developed novel waveform and signal processing concepts take advantage of the high degree of flexibility and diversity provided by OFDM to overcome previous limitations in radar performance, to enable new multiple-input multiple-output (MIMO) concepts, to enhance radar imaging performance, and to enable robust radar sensing in coexistence with other radars.

The close dependence between the attainable range resolution and the required modulation bandwidth has been a limiting factor for the achievable sensing performance and therefore for the realization of high-resolution OFDM radars so far. In this thesis, a novel flexible waveform design and high-performance imaging concept is developed that breaks the link between range resolution and instantaneous bandwidth. This significantly reduces the requirements for the sampling rate at both transmitter and receiver hardware. Furthermore, 2D compressed sensing (CS) methods are developed that enable joint range and Doppler processing. The novel concept allows to reduce the required modulation bandwidth and corresponding sampling rate up to a factor of eight. Nonetheless, the high range resolution of an equivalent wideband signal is achieved. In addition, the CS-based processing improves the peak-to-noise ratio (PNR) and thereby the target detection capabilities of the system. Using measurements of an experimental digital OFDM radar, it is shown that the novel narrow-

band waveform and CS-based processing approach achieve the same sensing performance as an equivalent wideband OFDM signal capable of the same resolution.

The developed random multiplexing (RM) allows multiple transmitters of the same radar node to operate simultaneously and continuously within the same frequency band by randomly distributing the elements of the discrete time-frequency measurement frame among them. Unlike the usual frequency-division multiplexing (FDM) and time-division multiplexing (TDM) MIMO radar approaches, the new approach does not suffer any losses in range or Doppler capabilities. Moreover, augmented by the developed corresponding multi-channel CS processing, the radar imaging performance is enhanced. Another MIMO strategy is explored by taking advantage of the code diversity provided by OFDM signals. Three distinct code-division multiplexing (CDM) MIMO OFDM concepts are developed that offer different benefits and limitations regarding their range and Doppler capabilities. In addition, hybrid MIMO concepts are developed combining two MIMO OFDM concepts into a new one in order to lessen the limiting constraints of both, while taking advantage of the benefits of both.

In radar sensing applications, robust radar operation in coexistence with other non-cooperative radar nodes is an important prerequisite. In this thesis, first, the interference impact of state-of-the-art frequency-modulated continuous-wave (FMCW) radars on the common and the new narrowband OFDM signals is analyzed. Then, three processing methods to mitigate the interference impact are developed that allow undisturbed radar sensing and imaging. It shows that the low-cost approach of eliminating interfered elements (zeroing) in the spectrogram is sufficient for a moderate amount of interference affecting only few elements. However, zeroing reduces the integration gain proportional to the number or eliminated elements. It is shown that if zeroing is followed by 2D CS signal recovery, the original signal of the eliminated elements is restored, and the PNR is improved. In addition to the common detect-and-mitigate countermeasures, the dual-CS OFDM evaluation is developed. It enables unchanged and robust radar sensing regardless of whether signals from other radars with comparatively low instantaneous bandwidth and high narrowband power interfere.

Kurzfassung

Jüngste Fortschritte in der Digitaltechnik und bei der Rechenleistung erlauben die Realisierung digitaler Radare, welche in ihrer Flexibilität und Leistungsfähigkeit den sich heute auf dem Markt befindlichen Sensoren überlegen sind. Dadurch eröffnen sich neue Möglichkeiten und Perspektiven bei der Gestaltung der Wellenform und Modulation. Zudem werden leistungsfähigere Signalverarbeitungsansätze möglich, die bisher nicht umsetzbar waren. Die wohl bekannteste Modulationsart für Digitalradare ist das *Orthogonal Frequency-Division Multiplexing* (OFDM), welches in den letzten zwei Jahrzehnten zunehmend an Interesse in der Radarforschung gefunden hat.

Ziel dieser Arbeit ist die Erforschung neuer Ansätze zur Wellenformgestaltung und leistungsstarker Signalverarbeitung für OFDM Radare, um zukünftige Digitalradare noch leistungsfähiger und zuverlässiger zu machen. Hierzu werden neue Wellenformen und Signalverarbeitungskonzepte entwickelt, welche das hohe Maß an Flexibilität und Diversität, das OFDM bietet, nutzt, um bisherige Beschränkungen in der Leistungsfähigkeit des Systems zu überwinden, neue *Multiple-Input Multiple-Output* (MIMO) Konzepte zu ermöglichen, die Leistungsfähigkeit der Radarbildgebung zu erhöhen und einen robusten Betrieb in Koexistenz mit anderen Radarsensoren zu erreichen.

Der enge Zusammenhang zwischen erreichbarer Abstandsauflösung und der dazu benötigten Modulationsbandbreite stellt bisher einen begrenzenden Faktor bei OFDM Radaren dar. In dieser Arbeit wird ein neues Konzept zur Gestaltung der Wellenform und ein leistungsfähiges neues Signalverarbeitungs- und Bildgebungskonzept entwickelt, welches diese Beschränkung überwindet. Durch die neue Methode werden die Anforderungen an die sende- und empfangsseitige Abtastrate deutlich verringert. Zudem wird ein 2D *Compressed Sensing* (CS) Algorithmus entwickelt, welcher es ermöglicht die Abstands- und Geschwindigkeitsinformation gemeinsam auszuwerten. Das neue Konzept erlaubt dabei eine Verringerung der Basisbandbandbreite und damit auch der erforderlichen Abtastraten um bis zu Faktor acht. Trotzdem wird dabei

die gleiche Abstandsauflösung wie bei einem breitbandigeren Signal erreicht. Die CS-basierte Signalverarbeitung erreicht darüber hinaus eine Verbesserung des *Signalpeak-zu-Rauschverhältnisses* (*peak-to-noise ratio*, PNR) und damit der Zieldetektionsfähigkeit des Sensors. Mittels Messungen mit einem Digitalradarprototypen wird gezeigt, dass die neue schmalbandigere Wellenform und der CS-basierte Signalverarbeitungsansatz genauso leistungsfähig sind wie ein vergleichbares breitbandiges OFDM Signal, welches dieselbe Auflösung erreicht.

Der entwickelte *Random Multiplexing* (RM) Ansatz erlaubt es mehreren Sendern desselben Radarsystems gleichzeitig und durchgängig im gleichen Frequenzband zu senden. Dies wird dadurch erreicht, dass die Elemente des diskreten Zeit-Frequenzbereichs des Signals zufällig und disjunkt auf die einzelnen Sender verteilt werden. Im Gegensatz zum sonst gebräuchlichen *Zeitmultiplex-* (*time-division multiplexing*, TDM) und *Frequenzmultiplexverfahren* (*frequency-division multiplexing*, FDM) verursacht der RM Ansatz keinerlei Einbußen bei der Eindeutigkeit von Abstand und Geschwindigkeit. Durch die Erweiterung der Signalauswertung um einen mehrkanalfähigen CS Algorithmus wird zusätzlich die Signalauswertung und Bildgebung verbessert. Mit *Codemultiplexverfahren* (*code-division multiplexing*, CDM) wird ein weiterer MIMO Ansatz untersucht, welcher sich die Codediversität des OFDM Signals zunutze macht. Es werden drei verschiedene CDM MIMO OFDM Ansätze entwickelt, welche unterschiedliche Vorteile und Beschränkungen hinsichtlich ihrer Abstands- und Geschwindigkeitseindeutigkeit aufweisen. Zusätzlich werden hybride MIMO Konzepte vorgestellt, welche zwei bekannte oder neue MIMO OFDM Konzepte miteinander kombinieren. Der sich dadurch ergebende hybride Ansatz ermöglicht es dann, die Beschränkungen der beiden enthaltenen Ansätze zu mindern, aber gleichzeitig von den Vorteilen beider zu profitieren.

Ein robuster Radarbetrieb in Koexistenz mit anderen, nicht-kooperativen Radarsensoren in der näheren Umgebung ist eine wichtige Voraussetzung in vielen Radaranwendungen. In dieser Arbeit wird daher zunächst der Einfluss von heute weit verbreiteten *Frequency-Modulated Continuous-Wave* (FMCW) Radaren auf die Signalverarbeitung und Bildgebung eines OFDM Radars untersucht. Anschließend werden drei Methoden zur Interferenzminderung entwickelt, welche eine ungestörte Bildgebung ermöglichen. Sind nur wenige Elemente im Zeit-Frequenzbereich des OFDM Signals von der Interferenz betroffen, genügt es, diese durch Nullsetzen vor der Auswertung zu entfernen. Damit wird der

störende Einfluss der Interferenz auf die Radarbildgebung verhindert, jedoch wird dabei auch der Integrationsgewinn des OFDM Signals um die Anzahl der entfernten Elemente verringert. Werden diese allerdings durch eine zusätzliche 2D-CS Signalrekonstruktion wiederhergestellt, kann der ursprüngliche Gewinn erreicht und zusätzlich das PNR verbessert werden. Zusätzlich zu den Interferenzminderungsmethoden wird auch ein neuer Signalverarbeitungsansatz entwickelt, welcher eine unveränderte Signalauswertung auch bei Störung durch Signale erlaubt, die eine vergleichsweise geringe instantane Bandbreite und hohe schmalbandige Leistung aufweisen.

Contents

1 Introduction **1**

2 Signal Processing of Digitally Modulated OFDM Radars **7**
2.1 Digital OFDM Modulation 8
2.2 Radar Imaging 11
2.2.1 Range Evaluation 15
2.2.2 Velocity Evaluation 17
2.2.3 2D Range-Velocity Map 19
2.3 MIMO OFDM 19
2.3.1 MIMO Array 19
2.3.2 MIMO OFDM Processing 22
2.3.3 Spectral Interleaving 24
2.3.4 Angle Estimation 27
2.4 Compressed Sensing 28
2.4.1 Approximate Message Passing 31
2.4.2 Split Augmented Lagrangian Shrinkage Algorithm . . . 33
2.4.3 Compressed Sensing Applied to Radar 34
2.5 Measurement Setups and Signal Parametrization 35

3 High-Resolution OFDM Radar with Reduced Baseband Bandwidth **37**
3.1 Frequency Agile Sparse OFDM 39
3.1.1 Transmit Signal Design and Generation 40
3.1.2 Receive Signal 42
3.2 Multidimensional Signal Recovery Using Compressed Sensing Approaches 44
3.2.1 2D-CAMP 48
3.2.2 2D-HAMP 52
3.2.3 2D-SALSA 55
3.2.4 Sensing Matrix Design and Recovery Guarantee 56

3.2.5 Pseudo PNR . . . 58
3.2.6 Complexity of the 2D Recovery . . . 58
3.3 Performance Evaluation and Analysis . . . 59
3.3.1 Radar Parametrization and CS Algorithm Tuning . . . 60
3.3.2 Recovery of Weak Targets . . . 60
3.3.3 Recovery of Close Targets . . . 63
3.3.4 Recovery of Extended Targets . . . 65
3.3.5 Recovery of Highly Thinned Signals . . . 68
3.4 Summary . . . 71

4 Novel Multiplexing Methods for MIMO OFDM Radars 73
4.1 Random Frequency-Time-Division MIMO OFDM . . . 73
4.1.1 Multi-Channel 2D Compressed Sensing Processing . . . 76
4.1.2 Analysis and Comparison to IOFDM . . . 78
4.2 Code-Division Multiplexing . . . 82
4.2.1 Zero-Correlation Zone CDM . . . 86
4.2.2 Modified Repeated Symbol CDM . . . 90
4.2.3 Auto-Correlation-Based CDM . . . 95
4.2.4 Analysis and Comparison . . . 103
4.3 Hybrid Approaches . . . 110
4.4 MIMO SOFDM . . . 113
4.5 Summary . . . 115

5 Robust Signal Processing and Coexistence of OFDM Radars and Traditional Automotive Radars 117
5.1 Impact of an FMCW Interference on the OFDM Radar Operation and Evaluation . . . 120
5.2 Impact of Interference on SOFDM . . . 124
5.3 Interference Detection . . . 126
5.4 Interference Mitigation . . . 129
5.4.1 Detect and Remove: Zeroing . . . 130
5.4.2 Detect and Mitigate: Leveling . . . 130
5.4.3 Detect and Recover: CS Signal Recovery . . . 131
5.4.4 Single-Stage Recovery: Dual-CS . . . 132
5.4.5 Evaluation and Comparison . . . 135
5.5 Summary . . . 138

6 Conclusion **141**

A Additional Notes on 2D CS **145**
A.1 Mathematical Notations and Relations 145
A.2 Kronecker CS for SOFDM 145
A.3 Equivalence of 1D- and 2D-AMP 146
A.4 Equivalence of 1D- and 2D-SALSA 148
A.5 Coherence of the Range and Doppler Dimensions in SOFDM . 149

B Derivation of the ITCT Part of the Range Evaluation **151**

C Optimal Design Parameters to Construct Complex-Valued ZCZ Sequences **153**

D Derivation of the MRS Velocity Profile **155**

E Additional Interference Measurement Results **157**

Index of Symbols, Indices, and Acronyms **159**

Bibliography **167**

1 Introduction

Driven by the growing demand for automotive comfort and safety systems, the development of enhanced and new radar systems and modulation concepts has made considerable advances in the last decades [1]. At the same time, also the functionality, tasks, and requirements on these systems have changed, demanding ever higher resolution, more precise imaging, robustness, reliability, or flexible and tuneable operation [2]. The task of traditional radar sensors used to be mainly distance measurement, whereas today the operational fields are becoming more diverse, and more advanced functional requirements such as target angle measurement or flexible waveforms are on demand in order to obtain more pictorial and accurate images of complex environments enabling situational awareness, environment perception, and prediction [1].

At the same time, advances in CMOS technology and growing availability of digital processing power open up completely new possibilities in digital signal processing [1], [3]. Driven by these advancements, a paradigm change can be observed in radar research and development with signal generation and processing shifting more and more from the analog to the digital domain. A simplified basic homodyne digital multiple-input multiple-output (MIMO) radar system is sketched in Fig. 1.1. The system is divided into two domains: One is the digital domain, comprising the digital transmit (Tx) signal generation as well as the digital receive (Rx) signal pre-processing, and the radar imaging unit. The analog front end is connected via an in-phase/quadrature (IQ) (de)modulator for each Tx and Rx path. The analog domain encompasses an IQ mixer, for shifting the sampled baseband signal to the desired radio frequency (RF) carrier, and the radar antenna array. For simplification, amplifiers and filters are omitted. So the essential function of the analog front end is merely to up- and downconvert the signal to the RF carrier in the Tx and Rx paths, respectively, and to emit the EM wave into the medium and receive it again. As both signal generation and evaluation are performed digitally, the complexity of the analog front end is reduced, and more flexibility is introduced to the radar signal modulation and

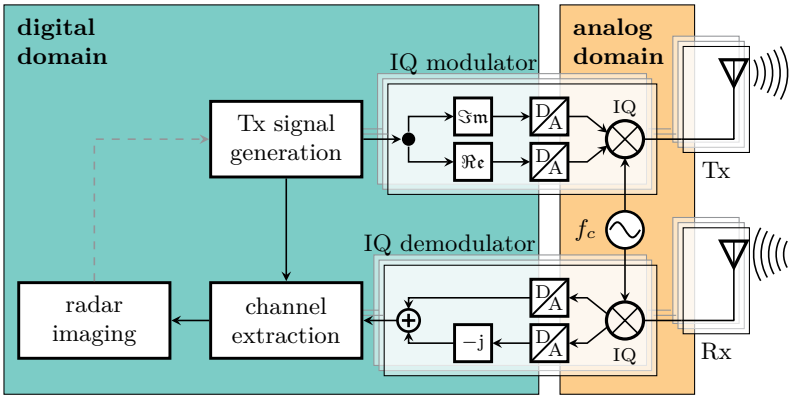


Fig. 1.1: Simplified fundamental structure of a digital radar system.

processing. This opens up completely new possibilities in waveform design and modulation, and new or so far impractical concepts become viable. Probably the most known digital radar modulation concept is orthogonal frequency-division multiplexing (OFDM). It has attracted increasing interest in radar research in the last two decades [4]–[14]. It was first proposed for radar operation in 2000 by Levanon [4]–[6], but its basic concept dates back to the 1960's, where Chang [15] proposed a so-called multi-carrier concept to transmit data simultaneously on multiple subbands. Back then, FDM systems used to be composed of a bank of filters and oscillators on the transmit and receive sides, making them complex and bulky. Weinstein and Ebert [16] showed that the OFDM baseband modulation and demodulation can be easily implemented digitally using the Discrete Fourier Transform (DFT) and the inverse Discrete Fourier Transform (IDFT), which might be considered the main breakthrough that made OFDM finally conceivable. Nevertheless, it took until the late 1980's when advances in technology, especially in digital signal processing, finally made OFDM feasible [17]. Since then OFDM gradually established itself in communications applications such as asymmetric digital subscriber line (ADSL), very-high-speed digital subscriber line (VDSL), digital audio broadcasting (DAB), digital video broadcasting – terrestrial (DVB-T), wireless local area networks (WLAN), or long-term evolution (LTE) standard [18]–[21].

Beyond this, recent advances on digital OFDM radars showed their great potential and opportunities for future generation radar systems [3], [22]–[24]. The OFDM signal employs frequency diversity by dividing a large allocated bandwidth into a large number of discrete sub-bands, so-called subcarriers. Furthermore, the radar measuring frame constitutes a temporal subdivision of the measurement time into short time intervals, so-called OFDM symbols, which introduces time diversity. Moreover, each of these time-frequency fragments typically carries a so-called modulation symbol, for example using phase modulation, providing additional code diversity to the signal. Due to this special signal structure, OFDM provides a high degree of freedom in the design of the emitted waveforms, since each of these discrete time-frequency pixels can be configured arbitrarily allowing a great variety of signal shapes to be generated. In addition, the growing digital processing power enables development of entirely new and advanced high-performance signal processing or waveform concepts that make digital radars even more powerful and open up new perspectives.

This thesis is concerned with signal processing and waveform design for digital OFDM radars, where its goals are the following:

- Development of a *novel digital waveform design and corresponding signal processing technique* to break the close relation between achievable range resolution and modulation bandwidth. OFDM radars require to sample the modulation and measurement bandwidth at both the transmitter and receiver. When demanding high range resolution, high modulation bandwidths are required, which constitutes a major limiting factor on the radar performance. Therefore, a novel OFDM waveform and corresponding high-performance signal evaluation concept is developed that achieves high range resolution at a considerably lower sampling rate and a narrower modulation bandwidth.

- Development of *novel MIMO OFDM concepts* utilizing the time, frequency, and code diversity of OFDM. So far, its flexibility and diversity has barely been exploited in MIMO signal design. Novel MIMO OFDM radar concepts are developed that take advantage of these properties, while being competitive or superior to the state-of-the-art FDM MIMO concept.

- Investigation of the *interference impact of state-of-the-art frequency-modulated continuous-wave (FMCW) radars and development of suitable*

countermeasures. The goal is to gain a better understanding of interference effects in OFDM radar signal evaluation and, based on that, to develop suitable interference countermeasures that enable interference-robust OFDM radar operation in coexistence with FMCW radars.

A separate chapter is devoted to each of these goals, and the work is organized as follows: **Chapter 2** first provides an introduction to the state-of-the-art OFDM radar signal generation, processing, and imaging of both single-channel and MIMO setups. Since in this thesis compressed sensing (CS) methods are repeatedly utilized in various contexts, the second part of the chapter provides an introduction to the concept of CS and CS algorithms. Finally, in the last part, a brief overview of the utilized measurement systems and evaluation details is given.

In **Chapter 3**, the bandwidth and sampling rate restrictions of high-resolution OFDM radar imaging are addressed, and a novel digital waveform design and corresponding signal processing technique are present to solve this obstructive issue. The developed adapted waveform and its generation is presented in the first part of this chapter. In the second part, the CS-based signal evaluation technique is presented. Since the proposed processing involves 2D CS methods, the extensions and adaptions to the CS concept and algorithms to this specific application are addressed, and the developed CS-based radar imaging is shown. Afterwards, the new waveform and processing concept is verified and compared to the standard approach using both simulations and measurements.

Chapter 4 deals with the novel MIMO OFDM radar concepts. In the first part, a MIMO concept is developed that combines the time and frequency diversity of OFDM and allows to achieve the maximum unambiguous range and velocity of the system. The concept is enhanced by utilizing an extension of the 2D CS method of Chapter 3 in the signal evaluation, which provides an additional improvement in the radar imaging. The focus of the second part is on code-division multiplexing (CDM) MIMO concepts. Three different strategies for channel separation via subcarrier coding are developed and presented. Afterwards, a comparison of the novel multiplexing methods among each other and with the standard interleaving FDM MIMO is given. In the third part of the chapter, hybrid MIMO concepts are presented that combine either two of the novel concepts or a novel and the standard FDM concept into a new one that enjoys the advantages of both, while having fewer potential limitations

than either on its own. Finally, the MIMO realization of the novel modulation concept from Chapter 3 is developed and verified using measurements.

Chapter 5 addresses the interference impact of traditional FMCW radar signals on OFDM and presents suitable countermeasures. First, the impact of an FMCW interference on the different OFDM processing domains and stages is analyzed. In the second part, an interference detection method based on power detection in the spectrogram is developed and verified. Then, different interference mitigation methods are presented, and their ability to eliminate the impact of the interference from the radar imaging is verified and compared based on measurements.

The thesis is concluded in **Chapter 6** with a summary of the achieved results and goals.

2 Signal Processing of Digitally Modulated OFDM Radars

About two decades ago, Levanon first suggested multi-carrier waveforms, i.e., OFDM, for radar usage [5]. The increasing research interest thereafter was characterized by the auspicious idea of developing a system that would enable joint radar and communications operations in so-called RadCom systems [8], [10], [13], [14], [25]–[27]. In communications technology, OFDM has already established itself within a short time due to its spectral efficiency and high achievable throughput [20], [21]. Yet, the dual functionality of the RadCom concept comes at the expense of freedom and flexibility in signal design. As a result, recent efforts and research have refocused on pure radar functionality and the development of advanced and new radar techniques that take advantage of the new benefits and perspectives digital radar processing is offering [3], [23], [24], [28]–[36]. This approach is also pursued hereafter. A key development in OFDM radar imaging was the introduction of the Fast Fourier Transform (FFT)-based range-Doppler processing [10], [11], [13] enabling efficient and fast radar imaging. The derivation of the state-of-the-art OFDM radar basics and the 2D-(I)DFT-based radar imaging in Sections 2.1 and 2.2, respectively, are based on the prior works [13], [14], [20], [24]. In Section 2.3, the state-of-the-art MIMO OFDM radar processing using spectral interleaving [37] and general MIMO radar basics are introduced. Due to the all-digital signal evaluation, new possibilities arise in signal processing. In this thesis, especially signal compression and sparse recovery using CS methods is repeatedly utilized and discussed in various applications. Therefore, CS basics for radar signal processing are introduced in Section 2.4. Finally, in Section 2.5, the OFDM signal parametrization applied in simulations and measurements throughout this work are discussed, and the utilized radar systems are described.

2.1 Digital OFDM Modulation

Typically, an OFDM signal that is suitable for both communication and radar applications is composed of a sequence of M OFDM symbols x_m, where $m \in \mathbb{Z}_M$, $\mathbb{Z}_M = \{0, \dots, M-1\}$. Each of these OFDM symbols again is composed of N orthogonal sinusoids, so-called subcarriers, each modulated with a modulation symbol d_{mn} taken from a given modulation alphabet $\mathcal{A}$. If not stated otherwise, $\mathcal{A}$ is assumed to be quadrature phase-shift keying (QPSK). Where in communication and RadCom applications these symbols carry the data of interest, in pure radar applications, the modulation symbols may be chosen at random offering an additional degree of freedom in adaptive waveform design. The subcarriers become orthogonal by applying an equidistant frequency spacing of

$$\Delta f = \frac{1}{T} \,, \tag{2.1}$$

where T is the duration of each OFDM symbol. This yields that each subcarrier wave always contains exactly an integer number of cycles. Consequently, the signal bandwidth becomes $B = N\Delta f$. In Fig. 2.1, the spectrum of a single OFDM symbol is shown. It is composed of a sum of sinc-functions, each corresponding to a subcarrier [12]. The subcarrier orthogonality becomes apparent in the fact that at the global maximum of each subcarrier spectrum all others are zero. Since the signal is only evaluated at frequencies $n\Delta f$, the different subcarriers do not interfere with each other. In the following, the collection of N contiguous subcarriers and the sequence of M OFDM symbols that constitute a single

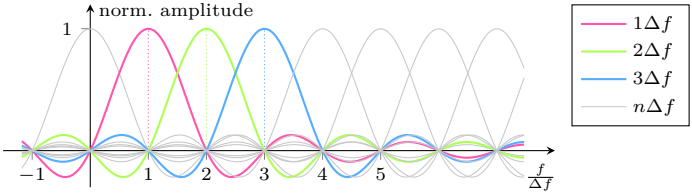


Fig. 2.1: Baseband spectrum of an OFDM symbol composed of subcarriers with spacing Δf. At the subcarrier frequencies $n\Delta f$, all but one subcarrier are zero. Therefore, the subcarriers are orthogonal.

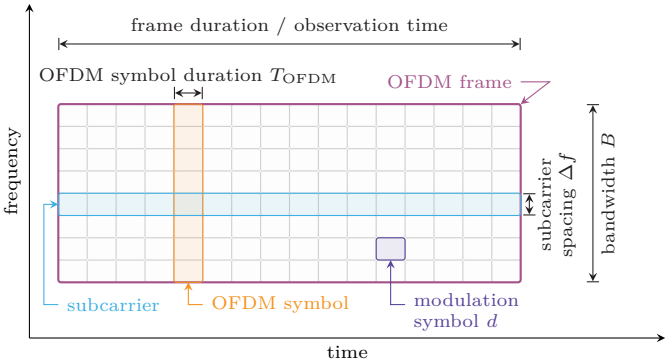


Fig. 2.2: Schematic of the OFDM spectrogram.

measurement is also referred to as a *frame*.

The continuous-time complex envelope of the mth OFDM symbol is

$$x_m(t) = \frac{1}{\sqrt{N}} \sum_{n=0}^{N-1} d_{mn}\, \mathrm{e}^{\mathrm{j}2\pi n \Delta f t}, \quad t \in [0, T)\,. \tag{2.2}$$

With sampling rate $f_s{=}N/T$ the discrete-time complex envelope of (2.2) becomes

$$x_m[k] = \frac{1}{\sqrt{N}} \sum_{n=0}^{N-1} d_{mn}\, \mathrm{e}^{\mathrm{j}2\pi \frac{nk}{N}}, \quad k = \lfloor t f_s \rfloor \tag{2.3}$$

with $k{\in}\mathbb{Z}_M$ the discrete fast-time index within an OFDM symbol of duration T. Accordingly, m represents the slow-time index of the frame. Consequently, (2.3) corresponds to the IDFT of the sequence $(d_{m0}, d_{m1}, \ldots, d_{m(N-1)})$. If N is a power of two, it may be implemented efficiently using an inverse Fast Fourier Transform (IFFT). Through this, the entire baseband modulation of OFDM is efficiently achieved in digital form.

The OFDM signal frame composed of N subcarriers and M OFDM symbols may be depicted in a 2D lattice or matrix notation. To this end, the modulation symbols d_{mn} are arranged in a matrix $\boldsymbol{d}{=}(d_{mn}){\in}\mathbb{C}^{M\times N}$. A schematic illustration of an OFDM frame is shown in Fig. 2.2. Basically, the elements d_{mn}

are the coefficients of the baseband OFDM transmit signal *spectrogram*.

In matrix notation, the discrete-time signal (2.3) of the entire frame is obtained by row-wise IDFTs of $\boldsymbol{d}$ yielding the complex envelope lattice

$$\boldsymbol{x} = \boldsymbol{d}\boldsymbol{U}^{\mathsf{H}}, \quad \boldsymbol{x} \in \mathbb{C}^{M\times N} \tag{2.4}$$

with elements (2.3). The columns hold the fast-time samples (k) and the rows the slow-time samples (m). $\boldsymbol{U}^{\mathsf{H}}$ is the unitary square IDFT matrix[1], which equals the inverse of the unitary square DFT matrix $\boldsymbol{U}$. Their respective elements are given by

$$u_{il} = \frac{1}{\sqrt{N}}\,\mathrm{e}^{-\mathrm{j}2\pi\frac{il}{N}}\ \text{(DFT)} \quad \text{and} \quad \bar{u}_{il} = \frac{1}{\sqrt{N}}\,\mathrm{e}^{\mathrm{j}2\pi\frac{il}{N}}\ \text{(IDFT)}\,. \tag{2.5}$$

To avoid so-called inter-symbol interference (ISI) caused by multipath propagation, i.e. different path delays at the receiver, and imperfect rectangular pulse shapes, a guard interval is usually inserted between consecutive OFDM symbols before transmission. This guard interval should be at least as long as the longest expected path delay of any spectral component, as the delay causes consecutive OFDM symbols to fade into each other, which causes ringing artifacts and self interference [11], [16], [17]. For OFDM radars, this translates into the maximum expected measurable distance. Two designs of the guard interval are prevalent: an empty guard and a cyclic prefix (CP). An empty guard would prevent symbols to fade into each other, however, it also leads to inter-carrier interference (ICI) at the receiver. On the other hand, when using a CP, first introduced by [39], a copy of the symbol tail of length $0 \leq T_{\mathrm{cp}} \leq T$ of each OFDM symbol is placed in front of it. Thereby, the actual symbol duration is extended to $T_{\mathrm{OFDM}} = T + T_{\mathrm{cp}}$, and the Rx signal becomes the cyclic convolution of the Tx signal and the channel impulse response (CIR), which prevents ICI. If the CP is longer than the CIR, the signal remains orthogonal over dispersive channels. For convenience in digital processing, T_{cp} should be an integer multiple of the sample duration $1/f_s$ resulting in $N_{\mathrm{cp}} = T_{\mathrm{cp}} f_s$ being the number of samples of the CP. In matrix notation, inserting the CP is equivalent to copying the last N_{cp} columns of $\boldsymbol{x}$ and appending them in front of the matrix to obtain the extended matrix $\boldsymbol{x}^{\mathrm{cp}} \in \mathbb{C}^{M\times(N+N_{\mathrm{cp}})}$. For conversion to

[1] A complex square matrix $\boldsymbol{U}$ of size $N\times N$ is unitary if its inverse equals its conjugate transpose: $\boldsymbol{U}^{\mathsf{H}} = \boldsymbol{U}^{-1}$ and $\boldsymbol{U}^{\mathsf{H}}\boldsymbol{U} = \boldsymbol{U}\boldsymbol{U}^{\mathsf{H}} = \boldsymbol{I}_N$ [38, p. 223].

analog domain, this matrix is serialized row-wise and fed into an IQ-unit, where the signal is sampled at Nyquist frequency and converted to the RF carrier frequency f_c, as illustrated in Fig. 1.1. Through this, the emitted RF Tx signal of (2.2) becomes

$$x_m^{\mathrm{RF}}(t) = \frac{1}{\sqrt{N}} \sum_{n=0}^{N-1} d_{mn}\, \mathrm{e}^{\mathrm{j}2\pi(n\Delta f + f_c)t}, \quad t \in [0, T)\ . \tag{2.6}$$

The described typical baseband processing chain for the Tx signal of an OFDM radar is illustrated in the first row of Fig. 2.3.

2.2 Radar Imaging

In the channel, the transmitted OFDM signal is reflected from surrounding objects and scattered back to the radar's receive unit. Neglecting multiple reflections between different point scatterers, the time-dependent time of travel of the RF Tx signal (2.6) with respect to the hth point target at range R_h and relative velocity v_h is well approximated in continuous time by

$$\tau_h(t) = \frac{2R_h}{c} + \frac{2v_h}{c}t = \frac{2R_h}{c} - \frac{f_{d,h}}{f_c}t\,, \tag{2.7}$$

where higher order motion terms are neglected, $f_{d,h} = -2v_h f_c/c$ is the Doppler shift due to the target motion, and c is the speed of light. At the Rx unit, the superposition of H target reflections are first down-converted to baseband using the same oscillator as for the up-conversion, which gives the continuous-time baseband signal

$$r_m(t) = \sum_{h=1}^{H} \alpha_h x_m^{\mathrm{RF}}\big(t - \tau_h(t)\big)\, \mathrm{e}^{-\mathrm{j}2\pi f_c t} \tag{2.8}$$

$$= \sum_{h=1}^{H} \sum_{n=0}^{N-1} \alpha_h d_{mn}\, \mathrm{e}^{\mathrm{j}2\pi n\Delta f t}\, \mathrm{e}^{-\mathrm{j}2\pi(n\Delta f + f_c)\frac{2R_h}{c}}\, \mathrm{e}^{-\mathrm{j}2\pi(n\Delta f + f_c)\frac{2v_h t}{c}} \tag{2.9}$$

with α_h the reflection and channel dependent magnitude that is assumed to be constant across the time-bandwidth coverage of the frame. Since the target reflections are coherently additive in the overall processing, in the following, it

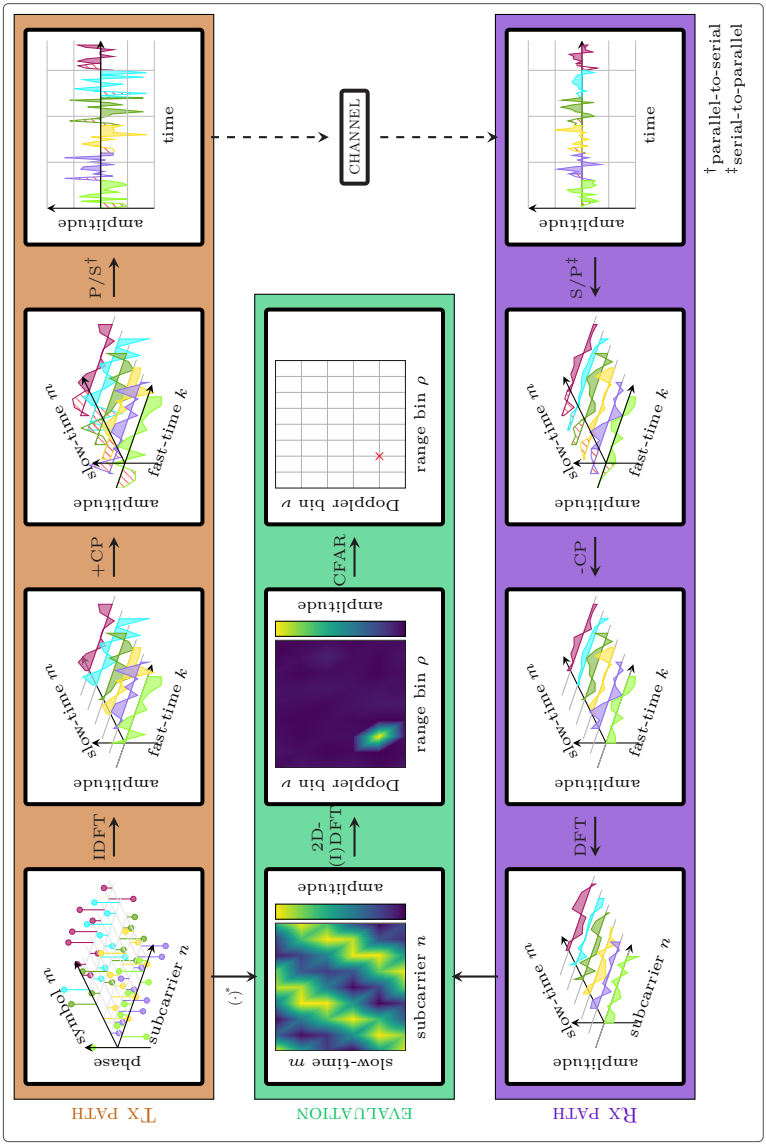


Fig. 2.3: OFDM radar signal processing and evaluation chain.

is assumed for simplicity that $H = 1$, and the subscript h is omitted.

For digital evaluation, the signal is sampled with at least the Nyquist frequency, i.e. w.l.o.g. $t = kT/N + mT_{\mathrm{OFDM}}$, and divided into M chunks of length T_{OFDM} or $N + N_{\mathrm{cp}}$ samples that resemble the receive OFDM symbols. Next, the CP is removed by discarding the initial N_{cp} samples of each OFDM symbol. Eventually, the complex envelope of the mth OFDM symbol is given by

$$r_m[k] = \alpha \sum_{n=0}^{N-1} \underbrace{d_{mn}\, \mathrm{e}^{\mathrm{j}2\pi \frac{nk}{N}}}_{\rightarrow (2.3)} \underbrace{\mathrm{e}^{-\mathrm{j}2\pi f_c \frac{2R}{c}}}_{\substack{\text{(I)} \\ \text{const.}}} \underbrace{\mathrm{e}^{-\mathrm{j}2\pi n \Delta f \frac{2R}{c}}}_{\substack{\text{(II)} \\ \text{range term}}} \underbrace{\mathrm{e}^{\mathrm{j}2\pi f_d m T_{\mathrm{OFDM}}}}_{\substack{\text{(III)} \\ \text{velocity term}}} \times \underbrace{\mathrm{e}^{\mathrm{j}2\pi f_d \frac{kT}{N}}}_{\substack{\text{(IV)} \\ \text{ICI term}}} \underbrace{\mathrm{e}^{-\mathrm{j}2\pi n \Delta f \frac{2v}{c} \frac{kT}{N}}}_{\substack{\text{(V)} \\ \text{fast-time compression}}} \underbrace{\mathrm{e}^{-\mathrm{j}2\pi n \Delta f \frac{2v}{c} m T_{\mathrm{OFDM}}}}_{\substack{\text{(VI)} \\ \text{migration term}}}, \tag{2.10}$$

which is a delayed and compressed or stretched version of the transmitted signal (2.3). It is composed of several phase terms, where the very first terms correspond to the original Tx signal. The phase term (I) is time and subcarrier invariant and therefore considered a target dependent constant for all samples. The phase of (II)

$$\varphi_R[n] = -2\pi n \Delta f \frac{2R}{c} \tag{2.11}$$

progresses at a frequency proportional to R along the subcarriers thus frequency dimension (n), while the phase of (III)

$$\varphi_v[m] = 2\pi f_d m T_{\mathrm{OFDM}} = -2\pi \frac{2v f_c}{c} m T_{\mathrm{OFDM}} \tag{2.12}$$

progresses at a frequency proportional to v along the time dimension (m) of the frame. Both phases are of central interest in radar imaging and target detection. Typically, the components (IV) to (VI) are negligible since: (IV) the motion induced Doppler is small, i.e. $f_d \ll \Delta f$; (V) the signal is narrowband compared to its RF frequency, i.e. $f_c \gg B$ (narrowband assumption); and (VI) the change of the target range within the frame due to its motion is $vMT_{\mathrm{OFDM}} < \Delta R$. For a comprehensive discussion see [40], which also discusses countermeasures against range migration and ICI in case (V) and (VI) are not negligible. In this thesis, it is assumed that the above assumptions are satisfied and the terms (IV) to (VI) are neglected unless explicitly addressed.

Similar to the transmit signal processing, the samples of (2.10) may be arranged in a 2D lattice $\boldsymbol{r} \in \mathbb{C}^{N \times M}$, where the rows hold the slow-time samples (m), i.e. the OFDM symbols, and the columns the fast-time samples (k). In the next step, the envelope $\boldsymbol{r}$ is separated into its subcarrier components, i.e., the spectrum of each OFDM symbol is computed via a DFT, which inverts the IDFT modulation of the Tx path. This operation corresponds to a Short-Time Fourier Transform (STFT) of duration T and length N across the fast-time samples and gives the modulated Rx spectrogram

$$\boldsymbol{y} = \boldsymbol{r}\boldsymbol{U} \tag{2.13}$$

with $\boldsymbol{U}$ the unitary square DFT matrix of dimension N with elements u_{li} (2.5). Note that no additional windowing is applied in this step. In the spectrogram (2.13), the columns hold the frequency components of the signal, i.e. the subcarriers, and the $[m, n]$th element of $\boldsymbol{y}$ is given by

$$y_{mn} = d_{mn}\alpha\, \mathrm{e}^{-\mathrm{j}2\pi \frac{2R}{\lambda_c}}\, \mathrm{e}^{\mathrm{j}\varphi_R[n]}\, \mathrm{e}^{\mathrm{j}\varphi_v[m]}\ . \tag{2.14}$$

Since the range and velocity dependent phases progress along different dimensions of the spectrogram, there is no substantial coupling between R and v enabling their independent identification. However, first, the modulation d_{mn} must be eliminated to access the desired phases. Since $\boldsymbol{d}$ is known in the coherent monostatic setup, this is conveniently achieved by dividing each component (2.14) by d_{mn} [11]. This step is universal and together with the following range and Doppler evaluation it yields the matched filter for the OFDM radar [9], [41]. In the most commonly used modulation alphabets in OFDM radar, e.g. QPSK or generally L-ary PSK, the elements have uniform amplitudes i.e. $|d_{mn}| = \text{const.}\ \forall\, m, n$. Hence, in this case, the division with the inverse equals the multiplication with the complex conjugate and, if $|d_{mn}| \neq 1$ and non-zero, by a normalization constant. The latter may be neglected, because it is only a scaling not influencing the further processing. This formulation is favored in this thesis as only unitary alphabets are deployed and, moreover, some proposed processing approaches are facilitated by this in the first place. Eventually, the (demodulated) Rx spectrogram is extracted by

$$\boldsymbol{\mathcal{D}} = \boldsymbol{y} \circ \overline{\boldsymbol{d}} \tag{2.15}$$

with $\circ$ the element-wise or Hadamard product and $\overline{\boldsymbol{d}}$ the element-wise complex conjugate of $\boldsymbol{d}$. The elements of the resulting demodulated spectrogram $\boldsymbol{\mathcal{D}}$ are

$$\mathcal{D}_{mn} = y_{mn}/d_{mn} = y_{mn}\left(d_{mn}\right)^* = \alpha\, \mathrm{e}^{-\mathrm{j}2\pi \frac{2R}{\lambda_c}}\, \mathrm{e}^{\mathrm{j}\varphi_R[n]}\, \mathrm{e}^{\mathrm{j}\varphi_v[m]}\ . \tag{2.16}$$

The simplified baseband processing chain of the Rx signal is illustrated in the bottom row of Fig. 2.3.

The state-of-the-art range-Doppler processing of OFDM radars is based on discrete Fourier transforms to extract the range and Doppler dependent frequencies describing the phase rotations of the two exponential terms in (2.16) [10], [13], [42]. Moreover, the estimation of R and v are independent of each other and thus may be carried out in arbitrary order.

2.2.1 Range Evaluation

The target range is evaluated by an IDFT along the frequency dimension of the spectrogram (2.15), i.e. the rows of $\boldsymbol{\mathcal{D}}$, which gives the range matrix or *range map*

$$\boldsymbol{\mathcal{R}} = \left(\boldsymbol{\mathcal{D}} \circ \boldsymbol{\Psi}\right)\boldsymbol{U}^{\mathsf{H}}\,. \tag{2.17}$$

In order to suppress sidelobes caused by the finite range IDFT and the subsequent velocity DFT, a windowing matrix $\boldsymbol{\Psi} \in \mathbb{C}^{M\times N}$ is applied. It holds complex window weighting coefficients given by the Kronecker product of the two basic 1D row and column window vectors of length M and N, respectively. Eventually, the coefficients of the range map (2.17) are

$$\mathcal{R}_m[\rho] = \alpha\, \mathrm{e}^{-\mathrm{j}2\pi \frac{2R}{\lambda_c}}\, \mathrm{e}^{\mathrm{j}\varphi_v[m]}\, \frac{1}{\sqrt{N}} \sum_{\rho=0}^{N-1} \Psi_{mn}\, \mathrm{e}^{-\mathrm{j}2\pi n \Delta f \frac{2R}{c}}\, \mathrm{e}^{\mathrm{j}2\pi \frac{n\rho}{N}} \tag{2.18}$$

$$= \alpha\, \mathrm{e}^{-\mathrm{j}2\pi \frac{2R}{\lambda_c}}\, \mathrm{e}^{\mathrm{j}\varphi_v[m]}\, \sqrt{N}\psi_m[\rho - \tfrac{2RB}{c}] \tag{2.19}$$

with Ψ_{mn} the $[m,n]$th element of $\boldsymbol{\Psi}$ and $\psi_m[\rho]{=}[\boldsymbol{\Psi}\boldsymbol{U}^{\mathsf{H}}]_{m\rho}$ the $[m,\rho]$th element of $\boldsymbol{\Psi}\boldsymbol{U}^{\mathsf{H}}$. For typical windowing functions, ψ_m and therefore $\mathcal{R}_m[\rho]$ (2.19) is only significantly different from zero at

$$\hat{\rho} = \left\lfloor \frac{2RB}{c} \right\rceil \tag{2.20}$$

and approximately zero for all other values. Here, $\lfloor \cdot \rceil$ denotes the rounding to the nearest integer.

Range resolution. Provided that the signal of bandwidth B is sampled at least at Nyquist rate, the *range resolution* is

$$\Delta R = \frac{c}{2B} = \frac{c}{2N\Delta f} \,. \tag{2.21}$$

Maximum unambiguous range. The *maximum unambiguous range* R_{ua} achievable by an OFDM radar signal is determined by the periodicity $N_{\mathrm{period}} \leq N$ of the IDFT and is upper bound by the processing interval T through

$$R_{\mathrm{ua}} = N_{\mathrm{period}} \Delta R \quad \leq \quad R_{\mathrm{ua}}^{\mathrm{max}} = \frac{cT}{2} \,. \tag{2.22}$$

In a dense OFDM signal, where all subcarriers are occupied and evaluated, it holds that $N = N_{\mathrm{period}}$. In most single-input single-output (SISO) OFDM radar applications, R_{ua} is of little importance since signals of delays larger than T do not add up coherently in the IDFT due to the mismatching demodulation. This can be observed in the illustration in Fig. 2.4 that shows the case of a viable signal delay. For $\tau \geq T$, the phase of the mth transmitted symbol is reversed by the phase of the $(m+1)$th symbol at the receiver as these overlap. Since these usually differ, the signal is spread by the code of the $(m+1)$th modulation instead of being compressed by the mth. Eventually, the phases do not add up coherently in the IDFT, thus neither an ambiguity nor a peak arises.

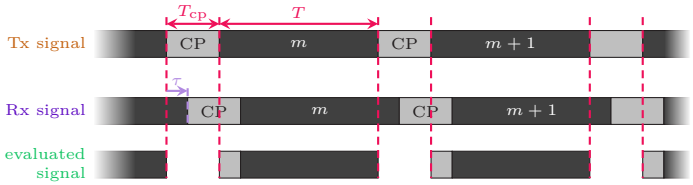


Fig. 2.4: Effectively evaluated part of the Rx signal with channel delay τ.

Maximum range. The *maximum range* is determined by the maximum delay τ a signal is allowed to experience such that the entire processing interval T contains a valid symbol. As observable in Fig. 2.4, this period is determined by T_{cp}. For delays $\tau \geq T_{\mathrm{cp}}$, the processing interval contains in part the valid symbol but also in part the preceding symbol not matching in phase. Thus, the integration gain decrease as only a part of the signal adds up coherently in the IDFT. The part of the mismatching signal additionally leads to ISI. Therefore, the *maximum range* is

$$R_{\max} = N_{\mathrm{cp}} \Delta R = \frac{c T_{\mathrm{cp}}}{2} \,. \tag{2.23}$$

In the signal design, T_{cp} should be chosen such that the maximum expected range does not exceed $R_{\max}$. At the same time, since the CP is removed at the receiver, the ratio T_{cp}/T should be as small as possible in order to maximize the effective processing time of the signal. To avoid ambiguities T_{cp} should be at most T.

2.2.2 Velocity Evaluation

The target velocity in terms of its corresponding Doppler frequency is determined by a DFT along the slow-time dimension of the spectrogram (2.15), i.e. the columns of $\boldsymbol{\mathcal{D}}$, which gives the velocity matrix or *velocity map*

$$\boldsymbol{\mathcal{V}} = \boldsymbol{U}\big(\boldsymbol{\mathcal{D}} \circ \boldsymbol{\Psi}\big) \tag{2.24}$$

with coefficients

$$\begin{aligned} \mathcal{V}_n[\nu] &= \alpha \, \mathrm{e}^{-\mathrm{j}2\pi \frac{2R}{\lambda_c}} \, \mathrm{e}^{\mathrm{j}\varphi_R[n]} \, \frac{1}{\sqrt{M}} \sum_{m=0}^{M-1} \Psi_{mn} \, \mathrm{e}^{\mathrm{j}2\pi f_d m T_{\mathrm{OFDM}}} \, \mathrm{e}^{-\mathrm{j}2\pi \frac{m\nu}{M}} \\ &= \alpha \, \mathrm{e}^{-\mathrm{j}2\pi \frac{2R}{\lambda_c}} \, \mathrm{e}^{\mathrm{j}\varphi_R[n]} \, \sqrt{M} \psi_n[\nu - f_d M T_{\mathrm{OFDM}}] \,. \end{aligned} \tag{2.25}$$

The profile $\mathcal{V}_n[\nu]$ exhibits a peak at index

$$\hat{\nu} = \big\lfloor f_d M T_{\mathrm{OFDM}} \big\rceil = \left\lfloor \frac{2 f_c v}{c} M T_{\mathrm{OFDM}} \right\rceil , \tag{2.26}$$

while the remaining elements are approximately zero.

Velocity resolution. The *velocity resolution* is inversely proportional to the observation time MT_{OFDM} and gives

$$\Delta v = \frac{c}{2 f_c T_{\mathrm{OFDM}} M} \,. \tag{2.27}$$

Maximum unambiguous velocity. The *maximum unambiguous velocity*

$$|v_{\mathrm{ua}}| = \frac{M_{\mathrm{period}}}{2} \Delta v \quad \leq \quad |v_{\mathrm{ua}}^{\mathrm{max}}| = \frac{c}{4 f_c T_{\mathrm{OFDM}}} = \frac{c \Delta f}{4 f_c (1 + T_{\mathrm{cp}}/T)} \tag{2.28}$$

is determined by the periodicity M_{period} of the DFT (2.25) where the $M_{\mathrm{period}} \leq M$. In addition, $|v_{\mathrm{ua}}^{\mathrm{max}}|$ is influenced by Δf and the ratio of prefix and symbol duration T_{cp}/T.

Maximum velocity and Doppler shift. The Rx signal in the described typical processing gets evaluated at the subcarrier frequencies $n\Delta f$. However, due to target motion, the Rx signal is modulated with the Doppler frequency f_d lifting the subcarriers out of their expected grid, as illustrated in Fig. 2.5. Compared to the Tx spectrum in Fig. 2.2, the sinc-functions, thus their peaks and zeros, are shifted by f_d while the evaluation remains at frequencies $n\Delta f$ (dotted lines). However, at $n\Delta f$ the signals are not orthogonal anymore, since not only the signal of the original subcarrier but also those of the other ones are non-zero. As a consequence, ICI proportional to f_d occurs [7], [42]. In addition, the shift also leads to a mismatch in the matched filter processing resulting in compression loss in (2.25) [7], [42]. In order to minimize the ICI, the Δf should be a factor

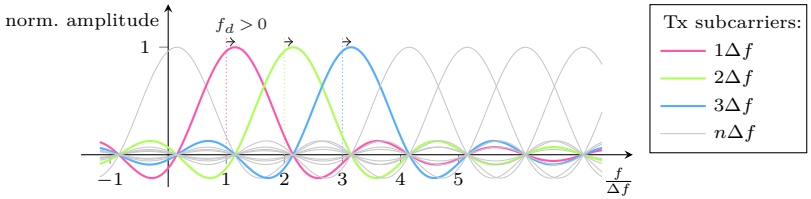


Fig. 2.5: Baseband Rx spectrum of an OFDM symbol composed of subcarriers of original Tx baseband frequencies $n\Delta f$ that experienced a Doppler shift f_d.

$\beta \geq 8$ of the maximum expected Doppler $f_{d,\max}$ in the scene [7], [13]. So

$$|v_{\max}| = \frac{|f_{d,\max}|\lambda_c}{2} = \frac{\Delta f \lambda_c}{2\beta} \quad \Leftrightarrow \quad |f_{d,\max}| = \frac{\Delta f}{\beta} \tag{2.29}$$

is a design parameter depending on the tolerated ICI loss controlled by β.

2.2.3 2D Range-Velocity Map

Usually, the order of the range and velocity estimation may be chosen arbitrarily. The entire range-velocity processing is referred to as 2D-(I)DFT processing and yields the *range-velocity image (R-v-image)*

$$\boldsymbol{\mathcal{I}} = \boldsymbol{U}\big(\boldsymbol{\mathcal{D}} \circ \boldsymbol{\Psi}\big)\boldsymbol{U}^{\mathsf{H}} \tag{2.30}$$

with coefficients $\boldsymbol{\mathcal{I}}[\nu, \rho] = \alpha \exp\{-\mathrm{j}2\pi \frac{2R}{\lambda_c}\}\sqrt{MN}\psi\big[\nu - f_d M T_{\mathrm{OFDM}}, \rho - \frac{2RB}{c}\big]$. The target reflection power gets compressed into the range-velocity bin $[\hat{\nu}, \hat{\rho}]$. The range-Doppler evaluation steps are depicted in the middle part of Fig. 2.3.

2.3 MIMO OFDM

In this section, state-of-the-art multiplexing methods and MIMO processing for OFDM radars are introduced. Beforehand, the characteristics of the investigated MIMO system that equals the radar system utilized for measurements in this work are briefly introduced. In Section 2.3.2, the typical signal processing of MIMO OFDM radars is detailed. Afterwards, in Section 2.3.3 the *spectral interleaving* concept [37] is introduced, which is the current state-of-the-art multiplexing strategy for MIMO OFDM radar. Finally, in Section 2.3.4, the utilized direction-of-arrival (DoA) estimation based on the DFT is briefly addressed.

2.3.1 MIMO Array

To achieve a spatial perception and angular localization of obstacles in the environment, MIMO radar systems employing multiple Tx and Rx antennas are used. A comprehensive overview of different MIMO radar systems and spatial signal processing is given in [43]. In this work, a MIMO system with spatially

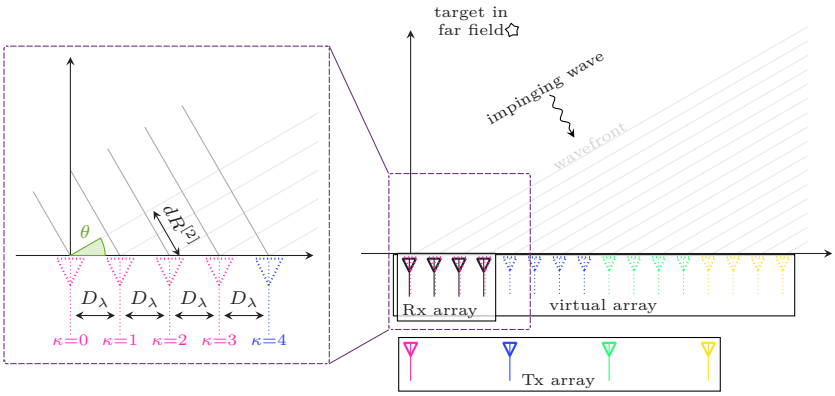


Fig. 2.6: Considered 4×4 ULA: right: physical (▽) and virtual (▽) array with impinging wavefront of a target in the far field. Left: magnification of the five virtual antennas on the far left and illustration of the geometric array and angle parameters comprising the equidistant spacing D_λ (2.31) of the virtual elements, the azimuth angle θ of the impinging wave that is measured towards the aperture front, and exemplarily for the second virtual element the resulting difference in signal path $dR^{[2]}$ (2.32) with respect to the reference element (κ=0).

different but closely spaced Tx and Rx antennas is considered. Furthermore, independent, usually mutually orthogonal waveforms are employed on the transmitters. The spatial characteristic of the impinging wave is sampled by the individual antennas. Together they constitute the physical *aperture*, which is the physical extent of the Tx and Rx array. Therefore, the size of the aperture determines the achievable angular resolution of the system [44], [45], whereas the sample length, which is the spacing of the antenna elements, determines the ambiguous region. MIMO systems have the peculiarity that their effective aperture can be increased beyond their physical one by the so-called *virtual aperture* obtained via convolution of the Tx and Rx apertures [43], [46]. Therefore, MIMO systems are superior when it comes to optimization of resolution using a minimal number of Tx and Rx antennas and thereby require less physical space. Define N_{tx} being the number of Tx antenna elements and N_{rx} the number of Rx antenna elements. Consequently, the virtual array consists of

at most $N_{\text{virt}} = N_{\text{tx}} N_{\text{rx}}$ elements [47]. The considered antenna setup here is a dense 1D uniform linear array (ULA) [48] whose virtual antenna elements are arranged uniformly on a grid with equidistant spacing D_λ, as illustrated in Fig. 2.6. With this setup, the azimuth characteristic of the impinging wave is measured. In general, non-uniform arrays, sparse arrays, different physical antenna arrangements, or a different number of elements are also conceivable [49]. In the 4×4 setup illustrated in Fig. 2.6, both the Tx and the Rx array exhibit 4 elements with equidistant spacing $4D_\lambda$ and D_λ, respectively. The far left antenna is arbitrarily declared the reference antenna. In order to enable unambiguous array steering that allows incident angles on the half plane $\theta \in [-\pi/2, \pi/2)$, the antenna element spacing must be

$$D_\lambda \leq \frac{\lambda_c}{2} \tag{2.31}$$

with λ_c the wavelength of the f_c. The condition (2.31) results in Nyquist sampling in the spatial dimension [48]. As depicted in the left image of Fig. 2.6, due to the different sensor locations, small differences in the traveled path

$$dR^{[\kappa]} = \kappa D_\lambda \sin\theta \tag{2.32}$$

of the Rx wave can be geometrically determined, where $\kappa = qN_{\text{tx}} + l$, $\kappa \in \mathbb{Z}_{N_{\text{virt}}}$ is the index of the virtual antenna and $q \in \mathbb{Z}_{N_{\text{tx}}}$ and $l \in \mathbb{Z}_{N_{\text{rx}}}$ are the respective indices of the Tx and Rx antenna element that make up this virtual element. The path difference may also be expressed by the phase difference

$$\Delta\varphi^{[\kappa]} = \frac{2\pi}{\lambda_c} dR^{[\kappa]} = \frac{2\pi}{\lambda_c} \kappa D_\lambda \sin\theta\,. \tag{2.33}$$

In the following the path from the qth Tx antenna to the target and directly reflected back to the lth Rx antenna is referred to as the $[q,l]$th MIMO path, which equals the κth virtual path. The target is assumed to be in the far field of the aperture such that $\Delta R \gg N_{\text{virt}} D_\lambda$ [50]. Hence, the target azimuth angle θ and observed relative velocity is considered constant among the channels. Eventually, the range observed in the $[q,l]$th or κth channel of the ULA gives

$$R^{[q,l]} = 2R_0 + (qN_{\text{tx}} + l) D_\lambda \sin\theta = 2R_0 + \kappa D_\lambda \sin\theta = R^{[\kappa]} \tag{2.34}$$

with $R^{[0,0]} = 2R_0$ the target range observed at the reference antenna.

2.3.2 MIMO OFDM Processing

In this section, MIMO OFDM radar signals and their processing are introduced using a more general description than is commonly given in literature such as [37], [51]. In general, an extension of the single channel concept introduced in Section 2.1 to a multiple transmitter scheme is achieved by choosing individual $d_{mn}^{[q]}$ for each transmitting channel $q \in \mathbb{Z}_{N_{\mathrm{tx}}}$. Accordingly, the Tx signal generation via IDFT (2.3) is modified such that the discrete-time transmit signal of the qth Tx channel is expressed by

$$x_m^{[q]}[k] = \frac{1}{\sqrt{N}} \sum_{n=0}^{N-1} d_{mn}^{[q]} \, \mathrm{e}^{\mathrm{j}2\pi \frac{nk}{N}} \,, \tag{2.35}$$

where the identical signal parameters are used for each Tx channel. Furthermore, the fundamental processing chain for each Tx channel remains as described in Section 2.1.

The signal at each Rx antenna is a coherent superposition of the back-scattered Tx signals. Similar to Section 2.2, only the single-target case is considered for brevity. The continuous-time signal of the mth OFDM symbol at the lth Rx channel after down-conversion to baseband yields

$$r_m^{[l]}(t) = \sum_{q=0}^{N_{\mathrm{tx}}-1} \sum_{n=0}^{N-1} \alpha^{[q,l]} d_{mn}^{[q]} \, \mathrm{e}^{\mathrm{j}2\pi n \Delta f t} \, \mathrm{e}^{-\mathrm{j}2\pi (n\Delta f + f_c)\tau^{[q,l]}} \,. \tag{2.36}$$

Using (2.34), the target and channel dependent delay of the Rx signal is

$$\tau^{[q,l]}(t) = \frac{R^{[q,l]}}{c} - \frac{f_d}{f_c} t = \frac{2R_0}{c} + \frac{(qN_{\mathrm{tx}} + l) D_\lambda \sin\theta}{c} - \frac{f_d}{f_c} t \,. \tag{2.37}$$

Maintaining the processing chain of Section 2.2, the following steps are performed identically but separately for each Rx channel. First, the signal gets sampled and the CP is removed. Afterwards, the signal is decomposed into its subcarriers via a DFT, which gives its modulated spectrogram $\boldsymbol{y}^{[l]}$ with

$$y_{mn}^{[l]} = \mathrm{e}^{-\mathrm{j}2\pi \frac{2R_0}{\lambda_c}} \, \mathrm{e}^{\mathrm{j}\varphi_R[n]} \, \mathrm{e}^{\mathrm{j}\varphi_v[m]} \sum_{q=0}^{N_{\mathrm{tx}}-1} \alpha^{[q,l]} d_{mn}^{[q]} \, \mathrm{e}^{-\mathrm{j}2\pi \frac{D_\lambda (qN_{\mathrm{tx}} + l) \sin\theta}{\lambda_c}} \,. \tag{2.38}$$

Similar to the SISO processing in Section 2.2, some negligible terms are omitted[2]. Comparing (2.38) of a single Tx path with (2.14), an additional phase

$$\varphi_\theta[q,l] = -2\pi D_\lambda (qN_{\mathrm{tx}} + l)\sin\theta/\lambda_c \tag{2.39}$$

proportional to θ appears that enables DoA estimation of the target. In the next step, (2.38) is split into its N_{tx} Tx paths via multiplication with the complex conjugate of the Tx symbols $d_{mn}^{[q]}$ of each Tx path q. Extracting the spectrogram of the $[q{=}\hat{q}, l]$th path gives

$$\boldsymbol{\mathcal{D}}^{[\hat{q},l]} = \boldsymbol{y}^{[l]} \circ \overline{\boldsymbol{d}^{[\hat{q}]}}\,, \tag{2.40}$$

which is equivalent to (2.15). Note that it is assumed that the non-zero elements in $\boldsymbol{d}^{[\hat{q}]}$ are unitary. Expanding the equation yields the superposition

$$\boldsymbol{\mathcal{D}}^{[\hat{q},l]} = \hat{\boldsymbol{\mathcal{D}}}^{[\hat{q},l]} + \breve{\boldsymbol{\mathcal{D}}}^{[\hat{q},l]} \tag{2.41}$$

where $\hat{\boldsymbol{\mathcal{D}}}^{[\hat{q},l]}$ is the desired spectrogram with elements

$$\hat{\mathcal{D}}_{mn}^{[\hat{q},l]} = \alpha^{[\hat{q},l]}\, \mathrm{e}^{-\mathrm{j}2\pi \frac{2R_0}{\lambda_c}}\, \mathrm{e}^{\mathrm{j}\varphi_R[n]}\, \mathrm{e}^{\mathrm{j}\varphi_v[m]}\, \mathrm{e}^{\mathrm{j}\varphi_\theta[\hat{q},l]}\,. \tag{2.42}$$

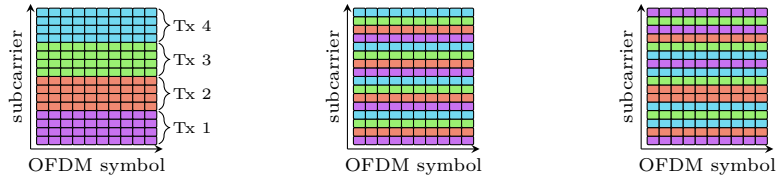
In contrast, $\breve{\boldsymbol{\mathcal{D}}}^{[\hat{q},l]}$ constitutes the undesired spectrogram contributions of other channels, hereafter referred to as inter-transmitter cross-talk (ITCT), with elements

$$\breve{\mathcal{D}}_{mn}^{[\hat{q},l]} = \mathrm{e}^{-\mathrm{j}2\pi \frac{2R_0}{\lambda_c}}\, \mathrm{e}^{\mathrm{j}\varphi_R[n]}\, \mathrm{e}^{\mathrm{j}\varphi_v[m]} \sum_{\substack{q=0 \\ q\neq\hat{q}}}^{N_{\mathrm{tx}}-1} \alpha^{[q,l]} d_{mn}^{[q]} \left(d_{mn}^{[\hat{q}]}\right)^* \mathrm{e}^{\mathrm{j}\varphi_\theta[q,l]}\,. \tag{2.43}$$

In case of mutually orthogonal Tx signals, the ITCT disappears and the range and Doppler evaluation may be carried out for each Tx-Rx path as in Section 2.2. If it does not cancel or disappear, self-interference occurs.

In general, the occupancy of the modulation symbol matrices $\boldsymbol{d}^{[q]}$ determines the multiplexing strategy. As the modulations $\boldsymbol{d}^{[q]}$ of all Tx channels may be chosen independently and, in addition, each element of the matrices may be chosen arbitrarily from $\mathcal{A}$, it is theoretically possible to realize FDM, TDM,

[2] This also includes an additional angle-dependent term with a phase proportional to $n\Delta f/f_c$, which is omitted due to $f_c \gg n\Delta f$.



(a) Sub-band scheme

(b) Equidistant spectral interleaving

(c) Non-equidistant spectral interleaving

Fig. 2.7: FDM strategies for MIMO OFDM.

and CDM. To date, spectral interleaving FDM is the predominant scheme for MIMO OFDM radar [23], [37], [51]–[53]. Other than the so-far popular TDM in MIMO FMCW radar [1], FDM enables uninterrupted observation of the channel on each Tx and Rx path combination.

2.3.3 Spectral Interleaving

In FDM MIMO OFDM, each subcarrier is dedicated to only one transmitter throughout the signal frame and no other transmitter is allowed to transmit on this very subcarrier. Especially in communication systems, it is distinguished between sub-band schemes, where each user is assigned a block of contiguous subcarriers, and interleaving schemes, where disjoint subcarrier sets are equidistantly interleaved [21], as illustrated in Figs. 2.7 (a) and (b), respectively. Since a sub-band scheme leads to a reduction of the effective bandwidth and thereby worsening of the range resolution [54], [55], usually interleaving schemes are preferred in OFDM radar systems. There, the subcarriers dedicated to a single Tx channel are distributed across the system bandwidth B, either equidistantly or non-equidistantly as illustrated in Figs. 2.7 (b) and (c), respectively. Then the effective bandwidth of each Tx channel is approximately B. Here, the former is discussed and is referred to as equidistant interleaving OFDM (IOFDM).

In IOFDM, the subcarriers are distributed disjoint and equidistantly among the transmitters, so that every N_{tx}th subcarrier is assigned to the same channel. To describe this assignment, the binary pattern $\boldsymbol{P}$ is introduced containing elements $P_{mn} \in \mathbb{B}$, $\mathbb{B}=\{0,1\}$. The notion of a pattern is helpful throughout various topics in this thesis. In the MIMO setup, N_{tx} spectrogram patterns $\boldsymbol{P}^{[q]} \in \mathbb{B}^{M\times N}$,

one for each Tx channel, are generated, where the binary entries $P_{mn}^{[q]}$ indicate if the corresponding element in $\boldsymbol{d}$ is active on the qth transmitter ($P_{mn}^{[q]}$=1) or not ($P_{mn}^{[q]}$=0). To this end, w.l.o.g the elements of $\boldsymbol{P}^{[q]}$ are defined by

$$P_{mn}^{[q]} = \mathbb{I}_{\{(n \bmod N_{\mathrm{tx}})=q\}}\,, \tag{2.44}$$

where $\mathbb{I}_{\mathcal{C}}$ is the indicator function with condition $\mathcal{C}$ that is defined by

$$\mathbb{I}_{\mathcal{C}} = \begin{cases} 1 & \text{if condition } \mathcal{C} \text{ is fulfilled} \\ 0 & \text{otherwise}\,. \end{cases} \tag{2.45}$$

Consequently, the sum of all patterns $\boldsymbol{P}^{[q]}$ gives a matrix of ones. Moreover, since the patterns are disjoint, it is sufficient to generate a single matrix $\boldsymbol{d}$ randomly from $\mathcal{A}$ and extract the individual modulation symbol matrices via

$$\boldsymbol{d}^{[q]} = \boldsymbol{d} \circ \boldsymbol{P}^{[q]} \tag{2.46}$$

that again are used in the Tx signal generation in (2.36). Skipping ahead in the MIMO OFDM radar signal processing of Section 2.3.2, the ITCT of the receive spectrogram (2.43) becomes zero, since it holds that

$$d_{mn}^{[q]} \left(d_{mn}^{[\hat{q}]}\right)^* = \begin{cases} 1, & \text{if } \hat{q} = q \text{ and } n \bmod N_{\mathrm{tx}} = \hat{q} \\ 0, & \text{if } \hat{q} \neq q \quad \text{or} \quad n \bmod N_{\mathrm{tx}} \neq \hat{q} \end{cases} \tag{2.47}$$

and in particular $\boldsymbol{d}^{[q]} \circ \overline{\boldsymbol{d}^{[\hat{q}]}} = \boldsymbol{0}_{MN}$ if $q \neq \hat{q}$, where $\boldsymbol{0}_{MN}$ is a zeros matrix of size $M \times N$. Note that in non-stationary scenarios, cross-talk between subcarriers and thereby different Tx signals is induced. Ultimately, this is the same as ICI in the SISO case and thus is not considered ITCT. Eventually, the elements of the Rx spectrogram (2.41) reduce to

$$\mathcal{D}_{mn}^{[\hat{q},l]} = \alpha^{[\hat{q},l]}\, \mathrm{e}^{-\mathrm{j}2\pi \frac{2R_0}{\lambda_c}}\, \mathrm{e}^{\mathrm{j}\varphi_R[n]}\, \mathrm{e}^{\mathrm{j}\varphi_v[m]}\, \mathrm{e}^{\mathrm{j}\varphi_\theta[\hat{q},l]}\, P_{mn}^{[\hat{q}]}\,, \tag{2.48}$$

which is only non-zero if $P_{mn}^{[\hat{q}]}$ is as well.

The range and velocity evaluation of each channel is performed as in Section 2.2, but close attention should be paid to the range evaluation. Through the interleaving structure, regular gaps are introduced in the spectrogram of each

channel. Thereby, the spectral sampling rate of the signal is decreased, since the effective subcarrier spacing of each channel gets increased. As a consequence, the maximum unambiguous range decreases compared to a dense SISO signal. Eventually, the range IDFT of (2.48) is

$$\boldsymbol{\mathcal{R}}^{[\hat{q},l]} = \left(\boldsymbol{\mathcal{D}}^{[\hat{q},l]} \circ \boldsymbol{\Psi}\right)\boldsymbol{U}^{\mathsf{H}} . \tag{2.49}$$

This gives (2.18) with an extra angle-dependent phase term and multiplied with $P_{mn}^{[q]}$. Since due to the interleaving, only every N_{tx}th summand is non-zero, by shifting of the summation bounds and of the summation index, the summands that are zero anyway are skipped, and the term simplifies to

$$\mathcal{R}_m^{[\hat{q},l]}[\rho] \propto \frac{1}{\sqrt{N}}\, \mathrm{e}^{\mathrm{j}2\pi\frac{\hat{q}}{N}\left(\rho-\frac{2R_0B}{c}\right)} \sum_{\eta=0}^{N/N_{\mathrm{tx}}-1} \tilde{\Psi}_{m\eta}\, \mathrm{e}^{-\mathrm{j}2\pi\eta N_{\mathrm{tx}}\Delta f\frac{2R_0}{c}}\, \mathrm{e}^{\mathrm{j}2\pi\frac{\eta\rho}{N/N_{\mathrm{tx}}}} \tag{2.50}$$

$$\propto \mathrm{e}^{\mathrm{j}2\pi\frac{\hat{q}}{N}(\rho-N\Delta f\frac{2R_0}{c})}\, \frac{\sqrt{N}}{N_{\mathrm{tx}}}\tilde{\psi}_m\left[\rho-\frac{R_0}{\Delta R}\right] \tag{2.51}$$

with index shift $n=\eta N_{\mathrm{tx}}+\hat{q}$, $\tilde{\boldsymbol{\Psi}}$ the truncated window of size $M\times N/N_{\mathrm{tx}}$, and $\tilde{\boldsymbol{\psi}}$ its image. In addition, terms independent of n and irrelevant to the profile are omitted. The evaluation yields a target at range bin $\hat{\rho}=R_0/\Delta R$, where the channel dependent phase term becomes one for $\hat{\rho}$. Since the pattern $\boldsymbol{P}^{[q]}$ does not truncate the spectrogram in size, but only inactive elements not belonging to the $\hat{q}$th Tx channel are set to zero before the N-point IDFT, in (2.50), each spectral coefficient $\mathcal{D}_{mn}^{[\hat{q},l]}$ is evaluated at the correct subcarrier frequency, and all Tx-Rx channels refer to a common carrier frequency. As a consequence, the phases in the range maps are correct across the channels and no phase correction as discussed in [56] is needed before angle estimation. Compared to (2.19), for the same N the peak power is reduced by the factor N_{tx}[3]. Moreover, the periodicity of the IDFT is reduced by the factor N_{tx} such that R_{ua} decreases to

$$R_{\mathrm{ua}}^{\mathrm{IOFDM}} = \frac{R_{\mathrm{ua}}}{N_{\mathrm{tx}}} = \frac{cT}{2N_{\mathrm{tx}}} . \tag{2.52}$$

The Doppler evaluation is not affected by the MIMO multiplexing and is

[3] Assuming the same output power on each subcarrier as in the SISO, the total peak-to-noise ratio (PNR) in the profile is reduced by $10\log_{10}(N_{\mathrm{tx}})$ dB since the non-coherently added noise is reduced by a factor $\sqrt{N_{\mathrm{tx}}}$ at the same time.

performed according to (2.25) for each channel.

2.3.4 Angle Estimation

Direction-of-arrival (DoA) estimation is achieved by digital beamforming (DBF). To this end, a conventional Bartlett beamformer is applied that in case of an ULA basically equals a DFT across the spatial dimension of the receive signals [57], [58]. Due to the physical extent of the aperture, the phase of the incoming wave progresses along the elements of the aperture relative to the observation angle θ. This phase progression is reflected by the angle dependent phase $\varphi_\theta[q,l]$ (2.39). Thus, to estimate θ, the frequency of the phase change along the virtual channels of the ULA is determined via another DFT. To this end, first the *R-v*-images of all channels are computed, added up non-coherently, and the bins that contain targets are identified using a constant false alarm rate (CFAR) detector [59] and peak search algorithm. For each target, the corresponding $[\hat{\nu},\hat{\rho}]$-bins of all virtual channels are extracted and stacked according to their position $\kappa = qN_{\mathrm{tx}}+l$ in the virtual ULA, where $\kappa = 0$ is the reference antenna located at an edge of the array. Hence, with increasing κ, the distance of the respective antennas to the reference one increases linearly and so progresses the phase. Eventually, the DFT across the spatial dimension of the $[\hat{\nu},\hat{\rho}]$th element of the *R-v*-images gives the azimuth angle profile

$$\Theta_{\hat{\nu}\hat{\rho}}[\vartheta] \propto \sum_{\kappa=0}^{N_{\mathrm{virt}}-1} \mathrm{e}^{-\mathrm{j}2\pi \frac{\kappa D_\lambda \sin\theta}{\lambda_c}} \, \Psi_{1\mathrm{D}}[\kappa] \, \mathrm{e}^{\mathrm{j}2\pi \frac{\kappa\vartheta}{N_{\mathrm{virt}}}} \tag{2.53}$$

$$\propto \psi\left[\vartheta - N_{\mathrm{virt}} \frac{D_\lambda}{\lambda_c} \sin\theta\right] \tag{2.54}$$

of this very bin. For each target angle θ, the profile exhibits a peak at azimuth index $\hat{\vartheta} = \left\lfloor N_{\mathrm{virt}} D_\lambda \sin\theta/\lambda_c \right\rceil$.

In general, any sophisticated beamforming or direction finding algorithm or estimator such as the multiple signal classification algorithm (MUSIC) or Capon's beamformer [57] may be applied for DoA estimation.

2.4 Compressed Sensing

In digital radar signal processing, the received analog signals get discretized at the analog-to-digital converters (ADCs) and are modeled and digitally processed as vectors or matrices. In order to unambiguously describe a band limited signal of interest by its discrete samples, it has to be sampled by at least the Nyquist rate specified by the Nyquist-Shannon theorem [60]. With increasing signal bandwidth, faster ADCs are required, which potentially are hard to realize, expensive, or unavailable. Additionally, demands on storage and computational power increase [3], [60]. The theory of CS enables signal sampling and acquisition at sampling rates much lower than the Nyquist rate. Through this, much less samples have to be stored or acquired in the first place, and sampling rate requirements to both analog and digital hardware can be relaxed. Since its introduction roughly two decades ago by Donoho [61] and Candès [62]–[64], the concept of CS has been gaining increased importance in signal processing. A comprehensive introduction and overview of CS may be found in [65].

The notion of signal *sparseness* is of central importance in CS theory. A sampled complex-valued signal represented as vector $\boldsymbol{\xi} \in \mathbb{C}^L$ is considered ς-*sparse* if it contains at most ς non-zero coefficients. Moreover, $\boldsymbol{\xi}$ is also called ς-sparse if it is not sparse itself but may be sparsely represented in some basis via a linear projection

$$\boldsymbol{\xi} = \boldsymbol{\Phi}\boldsymbol{x}\,, \tag{2.55}$$

where $\boldsymbol{x} \in \mathbb{C}^L$ is the sparse representation of $\boldsymbol{\xi}$ in a certain basis $\boldsymbol{\Phi} \in \mathbb{C}^{L \times L}$. For instance, a sine wave is not sparse in discrete-time representation, but it is sparse in the Fourier basis, where it can be represented by a single coefficient in the spectrum. In the following, it is assumed that $\boldsymbol{\Phi}$ is an orthonormal basis [60].

In practice, most signals of interest in sensing and signal processing applications are noisy and not strictly sparse. Therefore, a signal is considered approximately sparse or compressible if its components decay rapidly, e.g. by power law, when sorted in order of decreasing amplitude [64], [66]. Such signals are also characterized by the property that small coefficients may be omitted without major loss of information. The ς largest coefficients are also referred to as the *support* of the signal. In this thesis, only such signals are considered and referred to as ς-sparse if the signal can be represented by ς components with significant amplitude, while the remaining components are comparably small

and close to zero. In sensing applications, typically, $\boldsymbol{x}$ is not directly accessible but only its linear and noisy observations. The measurement is modeled by the linear projection

$$\boldsymbol{y} = \boldsymbol{A}\boldsymbol{x} + \boldsymbol{w} = \boldsymbol{\Xi}\boldsymbol{\Phi}\boldsymbol{x} + \boldsymbol{w} \tag{2.56}$$

with observation $\boldsymbol{y} \in \mathbb{C}^S$, non-adaptive sensing matrix $\boldsymbol{A} \in \mathbb{C}^{S \times L}$, CS or decimation matrix $\boldsymbol{\Xi} \in \mathbb{C}^{S \times L}$, and noise vector $\boldsymbol{w} \in \mathbb{C}^S$ with $w_i \sim \mathcal{CN}(0, \sigma^2)$. $\mathcal{CN}$ is the complex normal distribution and S the dimension of the measurement space. In case of $S \geq L$ the solution of the linear system of equations (2.56) is simply given by the standard matched filter $\boldsymbol{A}^{\mathsf{H}}\boldsymbol{y}$. On the contrary, CS is typically concerned with highly incomplete or undersampled measurements with $S \ll L$ where the ratio $\delta_{\text{cs}} = S/L$ is the undersampling of the signal thus indeterminacy of the system of equations (2.56) [67]. In this case, the problem (2.56) is ill-posed as the linear system of equations is underdetermined with infinitely many solutions $\hat{\boldsymbol{x}}$ [68]. However, when restricting $\boldsymbol{x}$ to be ς-sparse, CS theory states that it is possible to uniquely (and on relatively unrealistic theoretical conditions even exactly) recover $\boldsymbol{x}$ from its low-dimensional measurements (2.56) [62].

The goal now is to find the sparsest solution $\hat{\boldsymbol{x}}_0$ that satisfies (2.56) with an error at most proportional to the noise variance σ^2. This solution can be found by using the ℓ_0-optimization [69]

$$\arg\min_{\boldsymbol{x}} \|\boldsymbol{x}\|_0 \quad \text{subject to} \quad \|\boldsymbol{y} - \boldsymbol{A}\boldsymbol{x}\|_2 \leq \epsilon \tag{2.57}$$

where $\|\boldsymbol{x}\|_0 := |\text{supp}(\boldsymbol{x})|$ is the cardinality of the support $\text{supp}(\boldsymbol{x}) = \{i \mid x_i \neq 0\}$ of $\boldsymbol{x}$ [60], [61], hence the number of nonzero components of $\boldsymbol{x}$. Note that $\|\cdot\|_0$ is not a norm in the mathematical sense, since it neither is homogeneous nor does it satisfy the triangular inequality [70, p. 285]. Solving (2.57) gives the sparsest solution, however, the problem is non-convex and NP-hard to solve [61], [66]. Therefore, usually a convex relaxation is used, where instead of the ℓ_0-pseudonorm the ℓ_1-norm is used, resulting in the ℓ_1 regularized least-squares also known as least absolute shrinkage and selection operator (LASSO) [71]

$$\min_{\boldsymbol{x}} \|\boldsymbol{y} - \boldsymbol{A}\boldsymbol{x}\|_2^2 \quad \text{subject to} \quad \|\boldsymbol{x}\|_1 \leq \beta_{\text{LASSO}}\,, \tag{2.58}$$

where β_{LASSO} is a tuning parameter. An equivalent formulation of the problem is known as basis pursuit denoising (BPDN) [72]. Both problems are convex and

can be solved in polynomial time by linear programming, e.g. using interior point methods [66], [72], [73]. Moreover, it was shown that if the ℓ_0-optimization (2.57) has a sparse solution, then (2.58) will find it if it is sufficiently sparse [61], [74].

Whether the optimization problems (2.57) and (2.58) have a unique solution and whether a solution can be found for any ς-sparse $\boldsymbol{x}$ depends not only on its sparseness but also on the properties of the sensing matrix $\boldsymbol{A}$. The sensing matrix must ensure that both the relevant information is preserved, and the projection is unambiguous. For instance, it must be guaranteed that there are no two distinct sparse signals $\hat{\boldsymbol{x}}_0^{(1)}$ and $\hat{\boldsymbol{x}}_0^{(2)}$ such that $\boldsymbol{A}\hat{\boldsymbol{x}}_0^{(1)} = \boldsymbol{A}\hat{\boldsymbol{x}}_0^{(2)}$. In this case, it is impossible to infer the correct solution from the observation. In addition, the inference from the observations must also be sufficiently robust against distortions due to noise. So besides finding the solution, the design of an appropriate stable sensing matrix is a major challenge in CS. To date, a great deal of mostly theoretical analysis has been done in this area in order to derive generally valid statements [60], [62], [64], [75]. However, uniform recovery guarantees are often limited to randomized or Gaussian matrices, which are rather impractical and unusual with most acquisition hardware and real world sensing applications [76]. Therefore, the discussion is here confined to the coherence property [60]

$$\mu(\boldsymbol{A}) = \max_{1 \leq k \neq l \leq L} \frac{|\langle \boldsymbol{A}_k, \boldsymbol{A}_l \rangle|}{\|\boldsymbol{A}_k\|_2 \|\boldsymbol{A}_l\|_2} \,. \tag{2.59}$$

This is the maximum mutual inner product of any two columns of $\boldsymbol{A}$ and describes how unique they and their projections are. Hence, the coherence provides a measure for the guarantee that there is a solution and that this solution is unique [74], [77]. The coherence has an upper bound of 1 resembling strong coherence, and a lower bound defined by the Welch bound [60], [78]

$$\mu_{\text{welch}} = \sqrt{\frac{L - S}{S(L-1)}} \,. \tag{2.60}$$

The lower the coherence the more stable is the result and the better the recovery performance. However, the coherence (and its related analytic conditions, e.g. the restricted isometric property (RIP) [79]) only provides sufficient recovery guarantees and is rather pessimistic with the result that algorithms often outperform these theoretical guarantees [65], [80], [81]. Moreover, μ does not

allow to compare the performance of different recovery algorithms. For this purpose, the phase transition or ϱ_{cs}-δ_{cs}-tradeoff, can be used. It provides a measure of what degree of relative sparsity $\varrho_{\text{cs}} = \varsigma/S$, thus support size ς, an algorithm is able to recover given an undersampling ratio δ_{cs} [82]–[84]. It is based on the finding that for each δ_{cs}, when increasing the relative sparsity ϱ_{cs}, there is a sharp transition between the area where ℓ_1-minimization recovery using a specific algorithm succeeds with high probability and where it fails. Moreover, there exists a theoretical upper bound on the phase transition for ℓ_1-minimization. However, many popular iterative or greedy CS algorithms such as iterative soft thresholding (IST) [83], [85] or orthogonal matching pursuit (OMP) [86], [87], cannot reach this bound, even if optimally tuned [84].

In the following, first, the basic formulations of two iterative algorithms that are utilized in this thesis are introduced in Sections 2.4.1 and 2.4.2. Afterwards, in Section 2.4.3, the application of CS in radar processing is briefly discussed.

2.4.1 Approximate Message Passing

Approximate message passing (AMP) is an iterative thresholding approach and was proposed by Donoho et al. [67], [83], [88] to solve the LASSO (2.58). It is derived from a statistical framework and is inspired by message passing on bipartite graphs. Although derived from a statistical and not from an algebraic viewpoint, at first glance, it shows striking similarities to the popular IST algorithm. Proceeding from the sum-product message passing heuristics equivalence of (2.58), IST is obtained if weak dependencies in the graph are neglected. However, there will be an error introduced that is captured in the AMP approach by utilizing order one corrections [67], [83]. Basically, each iteration of the AMP algorithm consists of the three steps

$$\tilde{\boldsymbol{x}}^{[k]} = \boldsymbol{A}^{\mathsf{H}} \boldsymbol{e}^{[k-1]} + \hat{\boldsymbol{x}}^{[k-1]} \tag{2.61a}$$

$$\hat{\boldsymbol{x}}^{[k]} = \Gamma(\tilde{\boldsymbol{x}}^{[k]}; \Lambda) \tag{2.61b}$$

$$\boldsymbol{e}^{[k]} = \boldsymbol{y} - \boldsymbol{A}\hat{\boldsymbol{x}}^{[k-1]} + \frac{\|\hat{\boldsymbol{x}}^{[k]}\|_0}{S} \boldsymbol{e}^{[k-1]} \tag{2.61c}$$

with $k = 1, \ldots, K$ the iteration number and K the total number of iterations. In the first step (2.61a), a new noisy estimate $\tilde{\boldsymbol{x}}^{[k]}$ is obtained by the sum of the projection of the residual $\boldsymbol{e}^{[k-1]}$ of the last iteration and the previous sparse

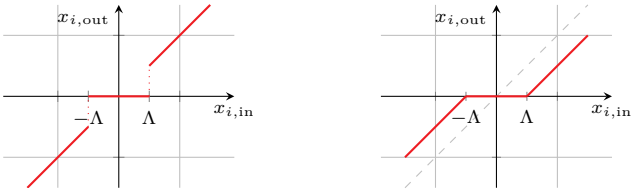
estimate $\hat{\boldsymbol{x}}^{[k-1]}$. Initially in the first iteration, $\boldsymbol{e}^{[0]} = \boldsymbol{y}$ and $\hat{\boldsymbol{x}}^{[0]} = \boldsymbol{0}$. In the second step (2.61b), the element-wise threshold function $\Gamma(\tilde{\boldsymbol{x}}^{[k]}; \Lambda)$ with threshold Λ is applied. In iterative thresholding algorithms this step is of key importance as it imposes sparsity on $\tilde{\boldsymbol{x}}^{[k]}$ and produces a denoised estimate $\hat{\boldsymbol{x}}^{[k]}$. The common soft- and hard-threshold functions are detailed at the end of this section. Finally, in the last step (2.61c), the residual is updated, where $\boldsymbol{e}^{[k-1]} \|\hat{\boldsymbol{x}}^{[k]}\|_0 / S$ is the so-called Onsager reaction [83], [89] or correction [90], [91] term. Interestingly, it is the only difference between AMP and IST (supposing a soft-threshold is applied in (2.61b)). The term is responsible for an asymptotic cancellation of the correlation of $\boldsymbol{A}$ and the current estimate that is introduced in each iteration [83], [92], [93]. Therefore, IST and AMP behave differently after the first iteration. It can be shown that the estimate of AMP converges to the solution of LASSO (2.58) with strictly decreasing mean-squared error (MSE) with the asymptotic limit being the noise variance σ^2 [80], [93]. Moreover, while IST falls short with respect to the ϱ_{cs}-δ_{cs}-tradeoff even if optimally tuned, AMP reaches the theoretical upper bound in the optimal setting [83], [92].

Hard- and soft-threshold function. The role of a threshold function in iterative CS algorithms is to impose sparseness on the input vector by allowing only certain elements to pass, while the remaining ones are set to zero. The intention is that ideally only elements belonging to the signal support pass, while noise and artifact elements are rejected. Depending on the choice of the threshold and the transfer characteristic, different threshold functions are realized. The element-wise applied discontinuous non-smooth *hard-threshold* function [84], [94], [95]

$$\hat{\boldsymbol{x}} = \text{hard}(\tilde{\boldsymbol{x}}; \Lambda) = \begin{cases} \tilde{x}_i, & \text{if } |\tilde{x}_i| \geq \Lambda \\ 0 & \text{otherwise} \end{cases}, \quad \forall i \in \mathbb{Z}_L \tag{2.62}$$

with threshold Λ sets all elements with amplitude smaller than Λ to zero, while all others pass unchanged. In contrary, with the *soft-threshold* function [96], [97]

$$\hat{\boldsymbol{x}} = \text{soft}(\tilde{\boldsymbol{x}}; \Lambda) \;= \begin{cases} \tilde{x}_i \left(1 - \frac{\Lambda}{|\tilde{x}_i|}\right), & \text{if } |\tilde{x}_i| \geq \Lambda \\ 0 & \text{otherwise} \end{cases}, \quad \forall i \in \mathbb{Z}_L \,, \tag{2.63}$$



(a) Hard-threshold function **(b)** Soft-threshold function

Fig. 2.8: Input-output relation of the soft- and hard-threshold function with threshold Λ.

each component that passes the threshold is damped by Λ thus shrunken towards zero by the amount of Λ in each iteration. Through this, no discontinuity is created. The threshold Λ is a free design parameter and should be chosen such that it allows to separate noise from support elements. In Fig. 2.8 the input-output relation of both threshold functions are illustrated. Both functions are applied element-wise to the input vector and are also valid for complex valued input signals in the given representations.

2.4.2 Split Augmented Lagrangian Shrinkage Algorithm

The split augmented Lagrangian shrinkage algorithm (SALSA) was proposed in [95] for the application of image restoration. It is derived from the LASSO optimization problem (2.58) by applying variable splitting and then addressing the resulting problem with an augmented Lagrangian method (ALM) and an alternating direction method of multiplier (ADMM) approach [95], [98]. Its convergence is shown in [95]. SALSA is further suitable for non-smooth optimization such as ℓ_1-optimization with soft-threshold. In [95], [99], detailed analyses and derivations of SALSA are given. With the requirement that the sensing matrix $\boldsymbol{A}$ in (2.56) is a normalized tight Parseval frame, i.e. $\boldsymbol{A}\boldsymbol{A}^{\mathsf{H}} = \boldsymbol{I}$ [60], the iterative SALSA algorithm is given by the steps [95], [99]

$$\boldsymbol{g}^{[k]} = \operatorname{soft}\left(\tilde{\boldsymbol{x}}^{[k-1]} + \boldsymbol{h}^{[k-1]}; \Lambda\right) - \boldsymbol{h}^{[k-1]} \tag{2.64a}$$

$$\boldsymbol{h}^{[k]} = \boldsymbol{A}^{\mathsf{H}}\left(\boldsymbol{y} - \boldsymbol{A}\boldsymbol{g}^{[k]}\right) \tag{2.64b}$$

$$\tilde{\boldsymbol{x}}^{[k]} = \boldsymbol{h}^{[k]} + \boldsymbol{g}^{[k]} \tag{2.64c}$$

with the inital estimate $\tilde{\boldsymbol{x}}^{[0]} = \boldsymbol{A}^{\mathsf{H}}\boldsymbol{y}$, $\boldsymbol{h}^{[0]} = \boldsymbol{0}$ an auxiliary variable, and $\tilde{\boldsymbol{x}}^{[k]}$ the noisy estimate of $\boldsymbol{x}$ in (2.56). To impose sparseness, the soft-threshold function (2.63) is utilized in (2.64a). Note that the tight frame assumption holds for unitary DFT matrices as well as partial DFT matrices obtained through mutliplying the DFT matrix with a decimation matrix that selects a subset of S unique rows from the $L \times L$ DFT to generate the $S \times L$ partial DFT matrix. In case of the sensing matrix being a frame, SALSA solves (2.58) much faster than other established algorithms [100].

2.4.3 Compressed Sensing Applied to Radar

With common radar systems, sensing is typically applied in various dimensions such as time, frequency, and sometimes also space in order to determine target parameters such as velocity, range, and angle. When evaluating radar measurements, the measured and processed signals are usually transformed to a parameter space with range, velocity (Doppler), and angle as ambient dimensions. Thereby, the target reflections get compressed, e.g. by applying Fourier transforms, into few cells in the parameter space. However, in order to obtain a high-resolution and unambiguous estimate over a large parameter range, a large number of samples must be acquired over the different measurement dimensions, regardless of the actual number of targets. Ultimately, even in densely populated scenes, far fewer targets are present and thus occupy cells in the large parameter space than samples have been acquired. Radar signals are therefore considered (approximately) sparse in their respective image dimension, which is why they were quickly recognized as suitable for use with CS [101]–[104]. An early review of CS radar applications is given in [105], [106]. More recent developments are found in [107], [108]. The applications of CS radars are diverse. It may be used to reduce hardware and processing effort by taking advantage of the compression capability of the target information. To this end, undersampling of one or more of the sensing dimensions is performed, and CS methods are applied in the evaluation in order to retrieve the target information. In [2], [101] the ADC rate is reduced whereas frequency agile radars allow to subsample the frequency dimension of the signal. In addition, spatial subsampling via sparse arrays is found very attractive for CS [109]–[111]. A different application area is the use of CS to replace the radar matched filter [102] or the topic of superresolution [112].

In the field of OFDM radars, CS has been used to increase the resolution of passive OFDM radars [9], [41], [113], to reduce the sampling rate [32], [114], to recover missing subcarriers in non-equidistant or random interleaving [53], [115], [116], to recover samples in OFDM-based radar networks [117], or in interference mitigation [116], [118], [119].

2.5 Measurement Setups and Signal Parametrization

With very few exceptions, all investigations and findings presented in this work are illustrated, validated, verified, and supported on the basis of measurements. To this end, two experimental digital OFDM radars are utilized. The first radar, referred to as R1, is an all-digital radar prototype that is presented and described in [3]. It is composed of a Xilinx ZCU111 RF system-on-chip (RFSoC) evaluation board [120] and a simple analog front end. In IQ operation, the systems offers four Tx and four Rx channels at a baseband bandwidth of about 400 MHz, limited by the data rate of the memory controller. The analog front end is equipped with a 4×4 ULA patch antenna array with a Tx element spacing of 2λ and an Rx element spacing of $\lambda/2$, as illustrated in Fig. 2.6 on page 20. This results in an ambiguity-free spatial region of $\pm 90°$. The antenna array is designed for a carrier frequency of 77 GHz. Although the system allows independent signal generation and evaluation, for the measurements in this work, the RFSoC board is connected to a PC running Matlab via Ethernet. The transmit sequence is generated in Matlab and transferred to the RFSoC. After each measurement, the raw baseband data is again transferred to Matlab and evaluated. R1 is used throughout this work except for Chapter 5.

The second measurement system, referred to as R2, is a SISO OFDM radar demonstrator based on measuring devices [31], [32]. The heterodyne system allows larger baseband bandwidths than R1 and is therefore utilized for interference investigations in Chapter 5.

Signal Parametrization. The OFDM modulation is designed and parametrized given system constraints, such as the available bandwidth, the maximum observation time, and the carrier frequency, and performance requirements, such as the minimal maximum range or velocity. The obtained parameters for both R1 and R2 are summarized in Table 2.1. The given radar performance corresponds

Tab. 2.1: OFDM radar modulation parameters and performance.

parameter	radar R1	radar R2
carrier frequency f_c	77 GHz	76 GHz
number of symbols M	2048	3072
number of subcarriers N	1024	2048
bandwidth B	409.6 MHz	1024 MHz
subcarrier spacing Δf	400 kHz	500 kHz
symbol duration T	2.5 µs	2.0 µs
CP duration T_{cp}	0.4 µs	0.5 µs
radar performance (SISO)		
range resolution ΔR	0.37 m	0.15 m
maximum range $R_{\max}$	60 m	75 m
max. unambiguous range R_{ua}	374.7 m	299.8 m
velocity resolution Δv	0.33 m/s	0.26 m/s
maximum velocity $v_{\max}$	97.3 m/s	123.3 m/s
max. unambiguous velocity v_{ua}	335.6 m/s	394.4 m/s

to the dense-frame SISO operation, hence, for instance in IOFDM operation, R_{ua} gets reduced by the factor N_{tx}. The utilized Doppler design parameter in (2.29) is $\beta = 8$. The given setups are used for the measurements investigated in this work. Any exceptions for individual investigations are explicitly stated.

Evaluation Details. OFDM radar imaging is achieved via the 2D-(I)DFT evaluation described in Section 2.2. The applied window matrix $\mathbf{\Psi}$ in (2.30) is a 2D Hann window. Target, or more precisely R and v, estimation is achieved by an ordered statistics constant false alarm rate (OS-CFAR) detector [59], followed by a peak search algorithm that extracts the target cells $[\hat{\nu}, \hat{\rho}]$. The OS-CFAR first identifies those cells that exceed the CFAR threshold composed of an estimate of the background noise and a scaling parameter. Next, a peak detection is performed that basically allows differentiation of two peaks if they exceed the CFAR threshold and exhibit a drop of at least 3 dB between them with respect to the lower peak. In MIMO processing, first the non-coherent integration (NCI) of the R-v-images is determined. This image is then used for range and velocity detection like in the SISO case. Afterwards, for each target angle estimation (2.53) is performed across all R-v-images of this very cell.

3 High-Resolution OFDM Radar with Reduced Baseband Bandwidth

The range resolution of an OFDM radar as described in Section 2.2.1 is determined by the effective bandwidth B of the signal in the channel via $\Delta R = c/(2B)$ (2.21). At the receiver, the signal is mixed to baseband or to a low intermediate frequency and then digitized at the ADCs. Hence, the entire instantaneous signal bandwidth (modulation bandwidth) has to be converted. Therefore, to achieve high-resolution radar imaging in the centimeter range, a sufficiently high signal bandwidth and correspondingly fast ADCs are required. For instance, a desired resolution of 10 cm translates into a signal bandwidth of about 1.5 GHz that has to be provided by both Tx and Rx hardware. However, such high bandwidths and sampling rates are not feasible with state-of-the-art and potential next-generation consumer hardware at moderate cost [3], [31], [121]. In addition, a huge amount of data has to be processed and stored [3].

Since high resolution is a key aspect for future radars to be competitive, OFDM radar research has been advanced in the last decade to reduce the sampling rate while achieving high range resolution at affordable and reasonable hardware effort. The most promising and intuitive approach is the frequency-agile or stepped-carrier strategy [29], [31], [121]–[127], which aims at synthesizing wideband signal frames in the channel from instantaneously narrowband baseband signals. The concepts typically combine narrowband baseband signals, an agile carrier frequency generation, and advanced digital signal processing. The idea of a frequency agile stepped-carrier OFDM strategy was first brought up in [122] where high-resolution range profiles are attained by synthesizing multiple consecutive narrowband OFDM pulses that are transmitted on varying carrier frequencies. In [123], a similar concept with stepwise frequency increments is proposed. Yet, both concepts are only suitable for stationary targets and only consider the Doppler as disturbance to the range processing. The first software-defined radio (SDR) platform utilizing a stepped-frequency OFDM is

presented in [124]. The proposed modulation concept uses a carrier frequency that is increased to the frequency of the highest subcarrier of the previous symbol after each OFDM symbol. In this way, overlapping frequency components of consecutive symbols are obtained that are required to adjust the phase progression for the Doppler evaluation. After a certain number of frequency jumps, the carrier is reset, which leads to a ramp-like pattern in the spectrogram similar to FMCW. In [31], for the first time, a linear stepped-frequency OFDM concept is presented that enables joint high-resolution range-Doppler processing based on the common 2D Fourier transform pulse compression. Moreover, it does not require overlapping frequency components, and a throughout mathematical description is given. However, the linear hopping pattern results in a linear undersampling of the signal's slow-time dimension. As a consequence, v_{ua} gets reduced by the number of frequency steps, and ambiguities arise in the Doppler dimension of the *R*-*v*-image. In [125], a strategy to partly solve these Doppler ambiguities by analyzing the phase progression and phase error along each subcarrier is presented. Implementation issues and constraints such as frequency accuracy for a stepped frequency or frequency agile radar hardware are discussed in [126]. In [121], a narrowband OFDM signal is combined with FMCW modulation in order to synthesize a wideband signal in the channel. The approach suffers from high sidelobes and distortions in the range-Doppler evaluation. Instead of synthesizing the wideband signal over the time dimension via frequency hopping, in [127], a frequency comb is utilized to simultaneously convert a single narrowband baseband signal to multiple RF carriers separated by the baseband bandwidth. Due to required constraints on the signal, R_{ua} gets severely reduced. As a consequence, the MIMO capabilities of the system are limited. Furthermore, the hardware complexity is increased.

Although some of these approaches are promising, most of them either lack Doppler processing strategies or exhibit reduced ambiguities compared to an equivalent wideband OFDM signal, in the following referred to as dense OFDM. In addition, the improvement of resolution is achieved at expense of flexibility in signal design. In this chapter, a flexible and non-deterministic processing concept is proposed that combines narrowband baseband OFDM signals, frequency hopping, and CS methods to achieve a high-resolution radar that is also capable of jointly and unambiguously processing range and Doppler. The new concept is referred to as *sparse OFDM (SOFDM)* and was first proposed in [32] by the

author. The focus here is on the signal processing aspect of the concept, potential hardware realizations or hardware-related constraints and non-idealities are addressed in [3], [33], [126], [128]. In Section 3.1, the Tx and Rx signal generation and high-performance processing concept are detailed and the differences to the dense concept are shown. The signal evaluation and imaging involves sparse methods suitable for joint 2D processing. For this purpose, 2D CS algorithms are developed that are specifically adapted to joint range-Doppler processing. The developed 2D algorithms are presented in Section 3.2. In Section 3.3, the SOFDM performance is validated using different measurement scenarios. The chapter is concluded by a summary in Section 3.4.

3.1 Frequency Agile Sparse OFDM

Suppose an OFDM radar system should meet certain requirements in terms of its achievable resolution and unambiguity for range and velocity. This requirements translate into a modulation parameter set $\{N, M, B, \Delta f\}$. However, if B exceeds the digital-to-analog converter (DAC) and ADC limitations for Nyquist rate sampling, unambiguous high-resolution dense OFDM imaging becomes unattainable. Based on the desired yet unrealizable modulation, an SOFDM modulation is developed that overcomes the limitations of the dense modulation. To meet the Nyquist criterion at both the DAC and the ADC, the baseband bandwidth and thus the number of subcarriers are first reduced to $\mathcal{B}_s \ll B$ and $N_s \ll N$, respectively. In analog domain, the OFDM symbols of viable bandwidth are then mixed to different RF carrier frequencies to synthesize the desired wider bandwidth in the channel over time. It is therefore differentiated between the narrowband baseband bandwidth $\mathcal{B}_s$, which is prescribed by the DAC and the ADC, and the high effective virtual bandwidth $B \gg \mathcal{B}_s$ of the frame. The former merely provides a low $\Delta R_s = c/(2\mathcal{B}_s)$, while the latter corresponds to the actually desired high resolution $\Delta R \ll \Delta R_s$. To differentiate from dense OFDM, SOFDM-specific signals and parameters are indicated by the superscript $\boxplus$ or the subscript s.

In Fig. 3.1, a simplified signal flow of the proposed SOFDM radar is depicted. At the transmitter, a narrowband OFDM signal composed of N_s subcarriers is digitally generated and reconstructed at the DAC. It should be explicitly clarified here that N_s does not need to be a constant but may be a function

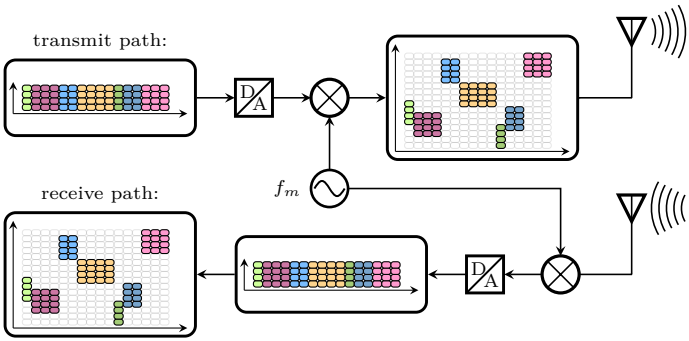


Fig. 3.1: Simplified signal flow for SOFDM Tx and Rx path. The coloring indicates the OFDM symbol mixed to the same carrier frequency. Adapted from [32] © 2018 IEEE.

of m, so that its value may vary for each symbol, not exceeding the maximum value of $N_s^{\max} = \mathcal{B}_s/\Delta f$. However, using less subcarriers than $N_s^{\max}$ would be a waste of valuable available resources, therefore $N_s = N_s^{\max}$ is assumed in the remainder of this chapter. In the next step of the processing chain, each OFDM symbol is mixed to an individual randomly chosen carrier frequency on a virtual wideband subcarrier grid of the same subcarrier spacing and symbol duration as the baseband signal and then transmitted. The so-called virtual wideband grid is indicated by the grayish boxes, where only colored boxes are utilized in SOFDM, whereas the dense OFDM signal with desired properties $\{N, M, B, \Delta f\}$ corresponds to the gray grid. At the receiver, the same individual frequency is used for down-conversion to baseband. After sampling, the virtual wideband signal is digitally restored from the narrowband signal before the signal evaluation and imaging.

3.1.1 Transmit Signal Design and Generation

The digital baseband signal generation for SOFDM is identical to that of dense OFDM described in Section 2.1 except for the utilization of a reduced number of subcarriers N_s. As sketched in Fig. 3.1, at the analog front end, the signal is mixed with an agile carrier frequency provided by a frequency agile local

oscillator (LO). In this step, the desired wideband signal is synthesized across the signal's slow-time dimension as each OFDM symbol is mixed to an individual RF carrier f_m on a virtual wideband subcarrier grid. The corresponding RF Tx signal (2.6) for SOFDM yields

$$x_m^{\mathrm{RF}\boxplus}(t) = \sum_{n_s=0}^{N_s-1} d_{mn_s}^{\boxplus}\, \mathrm{e}^{\mathrm{j}2\pi(n_s\Delta f+f_m)t}, \quad t\in[0,T) \tag{3.1}$$

with $f_m = f_c + b_m\Delta f$, $b_m \in \mathbb{Z}_{(N-N_s)}$ the carrier frequency of the mth OFDM symbol and $n_s\Delta f + f_m$ the virtual subcarrier. The sequence $\boldsymbol{b} = [b_0, b_1, \ldots, b_{M-1}]$ denotes the hopping pattern within the virtual subcarrier grid. It also determines if a structured or random hopping is performed. For instance, choosing $b_m = (mN_s \bmod N)$ results in the linear frequency stepping of [31]. In SOFDM, the elements b_m are chosen randomly from $\mathbb{Z}_{(N-N_s)}$. Hence, there are $N-N_s$ different hopping positions with no restrictions on how often or in which order the positions are allocated. Through this, the subcarriers of the virtual signal frame remain orthogonal, and the patchwork-like signal structure as illustrated in Fig. 3.1 is generated. Furthermore, the transmission structure is fully described by the so-called binary Tx pattern $\boldsymbol{P}\in\mathbb{B}^{M\times N}$ [32], where the binary entries indicate whether the $[m,n]$th element of the virtual wideband frame is occupied (=1) or not (=0). For instance, with $N_s=2$, $N=4$, and $M=8$, the Tx pattern could be

$$\boldsymbol{P}^{\mathsf{T}} = \begin{array}{c} \text{OFDM symbols } m \\ \left[\begin{array}{cccccccc} 0 & 0 & 0 & 1 & 0 & 0 & 0 & 1 \\ 0 & 1 & 0 & 1 & 1 & 1 & 0 & 1 \\ 1 & 1 & 1 & 0 & 1 & 1 & 1 & 0 \\ 1 & 0 & 1 & 0 & 0 & 0 & 1 & 0 \end{array}\right] \end{array} \begin{array}{l} \\ \\ \\ \\ \text{subcarriers } n \end{array} \tag{3.2}$$

with the corresponding hopping sequence

$$\boldsymbol{b}^{\mathsf{T}} = \begin{bmatrix} 2 & 1 & 2 & 0 & 1 & 1 & 2 & 0 \end{bmatrix}. \tag{3.3}$$

Relation to dense OFDM. From a wideband dense OFDM perspective, where a monofrequent LO is employed, (3.1) would be obtained by simply disabling certain symbols in $\boldsymbol{d}$ by element-wise multiplication with Tx pattern $\boldsymbol{P}$. Hence (2.4)

involving $\boldsymbol{P}$ becomes

$$\boldsymbol{x}^{\boxplus} = (\boldsymbol{d} \circ \boldsymbol{P})\boldsymbol{U}^{\mathsf{H}} . \tag{3.4}$$

3.1.2 Receive Signal

At the receiver, the Rx signal is down-converted to baseband using the identical LO that provides the hopping sequence. Through this coherent setup, the absolute phase of the LO does not influence the evaluation, frequency offsets are avoided, and the impact of phase noise is diminished. Moreover, as also illustrated in Fig. 3.1, the signal bandwidth is again reduced to $\mathcal{B}_s$ for each OFDM symbol such that the signal can be digitized at the ADC at a sampling rate far lower than the virtual channel bandwidth would require. Following the OFDM processing described in Section 2.2, next, the CP is removed, and the spectrogram is obtained via a DFT. Afterwards, the modulation symbols are removed through spectral division (2.15). This yields the fragmented spectrogram with elements

$$\mathcal{D}'_{mn_s} = \alpha \, \mathrm{e}^{-\mathrm{j}2\pi \frac{2R}{\lambda_c}} \, \mathrm{e}^{-\mathrm{j}2\pi b_m \Delta f \frac{2R}{c}} \, \mathrm{e}^{-\mathrm{j}2\pi n_s \Delta f \frac{2R}{c}} \, \mathrm{e}^{\mathrm{j}2\pi f_d m T_{\mathrm{OFDM}}} \tag{3.5}$$

assuming that the Doppler frequency shift is $f_d = -2vf_c/c \approx -2vf_m/c$ due to $f_c \gg b_m \Delta f$. It appears that compared to (2.16) the phase progression along the slow-time (m) of the individual baseband subcarriers (n_s) is impaired. In the dense OFDM, these elements contain the channel information observed on the same frequencies, whereas in (3.5) the n_sth baseband subcarrier is composed of fragments originating from different frequencies in the channel due to the hopping, hence depend on b_m. This is solved by first aligning the spectrogram digitally according to the virtual signal structure (3.2) before further processing. To this end, the virtual SOFDM Rx spectrogram $\boldsymbol{\mathcal{D}}^{\boxplus} \in \mathbb{C}^{M \times N}$ covering the bandwidth of the virtual frame is determined. By substituting $n = n_s + b_m$, the baseband coefficients in (3.5) are transferred to $\boldsymbol{\mathcal{D}}^{\boxplus}$, and unoccupied components are filled by zeros, as illustrated in Fig. 3.1. For instance, with the Tx pattern from (3.2), the equivalent virtual wideband spectrogram becomes

$$(\boldsymbol{\mathcal{D}}^{\boxplus})^{\mathsf{T}} = \begin{bmatrix} 0 & 0 & 0 & \mathcal{D}^{\boxplus}_{30} & 0 & 0 & 0 & \mathcal{D}^{\boxplus}_{70} \\ 0 & \mathcal{D}^{\boxplus}_{11} & 0 & \mathcal{D}^{\boxplus}_{31} & \mathcal{D}^{\boxplus}_{41} & \mathcal{D}^{\boxplus}_{51} & 0 & \mathcal{D}^{\boxplus}_{71} \\ \mathcal{D}^{\boxplus}_{02} & \mathcal{D}^{\boxplus}_{12} & \mathcal{D}^{\boxplus}_{22} & 0 & \mathcal{D}^{\boxplus}_{42} & \mathcal{D}^{\boxplus}_{52} & \mathcal{D}^{\boxplus}_{62} & 0 \\ \mathcal{D}^{\boxplus}_{03} & 0 & \mathcal{D}^{\boxplus}_{23} & 0 & 0 & 0 & \mathcal{D}^{\boxplus}_{63} & 0 \end{bmatrix} . \tag{3.6}$$

In general, the coefficients become

$$\mathcal{D}^{\boxplus}_{mn} = \begin{cases} \alpha\, \mathrm{e}^{-\mathrm{j}2\pi \frac{2R}{\lambda_c}}\, \mathrm{e}^{-\mathrm{j}2\pi n \Delta f \frac{2R}{c}}\, \mathrm{e}^{\mathrm{j}2\pi f_d m T_{\mathrm{OFDM}}}, & \text{if } n \in [b_m, b_m + N_s - 1] \\ 0, & \text{otherwise} \end{cases}, \tag{3.7}$$

where n is the index of the subcarrier of the wideband channel. Note that the non-zero components now coincide with those of an equivalent dense OFDM in (2.16) enabling correct Doppler evaluation along the rows of $\boldsymbol{\mathcal{D}}^{\boxplus}$. Moreover, (3.6) is linked to the equivalent dense wideband spectrogram $\boldsymbol{\mathcal{D}}$ (2.16) via

$$\boldsymbol{\mathcal{D}}^{\boxplus} = \boldsymbol{P} \circ \boldsymbol{\mathcal{D}}\,. \tag{3.8}$$

Signal evaluation challenge. Theoretically, the SOFDM radar image might be obtained via the common 2D-(I)DFT of (3.6), which gives

$$\boldsymbol{\mathcal{I}}^{\boxplus} = \boldsymbol{U}\boldsymbol{\mathcal{D}}^{\boxplus}\boldsymbol{U}^{\mathsf{H}} \tag{3.9}$$

$$= \boldsymbol{U}\big(\boldsymbol{P} \circ \boldsymbol{\mathcal{D}}\big)\boldsymbol{U}^{\mathsf{H}} = \boldsymbol{U}\boldsymbol{P}\boldsymbol{U}^{\mathsf{H}} \circledast \boldsymbol{U}\boldsymbol{\mathcal{D}}\boldsymbol{U}^{\mathsf{H}} \tag{3.10}$$

omitting windowing and $\circledast$ denoting the circular 2D convolution. However, the expansion (3.10) reveals that $\boldsymbol{P}$ acts like a windowing function resulting in the 2D-(I)DFT image of $\boldsymbol{P}$ being put over the target peaks in the *R-v*-image, thus potentially determining its dynamic and maximum peak-to-sidelobe ratio (PSLR). In Fig. 3.2, three images $\boldsymbol{U}\boldsymbol{P}\boldsymbol{U}^{\mathsf{H}}$ of three example patterns $\boldsymbol{P}$ for different N_s are depicted. The images exhibit high sidelobes along the zero range cut. In addition, a periodical sinc-pattern emerges in range caused by the N_s contiguous non-zero elements that constitute an individually shifted rectangular shape in each row of $\boldsymbol{P}$ (3.2). As each row exhibits the same block widths, the same pattern occurs in each range profile, except for an additional phase rotation proportional to f_m. In the velocity dimension, no distinct structure is discernible since the individual columns of the pattern are diversely and randomly occupied with zeros. Consequently, the patchwork structure of $\boldsymbol{P}$ and $\boldsymbol{\mathcal{D}}^{\boxplus}$, particularly their gaps, give rise to high sidelobes in the radar image when the standard 2D-(I)DFT pulse compression is applied. Basically, the highest target peak and the pattern determine the power of the highest sidelobe. This limits the achievable dynamic range and minimum peak power of a weaker target to be detectable and distinguishable from the sidelobes caused by the

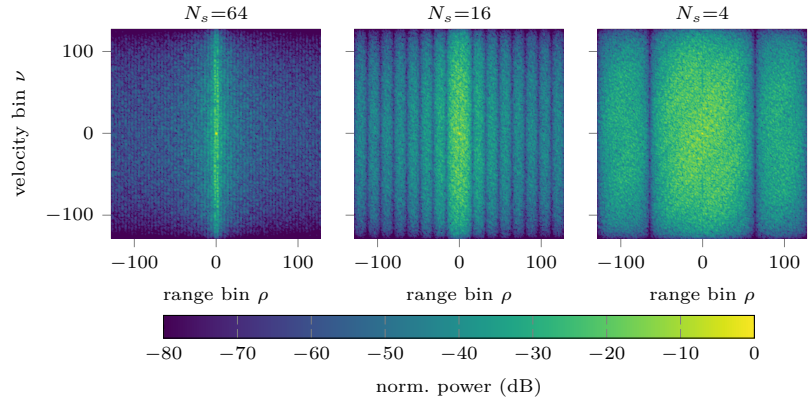


Fig. 3.2: 2D Fourier images $\boldsymbol{UPU}^{\mathsf{H}}$ of three randomly generated example Tx patterns $\boldsymbol{P}$ for different N_s of virtual frame size 256×256 and different N_s.

strongest target.

However, if one manages to reconstruct the missing signal components in $\boldsymbol{\mathcal{D}}^{\boxplus}$ (3.6), the sidelobes and artifacts caused by $\boldsymbol{UPU}^{\mathsf{H}}$ would disappear, and 2D-(I)DFT pulse compression becomes reasonable again. To accomplish this, a 2D CS-based method capable of this recovery is developed.

3.2 Multidimensional Signal Recovery Using Compressed Sensing Approaches

Due to the required frequency hopping, the signal of a single subcarrier over the fast time and the signal of a single symbol over the wideband are incomplete in the SOFDM spectrogram $\boldsymbol{\mathcal{D}}^{\boxplus}$. Hence, both the range and velocity compression are fragmented and disturbed. Moreover, regarding the isolated range compressions along the rows of $\boldsymbol{\mathcal{D}}^{\boxplus}$, only the narrow bandwidth is accessible, whereas considering the entire frame, the information of all subcarriers and the virtual bandwidth becomes accessible. Therefore joint recovery of both image dimensions of SOFDM is pursued that allows to share and exploit information of the entire measurement and thereby increase robustness and recovery performance.

Yet, classical CS theory and algorithms mostly deal with 1D problems in the sense that the signal of interest is sparse in a single dimension, and sparse recovery is performed based on a single snapshot measurement vector that was sensed in a single dimension. Such problems are described by the theory in Section 2.4 and are covered by (2.56). However, imaging OFDM radars aim at jointly retrieving multidimensional information such as range, radial velocity, or angle of targets by performing multidimensional, i.e. spectral, temporal, or spatial sensing of the channel, respectively. In SOFDM, the focus is on the *R-v*-image, which is the sparse 2D image domain with orthogonal bases range and Doppler. On the other hand, linked via the 2D-(I)DFT is the non-sparse spectrogram (2D observation) with orthogonal bases frequency and time.

Formulation of the 2D CS problem for SOFDM. In terms of CS, the following system of equation has to be solved:

$$\boldsymbol{\mathcal{D}}^{\boxplus} = \boldsymbol{P} \circ \left(\boldsymbol{\mathcal{D}} + \boldsymbol{W}\right) = \boldsymbol{P} \circ \left(\boldsymbol{U}^{\mathsf{H}} \boldsymbol{X} \boldsymbol{U} + \boldsymbol{W}\right). \tag{3.11}$$

The goal is to infer the high-resolution *R-v*-image $\boldsymbol{X}$ and its corresponding dense observation $\boldsymbol{\mathcal{D}}$ from the narrowband and noisy observation $\boldsymbol{\mathcal{D}}^{\boxplus}$. Other than in the classical CS formulation (2.56), the dimensions of $\boldsymbol{\mathcal{D}}^{\boxplus}$, $\boldsymbol{\mathcal{D}}$, and $\boldsymbol{X}$ are identical due to the compact matrix representation. The dimensionality reduction is hidden in $\boldsymbol{P}$, which maps only MN_s out of MN virtual samples, $N_s \ll N$, to the observation. For this reason, the SOFDM problem (3.11) is ill-posed.

From (3.11), the corresponding 2D extension of the LASSO (2.58) is

$$\min_{\boldsymbol{X}} \|\boldsymbol{\mathcal{D}}^{\boxplus} - \boldsymbol{P} \circ \left(\boldsymbol{U}^{\mathsf{H}} \boldsymbol{X} \boldsymbol{U}\right)\|_F^2 \quad \text{subject to} \quad \|\boldsymbol{X}\|_1 \leq \beta \tag{3.12}$$

with the matrix ℓ_1-norm $\|\boldsymbol{X}\|_1 = \sum_{i,j} |X_{ij}|$ and the squared Frobenius norm $\|\boldsymbol{X}\|_F^2 = \sum_{i,j} |X_{ij}|^2$.

Although there is an overwhelming amount of literature available on CS theory, algorithms, and applications, only a few deal with a multidimensional setting. The obvious solution of considering the various signal dimensions individually as separate 1D problems [129], while viable, is inferior to processing all dimensions jointly, since only then can the compression and processing gain of all dimensions be accomplished [130]. Moreover, the detached processing

of the range in SOFDM is ill-conditioned, since only a block of contiguous samples is available. This is highly unfavorable for CS recovery where randomness is a decisive criterion for reliable, stable, and unique recovery [60]. So far, a common approach in the multidimensional setting is to convert the multidimensional to a 1D problem (2.56) and then solve it with any 1D algorithm [81], [109], [131]–[133]. The key here is the Kronecker product that allows to convert the multidimensional formulation (3.11) into its corresponding vectorized representation [132]. However, the resulting sensing matrix would become huge such that it requires high computational load and storage [134]. An example assessment for SOFDM is given in Appendix A.2 on page 145. Hence, in high-resolution radar imaging, such an approach is infeasible. Yet, the related literature provides basic recovery guarantees and analyses for multidimensional signal recovery [75], [76], [81], [109], [132]. At the same time, there are also reverse efforts, where in case of impractically large 1D sensing matrices in (2.56), the problem is decomposed into multiple lower dimensional (smaller size) matrices by exploiting underlying matrix structures, e.g. Kronecker structure [75], [134], [135]. Thereby, a 2D CS problem is constructed. Finally, there are also a few efforts to directly solve a multidimensional CS problem [2], [32], [40], [97], [116], [118], [130], [133], [134], [136]–[138].

However, it shows that the task in SOFDM is exceptional and different from the usual CS setting such that most of these approaches are not directly applicable. The first difference is the objective and the targeted role of CS in the signal evaluation. In most CS radar applications, the CS framework is considered a target detector where the estimated signal support is the target detection result. It is also tempting to equate this estimate as a CFAR detection result. However, for most CS approaches, the relation between false-alarm rate (FAR) and detection probability and noise statistics is unknown [139]. In general, CS algorithms are not designed to balance such statistics but always seek the sparsest solution with minimum MSE via a sparsity imposing regularizer, for instance soft-thresholding, which in general does not coincide with a CFAR detection. Moreover, misusing the sparse estimate as target detection performs significantly worse than using a noisy signal estimate[1], provided by most iterative

[1] A noisy estimate typically consists of the sum of the sparse estimate and some kind of residual, which resembles so far inexplicable signal content in the CS sense, and is assumed to be the sum of the signal of interest and white Gaussian noise.

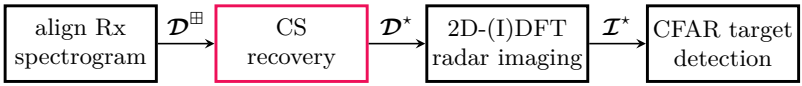


Fig. 3.3: SOFDM Rx signal processing chain.

CS algorithms, and perform CFAR detection on this very result [139]. Thus, instead of recovering the sparse coefficients, the objective in SOFDM is to recover the dense observation by means of retrieving the signal support. A similar methodology can be found for array extrapolation in [58]. To this end, the noisy sparse estimate provided by CS is utilized to infer the missing observation elements in (3.6) via reverse imaging processing steps using the inverted 2D-(I)DFT. This yields a *dense hybrid spectrogram* $\boldsymbol{\mathcal{D}}^{\star}$, where each element is either acquired or recovered. Eventually, $\boldsymbol{\mathcal{D}}^{\star}$ is evaluated using the common OFDM processing described in Section 2.2 obtaining the *recovered image* $\boldsymbol{\mathcal{I}}^{\star}$. The signal processing chain is depicted in Fig. 3.3. The proposed approach enables the common additional signal processing improvements such as sidelobe suppression via windowing or zero-padding in order to improve target detection.

The second difference is the problem formulation. Typically, 2D approaches aim at problems that are expressed by the model $\boldsymbol{Y}=\boldsymbol{A}\boldsymbol{X}\boldsymbol{B}$ obviously differing from the SOFDM problem in (3.11). In sensing, $\boldsymbol{A}$ and $\boldsymbol{B}$ are often decimated bases, for instance, partial DFT matrices composed of a subset of rows or columns of the complete DFT matrix, and $\boldsymbol{Y}$ is a dense but low dimensional observation [133]. Suppose that the rows and columns of $\boldsymbol{Y}$ contain fast-time and slow-time samples, respectively, as it is the case in many CS radar applications. So the decimation of the bases corresponds to omitting fast-time samples and entire pulses or frequency ramps. To obtain the same for $\boldsymbol{Y}=\boldsymbol{\mathcal{D}}^{\boxplus}$, this would require omitting entire OFDM symbols and subcarriers, while the remaining ones are fully occupied. However, this is in contradiction with the goal of reducing the bandwidth of the baseband signal.

Choice of algorithms and prerequisites. First of all, the algorithms must be able to deal with complex valued signals, and – because the problem is multidimensional – the algorithm should be also extendable to solve the 2D

minimization (3.12). Furthermore, the high-resolution SOFDM image is rather large in the range of some thousand by some thousand elements, so fast convergence using a small number of iterations and low-cost iteration steps are desired. In particular, matrix inversions should be avoided for reasons of computational complexity and numerical stability issues. In general, the algorithms' computational effort should scale well with the problem size. Because radar measurements are dynamic and scenes or environments are subject to changes, the algorithms should be preferably self-tuning without requiring much prior knowledge about the observation such as sparsity or noise variance. Along with this, they should be robust to noise and clutter. Appropriate candidates are found to be AMP and the SALSA, whose basic formulations are introduced in Sections 2.4.1 and 2.4.2, respectively. The SALSA is especially suitable for large scale problems but has also been successfully applied to FMCW radar measurements [22], [140], [141]. On the other hand, AMP is proven to run fast, even if exposed to large problems, due to its low complexity [83], [92], and was already shown to be suitable for complex valued signals [96]. Moreover, there is already profound knowledge on the performance of (1D) AMP with noisy signals [142] and in radar applications [139], [143].

3.2.1 2D-CAMP

The complex approximate message passing (CAMP) algorithm was proposed by [96] as an instance of AMP to solve the complex-valued LASSO. With the assumption that real and imaginary parts of the sparse signal are grouped, thus they are either both zero or non-zero, the resulting CAMP equals the algorithm (2.61) with Γ being the complex soft-threshold function (2.63). The proposed 2D-CAMP extension is obtained by adapting each step in (2.61) to solve the 2D LASSO (3.12) and applying an element-wise soft-threshold in (2.61b). To this end, the observation, residual, and estimate vectors are replaced by matrices. In addition, the matrix-vector projections get replaced by left and right side (column and row) projections. Because the soft-threshold is applied element-wise, it only requires an additional index in (2.63) to account for the

columns as well. Eventually, the 2D-CAMP algorithm yields

$$\tilde{\boldsymbol{X}}^{[k]} = \boldsymbol{U}\boldsymbol{E}^{[k-1]}\boldsymbol{U}^{\mathsf{H}} + \hat{\boldsymbol{X}}^{[k-1]} \tag{3.13a}$$

$$\hat{\boldsymbol{X}}^{[k]} = \operatorname{soft}\left(\tilde{\boldsymbol{X}}^{[k]}; \boldsymbol{\Lambda}^{[k]}\right) \tag{3.13b}$$

$$\boldsymbol{E}^{[k]} = \boldsymbol{\mathcal{D}}^{\boxplus} - \boldsymbol{P} \circ \left(\boldsymbol{U}^{\mathsf{H}}\hat{\boldsymbol{X}}^{[k-1]}\boldsymbol{U}\right) + \tfrac{\|\hat{\boldsymbol{X}}^{[k]}\|_0}{MN_s}\boldsymbol{E}^{[k-1]}, \tag{3.13c}$$

where the initial residual and estimate are $\boldsymbol{E}^{[0]} = \boldsymbol{\mathcal{D}}^{\boxplus}$ and $\hat{\boldsymbol{X}}^{[0]} = \boldsymbol{0}$, respectively. The residual (3.13c) is peculiar here and differs from the simple 2D extension. Since $\boldsymbol{U}^{\mathsf{H}}$ and $\boldsymbol{U}$ are not reduced in dimension, as it is usually the case in CS, $\boldsymbol{P}$ is required here to enforce decimation. It thereby guarantees that the residual is only determined for the acquired but not the missing elements in the spectrogram, since a residual is only meaningful for known data. In Appendix A.3 on page 146, it is shown that (3.13) may be transferred into an equivalent 1D algorithm (2.61), which verifies that AMP theory holds for 2D-CAMP and the algorithm converges to the correct result.

Threshold choice and tuning. The threshold $\boldsymbol{\Lambda}^{[k]}$ is chosen to be a scaled version of the noise standard deviation σ, which is a common design rule for soft-threshold in AMP [80], [83], [139], [142]. Because in general, the true σ is not known, an estimate $\hat{\sigma}$ is used instead. To this end, a modification of the median estimation [139], [144] is suggested. It is based on the assumption that the noise contribution in $\tilde{\boldsymbol{X}}^{[k]}$ is complex white Gaussian, where the real and imaginary parts are i.i.d. with $\mathcal{N}(0, \sigma^2/2)$. As a consequence, the elements of the complex noise matrix $\boldsymbol{W}$ are i.i.d. with $W_{ij} \sim \mathcal{CN}(0, \sigma^2)$. Moreover, the magnitudes W_{ij} follow a Rayleigh distribution with mode $\sigma/\sqrt{2}$ [145]. Given the set of samples $\tilde{\boldsymbol{X}}^{[k]}$, the median and the mode of the distribution and thereby the estimate $\hat{\sigma}$ are linked via

$$\hat{\sigma}^{[k]} = \frac{\operatorname{median}\left(|\tilde{\boldsymbol{X}}^{[k]}|\right)}{\sqrt{\ln 2}}. \tag{3.14}$$

If $\hat{\sigma}^{[k]}$ is newly determined in every iteration, it refines itself and adapts to the measurement. Moreover, it approaches the true σ with progressing recovery [139]. Compared to using the MSE, the median estimate is robust to outliers and high dynamics of the radar image. Since the SOFDM radar images are expected

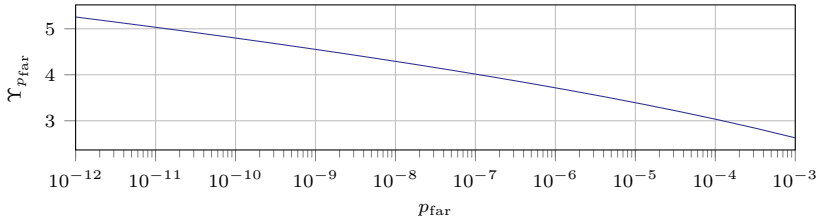


Fig. 3.4: Relation between FAR and scaling for the soft-threshold function.

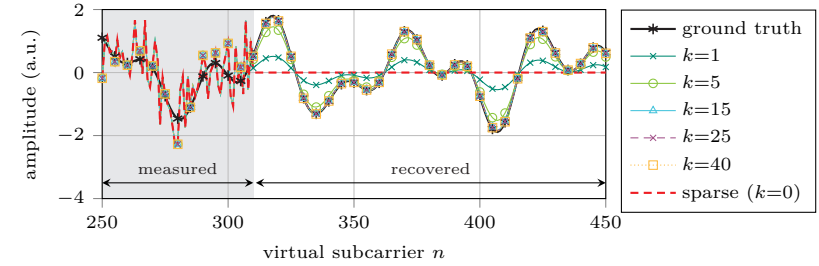
to be very sparse, i.e. $\varrho_{\text{cs}} \ll 1$, the number of high magnitudes in the image is expected to be much less than 50 % such that the estimate is stable. In SOFDM, the concept is further advanced by determining individual $\hat{\sigma}_{\nu\rho}^{[k]}$ for each element of $\tilde{\boldsymbol{X}}^{[k]}$, where ν and ρ are the range and Doppler indices, respectively. As shown in Fig. 3.2 on page 44, due to $\boldsymbol{P}$, high artifacts and a ridge along the Doppler bins of each target arise. If the common median estimate (3.14) would be used, such structures are ignored and either weak targets are getting missed, or artifacts will most likely be detected. Therefore, first row- and column-wise median estimates $\hat{\sigma}_{\nu:}^{[k]} = \text{median}(|\tilde{\boldsymbol{X}}_{\nu:}^{[k]}|)/\sqrt{\ln 2}$ and $\hat{\sigma}_{:\rho}^{[k]} = \text{median}(|\tilde{\boldsymbol{X}}_{:\rho}^{[k]}|)/\sqrt{\ln 2}$ are determined, respectively. Then the individual $\hat{\sigma}_{\nu\rho}^{[k]}$ of each matrix element is given by their maximum

$$\hat{\sigma}_{\nu\rho}^{[k]} = \begin{cases} \hat{\sigma}_{\nu:}^{[k]}, & \text{if } \hat{\sigma}_{\nu:}^{[k]} > \hat{\sigma}_{:\rho}^{[k]} \\ \hat{\sigma}_{:\rho}^{[k]} & \text{otherwise} \end{cases} . \tag{3.15}$$

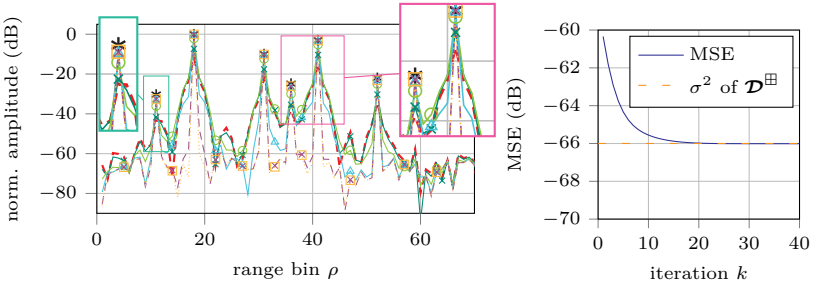
Eventually, the threshold parameter matrix holding the element-wise thresholds of the kth iteration yields

$$\boldsymbol{\Lambda}^{[k]} = \Upsilon \hat{\boldsymbol{\sigma}}^{[k]} \tag{3.16}$$

with Υ a scalar scaling that accounts for magnitude fluctuations. It is also the only free design parameter in 2D-CAMP. This enhanced self-tuning thresholding essentially resembles a primitive 2D-OS-CFAR with rank 0.5 and scaling Υ. Moreover, through Υ, the detection sensitivity can be controlled and with it the false detection rate of the threshold step. In [139] it is shown that, if the Gaussian assumption holds and (3.14) constitutes an approximation of σ, there is a direct relation between the FAR of the soft-threshold and Υ. In this case,



(a) Spectrum of a single OFDM symbol (m).



(b) Recovered range profiles at v=0 m/s. **(c)** MSE.

Fig. 3.5: Simulation example of recovery states of 2D-CAMP with Υ=4 for an OFDM radar frame of N=1024 by M=1024 with N_s=256 thus δ_{cs}=1/4. The simulated noise variance of $\mathcal{D}^{\boxplus}$ is σ^2=−66 dB. The scene comprises six stationary targets at range bins $\hat{\rho}$={11, 18, 13, 36, 41, 52}. (a) Excerpt of the spectrum of a single OFDM symbol for the noiseless ground truth and the 2D-CAMP recovery states at k={0, 1, 5, 15, 25, 40}. (b) The corresponding range profiles without windowing. (c) The evolution of the MSE for the recovery.

for an intended FAR p_{far}, the scaling should be [139]

$$\Upsilon_{p_{\text{far}}} = \sqrt{-\ln p_{\text{far}}}\,, \tag{3.17}$$

which is also illustrated in Fig. 3.4. Throughout the thesis, a scaling of $\Upsilon = 4$, which translates in $p_{\text{far}} = 10^{-7}$, is applied.

In Fig. 3.5, the recovery behavior for 2D-CAMP is illustrated for $\Upsilon = 4$,

undersampling $\delta_{\mathrm{cs}} = 1/4$, and six stationary targets. In Fig. 3.5 (a), the spectrum of a single OFDM symbol (row of $\boldsymbol{U}^{\mathsf{H}} \tilde{\boldsymbol{X}}^{[k]} \boldsymbol{U}$) for different iteration numbers k is shown along with the noiseless wideband ground truth. It shows that after about 15 to 20 iterations, hardly any improvement is observable anymore, and the recovered matches the true wideband signal. Note that the acquired samples remain unchanged in the grayish area. Figure 3.5 (b) shows the corresponding range profiles (zero-Doppler cut of $\tilde{\boldsymbol{X}}^{[k]}$), where $*$ indicates the true range bin and amplitude of the simulated targets. Figure 3.5 (c) shows the MSE $= \|\tilde{\boldsymbol{X}}^{[k]} - \boldsymbol{X}_0\|_F^2/(MN) \to (\sigma^2 + \epsilon)$ of the noisy estimate across the iterations with $\boldsymbol{X}_0$ the noiseless ground truth solution. The limit value of the MSE ideally approximates the noise variance σ^2 of the sparse observation $\boldsymbol{\mathcal{D}}^{\boxplus}$, in this case it was $-66\,\mathrm{dB}$. Often, instead of σ^2 the MSE approaches a value $\sigma^2 + \epsilon$, where ϵ with $0 \leq \epsilon \ll \sigma^2$ is a constant offset caused by imperfect reconstruction and thus corresponds to the reconstruction error. However, it is not possible to achieve an MSE $< \sigma^2$ even for $K \to \infty$. At about $k = 20$, the change in the MSE of successive iterations becomes negligible, and any further iterations do not contribute significant change to the results, and the iteration may be stopped.

Stopping criterion and final estimate of the algorithm. The tracking of the MSE is a natural stopping criterion, however, usually, the ground truth is unknown and therefore, the MSE is not feasible. Other possibilities are either tracking the absolute difference of the current and previous estimate and stop iterating when it comes below a given tolerance value ϵ [139] or tracking the ℓ_2-norm of the residual and stop iterating when it reaches a certain value [76], [146]. However, both options require at least a rough knowledge about the order of magnitude of the true σ. Therefore, here, the algorithm runs for exactly $K = 20$ iterations, if not stated otherwise. After K iterations, the hybrid spectrum estimate $\boldsymbol{\mathcal{D}}^{\star} = \boldsymbol{U}^{\mathsf{H}} \hat{\boldsymbol{X}}^{[K]} \boldsymbol{U} + \boldsymbol{E}^{[K]}$ is obtained and afterwards evaluated for radar imaging.

3.2.2 2D-HAMP

The hard-threshold approximate message passing (HAMP) algorithm is an instance of AMP where the sparsity enforcing threshold policy in (2.61b) is the hard threshold (2.62). Its 2D extension from (1D) AMP (2.61) and the extension

for the hard threshold is similar to the extensions applied for 2D-CAMP. Eventually, the resulting 2D-HAMP algorithm for SOFDM is

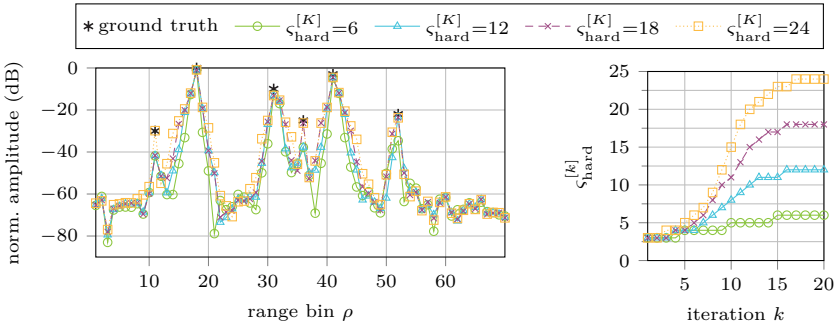
$$\tilde{\boldsymbol{X}}^{[k]} = \boldsymbol{U}\boldsymbol{E}^{[k-1]}\boldsymbol{U}^{\mathsf{H}} + \hat{\boldsymbol{X}}^{[k-1]} \tag{3.18a}$$

$$\hat{\boldsymbol{X}}^{[k]} = \operatorname{hard}\left(\tilde{\boldsymbol{X}}^{[k]}; \Lambda^{[k]}\right) \tag{3.18b}$$

$$\boldsymbol{E}^{[k]} = \boldsymbol{\mathcal{D}}^{\boxplus} - \boldsymbol{P} \circ \left(\boldsymbol{U}^{\mathsf{H}}\hat{\boldsymbol{X}}^{[k-1]}\boldsymbol{U}\right) + \tfrac{\|\hat{\boldsymbol{X}}^{[k]}\|_0}{MN_s}\boldsymbol{E}^{[k-1]}\,. \tag{3.18c}$$

Threshold choice and tuning. The threshold $\Lambda^{[k]}$ in (3.18b) is chosen such that in each iteration exactly the $\varsigma_{\text{hard}}^{[k]}$ elements that yield the best possible $\varsigma_{\text{hard}}^{[k]}$-sparse solution pass the threshold, while the remaining components are rejected [32]. In [80] this approach is also referred to as AMP with fixing the number of detections. To control the number or accepted elements for the kth iteration, $\Lambda^{[k]}$ is determined by the magnitude of the $\varsigma_{\text{hard}}^{[k]}$-th element when the elements of $\tilde{\boldsymbol{X}}^{[k]}$ are sorted in decreasing order according to their magnitudes. Therefore, $\varsigma_{\text{hard}}^{[k]}$ is essentially the only tuning parameter of 2D-HAMP. One could assume that accurate knowledge about the true sparseness of the signal is required in order to tune the algorithm optimally. Fortunately, this is only true for the ideal artificial case of point targets lying exactly on the image resolution grid, and no clutter being present. Real-world radar targets are usually not located on the grid, and the peaks are most likely not sharp but slightly broadened with slopes across multiple cells. Hence, even if the exact cardinality ς of the support is known, the ς largest components do not constitute the complete solution with high probability, since slopes of the high peaks are preferred to weak ones in the threshold. Therefore, the proposed approach allows generous overestimation of ς in order to account for multiple support components belonging to the same target. A rough estimate of the number of targets in the scene may be obtained from previous measurements or using model order selection estimates [147].

Another important point to account for is that in the first few iterations, the estimate still contains lots of high artifacts caused by strong targets. Yet, the highest peak is almost certainly a correct target, since the pattern induced artifacts are always lower than their causing main lobe. Therefore, it is advisable to initially let only a few elements pass the threshold to reduce the risk of capturing artifacts. After the strongest targets are detected and recovered,



(a) Recovered range profiles at v=0 m/s. **(b)** Course of $\boldsymbol{\varsigma}_{\text{hard}}$.

Fig. 3.6: Analysis of the choice of $\boldsymbol{\varsigma}_{\text{hard}}$ and recovery performance of 2D-HAMP. The simulated OFDM radar frame and scene is the same as utilized in Fig. 3.5 with $\delta_{\text{cs}} = 1/4$ and a PNR of 66 dB for the strongest target. The actual target locations and amplitudes of the simulated six targets are indicated by $*$ in the range profiles in (a). Different choices of $\boldsymbol{\varsigma}_{\text{hard}}$ are investigated that differ in $\varsigma_{\text{hard}}^{[K]}$ are illustrated in (b). The initial sparsity underestimate is $\varsigma_{\text{hard}}^{[0]} = 3$.

artifacts caused by them disappear such that the threshold can be lowered with less risk, and weak targets become detectable. It is therefore recommended to use a monotonously increasing sequence $\boldsymbol{\varsigma}_{\text{hard}}=\{\varsigma_{\text{hard}}^{[k]}\}_{k=1,\dots,K}$ starting from an underestimation of the support and increasing to an overestimation. As function model a logistic or sigmoid function is used. In Fig. 3.6, the behavior and performance of the proposed approach are illustrated. For this purpose, a simulation is performed with $\delta_{\text{cs}} = 1/4$, $K = 20$, and six stationary targets (identical to the example in Fig. 3.5). Four different sets of $\boldsymbol{\varsigma}_{\text{hard}}$ are investigated. They differ in their final values $\varsigma_{\text{hard}}^{[K]}$ of 1ς, 2ς, 3ς, and 4ς. The initial sparsity of all sequences is $\varsigma_{\text{hard}}^{[0]} = 3 = 0.5\varsigma$. The courses of $\varsigma_{\text{hard}}^{[k]}$ are illustrated in Fig. 3.6 (b), which shows the typical S-shape. The corresponding recovered range profiles (v=0 m/s) of the *R*-*v*-images are displayed in Fig. 3.6 (a). It shows that for the weak targets at bins 10 and 35 to be successfully recovered, $\varsigma_{\text{hard}}^{[K]}$ must be a factor 3 to 4 of the true ς. Moreover, even for an overestimation of factor 4, no false peaks are generated, but a broadening of the peaks is observable with increasing overestimation.

Stopping criterion and final estimate of the algorithm. An interesting property of 2D-HAMP is that its result is largely independent of K. Based on empirical investigations on simulated and measured radar data, it is found that if a critical number of iterations is exceeded, no improvements in the recovery is achieved when increasing K further. The determined lower bound on K is found to be about 20 iterations, which is used for 2D-HAMP. After the last iteration, the hybrid spectrum estimate $\boldsymbol{\mathcal{D}}^{\star} = \boldsymbol{U}^{\mathsf{H}} \hat{\boldsymbol{X}}^{[K]} \boldsymbol{U} + \boldsymbol{E}^{[K]}$ is obtained and afterwards evaluated for radar imaging.

3.2.3 2D-SALSA

Similar to the 2D-AMP approaches, the 1D vector representation of the SALSA (2.64) is transformed to 2D and adapted to the problem (3.11), which yields

$$\boldsymbol{G}^{[k]} = \operatorname{soft}(\tilde{\boldsymbol{X}}^{[k-1]} + \boldsymbol{H}^{[k-1]}; \boldsymbol{\Lambda}^{[k]}) - \boldsymbol{H}^{[k-1]} \tag{3.19a}$$

$$\boldsymbol{H}^{[k]} = \boldsymbol{U}\left(\boldsymbol{\mathcal{D}}^{\boxplus} - \boldsymbol{P} \circ \left(\boldsymbol{U}^{\mathsf{H}} \boldsymbol{G}^{[k]} \boldsymbol{U}\right)\right) \boldsymbol{U}^{\mathsf{H}} \tag{3.19b}$$

$$\tilde{\boldsymbol{X}}^{[k]} = \boldsymbol{H}^{[k]} + \boldsymbol{G}^{[k]}. \tag{3.19c}$$

The adaptions of (3.19a) and (3.19c) are straightforward as only element-wise operations are involved. The equivalence of (3.19b) and its 1D counterpart (2.64b) is shown in Appendix A.4 on page 148.

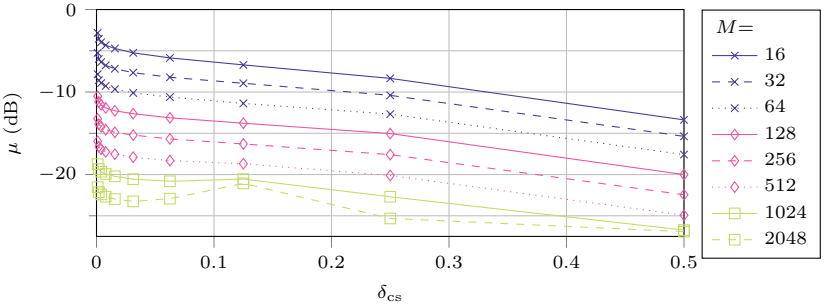
Threshold choice and tuning. The thresholding policy in 2D-SALSA is the same as in 2D-CAMP, only that the input variable is now $\tilde{\boldsymbol{X}}^{[k-1]} + \boldsymbol{H}^{[k-1]}$ instead of $\tilde{\boldsymbol{X}}^{[k]}$.

Stopping criterion and final estimate of the algorithm. Empirical investigations revealed that 2D-SALSA is more sensible to clutter and noise such that a slightly higher scaling of $\Upsilon = 4.5$ is advisable and is applied in this thesis. As the other approaches, the algorithm terminates after $K = 20$ iterations. After the last iteration, the hybrid spectrum estimate $\boldsymbol{\mathcal{D}}^{\star} = \boldsymbol{U}^{\mathsf{H}} \tilde{\boldsymbol{X}}^{[K]} \boldsymbol{U}$ is obtained and afterwards evaluated for radar imaging.

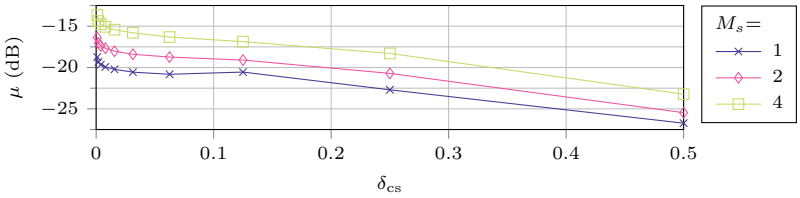
3.2.4 Sensing Matrix Design and Recovery Guarantee

Regardless of the applied recovery algorithm, the performance of the recovery and the uniqueness of a solution is determined by the design of the sensing matrix. The coherence property (2.59) provides a sufficient uniform recovery guarantee measure. Conveniently, μ corresponds to the reciprocal of the PSLR of the *R-v*-image [109], which is the ratio of the strongest target reflection to the highest sidelobe of the image. As the PSLR decreases, the main- and sidelobe level become more similar. In addition, the maximal resolvable dynamic range of the target reflections, i.e. the maximum ratio of magnitudes of a still detectable weak target to the strongest target in the radar image, gets reduced. If the peaks of weaker targets are lower than the highest sidelobe, they cannot be detected beyond doubt, because they are indistinguishable from the sidelobe and erroneous detections become likely. Hence, the smaller the PSLR, the larger μ and the less reliable and potent is the recovery.

In Section 3.1.2, it is shown that $\boldsymbol{P}$ determines the sidelobes, or more precisely, the artifacts caused by each target. As a consequence, the reciprocal of μ, which is the PSLR of (3.9), equals the side- to mainlobe ratio of $\boldsymbol{U}\boldsymbol{P}\boldsymbol{U}^{\mathsf{H}}$. Therefore, it is worth taking a close look at the design of $\boldsymbol{P}$. Its design parameters are the number of virtual subcarriers N, the number of OFDM symbols of the frame M, the number of subcarriers in the baseband N_s, and the hopping pattern $\boldsymbol{b}$. As before, $N_s = \mathcal{B}_s/\Delta f$ is set fixed, since using less subcarriers would mean a waste of available resources. Simulations have been carried out with $N = 1024$ virtual subcarriers. This yields no restriction to the generalization to other values, as the resulting characteristics depend on $\delta_{\mathrm{cs}} = N_s/N$ and not on the absolute value of N. First, it is analyzed how M influences μ. In Fig. 3.7 (a), the coherence for different M and δ_{cs} are shown. The hopping pattern was generated purely randomly within the virtual subcarrier grid. It shows that when M is increased, μ decreases. Hence, the more OFDM symbols so the longer the observation, the better. In addition, μ worsens with decreasing δ_{cs}, i.e. with less available samples per OFDM symbol. Next, it is analyzed how μ is influenced by the hopping pattern structure. Ideally, the elements of $\boldsymbol{b}$ should be chosen randomly, which guarantees a high degree of randomness. Suppose that due to hardware restrictions, for instance the settling time of the LO frequency, it is not possible to initiate a new hop after every OFDM symbol but only after a sequence of at least M_s symbols. In Fig. 3.7 (b), this constraint is investigated



(a) Influence of the number of OFDM symbols M.



(b) Influence of the block length M_s.

Fig. 3.7: Analysis of the influence of the frame length M on the coherence μ. The values are obtained from Monte Carlo simulations using randomly generated Tx patterns thus hopping patterns for virtual frame sizes of $N = 1024$ by (a) different M and (b) $M = 1024$ but different block lengths M_s.

for different block lengths M_s after which a hop is performed. It shows that when doubling M_s, μ deteriorates by 3 dB. This confirms that the pattern should be as random as possible to achieve low coherence. If structures or constraints are introduced to $\boldsymbol{b}$, the randomness of $\boldsymbol{P}$ dissolves. Note that periodic structures such as a stepped pattern as in [31] results in μ=0 dB, and the radar image becomes ambiguous. In this case, CS recovery is impossible. In the following simulations and measurements, randomly generated patterns with $M_s = 1$ are used. The superiority of the proposed joint 2D recovery capability over separate 1D recovery of range and Doppler in terms of μ is shown in Appendix A.5 on page 149.

3.2.5 Pseudo PNR

With 2D-CAMP, 2D-HAMP, and 2D-SALSA, a hybrid spectrogram $\boldsymbol{\mathcal{D}}^{\star}$ is obtained, where the prior gaps in $\boldsymbol{\mathcal{D}}^{\boxplus}$ (3.6) get restored, whereas the acquired data remains unchanged. Through this, the total desired signal energy in the spectrogram gets increased, while the total collected noise energy remains the same. Consequently, after pulse compression over the $M \times N$ frame, the image of the hybrid $\boldsymbol{\mathcal{D}}^{\star}$ achieves a higher peak-to-noise ratio (PNR) and PSLR compared to an equivalent wideband dense OFDM measurement. The reason is that the recovery retrieves the integration gain. Moreover, noise is only contained in the actually gathered elements but not in those recovered. This leads to a lower total noise energy contribution and thereby higher PNR by the factor $1/\delta_{\mathrm{cs}}$. Note that this assumes that the output power per subcarrier is identical for SOFDM and dense OFDM. However, if the output power of the OFDM symbol, i.e. the sum of active subcarriers, is kept equal, an increase of $1/\delta_{\mathrm{cs}}^2$ is obtained. Here, the former is considered, which also gives a fair comparison to an equivalent dense OFDM frame. The artificial increase of the PNR is referred to as *pseudo PNR* and is a characteristic property of SOFDM. Hence, if the recovery is successful, SOFDM is superior to dense OFDM in terms of PNR using the same time-bandwidth resources.

In addition, through the mitigation of artifacts and thereby lowering of the sidelobe level down to beneath the dense OFDM noise level, weak targets, even if not perfectly recovered or even missed by CS, may surface and become detectable by the CFAR. However, this is only possible for targets that a priori have a higher energy than the collected noise after compression of MN_{s} elements, otherwise they remain masked and can never be detected by CS either, since it cannot reach below this noise level.

3.2.6 Complexity of the 2D Recovery

Taking a closer look at 2D-CAMP (3.13), 2D-HAMP (3.18), and 2D-SALSA (3.19), three fundamental kind of operations are identified: element-wise multiplications, thresholding, and transforms. The element-wise operations have complexity $\mathcal{O}(MN)$, whereas the 2D-(I)DFTs have a complexity of $\mathcal{O}\big(MN \log(MN)\big)$ if an efficient implementation of the FFT is utilized. The element-wise thresholds of 2D-CAMP and 2D-SALSA require the median esti-

Tab. 3.1: Complexity and corresponding decisive operations of the developed 2D CS recovery algorithms.

	2D-CAMP	2D-HAMP	2D-SALSA
decisive operation	2D-(I)DFT	hard-threshold	2D-(I)DFT
complexity	$\mathcal{O}\big(MN\log(MN)\big)$	$\mathcal{O}\big(\varsigma_{\text{hard}}^{[K]}MN\big)$	$\mathcal{O}\big(MN\log(MN)\big)$

mate (3.15), which has a computational complexity of $\mathcal{O}(MN)$ [148], whereas the computation of the hard threshold in 2D-HAMP is dominated by the identification of the $\varsigma_{\text{hard}}^{[k]} \leq \varsigma_{\text{hard}}^{[K]}$-th largest amplitude of $\tilde{\boldsymbol{X}}$ with complexity $\mathcal{O}\big(\varsigma_{\text{hard}}^{[K]}MN\big)$. In usual OFDM radar setups, typically $\varsigma_{\text{hard}}^{[K]} > \log(MN) > 1$. Consequently, the complexity of 2D-HAMP is determined by the hard-threshold with complexity $\mathcal{O}\big(\varsigma_{\text{hard}}^{[K]}MN\big)$, which is slightly worse than that of 2D-CAMP and 2D-SALSA, both dominated by the 2D-(I)DFT operation with complexity $\mathcal{O}\big(MN\log(MN)\big)$. The identified complexity and corresponding decisive operations are summarized in Table 3.1.

3.3 Performance Evaluation and Analysis

In order to be competitive, it is essential for SOFDM to be able to cope with complex scenarios. First, in Sections 3.3.2, the basic recovery performance is evaluated using measurements of scenarios with high target dynamics, i.e. scenes, in which both a weak and a strong target are present. Next, the performance regarding differentiation of close targets is investigated in Section 3.3.3. Because the reconstruction performance is generally independent of the absolute range and velocity of the targets and thus is identical for each element of the range-velocity matrix, only stationary scenarios are measured for these analyses, since they are well controlled and easy to reproduce. On the contrary, the reconstruction performance is even slightly better for targets that share neither a common range bin nor a common velocity bin, since in this case, their tailing sidelobes do not overlap or mask the other target. However, the performance difference is negligible. Thus, the recovery of stationary multi-target scenarios is actually more challenging.

Measurements of extended and non-stationary targets in complex outdoor scenarios are analyzed in Section 3.3.4. In addition, the progress of a 2D-CAMP

recovery is analyzed and intermediate results are shown. Finally, in Section 3.3.5, the influence of δ_{cs} on the recovery performance is evaluated. Initially, the applied radar parametrization, the CS recovery algorithm tuning, and the evaluation configurations are summarized in Section 3.3.1.

3.3.1 Radar Parametrization and CS Algorithm Tuning

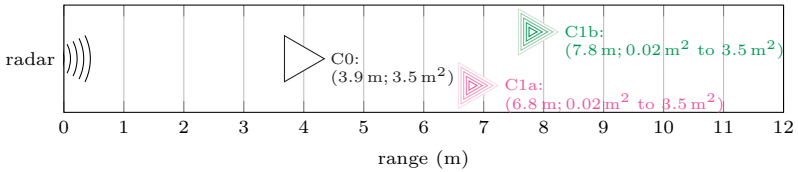
The utilized radar is R1 from Section 2.5 and Table 2.1, page 36, where the parameters $N = 1024$ and $M = 2048$ correspond to the virtual wideband frame. Furthermore, R1 is operated in SISO configuration. For each measurement, a dense OFDM frame is transmitted, which serves as the reference ground truth. From these dense frames, SOFDM measurements are generated by thinning out the Rx spectrogram using randomly generated SOFDM patterns of subsampling δ_{cs}. With the exception of Section 3.3.5, an undersampling of $\delta_{\mathrm{cs}} = 1/4$ is used, which translates to $N_s = 256$ active baseband subcarriers and a baseband bandwidth $\mathcal{B}_s = 102.4\,\mathrm{MHz}$.

The tuning of the CS algorithms follows the inferences and suggestions from Sections 3.2.1 to 3.2.3. The scaling Υ in 2D-CAMP and 2D-SALSA is set to 4 and 4.5, respectively. In 2D-HAMP, the monotonously increasing sparsity sequence $\varsigma_{\mathrm{hard}}$ ranges from $0.5H$ to $3H$, where H is the ground truth number of targets. With the exception of Section 3.3.5, every algorithm runs for 20 iterations without additional stopping criteria.

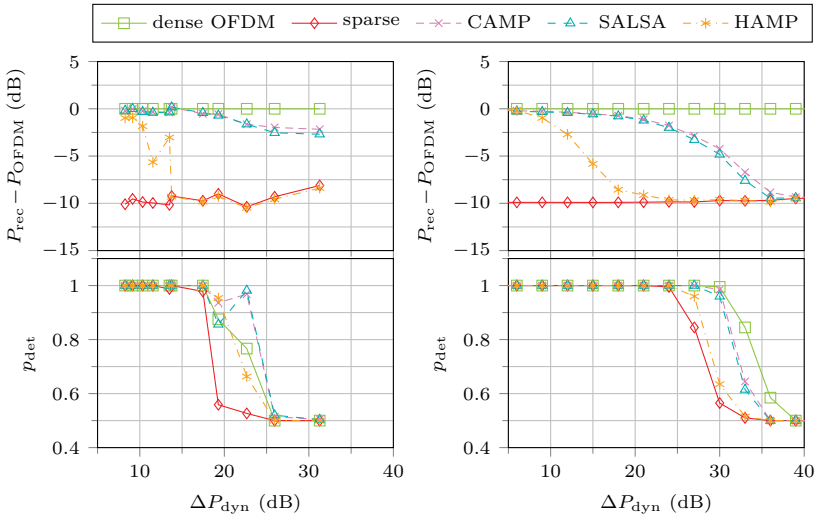
For evaluation, the processing chain of Fig. 3.3 is applied, where before the final imaging step a 2D Hann window is applied for sidelobe suppression in the radar image. In both the SOFDM and the reference dense OFDM evaluations, the identical configurations (detailed in Section 2.5), are applied.

3.3.2 Recovery of Weak Targets

Typically, the reflection power of vulnerable traffic participants such as pedestrians and cyclists is much lower than that of vehicles and trucks. Therefore, it is important to be able to reliably detect weak targets in presence of dominant stronger targets. In order to mimic such a scenario in a controlled measurement environment, two stationary corner reflectors C0 and C1 are positioned in front of the radar in an anechoic chamber, as illustrated in Fig. 3.8 (a). C0 represents the strong target with a radar cross-section (RCS) of $3.5\,\mathrm{m}^2$. It



(a) Measurement setups consisting of target C0 (▷) and either C1a (▷) or C1b (▷) with corresponding settings (R; RCS).



(b) Measurement results.

(c) Simulation results.

Fig. 3.8: Weak target recovery analysis using the measurement setups sketched in (a). The recovered peak magnitude (P_{rec}) of C1 compared to that obtained in a dense measurement (P_{OFDM}) for different target dynamics ΔP_{dyn} is shown in the top graph of (b). The bottom graph shows the corresponding detection rate p_{det}. In (c), the corresponding simulation results are shown using the same signal, target, and algorithm properties and a similar noise level as in the measurement.

remains unchanged at a range of $R_{C0} = 3.9\,\mathrm{m}$ throughout all measurements. On the other hand, C1 represents the weak participant. For C1, reflectors of different RCSs ranging from $0.02\,\mathrm{m}^2$ to $3.5\,\mathrm{m}^2$ (at 77 GHz) are used. To achieve a greater diversity of received target reflection dynamics, measurements at two different ranges $R_{C1a} = 6.8\,\mathrm{m}$ and $R_{C1b} = 7.8\,\mathrm{m}$ are performed, as illustrated in Fig. 3.8 (a) by the different colorings.

Each setting $(R_{C1a,b}; \mathrm{RCS}_{C1})$ is measured several times, and the wideband target dynamics ΔP_{dyn} are determined by averaging the difference of magnitudes of C0 and C1 in the dense OFDM radar image. To evaluate the weak target recovery performance of SOFDM, the obtained peak magnitude of C1 after recovery and the detection rate p_{det} are analyzed. To this end, for each setting thus ΔP_{dyn}, first, the peak magnitude P_{rec} of C1 in the *R-v*-images before (sparse) and after CS recovery is determined and compared to its magnitude P_{OFDM} in the dense OFDM measurements. The results are shown in the top graph of Fig. 3.8 (b). In the lower graph, the corresponding p_{det} is shown. A rate of 1 means both targets are detected, whereas a rate of 0.5 means that only C0 was detected. Note that the weak target may have been reconstructed even if it is not detected by the CFAR or the other way around. For comparison, in Fig. 3.8 (c), the results obtained from simulations using the same signal, target, and algorithm properties as well as the same amount of additive white Gaussian noise are shown. In the peak recovery, the measurement and simulation results are comparable. HAMP shows the worst performance and achieves recovery only up to ΔP_{dyn} of about 10 dB. CAMP and SALSA both achieve a similar performance and perfect peak recovery up to a peak difference of 20 dB. But even for higher ΔP_{dyn}, the recovery is still good with less than 5 dB magnitude difference after the recovery. Concerning the detection rate, there is an offset of about 10 dB observable between the simulation and the measurement results. Regarding the dense OFDM signal, perfect detection is possible up to $\Delta P_{\mathrm{dyn}} \approx 30\,\mathrm{dB}$ in the simulation, while in the measurement it is only up to $\Delta P_{\mathrm{dyn}} \approx 20\,\mathrm{dB}$. A similar behavior is observable for SOFDM. In addition, while in the simulation the detection rate for SOFDM is slightly worse than for OFDM, in the measurements, SOFDM with CAMP and SALSA outperforms the dense OFDM and achieves reliable detection up to $\Delta P_{\mathrm{dyn}} \approx 25\,\mathrm{dB}$. The FAR is less than 10^{-7} for each setting and approach.

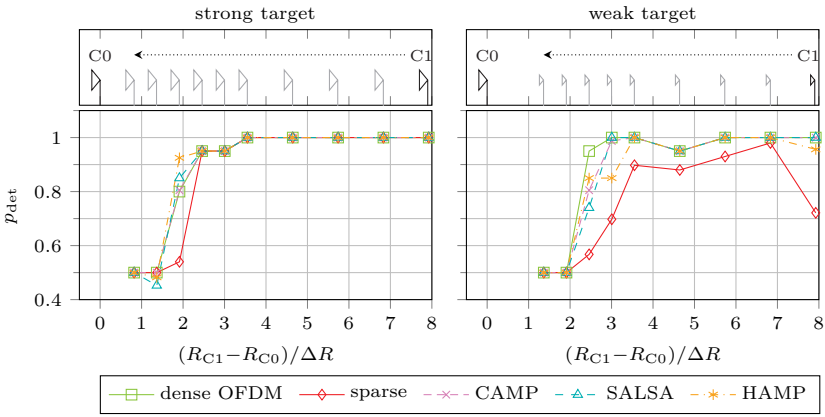
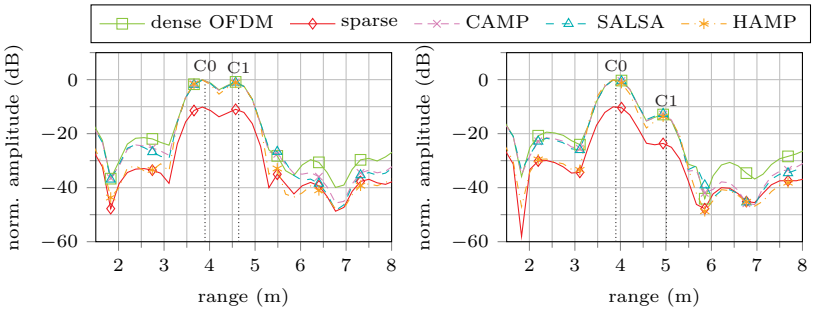


Fig. 3.9: Close targets measurement using two targets C0 and C1, where C1 is gradually moved towards C0 as sketched in the upper graph. The lower graph shows the obtained p_{det} averaged over multiple snapshots of each spacing $(R_{C1}-R_{C0})/\Delta R$. On the left, the targets C0 and C1 are equally strong, while on the right, C1 is much weaker than C0.

3.3.3 Recovery of Close Targets

The ability to distinguish two close targets is investigated by taking measurements of two stationary targets, where one is kept fixed while the other is gradually moved closer until they are no longer perceived as separate by the radar. As targets, two corner reflectors are used. The fixed target C0 is at range $R_{C0} = 3.9\,\mathrm{m}$ and has an RCS of $3.5\,\mathrm{m}^2$. The second target C1 has an initial range of $R_{C1} = 6.8\,\mathrm{m}$. Both a strong and weak reflector with $3.5\,\mathrm{m}^2$ and $0.33\,\mathrm{m}^2$, respectively, are used for C1.

In between measurements, C1 is moved in steps of about a resolution cell ΔR towards C0, as illustrated in the upper graphs of Fig. 3.9. When the targets get very close to one another, the step size is further reduced to $\Delta R/2$ to achieve higher discrimination in this critical range. In the processing, a factor two zero padding in range direction is applied to allow discrimination of peaks in adjacent resolution bins in the CFAR and peak detection. In the lower graphs of Fig. 3.9, the obtained p_{det} averaged over multiple snapshots of each spacing is shown.



(a) Strong-target measurement.

(b) Weak-target measurement.

Fig. 3.10: Extracted range profiles (R-v-images at $v = 0\,\mathrm{m/s}$) of two close targets measurements: (a) C1 is a strong target at critical spacing ($R_{\mathrm{C1}} - R_{\mathrm{C0}}$)=$2\Delta R$, and (b) C1 is a weak target at critical spacing $3\Delta R$ to C0.

A p_{det} value of 1 indicates that both targets are detected, while for a value of 0.5 differentiation or detection of one of the targets was not possible anymore. It shows that if both targets are equally strong, recovery and detection is possible up to a spacing of two resolution bins. The performance of SOFDM with any 2D CS approach and the equivalent dense OFDM are similar. The same is observable for the scene with the weaker C1, but the minimum possible distance increases to three resolution bins. This is expected, since the weaker target disappears beneath the mainlobe of the stronger C0 at a certain proximity to it.

In Fig. 3.10, two range profiles (R-v-images at $v = 0\,\mathrm{m/s}$) of measurements with targets at the critical spacings are shown for both the close strong target at spacing of $2\Delta R$ and the close weak target at spacing of $3\Delta R$. In the strong-target measurement in Fig. 3.10 (a), the peaks are about at the same level, and only a small dip is observable between them. However, the peaks will merge into one when they get even closer together. On the other hand, in the weak-target measurement in Fig. 3.10 (b), the weak target already disappears beneath the mainlobe of the stronger one, and when they get even closer, it is completely masked. Furthermore, it is observable that all 2D CS approaches achieve perfect target recovery.

3.3.4 Recovery of Extended Targets

Radar sensors in traffic are exposed to complex scenarios comprising several stationary and non-stationary targets. Furthermore, most of these objects do not constitute point-like but extended targets to a high-resolution radar sensor. Targets are considered *extended* if their physical extent exceeds ΔR of the sensor, hence give rise to several, potentially fluctuating, scattering centers, thus targets, in the radar imaging. The question arises if SOFDM and especially the 2D CS can cope with such complex scenarios as well. Therefore, outdoor measurements are taken of simple every-day traffic scenarios comprising a vehicle, a pedestrian, and a cyclist.

In Fig. 3.11, photos and measurements of two such scenarios are shown. The scenario on the left comprises a departing pedestrian next to an approaching vehicle, whereas the one to the right contains an approaching cyclist. The radar is in the lower right corner of the photo and observes the scene from an oblique angle and about 25 cm above ground to mimic the mounting height at a vehicle's bumper. Additionally, in both scenes, a corner reflector is positioned at the opposite wayside as a reference target. To increase the number of potential scattering centers of the objects, the observation time is extended by increasing M to 4000, which improves the velocity resolution to Δv=0.17 m/s. In the upper R-v-images in Fig. 3.11, the dense OFDM ground truth measurements are depicted. Below, the SOFDM R-v-images after 2D-CAMP recovery are shown. All objects and their various scatting centers are clearly discernible for both scenarios and both setups. It can be seen that despite reducing the bandwidth and applying 2D-CAMP, the various scattering centers of the objects agree very well with the dense OFDM measurement indicating they are recovered correctly. In addition, a pseudo PNR of about 4.6 dB is achievable in both scenarios with 2D-CAMP. This is about of 1.4 dB less than expected (6 dB) due to the remaining recovery error. This demonstrates that SOFDM is able to recover extended targets and operate in complex environments.

Next, the extended target measurement of the approaching vehicle is used to illustrate the progress of the 2D-CAMP recovery over the iterations. To this end, the spectrograms of the SOFDM measurement without recovery and of the dense OFDM are compared to those recovered after $k = \{1, 5, 10, 20\}$ iterations. Excerpts of the obtained spectrograms of the first 200 OFDM symbols are depicted on the left graphs in Fig. 3.12. In addition, the corresponding R-v-images

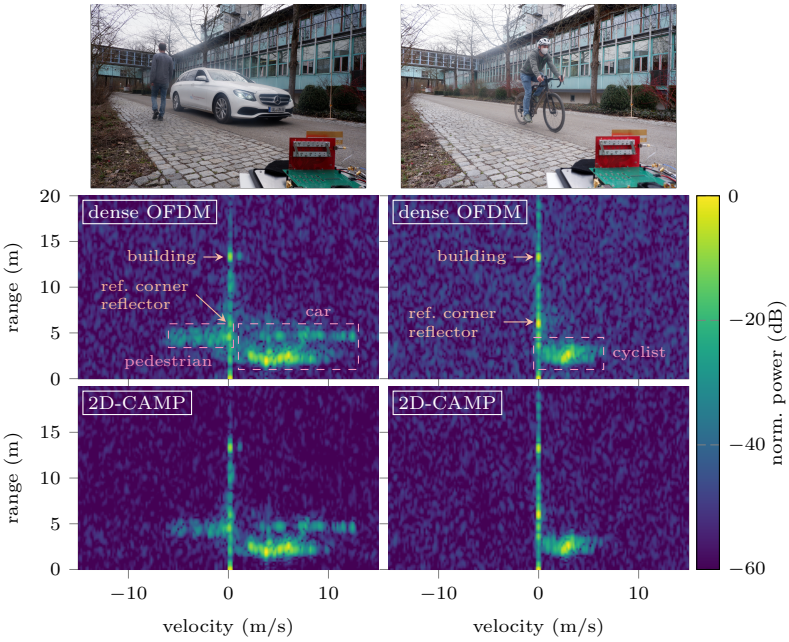


Fig. 3.11: Extended targets measurements of a departing pedestrian next to an approaching vehicle (left) and an approaching cyclist (right). The graphs show from top to bottom: a photo of the measured scene, the ground truth dense OFDM measurement, and the corresponding SOFDM measurement after 2D-CAMP recovery.

are computed, and a magnification of the vehicle area is shown on the right graphs in Fig. 3.12. With progressing recovery, the amplitude of the recovered coefficients in the spectrogram increase. It shows that the amplitudes of the signal in the spectrogram are lower than those of the noise. At the same time, the artifacts, thus noise level, decreases in the R-v-image, and the target reflections become more distinct. After K iterations, the texture of the spectrogram, especially the transverse stripes, is similar to the reference. In Fig. 3.13, excerpts of both a single subcarrier and a single OFDM symbol of the spectrogram are

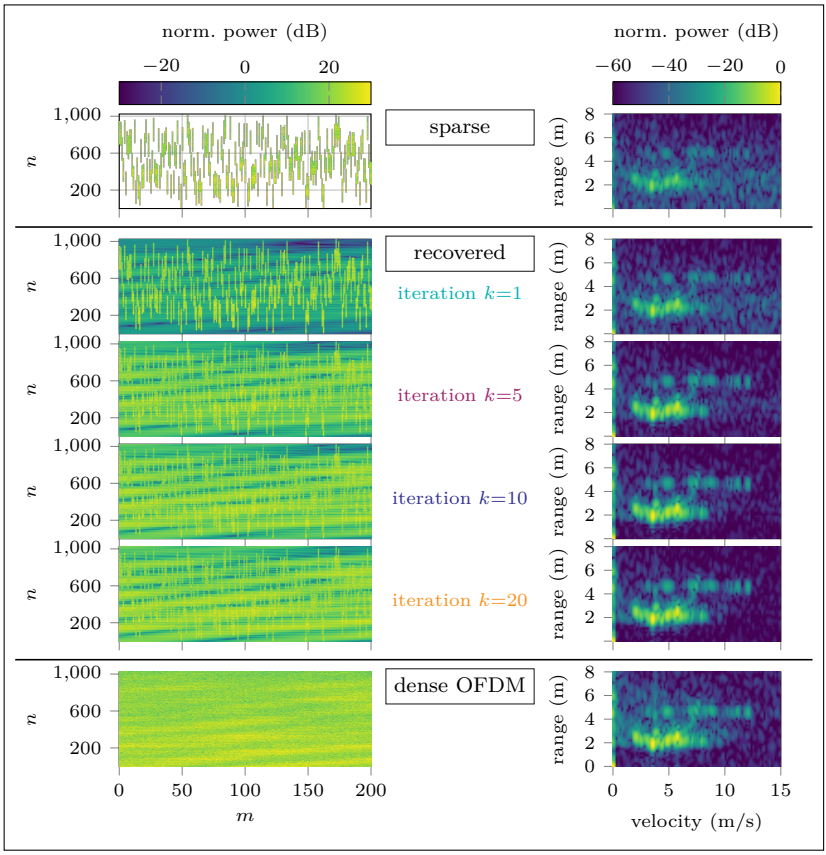


Fig. 3.12: Illustration of the 2D-CAMP recovery states in the spectrogram and R-v-image using the extended targets measurement of the approaching vehicle from Fig. 3.11. On the left, the spectrograms of the first 200 OFDM symbols are shown. On the right, the magnification of the range and velocity area $[0\,\mathrm{m}, 8\,\mathrm{m}]\times[0\,\mathrm{m/s}, 15\,\mathrm{m/s}]$ of the corresponding R-v-images containing the vehicle object is depcited. From top to bottom, the spectrograms and R-v-images correspond to the SOFDM measurement before recovery ($k=0$), the 2D-CAMP recovery state at iterations k=$\{1, 5, 10, 20\}$, and the dense OFDM reference.

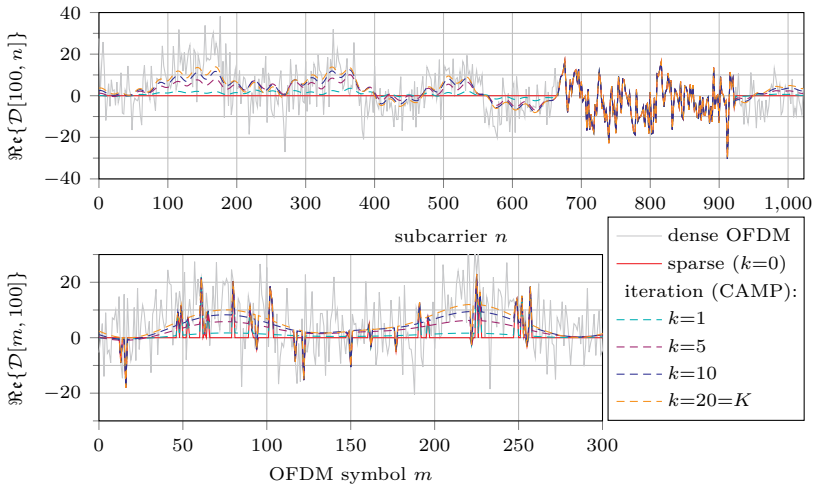


Fig. 3.13: Excerpts of the measured spectrograms from Fig. 3.12 for SOFDM without recovery, different 2D-CAMP recovery states $k = \{1, 5, 10, 20\}$, and the reference dense OFDM. The top graph shows the real part of the demodulated spectrum of the 100th OFDM symbol, the bottom graph the real part of the demodulated signal of the 100th subcarrier for the first 300 symbols.

shown. In both dimensions, a large part of the elements is missing. However, the measured elements are contiguous along the subcarriers (upper diagram), while they are randomly distributed along the symbols (lower diagram). Based on the noisy SOFDM spectrogram (——), the noiseless signal is gradually restored for these missing elements, where with increasing number of iterations, the signal estimate is refined. After $K = 20$ iterations, a good agreement between the course of the estimated signal and the reference (——) is observed.

3.3.5 Recovery of Highly Thinned Signals

In the previous investigations, an undersampling factor of $\delta_{\mathrm{cs}} = 1/4$ is considered. This means that, for instance, a baseband bandwidth of $\mathcal{B}_s$=100 MHz allows to cover a channel bandwidth of B=400 MHz. But how much further can δ_{cs}

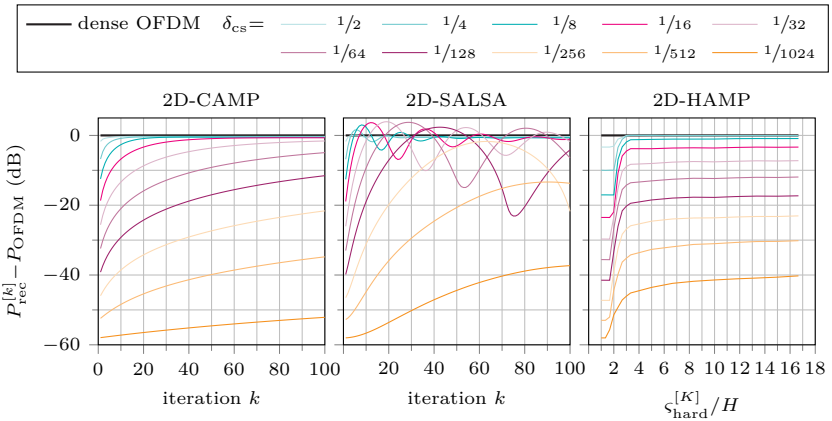


Fig. 3.14: Average relative recovered peak magnitude of the weakest target in measurements. The scene comprises $H = 3$ stationary targets at 3.9 m, 5.3 m, and 6.8 m. The framing two targets have an RCS of $3.5\,\mathrm{m}^2$ and the middle one of $0.33\,\mathrm{m}^2$. The recovered amplitude $P_{\mathrm{rec}}^{[k]} - P_{\mathrm{OFDM}}$ of the weakest (2nd) target is shown for different δ_{cs} after k iterations for 2D-CAMP (left) and 2D-SALSA (middle), and for different final sparsenesses $\varsigma_{\mathrm{hard}}^{[K]}$ normalized to H for 2D-HAMP (right).

be pushed while retaining acceptable radar operation? In order to examine the influence of δ_{cs} on the attainable recovery and to determine the limitations of the proposed recovery, dense OFDM measurements of a stationary target scene in an anechoic chamber are taken. For SOFDM evaluation, the measurements are thinned out by $\delta_{\mathrm{cs}} \in \{1/2, 1/4, \ldots, 1/1024\}$, where the minimum of the set translates to $N_s = 1$. The measured scene comprises three targets at ranges 3.9 m, 5.3 m, and 6.8 m, where the framing two targets have an RCS of $3.5\,\mathrm{m}^2$ and the middle target of only $0.33\,\mathrm{m}^2$. In order to asses the achieved performance limitations, first a close look is taken on the recovery of the weakest target among them, i.e. the middle one. Framed by nearby stronger targets, its recovery is the most challenging. First, for 2D-CAMP and 2D-SALSA, its reconstruction after the kth iteration is rated by its reconstructed peak magnitude $P_{\mathrm{rec}}^{[k]}$. To this end, the maximum number of iterations is increased to $K = 100$. In addition, the

examination is carried out for every δ_{cs} in the set. The results are depicted in the left and middle graphs of Fig. 3.14. The ordinate shows the difference of $P_{\mathrm{rec}}^{[k]}$ to the reference target peak amplitude P_{OFDM} of the dense OFDM measurements. It is observable that with decreasing δ_{cs}, it takes more iterations to entirely recover the weakest target. The convergence of 2D-SALSA seems faster than for 2D-CAMP, however, it also shows that 2D-SALSA is unstable in the first iterations, even for moderate δ_{cs}, and takes longer to stabilize when δ_{cs} decreases. Therefore, it is recommended to not use 2D-SALSA for $\delta_{\mathrm{cs}} \lesssim 1/8$, at least not without significantly increasing K to $K \gg 100$, which allows the algorithm to settle to a stable result. Note that the stability cannot be improved significantly by increasing Υ, which would also come at cost of the recovery performance for weak targets in general. In contrast, 2D-CAMP is stable, however, the recovery slows down with decreasing δ_{cs}. As a consequence, K should be increased for lower δ_{cs} in order to entirely recover weaker targets. In case of 2D-HAMP, K has only negligible influence on the performance, therefore, different terminal values $\varsigma_{\mathrm{hard}}^{[K]}$ ranging from 1 to 40 (fixed $K = 20$) are investigated instead. The results are depicted in the right graph of Fig. 3.14. It shows that for $\varsigma_{\mathrm{hard}}^{[K]} \geq 4H$ hardly any improvement in the recovery performance is achieved. Additionally, recovery is only possible up to $\delta_{\mathrm{cs}} \gtrsim 1/8$. As a consequence, 2D-SALSA and 2D-HAMP should only be applied with moderate undersampling of $\delta_{\mathrm{cs}} \gtrsim 1/8$, whereas 2D-CAMP may be utilized for far smaller δ_{cs} values with necessary adaption of K due to the slower convergence when δ_{cs} decreases.

Next, the relationship of K and δ_{cs} for 2D-CAMP is examined in more detail. In the top graph of Fig. 3.15, the achieved $P_{\mathrm{rec}} - P_{\mathrm{OFDM}}$ of the weakest target is plotted against δ_{cs}, where the different curves correspond to the results after $K = \{20, 50, 100, 500\}$ iterations. Additionally, the results for 2D-SALSA ($K = 20$) and 2D-HAMP ($\varsigma_{\mathrm{hard}}^{[20]} = 18$) are shown for comparison. In the bottom graph of Fig. 3.15, the corresponding achieved PNR of the strongest target is depicted. In addition, the theoretically expected PNR including the pseudo PNR is given (-·-·-). Up to about $\delta_{\mathrm{cs}} = 1/16$, all curves follow this line, where a small offset for the CS recovery is observable. In case of even lower δ_{cs}, it is necessary to increase K in order to continue to achieve the lower bound PNR. As a rule of thumb, it should hold that $K \approx 4/\delta_{\mathrm{cs}}$ to achieve sufficient recovery. Yet, although recovery is possible up to a surprisingly small δ_{cs}, the computational effort increases significantly at the same time.

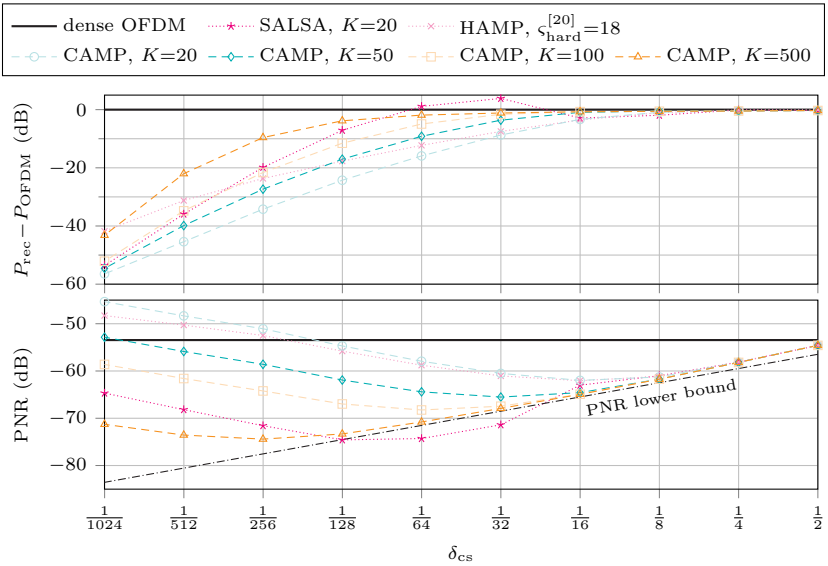


Fig. 3.15: Analysis of the influence of the undersampling factor δ_{cs} on the recovery performance using the same measurements as for Fig. 3.14. The relative recovered amplitude $P_{\text{rec}} - P_{\text{OFDM}}$ of the weakest target of the scene (top) and corresponding PNR (bottom) is plotted against δ_{cs} and for 2D-CAMP after different number of iterations K. The expected lower bound of the PNR (-·-·-) is determined by the measured noise of the dense OFDM and the theoretically achievable pseudo PNR.

3.4 Summary

SOFDM allows to break the close relation between achievable range resolution and signal bandwidth, which is particularly obstructive when demanding high resolution. By combining narrowband baseband OFDM signals and frequency hopping, the required sampling rate at both the Tx and the Rx unit can be lowered and thus, simpler and cheaper ADCs and DACs are sufficient. In addition, a CS-based recovery is introduced to the evaluation that allows to recover the missing part of the virtual wideband spectrogram and thereby reduce

artifacts in the wideband *R-v*-image caused by the Tx pattern. In order to avoid high artifacts and facilitate the recovery, the Tx pattern should be as random as possible. It is therefore recommended to perform a frequency hop after each symbol, if possible. To recover the wideband spectrogram, the 2D CS problem of the SOFDM signal evaluation is derived, and three suitable algorithms 2D-CAMP, 2D-HAMP, and 2D-SALSA, are developed. The approaches are validated using various measurements of different scenarios. It showed that the performance of SOFDM with 2D-CAMP and 2D-SALSA is similar to an equivalent wideband dense OFDM regarding scenarios with high target dynamics and close targets. On the other hand, with high target dynamics, 2D-HAMP fails to recover weak targets. It is shown that 2D-CAMP is able to recover complex outdoor scenarios in great detail while at the same time achieving an improvement of PNR compared to dense OFDM. Investigations regarding the undersampling factor showed that 2D-SALSA and 2D-HAMP require at least $1/8$th of the samples of the virtual wideband frame in order to recover the signal, whereas 2D-CAMP supports even thinner signals. However, with decreasing number of samples available, the recovery becomes more challenging, and more iterations are required to recover the signal, which significantly increases the computational effort. Yet, severe undersampling is not necessary in most radar applications. For instance, with $\delta_{\mathrm{cs}} = 1/8$ and a viable baseband bandwidth of $\mathcal{B}_s = 100\,\mathrm{MHz}$, a virtual bandwidth of 800 MHz and thereby a resolution of 19 cm is attainable.

Beyond that, further benefits of SOFDM compared to dense OFDM can be identified. For instance, occupying less subcarriers per OFDM symbol allows to increase the Tx power per subcarrier, which further improves the attainable pseudo PNR. In addition, due to its flexible Tx pattern design, SOFDM only occupies a fraction of the virtual wideband frame allowing on the one hand flexible spectrum allocation and spectrum sharing in case of multiple radar nodes operating at the same time and in the same frequency band. This may be realized by using spectrum sensing, coordination, or cognition [24].

4 Novel Multiplexing Methods for MIMO OFDM Radars

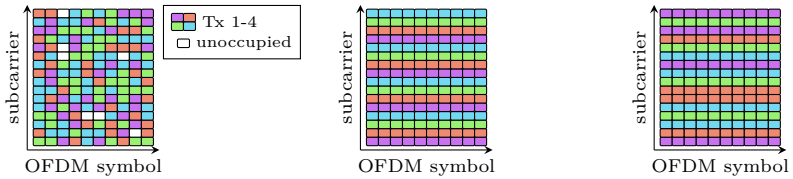
Due to its digital signal generation and evaluation as well as its special signal structure, OFDM supports various established multiplexing strategies but also enables the realization of largely unknown or completely new multiplexing strategies that were so far uncommon or unfeasible in radar signal processing. In this chapter, two novel MIMO OFDM strategies are discussed. The first concept detailed in Section 4.1 is the random frequency-time-division multiplexing or short random multiplexing (RM) and was introduced and analyzed in [116] by the author. It utilizes a randomized combination of FDM and TDM, thus achieves signal orthogonality through spectral and temporal avoidance.

With the second concept detailed in Section 4.2, the strategy of entire spectral and temporal avoidance is dropped and three CDM concepts suitable for MIMO OFDM are proposed and analyzed. The approaches were first presented in [36] by the author.

Both the new and established approaches offer individual advantages, each of which is accompanied by different constraints restricting the possible applications of a the approach. Therefore, hybrid approaches are proposed and discussed in Section 4.3. They merge two concepts into a new one and thereby enable the compliance with restrictions that go beyond the limits of the individual approaches and achieve optimized exploitation of unused parameter spaces. Finally, in Section 4.4, MIMO operation for SOFDM is detailed.

4.1 Random Frequency-Time-Division MIMO OFDM

With today's standard MIMO OFDM radar multiplexing approach, which is equidistant interleaving [37] or IOFDM as revised in Section 2.3.3 and illustrated in Fig. 4.1 (b), R_{ua} (2.52) gets reduced by a factor N_{tx} compared to the single output case (2.22). The random multiplexing (RM) concept [116] solves this



(a) Random. **(b)** Equidistant. **(c)** Non-equidistant.

Fig. 4.1: Spectral interleaving methods for a MIMO OFDM radar with N_{tx}=4.

issue by breaking the periodicity of the equidistant Tx pattern and assigning not only each subcarrier but each element of $\boldsymbol{d}$ to the transmitters randomly. In Fig. 4.1 (a), an exemplarily subcarrier assignment with $N_{\mathrm{tx}} = 4$ is shown. Note that there is no restriction on how many subcarriers are occupied by a single Tx channel for each OFDM symbol. Furthermore, it is also conceivable that certain elements remain entirely unoccupied if desired. Through this, R_{ua} of the equivalent dense signal, i.e. a SISO OFDM signal with identical time-bandwidth frame and parametrization, is preserved.

In the Tx signal design, the notion of a Tx pattern $\boldsymbol{P}^{[q]}$ as in IOFDM is taken up, where here, the patterns $\boldsymbol{P}^{[q]}$, $q \in \mathbb{Z}_{N_{\mathrm{tx}}}$, are populated randomly with zeros and ones. Furthermore, if the $[m,n]$th element of the frame is occupied by the $\hat{q}$th Tx channel, i.e. $P_{mn}^{[\hat{q}]} = 1$, then all other transmitters are inactive for this element, hence $P_{mn}^{[q]} = 0$, $\forall q \in \mathbb{Z}_{N_{\mathrm{tx}}} \setminus \{\hat{q}\}$. The Tx signal generation and Rx signal processing up to the spectrogram matches that of IOFDM in Section 2.3.3. Thus, the individual Tx paths are extracted from the modulated Rx spectrogram via

$$\boldsymbol{\mathcal{D}}^{[\hat{q},l]} = \boldsymbol{y}^{[l]} \circ \overline{\boldsymbol{d}} \circ \boldsymbol{P}^{[\hat{q}]} = \boldsymbol{\mathcal{D}}^{[l]} \circ \boldsymbol{P}^{[\hat{q}]}\,, \tag{4.1}$$

where $\boldsymbol{\mathcal{D}}^{[\hat{q},l]}$ is not dense, due to $\boldsymbol{P}^{[\hat{q}]}$. Furthermore, there is also a strong similarity to the spectrogram of SOFDM (3.8). Eventually, the 2D-(I)DFT range-Doppler evaluation of the $[\hat{q},l]$th path gives the image

$$\boldsymbol{\mathcal{I}}^{[\hat{q},l]} = \boldsymbol{U}\boldsymbol{\mathcal{D}}^{[\hat{q},l]}\boldsymbol{U}^{\mathsf{H}} = \boldsymbol{U}\boldsymbol{P}^{[\hat{q}]}\boldsymbol{U}^{\mathsf{H}} \circledast \boldsymbol{U}\boldsymbol{\mathcal{D}}^{[\hat{q},l]}\boldsymbol{U}^{\mathsf{H}}\,. \tag{4.2}$$

Similar to SOFDM, the transform $\boldsymbol{U}\boldsymbol{P}^{[\hat{q}]}\boldsymbol{U}^{\mathsf{H}}$ of the pattern is put over the targets in the radar image like a window function, potentially determining its

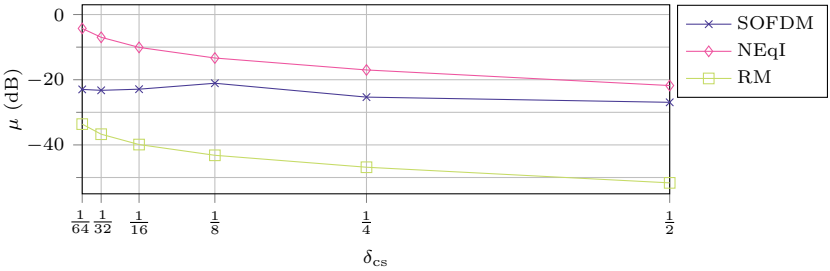


Fig. 4.2: Comparison of the average coherence μ of MIMO and SOFDM patterns of different undersampling factors μ determined by Monte Carlo simulations. The investigated frame size is 2048×1024.

PSLR. For this reason, the coherence μ of the RM pattern is examined in order to predict the expected performance. To this end, a large number of patterns are generated randomly for each N_{tx} and the average μ is determined for a frame size of $M = 2048$ by $N = 1024$, which is radar R1 from Table 2.1, and $N_{\mathrm{tx}} = \{2, 4, 8, 16, 32, 64\}$. The result is shown in Fig. 4.2. For comparison, μ of SOFDM and non-equidistant interleaving (NEqI) [149] patterns of the same undersampling factors are determined. An example interleaving pattern for NEqI is shown in Fig. 4.1 (c). For both NEqI and RM, the undersampling factor is $1/N_{\mathrm{tx}}$, thus $1/4$ corresponds to $N_{\mathrm{s}} = 256$ or $N_{\mathrm{tx}} = 4$. Compared to SOFDM, the coherence of RM is about 22 dB better, i.e. its PSLR is 22 dB higher. The reason is the degree of randomness of $\boldsymbol{P}$, which is higher for RM. Consequently, the artifacts are less pronounced in this case. NEqI employs randomness only in the subcarrier dimension. It therefore exhibits the worst μ with about 8 dB and 30 dB worse than SOFDM and RM, respectively. Therefore, CS recovery performs significantly worse for NEqI than for SOFDM and RM. Note that for IOFDM $\mu = 0$ dB due to the periodicity of the pattern.

Since the achieved randomness of the pattern and thus μ of RM is much better than of SOFDM, radar imaging may be carried out without further consideration of the Tx pattern [52]. Yet, due to the inevitable pattern artifacts, the maximal measurable target dynamic is at most μ which limits the performance. In order to improve the performance, the OFDM processing chain is modified as

illustrated in Fig. 3.3. An additional signal estimation step is inserted, whose task is to recover the dense hybrid spectrogram $\boldsymbol{\mathcal{D}}^{\star[\hat{q},l]}$ of all channels prior to the imaging step. Thereby, the artifacts are reduced, and the PNR is increased by the pseudo PNR. The recovery is realized using a modification of the 2D CS approaches from Chapter 3.2.

4.1.1 Multi-Channel 2D Compressed Sensing Processing

Considering the recovery of the dense Rx spectrogram of a single channel in RM, the task is similar to that in SOFDM. Yet, in RM, the signals of multiple channels are available that provide additional spatial but also redundant range-Doppler information, which cannot be exploited by the 2D CS approaches so far. But how to leverage the additional information and to integrate it into the algorithms to improve performance and robustness? In [2], the performance of 2D and 3D CS-based FMCW radar signal recovery is investigated. The study considered undersampling of the spatial dimension by a sparse ULA and additional undersampling of one or both of the remaining measurement dimensions (ramps, samples). The measurements are represented by a 3D data cube and are recovered using a multidimensional approach. It showed that if undersampling is present in two dimensions, as it is the case in RM with a dense ULA, a 3D recovery of the data cube performs worse than 2D recovery of the *R*-*v*-images of all channels followed by a 1D recovery of the azimuth profile of each detected target. Therefore, in this thesis, a modification of 2D-CAMP is proposed that allows to share spatial information in the recovery but does not estimate the angle during CS processing. As this goes beyond 2D CS but does not represent a full 3D estimation, the approach is designated as 2.5D-CAMP. The basic idea was originally presented for 2D-HAMP by the author [116] but is applied to 2D-CAMP in the following, since 2D-CAMP is shown to be superior to 2D-HAMP in terms of performance and stability in Chapter 3.

2.5D-CAMP basically consists of N_{virt} instances of 2D-CAMP (3.13) that run in parallel but utilize a modified soft-threshold function in (3.13b) that allows to share information across the different instances, i.e. channels, in order to determine a common support. After K iterations, the $N_{\text{tx}}N_{\text{rx}}$ dense hybrid spectrograms of all channels are obtained, and the range, Doppler, and azimuth angle of the targets get estimated as usual.

Common support multi-channel soft-threshold. The intention of the threshold step is to impose sparsity to the signal by estimating its support. For MIMO Rx signals, the support of the virtual channels is presumed to be identical as they observe the same target reflections. Therefore, one may benefit from this redundant information in support estimation. Thus, in the *common support* approach in each iteration, first, the NCI

$$\tilde{\boldsymbol{X}}^{\mathrm{NCI}} = \frac{1}{N_{\mathrm{virt}}} \sum_{\kappa=0}^{N_{\mathrm{virt}}-1} \left| \tilde{\boldsymbol{X}}^{[\kappa]} \right| \tag{4.3}$$

of the current noisy estimates of all channels is computed. For brevity, the iteration index in the superscript is dropped, and the superscript only accounts for the channel or path. Next, with (4.3), a common threshold $\boldsymbol{\Lambda}^{\mathrm{NCI}}$ is determined like in 2D-CAMP using (3.14) to (3.16) with a scaling of $\Upsilon = 4$. The benefit of using the NCI is that the noise gets smoothed and artifacts are reduced. The latter is due to the circumstance that paths originating from different Tx channels contain different sampling patterns, hence different artifact distributions. As a consequence, the threshold becomes more robust against random clutter and pattern artifacts. In addition, weak targets might be obscured by artifacts in one channel but are more prominent in other channels. By combining the channels, such shortcomings can be compensated. Finally, the common support is identified, which is expressed by the index set

$$\Omega = \left\{ (m,n) \mid \tilde{X}^{\mathrm{NCI}}_{mn} \geq \Lambda^{\mathrm{NCI}}_{mn}, m \in \mathbb{Z}_M, n \in \mathbb{Z}_N \right\} \tag{4.4}$$

with $|\Omega| = \varsigma$. Then, a modified soft-threshold function is applied. It yields the sparse estimates $\hat{\boldsymbol{X}}^{[\kappa]}$ with elements

$$\hat{X}^{[\kappa]}_{mn} = \begin{cases} \tilde{X}^{[\kappa]}_{mn} \left(1 - \frac{\Lambda^{\mathrm{NCI}}_{mn}}{|\tilde{X}_{mn}|} \right), & \text{if } (m,n) \in \Omega \text{ and } \Lambda^{\mathrm{NCI}}_{mn} \leq |\tilde{X}^{[\kappa]}_{mn}| \\ \tilde{X}^{[\kappa]}_{mn}, & \text{if } (m,n) \in \Omega \text{ and } \Lambda^{\mathrm{NCI}}_{mn} > |\tilde{X}^{[\kappa]}_{mn}| \\ 0, & \text{otherwise} \end{cases} \tag{4.5}$$

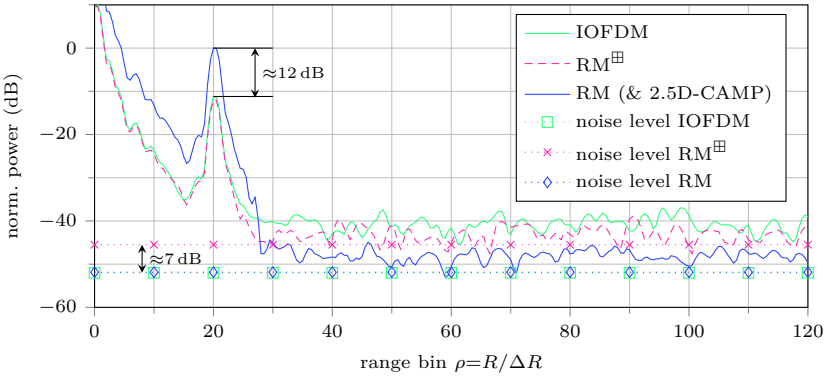
for each channel $\kappa \in \mathbb{Z}_{N_{\mathrm{virt}}}$. Other than in the usual soft-threshold, a third case (middle case in (4.5)) is introduced that takes care of elements that are contained in Ω but are lower than the corresponding threshold. These elements are allowed to pass exceptionally, but are not shrunk like those elements that

actually exceed the threshold. In the usual soft-threshold (2.63), these elements would be rejected. This exception considers that especially weak targets might not exceed the threshold in each channel, but only in some. However, recovering a differing support across the channels would lead to imbalances between them and eventually to distortions in the DoA estimation step. With the common support approach it is guaranteed that the same signal components are restored in each channel, such that they carrying the same support.

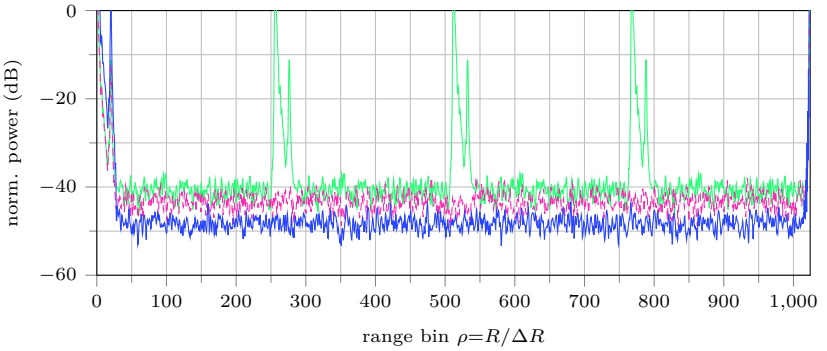
4.1.2 Analysis and Comparison to IOFDM

The proposed RM MIMO concept is validated using measurements with radar R1 from Section 2.5 using the available 4×4 ULA. To this end, for each measurement, a set of $N_{\text{tx}} = 4$ mutually disjoint RM Tx patterns is generated randomly and assigned to the Tx channels. The acquired RM measurements are evaluated and analyzed both without and with additional 2.5D-CAMP recovery. The former is referred to as RM$^{\boxplus}$ and the latter as RM in the remainder of this chapter. In addition, the results are compared to IOFDM measurements.

The first measurement scenario consists of two stationary corner reflectors, both located at a distance of 7.3 m (range bin $\hat{\rho}$=20) from the radar. Their respective azimuth angle and RCS (θ, RCS) are ($-7.8°, 1.13\,\text{m}^2$) and ($10.9°, 3.5\,\text{m}^2$). The measured range profiles (NCI R-v-images at $v = 0\,\text{m/s}$) are depicted in Fig. 4.3. The strong target at range zero is caused by Tx-Rx cross-talk. In Fig. 4.3 (a), the profiles up to range bin 120 are shown. In addition, the average noise or artifact level (AL) (whichever is more pronounced) of the R-v-images are indicated by the dotted lines. Note that the level in IOFDM is slightly below its apparent level in the range plot, since for IOFDM, the noise energy partly concentrates in the zero-Doppler-cut due to restrictions in the signal generation of the system, which causes deterministic errors to concentrate in these cells instead of being spread across all. The actual average noise level is therefore not reflected by the range profile. For RM, the restrictions are less severe so that the noise is more evenly spread. A comparison of the obtained profiles shows that with IOFDM and RM$^{\boxplus}$, the same target reflection power is obtained, however, the AL of RM$^{\boxplus}$ exceeds the noise level of IOFDM and its PNR is about 7 dB lower. On the other hand, applying 2.5D-CAMP, the peak power increases by 12 dB, and at the same time, the artifacts are reduced, and



(a) Excerpt of the range profile up to bin 120.



(b) Entire range profile.

Fig. 4.3: Range profile (v=0 m/s cut of the NCI R-v-image) of RM and IOFDM measurements of a scene with two stationary targets at range 7.3 m ($\hat{\rho}$=20). (a) Shows an excerpt and (b) the entire range profile of the frame. All plots are normalized to the strongest target reflection of the recovered RM measurement.

the noise level becomes similar to that of IOFDM. In summary, the PNR of RM is about 12 dB higher compared to IOFDM. This difference is explained by the fact that each channel of RM contains four times as much useful samples and subcarriers than IOFDM, moreover, 3/4 of them are recovered and noiseless.

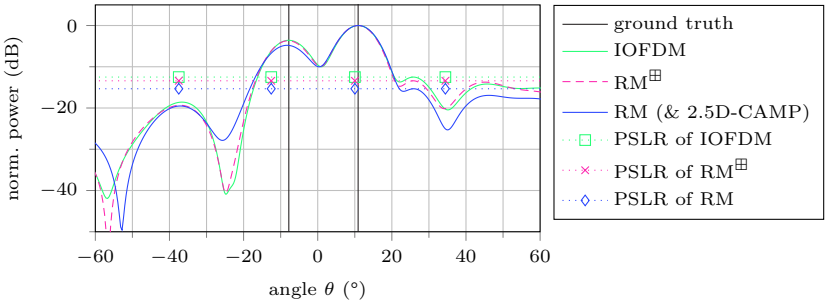


Fig. 4.4: Azimuth profile of the $[\hat{\nu}, \hat{\rho}]$th bin oft the R-v-images containing two targets (——) at −7.8° and 10.9°. The PSLRs of the measurements are −12.5 dB (IOFDM), −13.4 dB (RM), and −15.3 dB (RM & 2.5D-CAMP). Each profile is normalized to the strongest target reflection.

In Fig. 4.3 (b), the entire range profiles of the frame are shown. For RM, no ambiguities emerge, whereas for IOFDM ambiguities emerge with periodicity of $256 = N/N_{\mathrm{tx}}$.

Next, the azimuth profile of the $[\hat{\nu}, \hat{\rho}]$th bin of the R-v-images containing two target reflections is determined and depicted in Fig. 4.4. The curves are each normalized to the strongest peak of the target at 10.9°, and the dotted lines correspond to the PSLR of the respective profile. Both targets are well recognizable. Compared to IOFDM, the PSLR is improved by about 3 dB. However, the peak of the weaker target is decreased by about 1 dB in RM.

The second measurement scenario is similar to that in Fig. 3.11 and contains an outdoor scene of an approaching vehicle. The radar is positioned at about 25 cm above ground and oblique to the direction of motion of the vehicle. In addition, the observation time is extended by increasing M to 4000, which improves the velocity resolution to $\Delta v = 0.17\,\mathrm{m/s}$. In Fig. 4.5, the obtained R-v-images and range-azimuth detection results are shown. The latter are depicted in Cartesian coordinates with directions x and y, where the coordinates $(0\,\mathrm{m}, y)$ correspond to the boresight $\theta = 0°$ of the sensor. In addition, the ground truth vehicle shape and position is sketched in the x-y-plot. Comparing the RM$^{\boxplus}$ (left) with the RM with 2.5D-CAMP (right) results, a significantly better PNR of about 20 dB is observable for RM. Furthermore, it shows that much more scattering

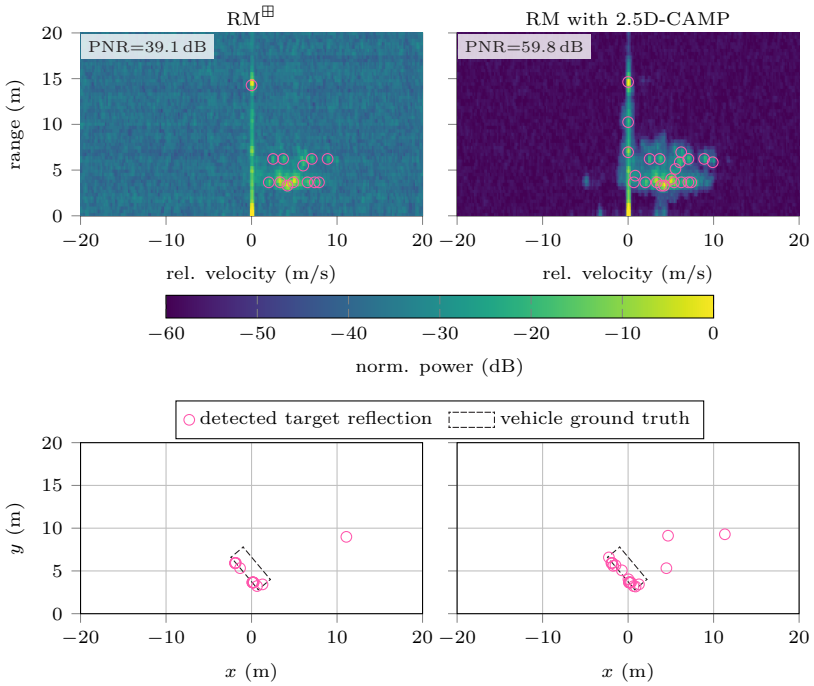


Fig. 4.5: RM extended target measurement of an approaching vehicle. The obtained R-v-images (top) and target detections in x-y-representation after DoA estimation (bottom) are shown for applying the common 2D-(I)DFT evaluation ignoring the signal gaps (left) and RM with 2.5D-CAMP recovery (right). The images are normalized to the strongest target reflection (building at $R = 14.3\,\mathrm{m}$).

points can be extracted from the latter, which also allows a better recognition of the vehicle's shape and extent. In Fig. 4.6, a comparable measurement using IOFDM is shown.

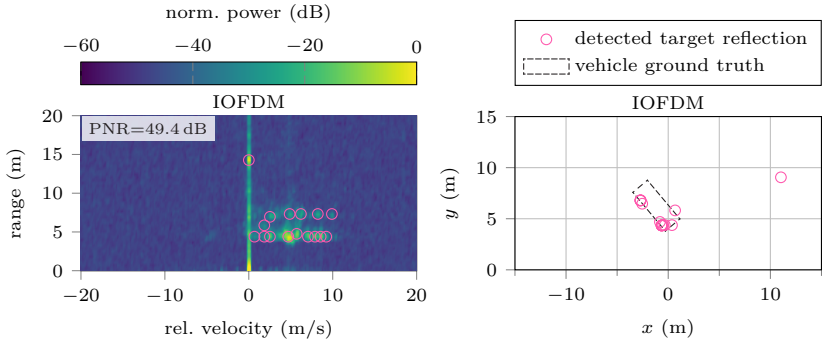


Fig. 4.6: Extended target measurements of an approaching vehicle using IOFDM. Left: R-v-image normalized to the strongest target reflection (building at $R = 14.3\,\mathrm{m}$). Right: x-y-representation after DoA estimation.

4.2 Code-Division Multiplexing

Instead of separating transmitters in time- or frequency dimension, the signal structure of OFDM also allows straightforward separation in the code dimension. To this end, a concept similar to the multi-carrier code-division multiple access (MC-CDMA) technique in communication systems [150] is utilized. Thereby, a code sequence is used for each OFDM symbol, where the chips of the sequence are assigned to the subcarriers and therefore, equal the sequence of modulation symbols across the subcarriers of an OFDM symbol. As a consequence, with N subcarriers, code sequences of length N are required. By applying different code sequences for each user or transmitter, this technique allows them to occupy the same frequency band and subcarriers simultaneously and continuously. This feature sparks the hope that thereby the disadvantages and limitations that radars experience in FDM and TDM MIMO operations, especially regarding ambiguities, may be easily overcome. Yet, there are also some limitations to CDM that have to be taken into account with respect to radar operation. In communication, the main interest lies in the robust and reliable detection of the transmitted information, while the correlation properties of the coding play a subordinate role. In contrast, in radar applications, the main interest lies in

the robust detection of the channel properties, while the transmitted data is of little interest. Moreover, the channel detection capability strongly depends on the waveform's auto- and cross-correlation properties in time domain. In particular, let the circular or periodic auto-correlation function (ACF) be

$$\chi_g^{\mathrm{ac}}[\eta] = \sum_{l=0}^{\mathcal{L}-1} \big(g[l]\big)^* g[l+\eta]_{\mathcal{L}} = \sum_{l=0}^{\mathcal{L}-1} \big(g[l+\eta]_{\mathcal{L}}\big)^* g[l] \tag{4.6}$$

and the circular or periodic cross-correlation function (CCF) [151] be

$$\chi_{gh}^{\mathrm{cc}}[\eta] = \sum_{l=0}^{\mathcal{L}-1} \big(g[l]\big)^* h[l+\eta]_{\mathcal{L}} = \sum_{l=0}^{\mathcal{L}-1} \big(g[l+\eta]_{\mathcal{L}}\big)^* h[l] \tag{4.7}$$

with two discrete waveforms g and h, and $g[l]_{\mathcal{L}}{=}g[l \bmod \mathcal{L}]$ indicating the modulo $\mathcal{L}$ operation. The output of the OFDM Rx matched filter is determined by the correlation of the Tx signal and the measured signal. In MIMO, the latter consists of a superposition of the reflected waveforms originating from different transmitters. Hence, in order to filter for a specific Tx signal and achieve optimal radar performance, the employed waveform should have a thumbtack-like ACF with a high correlation peak and almost zero values elsewhere. Ideally, the ACF is only non-zero at zero-delay, since the shape of the ACF combined with the window function yields the target's main lobe shape in the radar image, hence influences the detection capability and accuracy. Additionally, the CCF of two waveforms originating from different transmitters determines the amount of ITCT and their isolation. In communication applications, this is also known as multiple access interference (MAI) [150]. Ideally, the CCF is zero for any delay. Together, the two conditions yield the orthogonality criterion for CDM MIMO OFDM radar operation. Spectral and temporal avoidance via FDM and TDM naturally fulfill both constraints, while CDM has to achieve the desired orthogonality in the code-dimension. Unfortunately, perfect orthogonality in the code dimension is not achievable. The Welch bound [78] gives a theoretical lower bound on the achievable average isolation of two coded waveforms. Given the applied codes of length $\mathcal{L}$ are taken from a set of codes of cardinality $\mathcal{P}$,

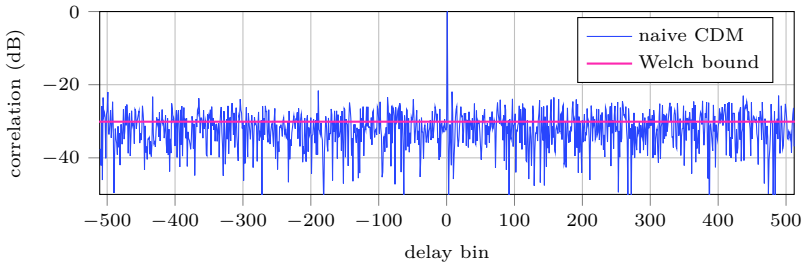


Fig. 4.7: Naive CDM MIMO OFDM example. Correlation result of two random QPSK code sequences of length 1024 and the corresponding Welch bound. Adapted from [36] © 2021 IEEE.

the Welch bound for the periodical correlation gives

$$\mu_{\text{circ}} = \sqrt{\frac{\mathcal{P}-1}{\mathcal{P}\mathcal{L}-1}} \overset{\mathcal{P}\to\infty}{\approx} \sqrt{\frac{1}{\mathcal{L}}}\,. \tag{4.8}$$

The severe influence of this bound on the achievable isolation of different transmitters is illustrated by the following naive CDM example: Assume two distinct waveforms composed of code sequences of length $\mathcal{L} = 1024$ generated randomly from the alphabet $\mathcal{A}$. This resembles the typical modulation symbol generation of any OFDM symbol. The code set thus has cardinality $\mathcal{P} = |\mathcal{A}|^{\mathcal{L}}$ resulting in $\mu_{\text{circ}} \approx -30\,\text{dB}$ as the lower bound (4.8) on the average signal isolation. This bound is also observable in the obtained results after the OFDM Rx matched filter depicted in Fig. 4.7. The output is a superposition of the ACF of the Tx waveform and the CCF with the second waveform assumed to originate from a second transmitter. Doubling and quadrupling the number of transmitters further worsens the result, since the additional signal overlaps cause a degradation of another 3 dB and 6 dB, respectively. Although the isolation may be improved by increasing the code length, a significant increase of $\mathcal{L}$ translates into a significant increase of N, which is not feasible for an appropriate level of isolation. Moreover, even the application of sophisticated code sets such as maximum length sequences (MLS), Gold codes, or almost perfect auto-correlation sequences (APAS) does not result in any improvement, as these

codes are designed for good ACF but suffer from a moderate CCF in the range of the Welch bound [152].

Yet, as shown in [118] by the author, it is possible to achieve optimal signal isolation not for the entire but for large regions of the OFDM radar image through appropriate signal design and code choice. To this end, first, the influence of the CCF on the matched filter output, i.e. the range evaluation, is investigated. In Section 2.3.2 the general expression of the MIMO OFDM radar Rx spectrogram is derived. The spectrogram (2.41) of the $[\hat{q},l]$th path is composed of an auto-correlation part $\hat{\boldsymbol{\mathcal{D}}}^{[\hat{q},l]}$ and an ITCT interference part $\breve{\boldsymbol{\mathcal{D}}}^{[\hat{q},l]}$. Similar to the SISO range evaluation (2.19), the IDFT of $\hat{\boldsymbol{\mathcal{D}}}^{[\hat{q},l]}$ yields the desired range map with coefficients

$$\hat{\mathcal{R}}_m^{[\hat{q},l]}[\rho] \propto \sqrt{N}\psi_m\left[\rho - \tfrac{R_0}{\Delta R}\right], \tag{4.9}$$

where terms irrelevant to this evaluation are omitted. The range map is the ACF of the transmitted waveform of the $\hat{q}$th transmitter and exhibits a peak at $\hat{\rho} = \lfloor R_0/\Delta R \rceil$. Performing the same operation on the undesired ITCT part (2.43) gives the undesired contribution

$$\breve{\mathcal{R}}_m^{[\hat{q},l]}[\rho] \propto \sum_{\substack{q=0\\q\neq\hat{q}}}^{N_{\mathrm{tx}}-1} \alpha^{[q,l]}\, \mathrm{e}^{\mathrm{j}\varphi_\theta[q,l]}\, \frac{1}{\sqrt{N}} \sum_{n=0}^{N-1} d_{mn}^{[q]} \left(d_{mn}^{[\hat{q}]}\right)^* \mathrm{e}^{-\mathrm{j}2\pi n\Delta f \frac{2R_0}{c}}\, \mathrm{e}^{\mathrm{j}2\pi \frac{n\rho}{N}}, \tag{4.10}$$

which can be transformed to

$$\propto \sum_{\substack{q=0\\q\neq\hat{q}}}^{N_{\mathrm{tx}}-1} \alpha^{[q,l]}\, \mathrm{e}^{\mathrm{j}\varphi_\theta[q,l]}\, \frac{1}{\sqrt{N}} \sum_{\eta=0}^{N-1} x_m^{[q]}\left[\eta + \rho - \tfrac{R_0}{\Delta R}\right]_N \left(x_m^{[\hat{q}]}[\eta]\right)^* \tag{4.11}$$

$$\propto \sum_{\substack{q=0\\q\neq\hat{q}}}^{N_{\mathrm{tx}}-1} \alpha^{[q,l]}\, \mathrm{e}^{\mathrm{j}\varphi_\theta[q,l]}\, \frac{1}{\sqrt{N}} \chi^{\mathrm{cc}}_{x_m^{[q]}x_m^{[\hat{q}]}}\left[\rho - \tfrac{R_0}{\Delta R}\right]. \tag{4.12}$$

A detailed derivation is given in Appendix B on page 151. The window function is neglected here for brevity. The ITCT results in a superposition of the CCFs of the Tx waveforms shifted by the target position in the image due to the introduced signal delay. Consequently, to reduce the ITCT impact, the CCFs of

the sampled time-domain Tx signals must be minimized. The task in the CDM MIMO waveform design, hence code design, is therefore to keep the influence of the CCF as small as possible without noticeably impairing the ACF properties, since this could worsen the target detection and radar performance. In this context, it is important to point out that the typical OFDM coding is done in the spectrogram, but in (4.12) the correlation of their Fourier transforms, thus the discrete time signals, is decisive. Therefore, in this thesis, two coding strategies are distinguished: direct coding of the modulation symbols $\boldsymbol{d}$, which is the typical OFDM approach, and indirect coding of the modulation symbols through coding of the discrete time signals. In direct coding, either the row or column vectors $\boldsymbol{d}_{m,:}^{[q]}$ or $\boldsymbol{d}_{:,n}^{[q]}$ hold the code sequences of length N or M, respectively, depending of whether the code is applied along the frequency or time dimension of the frame. Direct coding along the OFDM symbol dimension is adopted in the developed modified repeated symbol CDM concept [36] detailed in Section 4.2.2, whereas direct coding along the subcarrier dimension is adopted in the developed auto-correlation CDM approach [36], presented in Section 4.2.3. On the other hand, in indirect coding, the N-period IDFT of $\boldsymbol{d}_{m,:}^{[q]}$, i.e. the N coefficients of $\boldsymbol{x}_m^{[q]}$ holds the code sequence. The signal resulting from indirect coding mimics a phase-modulated continuous-wave (PMCW) signal. Apart from that, the OFDM signal processing chain is maintained, which is a significant difference to common PMCW signal processing in terms of flexible signal design. This principle is adopted for the developed zero-correlation zone CDM approach [36] presented in Section 4.2.1. In Section 4.2.4, the CDM approaches are analyzed and their performance is compared to the IOFDM and RM concepts using measurements.

4.2.1 Zero-Correlation Zone CDM

Zero-correlation zone (ZCZ) code sets have the special property that their ACF and CCF are optimal up to a certain delay, which is the zero-correlation zone. Zero-correlation zone (ZCZ) code sequences are utilized in asynchronous or approximately synchronized code-division multiple access (CDMA) communication systems for synchronization or to reduce the co-channel interference [153]–[155]. Besides, the sequences also attracted interest in the field of PMCW MIMO radars [152], [156]. The concept of a ZCZ-CDM MIMO OFDM radar, hereafter

abbreviated as ZCZ-CDM, that was presented in [36] by the author, is detailed in this section.

The ZCZ code set composed of $\mathcal{P}$ sequences of length $\mathcal{L}$ that exhibit a ZCZ $\mathcal{Z}$ is described by the tuple $(\mathcal{L}, \mathcal{P}, \mathcal{Z})$. Although achieving perfect orthogonality up to delay $\mathcal{Z}$, the sequence set cannot elude the Welch bound, which defines the theoretical upper bound on $\mathcal{Z}$ of [154]

$$\mathcal{Z}_{\max} = \frac{\mathcal{L}}{\mathcal{P}} - 1\,. \tag{4.13}$$

The desired ZCZ develops when computing the CCF of two sequences of the set. In order to utilize this property to eliminate the ITCT up to $\mathcal{Z}$ in (4.12), indirect or time domain coding is applied and the ZCZ codes become the discrete samples of the discrete time signal $\boldsymbol{x}_m^{[q]}$.

Transmit signal design and radar evaluation. Given a ZCZ sequence set of at least $\mathcal{P} \geq N_{\mathrm{tx}}$ unique members, first N_{tx} distinct sequences $\boldsymbol{z}_m^{[q]} = \left(z_m^{[q]}[\eta]\right)_{\eta=0}^{\mathcal{L}-1}$ of this set are selected and each assigned to a transmitter as its time domain signal. Consequently, $x_m^{[q]}[\eta] = z_m^{[q]}[\eta]$, where η is the chip index of the sequence. Next, the corresponding modulation symbols are deduced inversely to (2.3) via the DFT

$$d_{mn}^{[q]} = \frac{1}{\sqrt{N}} \sum_{\eta=0}^{N-1} z_m^{[q]}[\eta]\, \mathrm{e}^{-\mathrm{j}2\pi \frac{n\eta}{N}}\,. \tag{4.14}$$

Since the number of subcarriers should be N, the length of the DFT, hence the length of the sequence, has to be $\mathcal{L} = N$. Furthermore, through (4.14), the amplitudes of $d_{mn}^{[q]}$ become non-uniform and the phases arbitrary. Theoretically, this violates the assumption of uniform amplitudes required in (2.40) of the evaluation when removing the modulation from the spectrogram using the complex conjugate of the symbols. Yet, only through this mismatch the CCF in (4.12) disappears for delays up to $\mathcal{Z}$. Otherwise, especially when multiplying with the inverse of the modulation instead as suggested by OFDM radar theory, self-interference in the range of the Welch bound occurs similar to Fig. 4.7. Except for the adapted design of the modulation symbols via (4.14), no further modifications or changes to the usual MIMO OFDM radar processing and evaluation chain are required, nor any special treatment of the ITCT.

Generation of suitable ZCZ sequence sets. In literature, several construction rules for ZCZ sequence sets have been reported [153], [154], [157]. Most of them aim at generating binary sets or are suboptimal regarding the width of $\mathcal{Z}$. But purely binary or real-valued time domain signals are disadvantageous for IQ mixing, which is an important component of digital radars. In this case, the image rejection would be reduced at the receiver [128]. In [155], a concept to construct complex valued QPSK based ZCZ sequence sets is proposed that is adopted here for OFDM radar. The complex-valued sequences are constructed from recursively interleaved Hadamard matrices of initial order Q. The approach allows to generate codes of length $\mathcal{L} = 2^{i+2}Q$, where $i \geq 0$ is the interleaving depth. The cardinality of the generated sets is $\mathcal{P} = 4Q$, and the width of the ZCZ is $\mathcal{Z} = 2^{i-2}3$, hence each set is described by the tuple $(2^{i+2}Q, 4Q, 2^{i-2}3)$. An optimal choice of Q and i proportional to the OFDM radar parameters N and N_{tx} is

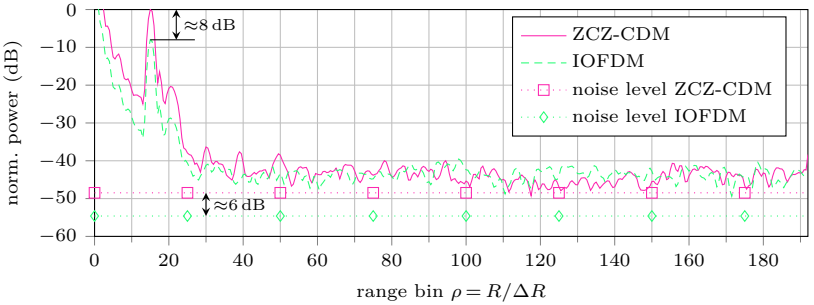
$$Q = \left\lceil \frac{N_{\mathrm{tx}}}{4} \right\rceil = \frac{N'_{\mathrm{tx}}}{4}, \quad \text{and} \quad i = \log_2\left(\frac{N}{\mathcal{P}}\right) = \log_2\left(\frac{N}{N'_{\mathrm{tx}}}\right) \tag{4.15}$$

with $N'_{\mathrm{tx}} \geq 4$ the smallest power of two equal or larger than N_{tx}. A detailed derivation is given in Appendix C and [36]. The code sequence construction procedure using the parameters (4.15) is described in [155]. With this approach, the smallest set possible has member size four ($\mathcal{P} = 4Q$, $Q \geq 1$), hence for $N_{\mathrm{tx}} = 2$, the same set as with $N_{\mathrm{tx}} = 4$ has to be utilized. However, the generated code sets have the peculiarity that they can be divided in two disjoint equally large sets that both exhibit a ZCZ twice as wide as that of the combined set. Sets with this property are also referred to as asymmetric ZCZ sequence sets [158]. Hence, if $N_{\mathrm{tx}} = 2$ is desired, it is suggested to generate a set with $\mathcal{P} = 4$ and extract the subset of $\mathcal{P}/2$ codes that yield the widest ZCZ. Finally, the sequences obtained with (4.15) have a ZCZ of

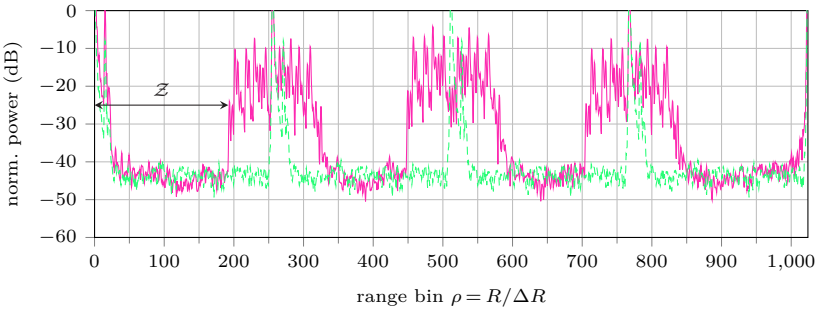
$$\mathcal{Z} = \frac{3N}{4\mathcal{P}} = \frac{3N}{4N'_{\mathrm{tx}}} \approx \frac{3}{4}\mathcal{Z}_{\max}\,. \tag{4.16}$$

With this, the maximum unambiguous range of ZCZ-CDM is

$$R_{\mathrm{ua}}^{\mathrm{ZCZ}} = \mathcal{Z}\Delta R = \frac{3N}{4N_{\mathrm{tx}}}\Delta R\,. \tag{4.17}$$



(a) Range profile of the ZCZ.



(b) Entire range profiles.

Fig. 4.8: Range profiles of MIMO OFDM radar measurements using ZCZ-CDM and IOFDM. The scene contains a single static target at $\hat{\rho} = 15$ ($R = 5.5\,\mathrm{m}$). The profiles are extracted at the constant target velocity bin $v/\Delta v = 0$ from the NCI of all channels after 2D-(I)DFT evaluation and are normalized to the target peak of ZCZ-CDM. (a) Range profiles of the ZCZ. (b) Entire range profiles.

In Doppler dimension, no distortions or additional ambiguities emerge. Choosing $Q = 1$ and $i = 8$, the suitable ZCZ sequence set $(1024, 4, 192)$ for radar R1 is obtained. In Fig. 4.8, the range profiles ($v/\Delta v = 0$ of the *R-v*-images) of MIMO OFDM measurements using the proposed ZCZ-CDM and the standard IOFDM approach are shown. In both settings, the same output power per OFDM symbol is used. The measured scene comprises a single stationary target at range bin

$\hat{\rho} = 15$ ($R = 5.5\,\mathrm{m}$). In Fig. 4.8 (a), the range profiles up to $\mathcal{Z} = 192$ are depicted. It shows that in ZCZ-CDM both the peak and the total noise level get increased by about 8 dB and 6 dB, respectively. The target peak magnitude increases due to the increased number of effective subcarriers in each channel, which in turn comes at an increase of the collected total noise power by about the same factor. In Fig. 4.8 (b), the entire range profile is depicted. Intervals of ZCZs and high correlation alternate, which is typical for the ACF and CCF of ZCZ sequences. Although the regions of high correlation and strong ITCT do not constitute ambiguities and very likely will not cause ghost targets, they should be kept out of the radar's operational range, as their high sidelobes cause disturbance.

4.2.2 Modified Repeated Symbol CDM

Repeated symbol OFDM (RS-OFDM) [159] is a special case of OFDM radar that uses the same modulation symbol on each subcarrier for the entire measurement, i.e., the same OFDM symbol is repeated M times until the end of the frame. Through this, the signal becomes periodic as no longer phase shifts occur at the transitions of the OFDM symbols. Therefore, the CP can be neglected. The modified repeated symbol (MRS)-CDM concept, which was presented in [36], combines RS-OFDM with space-time coding (STC) [160]. STC was also applied in MIMO FMCW radar [160]–[162] or MIMO PMCW radar [152]. The common idea of these concepts is to cancel the ITCT through accumulating consecutive signal pulses at the receiver. In MRS-CDM, an accumulation of OFDM symbols is achieved within the signal compression along the time dimension, which is the Doppler DFT. Moreover, an STC structure is implemented using Hadamard matrices $\boldsymbol{\mathcal{H}}_Q$ of order Q, where

$$\boldsymbol{\mathcal{H}}_2 = \begin{bmatrix} 1 & 1 \\ 1 & -1 \end{bmatrix}, \quad \text{and} \quad \boldsymbol{\mathcal{H}}_Q = \begin{bmatrix} \boldsymbol{\mathcal{H}}_{Q/2} & \boldsymbol{\mathcal{H}}_{Q/2} \\ \boldsymbol{\mathcal{H}}_{Q/2} & -\boldsymbol{\mathcal{H}}_{Q/2} \end{bmatrix}. \tag{4.18}$$

Hadamard matrices feature the peculiarity that the inner product, i.e. the Euclidean norm, of each row and column is Q, while the inner product of different rows and columns is always zero. The former property contributes in the ACF, and the latter is exploited to eliminate the ITCT.

Transmit signal design. The MRS OFDM signal frame is composed of a concatenation of M/N_{tx} identical blocks each encompassing all N subcarriers, N_{tx} consecutive OFDM symbols, and all N_{tx} transmitters. STC coding is implemented within the block independently on each subcarrier across all transmitters using Hadamard matrices of order $Q = N_{\mathrm{tx}}$. To this end, the rows of $\boldsymbol{\mathcal{H}}_{N_{\mathrm{tx}}}$ are assigned to the transmitters (*space*), and the columns of $\boldsymbol{\mathcal{H}}_{N_{\mathrm{tx}}}$ are assigned to the N_{tx} consecutive symbols of the block (*time*). For each subcarrier, the modulation symbol sequences of all transmitters are jointly determined as follows. First, N_{tx} modulation symbols a_i, $i \in \mathbb{Z}_{N_{\mathrm{tx}}}$, are chosen randomly and independently from $\mathcal{A}$ and get assigned to the different transmitters and the involved N_{tx} consecutive symbols according to the Hadamard matrix structure. Here, also permutations of the basic matrix structure in (4.18) are allowed but have to be maintained on this subcarrier until the end of the signal frame, i.e. for all blocks. The total number of possible permutations depends on N_{tx}. For $N_{\mathrm{tx}} = 2$, four conceivable designs are

$$\boldsymbol{\mathcal{S}}_1 = \begin{bmatrix} m & m+1 \\ a_0 & a_0 \\ a_1 & -a_1 \end{bmatrix} \begin{matrix} \\ \text{Tx } 0 \\ \text{Tx } 1 \end{matrix}, \quad \boldsymbol{\mathcal{S}}_2 = \begin{bmatrix} m & m+1 \\ a_0 & -a_0 \\ a_1 & a_1 \end{bmatrix} \begin{matrix} \\ \text{Tx } 0 \\ \text{Tx } 1 \end{matrix},$$
$$\boldsymbol{\mathcal{S}}_3 = \begin{bmatrix} m & m+1 \\ a_0 & a_0 \\ -a_1 & a_1 \end{bmatrix} \begin{matrix} \\ \text{Tx } 0 \\ \text{Tx } 1 \end{matrix}, \quad \boldsymbol{\mathcal{S}}_4 = \begin{bmatrix} m & m+1 \\ a_0 & a_1 \\ a_1 & -a_0 \end{bmatrix} \begin{matrix} \\ \text{Tx } 0 \\ \text{Tx } 1 \end{matrix}. \tag{4.19}$$

The design $\boldsymbol{\mathcal{S}}_1$ corresponds to the basic structure in (4.18) and the repeated symbol principle. Furthermore, it is possible to change the order of rows or columns of the Hadamard structure such that the alternating sign is either on the first instead of the second transmitter ($\boldsymbol{\mathcal{S}}_2$) or the alternating sign is on the first instead of the second symbol ($\boldsymbol{\mathcal{S}}_3$). Beyond that, it is also allowed to break up the repeated symbol structure and distribute the symbols across the subcarriers ($\boldsymbol{\mathcal{S}}_4$) such that the symbols a_0 and a_1 are distributed alternately among the Tx channels. This means that neither of the symbols a_i is designated to a specific Tx channel only, however, at no time may the same symbol be transmitted by both transmitters simultaneously. In addition, once set, the chosen design on each subcarrier may not be changed until the end of the frame. However, it is possible to utilize different designs on different subcarriers

simultaneously. For instance, for $N{=}8$, it is possible to apply $\boldsymbol{\mathcal{S}}_1$ on subcarriers $\{2,5,8\}$, $\boldsymbol{\mathcal{S}}_2$ on $\{1,6\}$, and $\boldsymbol{\mathcal{S}}_4$ on $\{3,4,7\}$. In the following derivations, only design $\boldsymbol{\mathcal{S}}_1$ is considered, but the same can be shown analogously for the other designs as well. In the MRS-CDM setup, the sequences of modulation symbols $\boldsymbol{d}_{:n}^{[q]}$ along the time dimension of each subcarrier is decisive, which yields for instance for $N_{\mathrm{tx}}=2$

$$\boldsymbol{d}_{:n}^{[0]}=\big[a_0,a_0,a_0,a_0,\ldots,a_0,a_0\big]^{\mathsf{T}},\quad \boldsymbol{d}_{:n}^{[1]}=\big[a_1,-a_1,a_1,-a_1,\ldots,a_1,-a_1\big]^{\mathsf{T}}$$

for any subcarrier n. Given the modulation symbols, the remaining Tx signal generation is as described in Section 2.1. In particular, unlike RS-OFDM, MRS requires a CP, because the phase shifts introduced by the Hadamard matrix STC between symbols otherwise cause ISI due to signal delays at the receiver.

Receive signal and evaluation. At the receiver, the usual OFDM radar signal evaluation as described in Section 2.2 is performed, and no additional effort is required compared to IOFDM. The Doppler or velocity evaluation is of particular importance here, since in this step, the ITCT gets eliminated within the DFT, regardless if the range evaluation is performed prior or after the Doppler DFT. Similar to the range profile, the Doppler profile $\boldsymbol{\mathcal{V}}_n^{[\hat{q},l]}$ of the nth subcarrier of the $[\hat{q},l]$th channel may be divided into a desired part $\hat{\boldsymbol{\mathcal{V}}}_n^{[\hat{q},l]}$ and ITCT part $\check{\boldsymbol{\mathcal{V}}}_n^{[\hat{q},l]}$. The desired part of the Doppler profile is the row-wise DFT of $\hat{\boldsymbol{\mathcal{D}}}^{[\hat{q},l]}$ (2.42), which yields the coefficients

$$\hat{\mathcal{V}}_n^{[\hat{q},l]}[\nu]\propto\sqrt{M}\psi_n\big[\nu-\tfrac{v}{\Delta v}\big] \tag{4.20}$$

and has a peak at $\hat{\nu}=\lfloor f_d M T_{\mathrm{OFDM}}\rceil{=}\lfloor v/\Delta v\rceil$. Accordingly, the DFT of $\check{\boldsymbol{\mathcal{D}}}^{[\hat{q},l]}$ (2.43) yields the ITCT part

$$\check{\mathcal{V}}_n^{[\hat{q},l]}[\nu]\propto\frac{\sqrt{M}}{N_{\mathrm{tx}}}\psi_n[\nu-\hat{\nu}]_{\frac{M}{N_{\mathrm{tx}}}}\sum_{\substack{q=0\\q\neq\hat{q}}}^{N_{\mathrm{tx}}-1}\mathrm{e}^{\mathrm{j}\varphi_\theta[q,l]}\,a_q a_{\hat{q}}^*\sum_{u=0}^{N_{\mathrm{tx}}-1}h_{qu}h_{\hat{q}u}\,\mathrm{e}^{-\mathrm{j}2\pi\frac{u}{M}(\nu-\hat{\nu})} \tag{4.21}$$

with h_{qu} the $[q,u]$th entry of the (permuted) Hadamard matrix. The derivation of (4.21) is detailed in Appendix D, page 155. Eventually, $\check{\mathcal{V}}_n^{[q,l]}[\nu]$ disappears except for ambiguous peaks at $\nu=\hat{\nu}+\eta M/N_{\mathrm{tx}}$, $\eta{=}1,\ldots,(N_{\mathrm{tx}}{-}1)$. In particular,

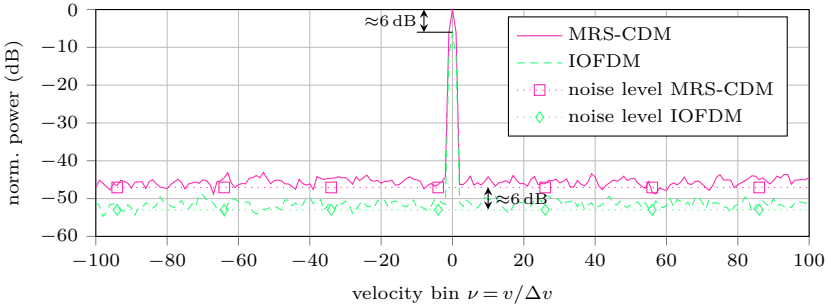
there is no peak at $\nu = \hat{\nu}$, since in this case the last sum in (4.21) becomes the inner product of two distinct columns of the Hadamard matrix, which is zero. Moreover, compared to the main peak magnitude of (4.20), the ambiguities are a factor N_{tx} smaller due to a reduced scaling of $\sqrt{M}/N_{\mathrm{tx}}$. Still, target dependent ambiguities emerge, hence limit v_{ua} and the maximum unambiguous Doppler frequency in MRS-CDM to

$$\left| v_{\mathrm{ua}}^{\mathrm{MRS}} \right| = \frac{M}{2N_{\mathrm{tx}}} \Delta v \quad \Leftrightarrow \quad \left| f_{d,\mathrm{ua}}^{\mathrm{MRS}} \right| = \frac{\Delta f}{2N_{\mathrm{tx}}(1 + T_{\mathrm{cp}}/T)} \,, \tag{4.22}$$

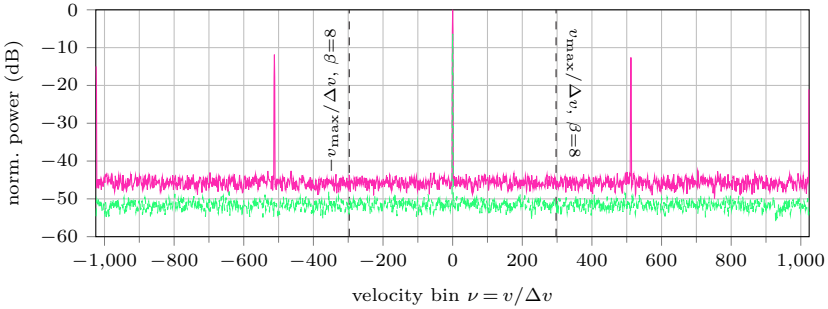
respectively. However, considering the reduced $v_{\mathrm{ua}}^{\mathrm{MRS}}$ in the context of existing signal design constraints for ICI suppression, the additional ambiguities turn out to be acceptable up to a certain N_{tx}. As addressed in Section 2.2.2, in order to keep the ICI influence low, a generous excess of the Doppler offset is typically included in the OFDM signal design but usually goes unused. Demanding $f_{d,\mathrm{ua}}^{\mathrm{MRS}} \geq f_{d,\mathrm{max}}$, it follows from (2.29) and (4.22) that the Doppler margin design parameter should be $\beta \geq 2N_{\mathrm{tx}}(1+T_{\mathrm{cp}}/T)$. It follows from $0 \leq T_{\mathrm{cp}} \leq T$ that for $\beta = 8$ and $N_{\mathrm{tx}} = 4$, like radar R1, the ambiguities of MRS-CDM are outside the utilized Doppler interval, hence are no impairment. In case of $N_{\mathrm{tx}} \geq 8$ and $T_{\mathrm{cp}} > 0$, the subcarrier spacing must be increased in order to meet $f_{d,\mathrm{ua}}^{\mathrm{MRS}} \geq f_{d,\mathrm{max}}$.

In Fig. 4.9, the velocity profiles of MIMO OFDM measurements of radar R1 using the proposed MRS-CDM and the standard IOFDM approach are shown. The applied MRS block design on each subcarrier is $\boldsymbol{\mathcal{S}}_1$ (4.19) with $N_{\mathrm{tx}} = 4$, and the signs are distributed according to a non-permuted $\boldsymbol{\mathcal{H}}_4$ (4.18). In Fig. 4.9 (a), the velocity profiles around the target peak are shown. Compared to IOFDM, both the peak and the total noise level get increased by about 6 dB. This is due to the increased number of effective subcarriers in each channel, which in turn is accompanied by an increase in the collected total noise power by about the same factor. In Fig. 4.9 (b), the entire velocity profile and the $v_{\mathrm{max}}/\Delta v$ ICI limits for $\beta = 8$ are depicted. Here, it is observable all ambiguities that emerge in MRS-CDM are outside the relevant velocity region.

Finally, the question arises if MRS-CDM may also be applied in the range dimension, i.e. along the subcarriers. Although this is theoretically possible, it is not advisable, since through the repeated symbol characteristic, the subcarriers of the same OFDM symbol would be modulated by the identical phase or its π-shifted counterpart. This results in a so-called uncoded OFDM. However, in



(a) Excerpt from bin −100 to 100; bin 0 corresponds to v=0 m/s.



(b) Entire velocity profile.

Fig. 4.9: Velocity profiles of MIMO OFDM radar measurements using MRS-CDM and IOFDM. The scene contains a single static target at range bin $\hat{\rho} = 15$ ($R = 5.5$ m) and velocity bin $\hat{\nu}$=0 (v=0 m/s). The profiles are extracted at the constant range bin $\hat{\rho}$=15 from the NCI of all channels after range-Doppler evaluation and are normalized to the target peak of MRS-CDM. (a) Excerpt of the profile around the target bin. (b) Entire velocity profile.

this case, the IDFT in (2.3) along the modulation symbols applied for Tx signal generation (2.3) resembles a summation of orthogonal (co-)sine waves of the same initial phase resulting in a sharp pulse-like time domain signal with high amplitude fluctuations and a high peak-to-average power ratio (PAPR). Such signals are highly unfavorable for amplification using linear power amplifiers.

4.2.3 Auto-Correlation-Based CDM

Auto-correlation (AC)-based-CDM takes advantage of the fact that the ACF is a special instance of the CCF and the ACF shape is nearly optimal in usual OFDM radar operation. Essentially, the CCF of two different signals, where one signal is a shifted or delayed version of the other, becomes a shifted ACF. This is again the property that is usually exploited by the matched filter of the radar. To illustrate the idea of AC-CDM, imagine the following scenario: Multiple nearby transmitters are emitting identical signals. In this case, after the matched filtering, the desired part of the range profile (4.9) and the ITCT part (4.12) would become equal, since the CCF within the latter becomes a periodic ACF. In this scenario, the transmitters become indistinguishable at the receiver, as their signals coalesce and appear to emanate from a single node located at the physical center of the transmitters. However, if the Tx signals would be identical but time-shifted, differentiation becomes possible again in the time dimension, which is the basic principle of AC-CDM [36].

In radar literature, signal separation through asynchronous transmission across the transmitters is also referred to as time-staggered MIMO [161], [163]. However, an asynchronous transmission introduces phase shifts between the channels complicating the evaluation, as these phases need to be compensated before DoA estimation. Due to its special signal structure and flexible digital signal generation, OFDM allows to circumvent this issue by only virtually delaying the signals by rotating them cyclically within each OFDM symbol [36]. This virtual delay keeps the signals synchronous at both Tx and Rx side.

Transmit signal generation. Let the virtual delay between the qth and $\hat{q}$th Tx channel be $\zeta^{(q\hat{q})}\tau_s \in [-T/2, T/2]$, where $\tau_s = T/N$ is the discrete time sample duration without oversampling and $\zeta^{(q\hat{q})} \in [-N/2, N/2]$ the integer relative mutual sample shift. The discrete-time Tx signals are then designed with respect to the $\hat{q}$th Tx channel according to

$$x_m^{[q]}(t) = x_m^{[\hat{q}]}\left((t - \zeta^{(q\hat{q})}\tau_s)_T\right), \tag{4.23}$$

where $(\cdot)_T$ denotes the modulo T operation. Note that the signal not yet contains a CP. In OFDM, the time delays do not have to be implemented in time domain but may conveniently be integrated in the digital modulation symbol generation

so that the common processing chain does not have to be modified. The key to this is the Fourier relation [70]

$$x(t-\Delta t) \quad \circ\!\!-\!\!\bullet \quad X(f)\,\mathrm{e}^{-\mathrm{j}2\pi\Delta t f}\,, \tag{4.24}$$

which allows the virtual time delay to be translated into a phase modulation in the Tx spectrogram. Through this, the corresponding modulation symbols to the signal in (4.23) become

$$d_{mn}^{[q]} = d_{mn}^{[\hat{q}]}\,\mathrm{e}^{-\mathrm{j}2\pi\zeta^{(q\hat{q})}\tau_s n\Delta f} = d_{mn}^{[\hat{q}]}\,\mathrm{e}^{-\mathrm{j}2\pi\zeta^{(q\hat{q})}\frac{n}{N}}\,. \tag{4.25}$$

Therefore, in the Tx signal generation, first the symbols of a single reference channel $\hat{q}$ are chosen randomly from $\mathcal{A}$. Then, the symbols of the other transmitters are determined by (4.25), given the relative mutual sample shifts and the phases of $d_{mn}^{[\hat{q}]}$. Note that the modulation symbols $d_{mn}^{[q]}$, $q \neq \hat{q}$ may not be elements of $\mathcal{A}$ anymore but have arbitrary continuous phases. Since in pure radar operation the modulation does not carry useful information, this does not matter. Finally the Tx signals of all channels are generated through the usual IDFT step.

Receive signal and evaluation. The receive side evaluation steps are the same as in the standard and IOFDM processing. Through the introduced virtual signal delay and specially adapted modulation symbols (4.25) and time signals (4.23), the ITCT part (4.11) of the range evaluation becomes

$$\breve{\mathcal{R}}_m^{[\hat{q},l]}[\rho] \propto \sum_{\substack{q=0\\q\neq\hat{q}}}^{N_\mathrm{tx}-1} \alpha^{[q,l]}\,\mathrm{e}^{\mathrm{j}\varphi_\theta[q,l]}\,\frac{1}{\sqrt{N}}\sum_{\eta=0}^{N-1} x_m^{[\hat{q}]}[\eta+\rho-\tfrac{R_0}{\Delta R}-\zeta^{(q\hat{q})}]_N\left(x_m^{[\hat{q}]}[\eta]\right)^* \tag{4.26}$$

$$\propto \sum_{\substack{q=0\\q\neq\hat{q}}}^{N_\mathrm{tx}-1} \alpha^{[q,l]}\,\mathrm{e}^{\mathrm{j}\varphi_\theta[q,l]}\,\frac{1}{\sqrt{N}}\chi^{\mathrm{ac}}_{x_m^{[q]}x_m^{[\hat{q}]}}\left[\rho-\tfrac{R_0}{\Delta R}-\zeta^{(q\hat{q})}\right] \tag{4.27}$$

$$\propto \sum_{\substack{q=0\\q\neq\hat{q}}}^{N_\mathrm{tx}-1} \alpha^{[q,l]}\,\mathrm{e}^{\mathrm{j}\varphi_\theta[q,l]}\,\sqrt{N}\psi_m\left[\rho-\tfrac{R_0}{\Delta R}-\zeta^{(q\hat{q})}\right]. \tag{4.28}$$

It yields a superposition of $(N_{\mathrm{tx}}-1)$ ACFs, each shifted by the sum of the target position $\hat{\rho} = R_0/\Delta R$ and the respective sample shift $\zeta^{(q\hat{q})}$ of the qth channel. Since target peaks are generated at each of these positions, a total of N_{tx} peaks per target are generated after evaluation. In every channel, one peak is at the true target position and caused by the ACF in (4.9) that contains no additional shift. The remaining $(N_{\mathrm{tx}}-1)$ peaks are ambiguous and are caused by the shifted ACFs of the ITCT part in (4.28).

Favorable choice of $\zeta^{(q\hat{q})}$. Another challenge in AC-CDM is to identify the correct peaks among all peaks. However, in general, this is not possible as they are indistinguishable. In [36], a special design rule to choose a favorable set of mutual shfits $\zeta^{(q\hat{q})}$ and a smart post-processing method are presented that allow to identify correct peaks up to the maximum unambiguous range achievable by an OFDM frame composed of N subcarriers. The basic idea of the concept is that depending on $\zeta^{(q\hat{q})}$, the location of the ambiguities in each Tx-Rx channel can be controlled. Moreover, if the delays $\zeta^{(q\hat{q})}\tau_s$ between the individual channel pairs differ, the ambiguities emerge at different locations for each pair due to varying shifts in (4.28). Note that this only applies for ambiguous peaks but not for the correct target peaks that remain unaffected by these shifts. This feature shall be exploited to identify the correct peaks among the set of peaks. Initially, some constraints are introduced to generate a favorable choice of mutual shifts:

(I) The mutual shifts $\zeta^{(q\hat{q})}$, $q \neq \hat{q}$ of the set have to be unique. Additionally, the minimum difference between any two shifts has to be at least $N_{\mathrm{guard}} \geq 0$, where N_{guard} is a free design parameter.

(II) The number of guard samples N_{guard} should be small and approximately equal to the number of resolution cells needed to distinguish two distinct targets in range. This usually depends on the applied window function and is typically in the range of 3 to 10 bins.

(III) The spacing between any target's true peak and any of its ambiguous peaks must be maximized in each channel.

Through these constraints, the peaks caused by each target become both separable and unique across all channels of the radar. Additionally, the fundamental R_{ua} of the approach, i.e. without ambiguous peak identification, gets

Tab. 4.1: AC-CDM mutual shifts $\zeta^{(q\hat{q})}$ example for $N_{\mathrm{tx}}=4$, $N=1024$, and $N_{\mathrm{guard}}=7$ using (4.31). The values in parentheses equal $\zeta^{(q\hat{q})}+N$ in case of negative shifts. The highlighted values violate the spacing constraint (II). Adapted from [36] © 2021 IEEE.

q \ $\hat{q}$	1	2	3	4
1	0	−245 (779)	−497 (527)	268
2	245	0	−252 (772)	−511 (513)
3	497	252	0	−259 (765)
4	−268 (756)	511	259	0

maximized. The maximum number of unambiguous resolution cells is therefore

$$N_{\mathrm{ua}}^{\mathrm{AC}} = \left\lfloor \frac{N}{N_{\mathrm{tx}}} - \frac{N_{\mathrm{guard}}(N_{\mathrm{tx}}+1)}{2} \right\rfloor \tag{4.29}$$

in the proposed design. Note that $N_{\mathrm{ua}}^{\mathrm{AC}}$ considers a safety margin of N_{guard} such that the minimum spacing between the actual target and its nearest ambiguity is $N_{\mathrm{ua}}^{\mathrm{AC}}+N_{\mathrm{guard}}$ bins. Along with this parameter, the maximum unambiguous range of the signal becomes

$$R_{\mathrm{ua}}^{\mathrm{AC}} = N_{\mathrm{ua}}^{\mathrm{AC}}\Delta R = \left\lfloor \frac{N}{N_{\mathrm{tx}}} - \frac{N_{\mathrm{guard}}(N_{\mathrm{tx}}+1)}{2} \right\rfloor \Delta R\,. \tag{4.30}$$

Finally, the mutual sample shifts between the qth and $\hat{q}$th Tx channel are determined via

$$\zeta^{(q\hat{q})} = (q-\hat{q})N_{\mathrm{ua}}^{\mathrm{AC}} + \frac{q(q-1)-\hat{q}(\hat{q}-1)}{2} N_{\mathrm{guard}}\,, \tag{4.31}$$

which guarantees unique peaks and maximizes (4.30) as demanded by constraint (I) and (III).

In Table 4.1, the resulting shifts for radar R1 with $N_{\mathrm{tx}}=4$ and $N=1024$ are given. The number of guard samples is $N_{\mathrm{guard}}=7$. In addition, to demonstrate the effect of (4.29) and (4.31) on the different Tx channels, in Fig. 4.10, the simulated range profiles of a single Rx channel using the shift setup in Table 4.1 is illustrated. In this single target setup, peaks emerge at $\hat{\rho}$ as well as at $\hat{\rho}+\zeta^{(q\hat{q})}$

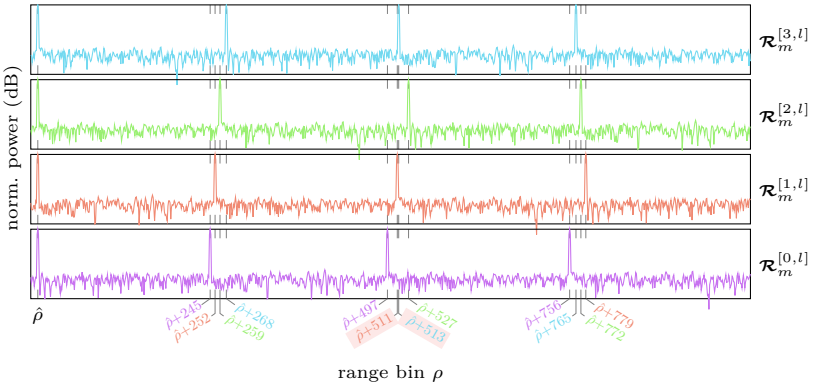
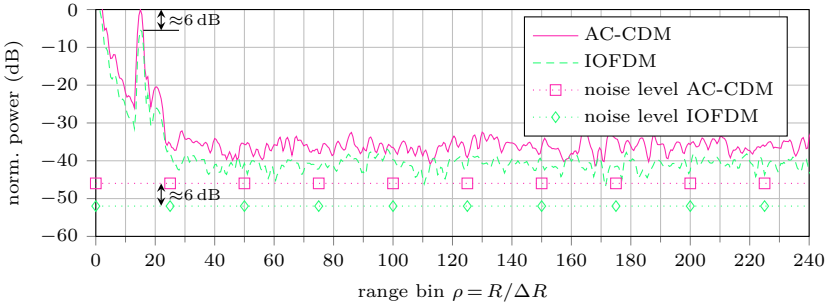


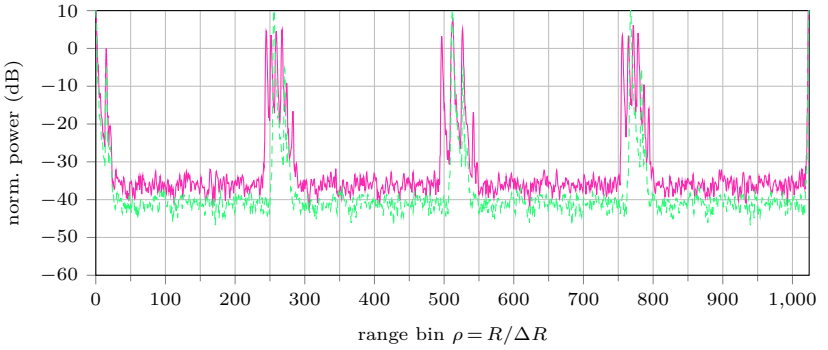
Fig. 4.10: Illustration of an example ambiguity distribution in AC-CDM across the channels of a single receiver l for a system with $N_{\mathrm{tx}} = 4$, $N = 1024$, $N_{\mathrm{guard}} = 7$, and mutual shifts from Table 4.1. The simulation comprises a single target at $\hat{\rho}$. The highlighted range bins violate the spacing constraint (II). Adapted from [36] © 2021 IEEE.

with spacings according to Table 4.1 that lead to different ambiguities in each channel. Note that since the modulo operation of the virtual delay was neglected in the above derivation, constraint (II) gets violated for two shifts that only exhibit a spacing of 2. These are highlighted in both Table 4.1 and Fig. 4.10. However, this is tolerable in the peak identification step.

In addition, measurements are performed with radar R1 using the AC-CDM setting of Table 4.1. The resulting range profiles are shown in Fig. 4.11, where Fig. 4.11 (a) shows the profiles up to $R_{\mathrm{ua}}^{\mathrm{AC}}/\Delta R = N_{\mathrm{ua}}^{\mathrm{AC}} = 238$. Compared to IOFDM, both the target mainlobe and the noise level get increased by about 6 dB, due to the increased number of effective subcarriers in each channel. In Fig. 4.11 (b), the entire range profile is depicted. Especially for the Tx-Rx cross-talk, the differing and irregular distribution of ambiguities similar to Fig. 4.10 is clearly discernible. In Doppler dimension, no additional ambiguities emerge.



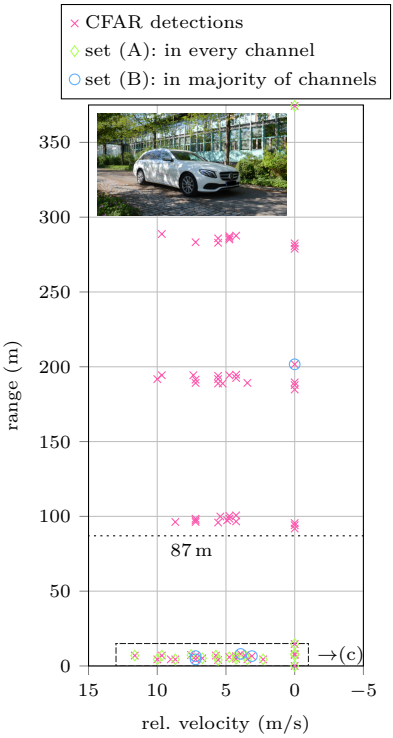
(a) Range profile excerpts.



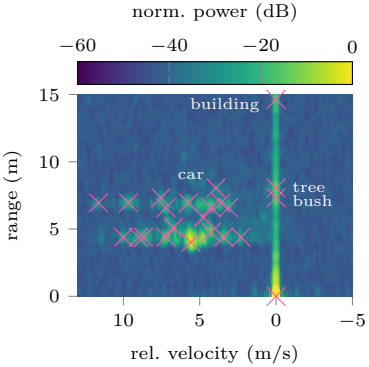
(b) Entire range profiles.

Fig. 4.11: Range profiles of MIMO OFDM radar measurements using AC-CDM and IOFDM. For both setups, the same signal parameters and output power are applied. The scene contains a single static target at range bin $\hat{\rho} = 15$ ($R = 5.5\,\mathrm{m}$). The profiles are extracted at the constant target velocity bin $v/\Delta v = 0$ from the NCI of all channels after range-Doppler evaluation and are normalized to the target peak of AC-CDM. In the AC-CDM setup, $\zeta^{(q\hat{q})}$ from Table 4.1 is applied. (a) Range profile excerpts up to $R_{\mathrm{ua}}^{\mathrm{AC}}/\Delta R$. (b) Entire range profiles.

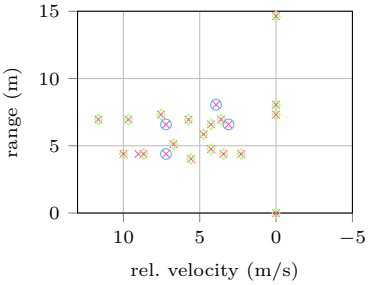
Identifying correct target peaks. The forced uniqueness regarding the positions of the ambiguities of each target allows to identify the correct peaks from the set of peaks. If it is guaranteed that no target is farther away than $R_{\mathrm{ua}}^{\mathrm{AC}}$ (4.30)



(a) CFAR detections and classifications. Adapted from [36] © 2021 IEEE.



(b) *R*-*v*-image. Adapted from [36] © 2021 IEEE.



(c) CFAR detections and classification of peaks up to R=15 m. Adapted from [36] © 2021 IEEE.

Fig. 4.12: Application of target identification for AC-CDM OFDM radar measurement of an approaching vehicle (XAC). Applied parameters are $N_{\text{tx}} = 1024$ and $N_{\text{guard}} = 7$ with shifts $\zeta^{(q\hat{q})}$ from Table 4.1. (a) CFAR detections and target classification results up to $R_{\text{ua}}^{\max}$ (2.22). The photo on the upper left shows the measured scene from the radar's point of view. (b) Excerpt of the *R*-*v*-image (NCI of the radar images of all channels) area, i.e. encircled area in (a), containing the vehicle object and involved CFAR detections. (c) CFAR detections and classification results of the area depicted in (b) and framed in (a).

or a reflection from this distance is excluded, identification and assignment is not necessary, since all targets up to this distance are unambiguous and correct. Otherwise, it has to be verified which peaks are correct and which are ambiguous. The method proposed in [36] by the author takes advantage of the different peak ranges within the different Tx-Rx channels in such a way that the peaks occurring in each or almost each channel are classified as correct, while the remaining peaks are rejected in the detection. As illustrated in the example in Fig. 4.10, only the peak at $\hat{\rho}$ occurs in each channel, while its ambiguities are displaced. AC-CDM with peak identification is referred to as extended AC-CDM with target identification (XAC) hereafter. The peaks are classified according to their occurrence in the channels as

(A) matching in every channel,

(B) matching in almost ($\gg$50%) every channel,

(C) remaining other.

The peak detection may be implemented using a CFAR or a simple threshold.

It should be noted that it is possible to distinguish ambiguous and true targets in IOFDM as well by analyzing the phase progression of each peak across all channels similar to [125], [164]. However, the method is not applicable for large N_{tx} and overlapping or multiple peaks per bin [125], [138]. In contrast, verified by simulations, XAC achieves robust classification results even in crowded scenes with many targets and large N_{tx} having overlapping peaks and a small $R_{\mathrm{ua}}^{\mathrm{AC}}$.

To verify the applicability of the XAC peak identification, outdoor measurements with radar R1 of an approaching vehicle are investigated. The recorded scene is shown in the upper part of Fig. 4.12 (a). In Fig. 4.12 (b), the NCI of the R-v-images of all channels along with the CFAR detections is depicted. The detected target points are also plotted in Fig. 4.12 (a) along with the peak classification result (only (A) and (B)). Unmarked detections are classified ambiguities (C) and are ignored in the final target list. Regarding the CFAR detections, four clusters of targets are recognizable as would be also expected for IOFDM with $N_{\mathrm{tx}} = 4$. Moreover, each cluster in AC-CDM is unique, while the clusters in IOFDM are always exact copies of each other shifted by integer multiples of N/N_{tx} range bins, due to the reduced periodicity of the IDFT, . Applying the proposed target identification, it turns out that even with this complex outdoor and non-static scene, almost all targets within the field of

Tab. 4.2: Comparison of the maximum unambiguous ranges achievable by the different MIMO approaches. Adapted from [36] © 2021 IEEE.

	IOFDM	ZCZ	AC†	XAC	MRS	RM
$\frac{R_{\mathrm{ua}}}{\Delta R}$	$\frac{N}{N_{\mathrm{tx}}}$	$\frac{3N}{4N_{\mathrm{tx}}}$	$\left\lfloor \frac{N}{N_{\mathrm{tx}}} - \frac{N_{\mathrm{guard}}(N_{\mathrm{tx}}+1)}{2} \right\rfloor$	N	N	N
$\frac{v_{\mathrm{ua}}}{\Delta v}$	M	M	M	M	$\frac{M}{2N_{\mathrm{tx}}}$	M

† without ambiguity detection

view (FoV) (see also Fig. 4.12 (c)) are assigned correctly to be real targets, while almost all farther distant targets are classified ambiguous. This result fits the expectations, since with the sensor used and the scene observed, neither ambiguities within the first cluster nor reflections farther away than the first clusters are to be expected.

4.2.4 Analysis and Comparison

Just as the developed CDM approaches are different, each of them offers advantages and limitations in different areas. In the following, their performance is analyzed and compared with focus on the achievable maximum unambiguous range and velocity, the achievable PNR and PSLR, the Doppler offset sensitivity, the required processing effort, and the potential areas of application. Furthermore, the performance is compared to the IOFDM and RM approaches.

Maximum unambiguous range and velocity

The achievable unambiguous ranges of the CDM approaches are derived in Sections 4.2.1 to 4.2.3. In Table 4.2, R_{ua} and v_{ua} are summarized. In addition, Fig. 4.13 shows the corresponding progressions of R_{ua} proportional to N_{tx} for $N = 1024$ and $N_{\mathrm{guard}} = 7$. RM, MRS, and XAC-CDM achieve the theoretical upper bound of $R_{\mathrm{ua}}^{\mathrm{max}}$ (2.22), thus outperform IOFDM by the factor N_{tx}. On the other hand, ZCZ achieves only a factor 3/4 of the IOFDM limit, whereas that of AC-CDM is the amount $N_{\mathrm{guard}}(N_{\mathrm{tx}}+1)/2$ less. In Fig. 4.13, it becomes apparent that up to about ten transmitters, the difference between IOFDM and AC-CDM is negligible. Examining v_{ua}, only MRS-CDM experience losses, while the other approaches achieve the theoretical upper bound $v_{\mathrm{ua}}^{\mathrm{max}}$ (2.28).

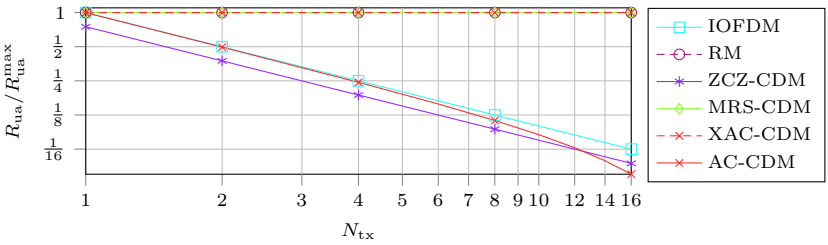


Fig. 4.13: Comparison of the maximum unambiguous ranges R_{ua} (Table 4.2) in MIMO OFDM operation with respect to $R_{\mathrm{ua}}^{\max}$ (2.22) proportional to N_{tx} with $N = 1024$ and $N_{\mathrm{guard}} = 7$. Adapted from [36] © 2021 IEEE.

Tab. 4.3: Numerical examples for R_{ua} and v_{ua} given the OFDM radar R1 with $N_{\mathrm{tx}} = \{2, 4, 8, 16\}$ transmitters. Adapted from [36] © 2021 IEEE.

	N_{tx}	IOFDM	ZCZ	AC	XAC	RM	MRS
R_{ua}	2	187.4 m	140.5 m	183.3 m	374.7 m		
	4	93.7 m	70.3 m	87.1 m			
	8	46.8 m	35.1 m	35.1 m			
	16	23.4 m	17.6 m	1.5 m			
v_{ua}	2	335.6 m/s					167.8 m/s
	4						83.9 m/s
	8						42.0 m/s
	16						21.0 m/s

As discussed in Section 4.2.2, this loss is negligible up to $N_{\mathrm{tx}} \approx 8$. Finally, in Table 4.3, the actual limitations for R_{ua} and v_{ua} of the different MIMO OFDM radar options are given for radar R1 from Table 2.1.

Achievable PNR and PSLR

To evaluate the achievable PNR and PSLR improvement of the proposed CDM and RM approaches over IOFDM, several measurements of different static scenes with up to three targets are performed in an anechoic chamber. For each approach and scene, first, the average PNR and PSLR are determined over

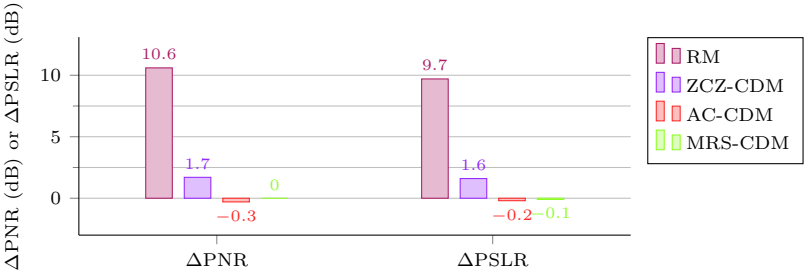


Fig. 4.14: Relative measured PNR and PSLR improvements ΔPNR and ΔPSLR, respectively, achieved by the different new MIMO approaches in relation to IOFDM. The obtained results are averaged over several measurements and scenes.

several measurements, where the PNR is taken as the ratio of the strongest reflection to the average noise level in the NCI *R-v*-images of all channels. The PSLR is the ratio of the very same reflection and the strongest clutter or noise peak not assigned to a valid target. Since the radar system only allows to generate a limited number of independent OFDM symbols, an increased noise level is observable in the zero-velocity cells. Therefore, only non-static cells are considered for the sidelobe level determination. Finally, the performance of each approach with respect to IOFDM is evaluated using the achieved relative ΔPNR and ΔPSLR, which are differences of the average PNR and PSLR achieved by a single approach compared to that achieved by IOFDM averaged over all scenes, respectively. The obtained results are shown in Fig. 4.14, where positive values mean an improvement over IOFDM. A significant improvement of about 11 dB is observable for RM, which benefits from the high pseudo PNR generated through the CS recovery. In addition, the high sidelobes of the static cells caused by the transmission limitations dissolve within the recovery. As already indicated in Fig. 4.8, ZCZ-CDM achieves an improvement of about 1.8 dB and 1.6 dB in PNR and PSLR, respectively. The performances of MRS-CDM and IOFDM are similar, and AC-CDM is marginally worse.

The results are additionally verified by measurements of complex non-static scenes. To that end, the same scenario as in Figs. 4.5 and 4.12 of an approaching

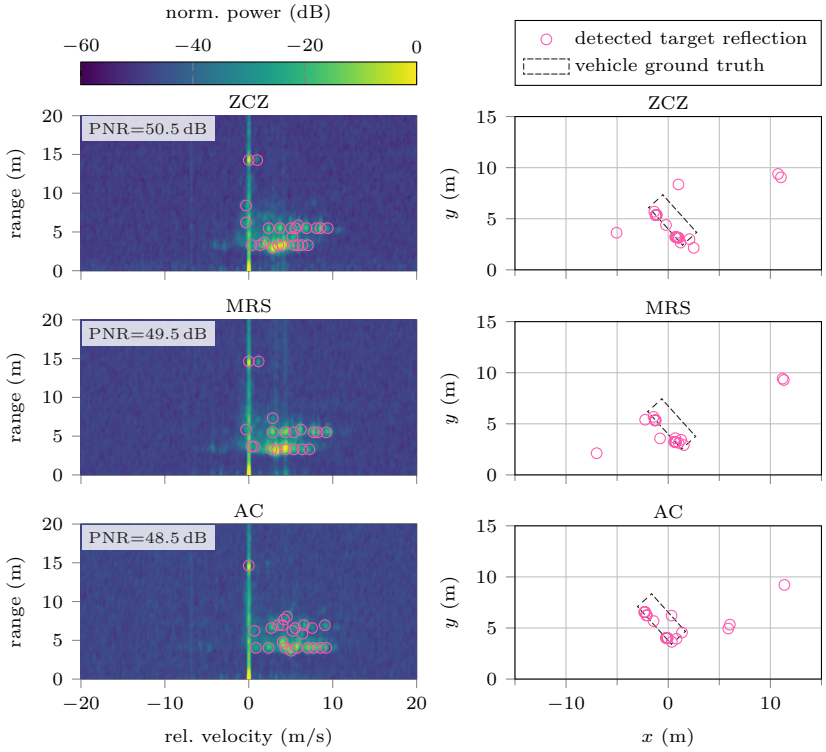


Fig. 4.15: Extended target measurements of an approaching vehicle using the ZCZ, MRS, and AC-CDM approaches. Left: R-v-images with obtained PNRs and CFAR detection results. The images are normalized to the strongest target reflection (building at $R = 14.3\,\mathrm{m}$). Right: x-y-representation after DoA estimation.

vehicle is investigated. The obtained R-v-images and x-y-plots of measurements using the developed CDM approaches are depicted in Fig. 4.15. Comparing the PNRs of these measurements with those of the same scene using RM and IOFDM as shown in Figs. 4.5 and 4.6 confirms the findings summarized in

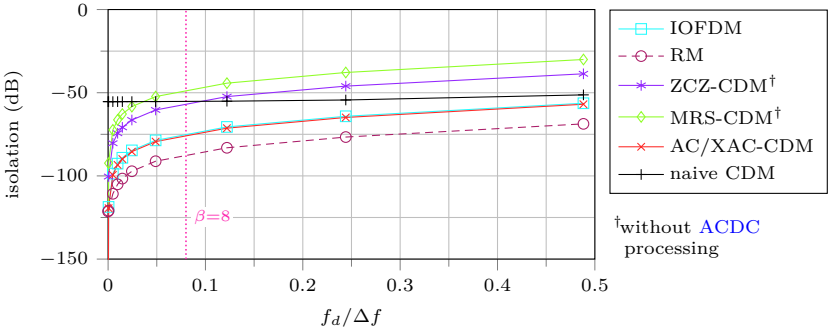


Fig. 4.16: Doppler sensitivity of the IOFDM, naive CDM, RM, and CDM MIMO approaches. Results obtained from Monte Carlo simulations. Adapted from [36] © 2021 IEEE.

Fig. 4.14 also for the non-static and extended target scenarios.

Doppler and frequency offset sensitivity

Doppler and frequency offsets typically lead to an impairment of the subcarrier orthogonality of the OFDM signal [7], [13], [37], which results in the aforementioned ICI. The reason is that the signal is evaluated at frequencies $n\Delta f$, although the signal and thus each of its subcarriers experienced a shift in frequency due to the target's relative motion. Due to the Doppler-induced shift of the Rx spectrogram, as illustrated in Fig. 2.5 on page 18, signals of different subcarriers interfere with each other, which results in an impaired isolation of the subcarriers. Additionally, the integrated signal power on each subcarrier gets reduced leading to a reduced peak power after pulse compression, yet this effect is negligible compared to the ICI. The impairment of the subcarrier isolation in MIMO operation is investigated by simulations using the signal parameters of radar R1 and $N_{\mathrm{tx}} = 4$. The obtained simulated theoretical isolation of subcarriers in presence of a relative Doppler shift $f_d/\Delta f$ is depicted in Fig. 4.16 for IOFDM, RM, and the CDM approaches, as well as the naive coding using randomly chosen phases (see example in Fig. 4.7). For the naive coding approach, the ITCT exceeds the ICI such that the loss in isolation is

subordinate, even for high Doppler shifts. The performance of IOFDM and (X)AC, which show the typical ICI loss of an OFDM signal frame of size $M \times N$, is significantly better. In comparison, RM turns out to be the most robust of the group against isolation loss with about 12 dB improvement. On the other hand, ZCZ and MRS-CDM are much more sensitive to Doppler shifts with about 18 dB and 26 dB less isolation, respectively. In both approaches, the ITCT should get eliminated through cancellation, which however dissolves with increasing code and thus signal compression or spreading due to the Doppler shift. As a consequence, the ITCT impact increases. Fortunately, this degradation may be counteracted by applying the so-called all-cell Doppler correction (ACDC) [165]. With the constraint that the OFDM symbols are linearly dependent, thus $\boldsymbol{d}$ is a rank-one matrix, the method allows to compensate the compression. In brief, to this end, the evaluation steps are rearranged such that the Doppler DFT gets brought forward and is performed directly on the complex envelope (2.10) of the receive signal. This is allowed only if $\boldsymbol{d}$ is a rank-one matrix. Afterwards, a correction term is multiplied to each component that compensates the Doppler shift of each Doppler bin independent of the targets in the scene. Finally, the spectrogram is computed, the modulation is reversed, and the range IDFT is computed yielding the R-v-image. MRS-CDM obviously exhibits linearly dependent OFDM symbols and thus supports ACDC processing. However, other than in the usual ACDC approach, for those transmitters carrying alternating symbol signs, the sign alternation has to be reversed before the Doppler DFT, since the desired signal would cancel itself otherwise. Consequently, the modulation symbol matrix applied in the spectrogram must be adjusted to account for the prior partial code removal. ZCZ sequence sets as generated through [155] are also linearly dependent and thus suitable for ACDC without any adaption. After applying ACDC processing, ideally, a perfect subcarrier isolation is restored.

Complexity and computational effort

IOFDM, ZCZ, AC, and MRS-CDM perform the same signal generation and evaluation steps as described in Chapter 2 and differ only in the design of the modulation symbols. The target identification in XAC requires some additional effort to identify and compare the target peaks of the different channels. ACDC does not require additional effort in the evaluation, which is why ZCZ-CDM with ACDC has the same complexity as IOFDM. However, in case of MRS

Tab. 4.4: Comparison overview of the discussed MIMO OFDM radar approaches using performance ratings. Ratings range from ++ (best) to −− (worst among the considered set).

	IOFDM	RM	ZCZ	AC/XAC	MRS
R_{ua}	−	++	−−	−−/+	++
v_{ua}	++	++	++	++	−−
f_d sensitivity	o	+	−/++[†]	o	−−/++[†]
PNR	o	++	+	−	o
PSLR	o	++	+	−	o
effort/complexity	++	−−	++	++/o	++/+[†]

[†] without/with ACDC processing

with ACDC, it is necessary to remove the alternating signs of the modulation symbols of some channels prior to the ACDC step, which can be considered a minor computational overhead. Finally, RM requires the most effort among the considered approaches, due to the higher complexity of the CS-based post-processing.

Discussion

As demonstrated in the signal design descriptions and validated in the analysis in this section, the individual MIMO approaches follow distinct strategies in signal design, which in turn leads to varying advantages and limitations in the different sensing performance areas. In Table 4.4, a comparison regarding the achievable unambiguous range-Doppler field of view, the Doppler tolerance, the PNR, the PSLR, and the required signal generation and evaluation complexity is given. The approaches are rated with respect to the others in each property. It turns out that RM yields the best performance and is either better or comparable to the others in all areas except for the complexity. It is therefore suitable for a wide range of applications, especially when high requirements are placed on both range and Doppler. However, it requires the most processing effort. On the other hand, each of the CDM approaches is able to outperform IOFDM in at least one feature, however, this comes at other individual limitations. MRS-CDM overcomes the limitations in range but at cost of flexibility in the Doppler domain. However, it is derived that the reduced v_{ua} is acceptable up

to $N_{\mathrm{tx}} \approx 8$. Therefore, it is suitable for applications with a moderate N_{tx} or where the expected Doppler shift is not too high but the range requirements are demanding. (X)AC-CDM and IOFDM – although using different waveform designs – are comparable in performance, where AC achieves a smaller R_{ua}. This in turn is a strength of XAC, which outperforms IOFDM here at cost of slightly increased processing effort due to the additional target identification steps. Finally, ZCZ-CDM achives a slightly smaller R_{ua} but offers an improved PNR compared to IOFDM. However, it comes nowhere close to RM. In addition, both ZCZ and MRS-CDM allow ACDC processing making them insensitive to ICI. Therefore, ZCZ-CDM is a good alternative to IOFDM in applications with medium ranges but demanding Doppler (even beyond $\Delta f/\beta$).

4.3 Hybrid Approaches

As illustrated and discussed in Section 4.2.4, both the new and established MIMO approaches offer individual benefits that come at different limitations, for instance regarding the maximum unambiguous range-Doppler field of view, that may restrict their possible fields of application. In particular if the number of required transmitters or the sensor requirements aggravate, it may become impossible to implement a particular approach. See here also Tables 4.3 and 4.4 on pages 104 and 109, respectively. The use of a single concept usually implies strong individual losses in one domain, e.g. range, while there are no losses in others, e.g. Doppler, although there is considerable scope to spare there. Yet, in addition to their individual use, some of the MIMO OFDM radar approaches allow to be combined and thereby benefit from each other.

Consider the following example: A radar system with parametrization of R1 as in Table 2.1 and $N_{\mathrm{tx}} = 8$ should be realized for both high $R_{\mathrm{ua}} \approx 150\,\mathrm{m}$ and high $v_{\mathrm{ua}} \approx \pm 200\,\mathrm{km/h}$ ($\pm 56\,\mathrm{m/s}$), for instance a two-way highway traffic scenario. Investigating Table 4.3, it shows that except for RM and XAC-CDM, none of the approaches meet all the requirements. Even more, IOFDM and AC-CDM both overaccomplish v_{ua} and at the same time are very restrictive for R_{ua}. The same holds the other way around for MRS-CDM. However, by combining MRS-CDM with either IOFDM or AC-CDM would allow to fulfill both requirements. Therefore, hybrid setups are introduced. Considering the individual advantages, limitations, and demands of the approaches, three viable combinations are

Tab. 4.5: Numerical examples for R_{ua} and v_{ua} for the hybrid approaches given the OFDM radar R1 with $N_{\mathrm{tx}} = 4$ transmitters, where both elements of the hybrid setup utilize two-times multiplexing.

	MRS-IOFDM	MRS-AC-CDM	AC-RM
R_{ua}	187.4 m	183.3 m	183.3 m
v_{ua}	167.8 m/s	167.8 m/s	335.6 m/s

identified: MRS-IOFDM, MRS-AC-CDM, and AC-RM. The application of ZCZ in combination with MRS-CDM is not recommended since both approaches tend to exhibit high sidelobes in case of moving targets, which aggravates in this case. Also, any combinations of IOFDM, AC, and ZCZ-CDM is not beneficial, since all are constrained in R_{ua}. At first glance, AC-RM seems to be a bad combination, since RM alone already achieves the optimum R_{ua} and v_{ua}, while the combination with AC-CDM reduces R_{ua}. However, as N_{tx} increases, the undersampling factor δ_{cs} of the system decreases and makes reconstruction more difficult, as discussed in Section 3.3.5. Therefore, N_{tx} should not be too large to allow reconstruction in pure RM. This issue is mitigated in AC-RM.

For the previous highway traffic example, the MRS-IOFDM setup could be as follows: Initially, apply a two-times interleaving with $N_{\mathrm{tx}}^{\mathrm{IOFDM}} = 2$ transmitters. Then, on each of the two subcarrier subsets, additionally, four transmitters are multiplexed using the MRS-CDM approach with $N_{\mathrm{tx}}^{\mathrm{MRS}} = 4$. Together, this allows to multiplex $N_{\mathrm{tx}} = N_{\mathrm{tx}}^{\mathrm{IOFDM}} N_{\mathrm{tx}}^{\mathrm{MRS}} = 8$ transmitters. The achieved performance is $v_{\mathrm{ua}} = \pm 83.9\,\mathrm{m/s}$ and $R_{\mathrm{ua}} = \pm 187.4\,\mathrm{m}$, where the restriction in v_{ua} is due to MRS-CDM ($N_{\mathrm{tx}}^{\mathrm{MRS}} = 4$) and the restriction in R_{ua} due to IOFDM ($N_{\mathrm{tx}}^{\mathrm{IOFDM}} = 2$). A similar setting is conceivable with AC and MRS-CDM.

The hybrid approaches are validated by measurements using radar R1. The $N_{\mathrm{tx}} = 4$ transmitters are multiplexed by applying two-times multiplexing for either of the approaches in the hybrid ensemble. Therefore, the combined experienced losses in range and Doppler according to Table 4.4 are determined by that of $N_{\mathrm{tx}} = 2$ for either of the approaches. The corresponding range-Doppler performance for the hybrid approaches using R1 and $N_{\mathrm{tx}} = 4$ are summarized in Table 4.5. In Fig. 4.17, the measured *R-v*-images using the three hybrid approaches are depicted. The observed scenario is again that of the approaching vehicle as considered before in Figs. 4.5, 4.12, and 4.15. It shows that for each

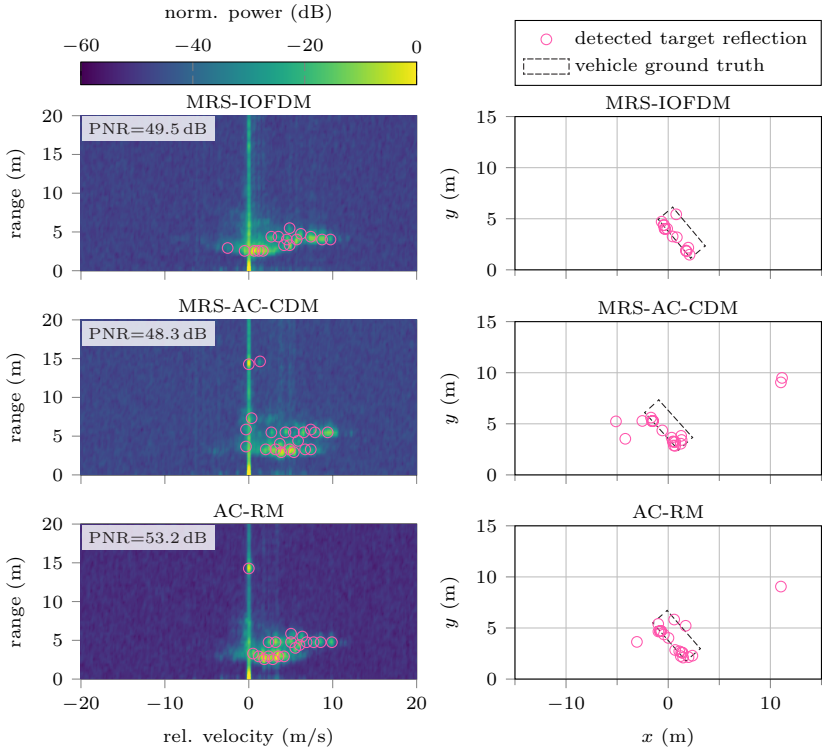


Fig. 4.17: Extended target measurements of an approaching vehicle using the hybrid MIMO methods MRS-IOFDM, MRS-AC-CDM, and AC-RM with radar R1. In each setup, always two transmitters are multiplexed with each of the two approaches A and B of the ensemble ($N_{\mathrm{tx}} = N_{\mathrm{tx}}^{\mathrm{A}} N_{\mathrm{tx}}^{\mathrm{B}} = 4$). Left: *R*-*v*-images with obtained PNRs and CFAR detection results. The images are normalized to the strongest target reflection (building at $R = 14.3\,\mathrm{m}$). Right: *x*-*y*-representation after DoA estimation.

setup, the vehicle is clearly discernible. For MRS-AC-CDM, more clutter is recognizable. Comparing the obtained PNRs with the results of the RM, IOFDM, and the pure CDM measurements in Figs. 4.5, 4.6, and 4.15, respectively, it

shows that the performance of MRS-IOFDM and MRS-AC-CDM are comparable to that of IOFDM, MRS, and AC-CDM. For AC-RM, the PNR is increased compared to AC-CDM by about 6 dB but decreased compared to pure RM by the same amount. This is explained by the reduced pseudo-PNR generated, since only half as much samples get recovered.

4.4 MIMO SOFDM

The CS-based signal evaluation makes SOFDM perfect to be combined with RM to realize MIMO operation. Combinations with the various other CDM approaches from Sections 4.2 and 4.3 are conceivable and possible, but SOFDM and RM may profit most from each other, since the necessary CS recovery in RM and SOFDM may be merged. Through this, the recovery effort compared to SISO SOFDM gets slightly increased by the multi-channel treatment. In RM SOFDM, the undersampling of both get merged yielding the total undersampling $\delta_{\mathrm{cs}}{=}\delta_{\mathrm{cs}}^{\mathrm{SOFDM}}{\cdot}\delta_{\mathrm{cs}}^{\mathrm{RM}}$ being the product of both. Consequently, for radar R1 with $N_{\mathrm{tx}} = 4$ and an SOFDM undersampling of $\delta_{\mathrm{cs}}^{\mathrm{SOFDM}} = 1/4$ as in the measurements and analyses of Section 3.3, the total undersampling is $\delta_{\mathrm{cs}} = 1/16$. Therefore, it is expected that the recovery gets more challenging, and it is recommended to increase the number of iterations as suggested by the findings from Section 3.3.5.

To examine the performance of RM SOFDM, the measurement of the approaching vehicle in Fig. 4.5 of the RM evaluation is utilized. For this purpose, an SOFDM Tx pattern of $\delta_{\mathrm{cs}}^{\mathrm{SOFDM}}{=}1/4$ is additionally superimposed on the measured spectrogram before evaluation. Through this, the resulting *R*-*v*-image and the detection results become comparable. Figure 4.18 shows on the left the *R*-*v*-images of the RM dense measurement (from Fig. 4.5) and on the right the RM SOFDM measurement after the 2.5D-CAMP evaluation. For recovery of RM SOFDM, 40 iterations are performed. It shows that despite the high degree of undersampling, the scene gets restored quite well, despite the fact that in each channel only 25 % of the data compared to RM and only 6.25 % of the data compared to a dense SISO signal is available. The sidelobe emerging at about $(0.7\,\mathrm{m}, -5\,\mathrm{m/s})$ is an artifact that is probably caused by a non-ideality in the system, which gets identified and amplified by the recovery. Through the anew pseudo PNR the total PNR gets increased by another 4.1 dB compared to the dense RM OFDM measurement.

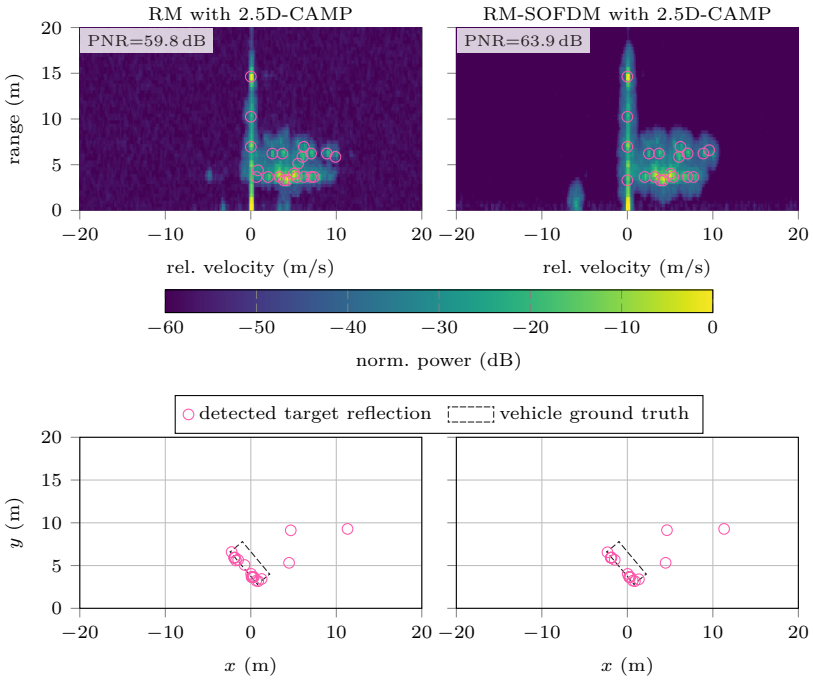


Fig. 4.18: Evaluation results of an RM SOFDM extended target measurement of an approaching vehicle. The measurement is generated from the original RM measurement of Fig. 4.5 through superposition with an SOFDM pattern. Left: Evaluation results for the dense RM reference measurement from Fig. 4.5. Right: Evaluation results for the RM SOFDM measurement with $\delta_{\mathrm{cs}}^{\mathrm{SOFDM}} = 1/4$. Top: The obtained R-v-images and CFAR detections. Bottom: x-y-representation after DoA estimation. The images are normalized to the strongest target reflection (building at $R = 14.3\,\mathrm{m}$).

4.5 Summary

OFDM offers time, frequency, and code diversity enabling a wide range of MIMO multiplexing strategies to be realized. The developed RM approach takes advantage of time and frequency diversity by randomly assigning each time-frequency element of the discrete modulation matrix to the different Tx channels. By recovering the thereby introduced gaps in the spectrogram of each Tx-Rx channel using CS methods, the fully occupied frame of each channel can be restored at the receiver, which increases the effective processing gain and suppresses sidelobes and artifacts caused by the random assignment. To this end, a 2.5D-CAMP approach based on 2D-CAMP is developed. RM is validated to achieve both the maximum unambiguous range and Doppler and thereby overcome the range impairment of IOFDM. Moreover, it achieves a higher PNR at the same total Tx power per OFDM symbol.

Because OFDM allows to configure the magnitudes and phases of each modulation symbol arbitrarily, code diversity offers an additional opportunity in OFDM waveform design. A major challenge in channel separation via codes is to achieve a high channel isolation between the Tx signals. The developed ZCZ-, AC-, and MRS-CDM approaches are especially suitable for OFDM radars. Measurements and simulations validate that the proposed strategies offer competitive alternatives to today's state-of-the-art IOFDM multiplexing strategy. Since the developed CDM methods do not require modifications or supplements to the conventional OFDM evaluation chain, they can be straightforwardly used on any digital MIMO OFDM radar system that uses a similar evaluation as described in Section 2.2. Thereby, it is also conceivable that the utilized multiplexing strategy of the next frame may be changed during operation, and the best suitable one may be chosen for the present situation, depending on the individual requirements and characteristics of the methods. Furthermore, it is shown that the limitations and advantages of two individual approaches may complement each other in a hybrid approach that enjoys the advantages of both while having fewer restrictions than the individual approaches alone.

In order to realize MIMO SOFDM, RM yields the most appropriate choice as they both utilize random patterns and CS-based evaluations that can be easily merged such that the evaluation effort gets only slightly increased in the MIMO SOFDM setting.

5 Robust Signal Processing and Coexistence of OFDM Radars and Traditional Automotive Radars

In the last decades, driven by the demand for driver assistance and safety systems, automotive radar systems are becoming more and more powerful and diverse, and new approaches are being developed [22], [23], [44]. At the same time, the number of radars in daily traffic increases every day, making the probability of interference more likely [1]. Thus, the topic of interference has recently been gaining more and more attention, especially since it is also to be expected that new digital modulation concepts become commercially available in the near future.

In the past, research on mutual interference and its countermeasures largely focused on FMCW and pulsed radar systems [22], [166]–[172], which are today's prevalent sensor types in automotive radar [1], [22]. With growing interest in new digital modulation concepts such as OFDM, the question arises as to how they behave in the likely event of interference and what losses and effects can occur and, if necessary, how they must be counteracted. In this chapter, the impact of fast-chirp FMCW radar interference on OFDM and SOFDM radar operation is investigated and countermeasures are proposed. The results have been partially reported in [118], [119], [173] by the author.

To date, few profound literature is available on OFDM radar interference. Among them, many deal with multi-user interference of OFDM based radar communication networks [13], [27], [37], [53], [174]–[177]. In [178], the impact of an FMCW radar transmitting slow ramps in the range of some milliseconds is investigated. The impact on the OFDM signal processing is derived and a frequency-domain interference detection based on symbol-wise CFAR detection is proposed. Affected subcarriers are removed, and their signal is restored using forward-backward linear prediction (FBLP). In [179], it is proposed to

Tab. 5.1: Chirp-sequence interferer signal properties.

parameter	interferer I1	interferer I2
bandwidth $\mathcal{B}_{\text{chirp}}$	2 GHz	2 GHz
up-ramp time T_{up}	89.92 µs	50 µs
down-ramp time T_{down}	–	5 µs
ramp repetition time T_{r2r}	119.92 µs	60 µs
carrier frequency f_{chirp}	76 GHz	75.5 GHz

replace this autoregressive prediction by CS methods, which also improves the signal-to-interference ratio (SIR). The impact and countermeasures in case of fast-chirp FMCW or chirp-sequence radars is investigated in [118], [119], [173] using measurements of up to two interferers. In [173] a simple interference power detection in the spectrogram using a local filter mask is proposed. Instead of zeroing the corrupted signal and thereby eliminating also the desire signal part of the samples, it is further proposed to only mitigate the amplitude of the corrupted samples. The developed concept is detailed in Section 5.4.2. In [118], a CS-based OFDM signal evaluation with inherent interference detection and mitigation suitable for interferers with low instantaneous bandwidth is presented. This so-called dual-CS approach is detailed in Section 5.4.4. Finally, in [119], the impact of FMCW or chirp-sequence interference on frequency agile OFDM radar concepts such as stepped OFDM [31] and SOFDM is investigated and suitable countermeasures are presented. The results for SOFDM are detailed in Section 5.2.

Throughout this chapter, the presented results are based on measurements using up to two different and independently operating interfering fast-chirp FMCW radars and a victim OFDM radar. The two interfering FMCW radars, denoted as I1 and I2, are radar prototypes with basic signal parameters as given in Table 5.1. Unless otherwise specified, these parameters are used in the following. Note that f_{chirp} is not the center frequency but the base frequency of the ramp. The victim OFDM radar is radar R2 from Table 2.1 on page 36. It has a larger bandwidth than radar R1, and is therefore exposed to higher risk and impact of interference. Example spectrograms of the FMCW and OFDM signals are sketched in Fig. 5.1. A photo from the victim OFDM radar's perspective and a sketch of the measurement setup from above in the anechoic chamber

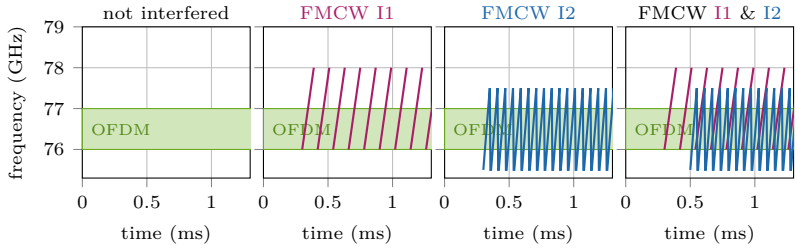


Fig. 5.1: Illustration of the examined basic signal configurations of the measurements using OFDM radar R2 with parametrization as in Table 2.1 and up to two interferer (I1 and I2, see Table 5.1).

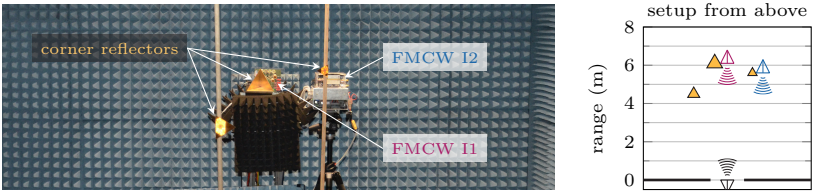
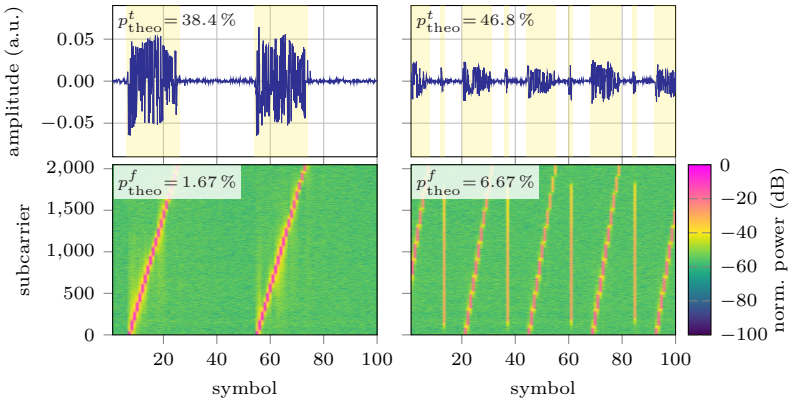


Fig. 5.2: Interference measurement setup. Left: photo of the setup from the OFDM radar's perspective. Right: sketch of the setup from above. The setup contains the victim OFDM radar R2 (▽), three corner reflectors (△), and the two interfering FMCW radars I1 (▽) and I2 (▽).

with the two interfering radars and three corner reflectors is shown in Fig. 5.2. The measured scene consists of three stationary targets at ranges 4.5 m, 5.6 m, and 6.1 m. Interferer I1 is at range 6.1 m and I2 at 5.6 m.

In this chapter, initially the impact of the FMCW interference on the individual processing stages of a dense OFDM and SOFDM radar is examined and evaluated in more detail in Sections 5.1 and 5.2, respectively. Based on these analyses, an interference detection method is developed in Section 5.3. In Section 5.4, four different interference mitigation methods are presented and analyzed that allow to remove the interference from the (S)OFDM measurements and recover the undisturbed *R-v*-image.



(a) Interfered by I1. **(b)** Interfered by I2.

Fig. 5.3: Interference measurements using OFDM radar R2 and interfering FMCW radars (a) I1 and (b) I2. The upper graphs show excerpts of the respective received time domain signals and the lower graphs excerpts of the corresponding spectrograms. In time domain, interfered time intervals are highlighted. The values p^t_{theo} (5.1) and p^f_{theo} (5.3) correspond to the relative number of interfered samples in the respective domain.

5.1 Impact of an FMCW Interference on the OFDM Radar Operation and Evaluation

The presence of disturbing incoherent FMCW signals within the signal frame of a victim OFDM radar has several implications on the different digital processing and evaluation stages that are analyzed in this section. Following the usual Rx processing chain of the OFDM measurement, the impact on the time domain signal, the spectrogram, and finally the *R*-*v*-image is examined.

Time Domain. Assuming that both the victim and interfering radars radiate approximately the same power, the received power of the interfering signal at the victim's receiver is considerably higher than the desired reflections of its own signal, since the path loss of the reflections is much higher [22]. After

sampling and filtering, samples affected by interference exhibit considerably higher amplitudes than unaffected ones. Both upper graphs in Fig. 5.3 show the time domain samples of the first 100 OFDM symbols of two measurements interfered by I1 and I2. Additional measurements, including scenarios where both interferers are active at the same time or where modified modulation settings are used for the interferers, are depicted in Appendix E on page 157. Comparing the time signals shows that the power impact from I1 is higher than from I2. This might be due to the fact that I1 is aimed directly at the victim sensor, while I2 is pointed slightly away from the victim's main beam. In addition, both the duration of contiguously interfered samples as well as the total number of affected samples differ. Both properties are a function of the victim's and interferers' signal parameters and are described by the relative number of interfered samples p^t_{theo} [119] in discrete-time domain, whose respective value is also given in the graph. Given L FMCW ramps are received within the OFDM measurement frame, its value is defined by

$$p^t_{\text{theo}} = L \frac{T_{\text{up}} + T_{\text{down}}}{M T_{\text{OFDM}}} \frac{\mathcal{B}_{\text{int}}}{\mathcal{B}_{\text{chirp}}} \,. \tag{5.1}$$

$\mathcal{B}_{\text{int}} \leq \mathcal{B}_{\text{chirp}}$ is the affected bandwidth, i.e., the amount of the OFDM bandwidth B that is actually interfered by the FMCW signal corresponding to the overlap of the operating bandwidths of the two radars. The largest relative interference p^t_{theo} by I1 and I2 on radar R2 is reached, when the interference continues throughout the measured frame, i.e. $L T_{\text{r2r}} \approx M T_{\text{OFDM}}$. This is achieved for $L_{\text{I1}} \approx 64$ and $L_{\text{I2}} = 128$ FMCW ramps and yields p^t_{theo} of 37.5 % and 45.8 %, respectively. In case of both I1 and I2 are active at the same time, see for instance the measurements in Fig. E.1 (b) in Appendix E, (5.1) is approximated by the expected value $\mathrm{E}[p^t_{\text{theo}}]$, which is numerically computed using the modulation parameters of the involved radars. To sum up, the relative interference in discrete time domain by a state-of-the-art FMCW interferer depends upon the modulation parametrization and is upper bound by the effective operational time of the interferer. In the worst case scenario, each sample might be impaired.

Spectrogram. In the spectrogram, the frequency diversity of the OFDM signal becomes apparent. The OFDM signal is wideband and its power is usually evenly spread over time and frequency. On the other hand, the entire instantaneously

radiated power of the FMCW radars gets compressed into a narrow band and therefore gets concentrated in only a few contiguous subcarriers per OFDM symbol. As a consequence, the magnitudes of these frequency components are comparably higher. This is observable on the lower graphs in Fig. 5.3. The number of affected contiguous interfered subcarriers of a single OFDM symbol for the up and down ramps are

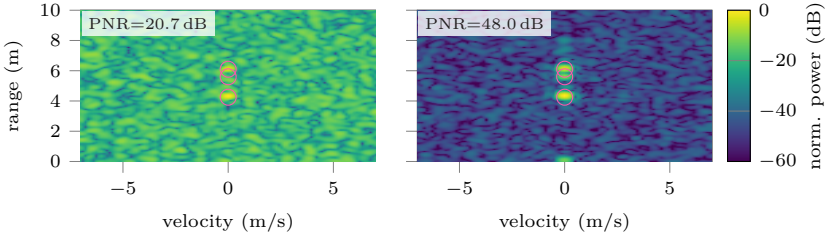
$$N_{\text{int,up/down}} = \frac{\mathcal{B}_{\text{chirp}}}{\Delta f} \frac{T}{T_{\text{up/down}}}\,, \tag{5.2}$$

respectively. With the given radar modulation parameters, it yields $N^{\text{I1}}_{\text{int,up}} \approx 89$ and $N^{\text{I2}}_{\text{int,up}} = 160$ for the up chirps of I1 and I2, respectively, and $N^{\text{I2}}_{\text{int,down}} = 1600$ for the down chirps of I2. Similar to p^t_{theo} (5.1) for the time domain, the relative interference in the spectrogram is described by the relative number of impaired coefficients defined by

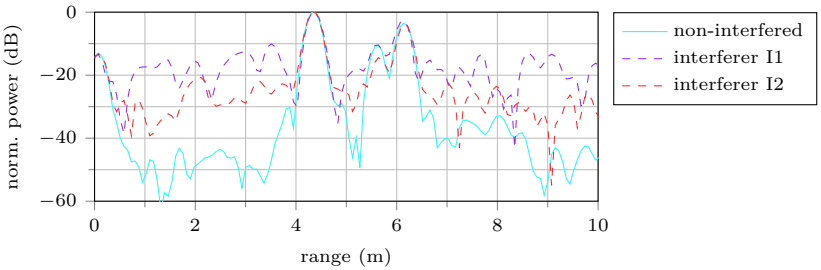
$$p^f_{\text{theo}} = L \frac{\mathcal{B}_{\text{int}}}{B} \frac{T}{M T_{\text{OFDM}}} (1 + \mathbb{I}_{T_{\text{down}}>0}) \tag{5.3}$$

for a single interferer. The factor in parentheses becomes either 2 or 1, depending on whether there is also a down chirp or not. Interestingly, p^f_{theo} largely depends on OFDM parameters. The theoretical maximum values for p^f_{theo} are 1.67 % and 6.67 % for I1 and I2, respectively. They are also given in the spectrograms of Fig. 5.3. Compared to the time domain values (p^t_{theo}), a significantly lower relative interference is obtained in the spectrogram. Moreover, due to the spectral compression, it always holds that $p^t_{\text{theo}} \leq p^f_{\text{theo}}$, where equality is achieved if the slope $\mathcal{B}_{\text{chirp}}/T_{\text{up}}$ of the chirp equals or exceeds B/T. However, this very unlikely, since this would require an FMCW slope of at least 1 GHz per 2.5 µs, which is not achievable by today's state-of-the-art radars. Furthermore, a large p^t_{theo} does not necessarily lead to a large p^f_{theo}, as can be observed by comparing the measurement of Fig. 5.3 (a) with that of Fig. E.1 (a). Due to the smaller utilized signal bandwidth, the latter has twice the value of p^t_{theo} in the time domain but only about half of p^f_{theo} in the spectrogram compared to the former.

Image Domain. The image domain is obtained via the 2D-(I)DFT of the spectrogram. In this step, the target reflections of the own radar signal are coherently summed up and compressed into a few range-Doppler bins, while



(a) Interfered measurement. **(b)** Non-interfered measurement.



(c) Comparison of range profiles of the interfered and non-interfered measurements.

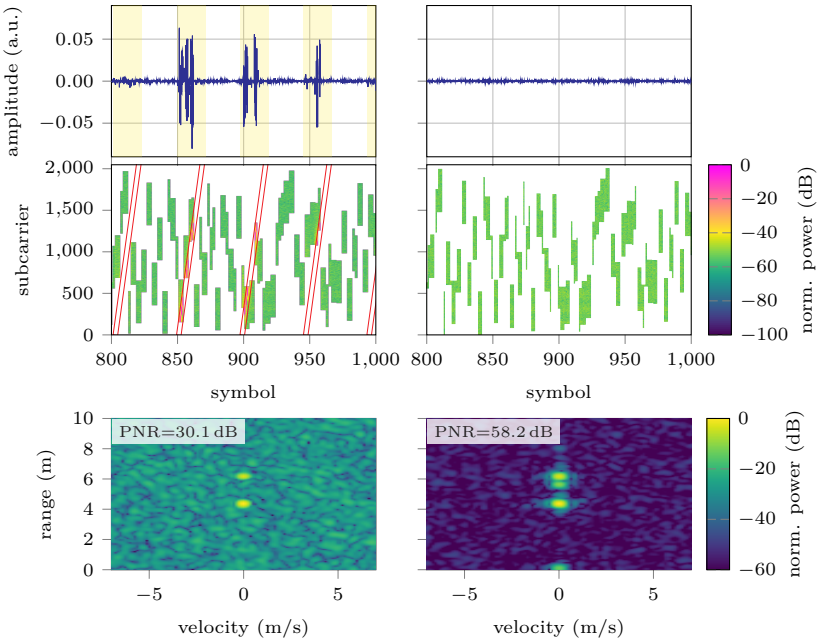
Fig. 5.4: Radar images and PNRs of (a) the interfered measurement from Fig. 5.3 (a), and (b) a non-interfered measurement of the same scene. The ground truth target positions are marked by ○. In (c), the range profiles of all measurements from Fig. 5.3 and of the non-interfered one are depcited. The range profiles correspond to the $v = 0\,\mathrm{m/s}$ cut of the R-v-images. All curves and images are normalized to the strongest target.

decorrelated noise and interference are evenly spread over the obtained R-v-image. The latter was first reported in [13] and holds for any interfering signal that is both incoherent and decorrelated to the OFDM signal or simply non-deterministic. Through this, the interference contributes to a potential rise of the noise level but does not cause ghost targets, since it does not add up during evaluation. The relative interference in the image domain is therefore 100 %. In Fig. 5.4 (a), the radar image and corresponding PNR of the measurement from Fig. 5.3 (a) is depicted. For comparison, Fig. 5.4 (b) shows a non-interfered

measurement of the same scene. In addition, the obtained range profiles (zero-Doppler cut of the R-v-images) of the non-interfered and the two interfered measurements are shown in Fig. 5.4. In both interfered measurements, a notable decrease of the PNR of about 27 dB and 18 dB for I1 and I2, respectively, is observable. Moreover, in case of interference, the weak target at 5.6 m is hardly distinguishable from clutter and artifacts anymore.

5.2 Impact of Interference on SOFDM

The essential impact of an FMCW interferer on an SOFDM victim radar is identical to that of the dense OFDM [119] discussed in Section 5.1. So, distinct FMCW ramps are observable in the spectrogram, while the noise level gets increased in the R-v-image, if no countermeasures are taken. In Fig. 5.5, excerpts of the different processing domains of both an interfered and a non-interfered SOFDM measurement are depicted. In both measurements, the identical sparse Tx pattern was used. In the discrete-time signals shown in the top graphs, the time intervals during which the FMCW signal crosses the virtual wideband frame are highlighted. While for an OFDM signal with a dense spectrum occupancy as in Section 5.1, the interference occurs in the entire highlighted interval, in case of SOFDM only parts of it are actually affected. For comparison, the relative measured interference here is only p^t_{meas}=10 %, while 37.5 % are expected in the dense OFDM case. The reason for this becomes visible in the spectrogram in the middle graph. Due to the pattern, only parts of the chirps are collected by SOFDM, as if cut out by the pattern template. The true chirps within the virtually covered bandwidth B are therefore framed by the red boxes in the spectrogram to make the interfering signal recognizable. At first glance, it appears as if the amount of interference in the spectrogram is less for SOFDM, but this is only partly true. While the absolute collected interfering energy throughout the frame is less than in the dense OFDM due to the pattern, the expected relative amount of interfered samples remains the same. The reason is that SOFDM imitates random subsampling of the equivalent dense signal frame. But when randomly sampling from a certain distribution, eventually the same distribution is to be expected in the resulting subset. Hence, p^f_{theo} is about the same for OFDM and SOFDM. To this end, the true measured interference of Fig. 5.5 (a) is determined and yields 1.73 %. This value agrees well with the



(a) Interfered by I1. **(b)** Not interfered.

Fig. 5.5: Measurement of a victim SOFDM (δ_{cs}=1/4) radar R2 (a) interfered by interferer I1 and (b) non-interfered. From top to bottom, the graphs show the time signals, the spectrograms, and *R*-*v*-images after 2D-CAMP recovery. In time domain, intervals in which the FMCW signal crosses the virtual wideband frame are highlighted. In the spectrogram, the true chirps are framed red.

theoretically expected interference for the dense signal, which is 1.67 %, However, suppose the victim radar is capable of some kind of perception, so that it can predict the time-frequency behavior of the periodic and structured interfering signal. While dense OFDM is hardly able to avoid FMCW interference spectrally or temporally without completely changing its operational frequency or inserting gaps in the spectrogram, an SOFDM radar capable of perception would be able to entirely avoid predictable interferences in the operational time-frequency

range by simply adjusting its Tx pattern accordingly.

Ignoring the FMCW impact and evaluating the SOFDM signal using the 2D-CAMP processing from Chapter 3.2.1, the radar images in the lower graphs of Fig. 5.5 are obtained. A significant increase of the noise level is observable in the interfered case where the PNR decreases from 58.2 dB in the non-interfered measurement to about 30.1 dB in the interfered one. This is a similar drop as in the dense OFDM case.

5.3 Interference Detection

As illustrated in Sections 5.1 and 5.2, for both dense OFDM and SOFDM the FMCW interference gets most compressed in the spectrogram such that the relative interference is minimal in this domain. At the same time, the power spectral density of the OFDM signal is flat in the spectrogram. As a consequence, the power difference between interfered and non-interfered coefficients is maximal in this domain. Therefore, it is proposed to identify interfered samples via power detection in the spectrogram. One possible approach is using either a symbol- [178] or subcarrier-wise [173] CFAR, which yields a local threshold. However, these approaches are only suitable for dense OFDM spectrograms and interference impacts affecting only a limited number of contiguous subcarriers or OFDM symbols. Hence, in case of multiple interferer, see for instance Fig. E.1 (b) on page 158, or in case of SOFDM, the local CFAR estimation becomes unreliable or even fails. Therefore, a different approach is developed that derives a single global threshold from all elements in the spectrogram [119]. Unlike the local threshold, this global threshold is less complex to determine, independent of the distribution of interfered elements or of the spectral shape of the interfering signal, e.g. chirp, continuous-wave (CW), pulsed, or broadband. Moreover, it does not require a dense OFDM spectrogram, making it applicable to SOFDM as well.

The approach is based on the observation that the majority of coefficients $\mathcal{D}_{mn}$ (2.16) or $\mathcal{D}^{\boxplus}_{mn}$ (3.7) of the spectrograms (2.15) or (3.6), respectively, is non-interfered. In addition, the desired (S)OFDM spectrogram can be considered approximately complex white Gaussian with zero mean and standard deviation $\sigma_{\mathcal{D}}$. Therefore, the magnitudes are expected to be Rayleigh distributed with mode $\sigma_{\mathcal{D}}/\sqrt{2}$. If the true $\sigma_{\mathcal{D}}$ is known, interfered samples are easily identified by

their differing magnitudes, i.e., through power detection. However, in general $\sigma_{\mathcal{D}}$ of the Rx spectrogram is not known and is also subject to fluctuations. Hence, instead an estimate

$$\hat{\sigma}_{\mathcal{D}} = \frac{\operatorname{median}\left(|\boldsymbol{\mathcal{D}}_{\Omega_P}|\right)}{\sqrt{\ln 2}} \tag{5.4}$$

is obtained from the the measured Rx spectrogram $\boldsymbol{\mathcal{D}}_{\Omega_P}$ similar to the median estimation of the soft-threshold within the 2D-CAMP in Section 3.2. Here, $\boldsymbol{\mathcal{D}}_{\Omega_P}$ denotes occupied spectrogram containing only the coefficients of the set

$$\Omega_P = \left\{(m,n) \mid \mathbb{I}_{P_{mn}=1}\right\} \tag{5.5}$$

specified by the Tx pattern. For the dense OFDM define $\boldsymbol{P} = \mathbf{1}$ and $\boldsymbol{\mathcal{D}} = \boldsymbol{\mathcal{D}}_{\Omega_P}$. The approach is robust against outliers, is invariant to the distribution of interfered coefficients, and as long as the majority of the coefficients are undisturbed, the obtained result is reliable. With increasing number of affected coefficients, it is further expected that (5.4) tends to overestimate the true value. In case the OFDM amplitudes show a frequency variant behavior, for instance caused by non-ideal components at the receiver, the amplitudes must be calibrated prior to the median estimation. Otherwise, $\hat{\sigma}_{\mathcal{D}}$ (5.4) is biased and non-interfered frequency components that experienced higher amplifications are at higher risk of being erroneously detected, while interfered samples with lower amplification might get missed. Therefore, before interference detection, each of the investigated measurements is calibrated using the a priori measured frequency-dependent amplitude behavior of the system.

Finally, the threshold Λ is given by the product

$$\Lambda = \Upsilon \hat{\sigma}_{\mathcal{D}}\,, \tag{5.6}$$

with scaling factor $\Upsilon \geq 1$, similar to the threshold in 2D-CAMP. Each coefficent $|\mathcal{D}_{mn}| > \Lambda$ or $|\mathcal{D}^{\boxplus}_{mn}| > \Lambda$ exceeding the threshold is considered interfered. The scaling Υ accounts both for signal magnitude fluctuations and influences the sensitivity of the detection. It should therefore be chosen in such a way that all corrupted samples are detected, while the number of false detections of non-interfered samples is low. The relation of the false detection probability and Υ for the median estimate (5.4) is given by (3.17) on page 50, assuming that the magnitudes are truly Rayleigh distributed. In interference detection,

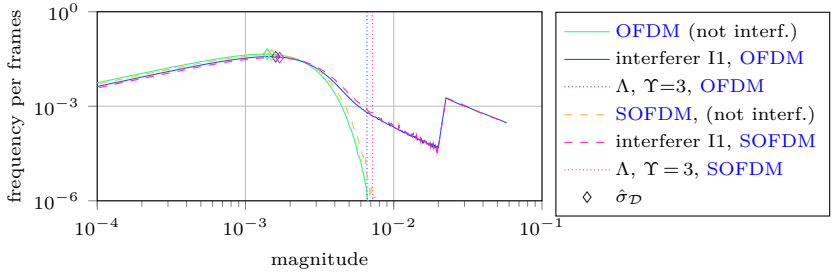
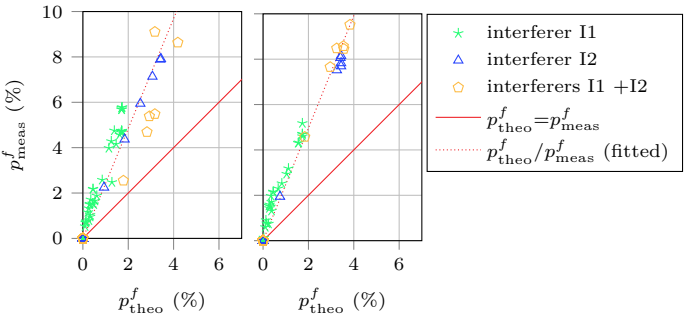


Fig. 5.6: Magnitude distribution, estimated standard deviation $\hat{\sigma}_{\mathcal{D}}$ (5.4), and detection threshold Λ (5.6) of the spectrogram elements of an interfered (I1, entire frame) and non-interfered dense OFDM and SOFDM measurement.

the aim is to identify as many disturbed elements as possible. In return, it is tolerated that some undisturbed samples may also exceed the threshold value. Therefore, a scaling of $\Upsilon = 3$ is suggested providing a theoretical FAR of 0.012%. With this choice, the actual FAR obtained with non-interfered measurements is on average 0.012% and 0.032 % for dense OFDM and SOFDM, respectively. This agrees well with the predicted value. Increasing Υ worsens the sensitivity of the detection and weaker or farther distant interferers might get missed. In Fig. 5.6, the magnitude distributions of the spectrogram coefficients of non-interfered and interfered OFDM and SOFDM measurements are depicted along with the determined corresponding Λ with $\Upsilon = 3$. For both the OFDM and SOFDM measurement, the magnitude distribution shows the typical shape of a Rayleigh density in a log-log-graph, whereas the magnitudes of the interfered measurement only do so up to about the mode $\sigma_{\mathcal{D}}/\sqrt{2}$ of the distribution. Beyond this point, the expected density gets more and more masked by the density of the interfered coefficients. The determined thresholds Λ separate these areas well.

In Fig. 5.7, the ratio of actually measured and expected relative interferences p^f_{meas} and p^f_{theo}, respectively, are shown for the collected interfered OFDM and SOFDM measurements. Since in each measurement, the ground truth number of ramps and the start and end points of each interference is known, the theoretical value p^f_{theo} is determined with (5.3), in case of interference by either I1 ($\star$) or



(a) OFDM **(b)** SOFDM

Fig. 5.7: Comparison of predicted and actually detected relative interferences, p^f_{meas} and p^f_{theo}, respectively, of several measurements using radar R2 and interferers I1 and I2. Adapted from [119] © 2021 IEEE.

I2 (△). In case both I1 and I2 (⬠) are active, the value is determined analytically. The measured value p^f_{meas} is the ratio of elements identified as interfered and the total number of occupied elements in the spectrogram. It can be observed that in all measurements more samples are identified as interfered than predicted by p^f_{theo}. The overestimation factor is about 2.4 for both signals. This is because p^f_{theo} (5.3) assumes perfect compression and neglects sidelobes and smearing effects in the vicinity of the interference in the spectrogram. However, these are recognized as disturbed in the detection, due to their increased magnitude.

5.4 Interference Mitigation

Since the FMCW interference leads to an increase of the noise level in the *R-v*-image and therefore reduced detection performance, especially weak targets are at risk of being missed. In this section, four interference mitigation methods of different complexity are developed and discussed. The first three approaches in Sections 5.4.1 to 5.4.3 pursue two-stage approaches, where the first stage always is the *detection* as described in Section 5.3. The actual interference mitigation takes place in the second stage using the strategies *remove* [119], *mitigate* [173], and *recover* [119]. In addition to the common two-stage approaches, in Section 5.4.4,

a single-stage interference mitigation method is presented that enables an interference-robust signal evaluation that does not require prior knowledge about the presence of an interference nor about its spectral shape [118]. In Section 5.4.5, the developed approaches are evaluated and compared.

5.4.1 Detect and Remove: Zeroing

Zeroing is the most straightforward strategy. Any coefficient found to be interfered is eliminated from the spectrogram via

$$\mathcal{D}_{mn} = \begin{cases} 0, & \text{if } |\mathcal{D}_{mn}| \geq \Lambda \\ \mathcal{D}_{mn}, & \text{otherwise,} \end{cases} \tag{5.7}$$

which sets all $\mathcal{D}_{mn}$ whose magnitude exceed Λ to zero. Through this, the interfering power of the disturbing signal gets, ideally entirely, removed. Next, the signal is evaluated as usual. If the interfering signal is removed completely, the noise level reduces significantly to about the level of the system noise. Along with the interference, also a part of the useful signal gets eliminated. The target peaks therefore are lowered by about the factor $(1-p^f_{\text{meas}})$. However, this loss is less than 1 dB for $p^f_{\text{meas}} < 10\,\%$. Zeroing or canceling is also found in FMCW literature [166], [170], [180], [181], where it is reported that introducing gaps in the signal may lead to ringing artifacts in the radar image. Since $N_{\text{int,up/down}} \ll N$ and, furthermore, not every OFDM symbol is disturbed, peak broadening or ringing effects are negligible here. Zeroing is especially suitable for dense OFDM signals with small p^f_{meas}, i.e. FMCW interference. In case of SOFDM, it is suggested to include the zeroed coefficients in the CS recovery [119] leading to the mitigation approach discussed in Section 5.4.3.

5.4.2 Detect and Mitigate: Leveling

Instead of eliminating interfered coefficients, the developed *leveling* approach [173] only scales the signal amplitude to the estimated level $\hat{\sigma}_{\mathcal{D}}$ via

$$\mathcal{D}_{mn} = \begin{cases} \mathcal{D}_{mn} \frac{\hat{\sigma}_{\mathcal{D}}}{|\mathcal{D}_{mn}|}, & \text{if } |\mathcal{D}_{mn}| \geq \Lambda \\ \mathcal{D}_{mn}, & \text{otherwise,} \end{cases} \tag{5.8}$$

while preserving any phase information of the elements. Through this, the interference power gets reduced, and the desired signal contribution of each sample persists. The approach is suitable for both OFDM and SOFDM.

5.4.3 Detect and Recover: CS Signal Recovery

In the *detect-and-recover* method, the interfered samples get first eliminated via zeroing (5.7) and afterwards recovered. Through this, the interference is removed, and ideally the non-interfered spectrogram is restored. The detect-and-recover principle is also known as an effective method of interference mitigation for FMCW radars [22], [166], [182], where signal recovery is achieved by linear prediction methods [166] or sparse methods [182]. A similar idea for OFDM is suggested by [178], where OFDM-symbol-wise FBLP is applied to fill the gaps introduced by zeroing. The idea was taken up by [179], that replaced the FBLP by a CS recovery. In [119], a 2D CS recovery for interfered SOFDM measurements is presented by the author. FBLP is rather complex and costly as each gap has to be treated individually, especially in case of multiple interferers, where the spectrum becomes quite riddled with gaps after zeroing. CS on the other hand offers the possibility to recover all of these gaps at once. Moreover, SOFDM allows zeroed coefficients to be merged with the sparse pattern and thereby to be also considered in the recovery, as if they had not been measured in the first place. It is therefore proposed to use 2D-CAMP to recover the spectrogram. To this end, the binary Tx pattern[1] $\boldsymbol{P}$ is updated such that

$$P_{mn} = \begin{cases} 0, & \text{if } |\mathcal{D}_{mn}| \geq \Lambda \\ P_{mn}, & \text{otherwise} \end{cases} \tag{5.9}$$

encompasses also the zeroed elements and indicates, whether an element is missing and has to be recovered or not, no matter if is was zeroed or not occupied. With this, the incomplete spectrogram $\boldsymbol{\mathcal{D}}^{\boxplus}$ becomes

$$\boldsymbol{\mathcal{D}}^{\boxplus} = \boldsymbol{P} \circ \boldsymbol{\mathcal{D}} = \boldsymbol{P} \circ \boldsymbol{y} \circ \overline{\boldsymbol{d}} \tag{5.10}$$

and serves as the input to the 2D-CAMP algorithm of Section 3.2.

The approach is particularly suitable for SOFDM. In case of dense OFDM

[1] For dense OFDM the initial transmission pattern is $\boldsymbol{P} = \boldsymbol{1}$.

and $p^f_{\text{meas}} < 10\,\%$, the expected improvement compared to simple zeroing is in the range of a few decibels and therefore may not justify the recovery effort.

5.4.4 Single-Stage Recovery: Dual-CS

The previous methods follow a two-stage detect-and-mitigate principle. In the *dual-CS* approach [118], on the other hand, both steps are fused. Since there is no distinct detection, the algorithm does not know whether there is interference and if so, which elements are affected. The approach is therefore not an interference countermeasure, but an interference-robust processing method enabling robust radar sensing regardless of whether external signals are interfering. The approach is based on the property that the desired and interfering signals are sparse in different domains. A superposition of such signals can be again separated using a variation of the morphological component analysis and CS [140], [141]. Based on this idea, a dual version of SALSA was proposed to separate CW [140] and FMCW [141] disturbances from an FMCW receive signal. However, the case of OFDM is somewhat different due to its different signal properties and processing domains. In [118], the idea is transferred to OFDM radar and extended to 2D CS by the author. To this end, consider the noisy and interfered spectrogram after inversions of the modulation

$$\tilde{\boldsymbol{\mathcal{D}}} = \boldsymbol{P} \circ \left(\boldsymbol{\mathcal{D}} + (\boldsymbol{W} + \boldsymbol{Z}) \circ \overline{\boldsymbol{d}} \right), \tag{5.11}$$

where $\boldsymbol{\mathcal{D}}$ is the desired dense demodulated OFDM spectrogram (2.15), $\boldsymbol{d}$ the modulation symbol matrix, $\boldsymbol{W}$ the noise contribution whose elements are assumed to be white Gaussian, $\boldsymbol{Z}$ the interference, and $\boldsymbol{P}$ the binary Tx pattern. Carrying out the usual 2D-(I)DFT evaluation, (2.30) gives the noisy and interfered radar image

$$\tilde{\boldsymbol{\mathcal{I}}} = \left(\boldsymbol{U}(\boldsymbol{\mathcal{D}} + (\boldsymbol{W} + \boldsymbol{Z}) \circ \overline{\boldsymbol{d}})\boldsymbol{U}^{\mathsf{H}} \right) \circledast \boldsymbol{U}\boldsymbol{P}\boldsymbol{U}^{\mathsf{H}} = \left(\boldsymbol{\mathcal{I}} + \boldsymbol{\mathcal{W}} + \boldsymbol{\mathcal{Z}} \right) \circledast \boldsymbol{U}\boldsymbol{P}\boldsymbol{U}^{\mathsf{H}} \tag{5.12}$$

with the desired radar image $\boldsymbol{\mathcal{I}}$ (2.30), and $\boldsymbol{\mathcal{W}}$ and $\boldsymbol{\mathcal{Z}}$ the 2D-(I)DFTs of the demodulated noise and interference contributions, respectively. In case of dense OFDM, $\boldsymbol{P}$ is a matrix of ones and the equation simplifies to $\tilde{\boldsymbol{\mathcal{I}}} = \boldsymbol{\mathcal{I}} + \boldsymbol{\mathcal{W}} + \boldsymbol{\mathcal{Z}}$. Furthermore, by analyzing the range IDFT part of the noise and interference contributions in (5.12), i.e. $\left((\boldsymbol{W} + \boldsymbol{Z}) \circ \overline{\boldsymbol{d}} \right) \boldsymbol{U}^{\mathsf{H}}$, the decorrelation of these parts in the radar image can be shown. Just like for the ITCT in CDM MIMO

of Section 4.2 (equations (4.10) to (4.12) and Appendix B), it can be shown that the above term eventually yields a circular convolution of the complex conjugate of the discrete time OFDM Tx signal (2.3) and the sampled discrete time noise and interference contribution. Since in general, these time signals are independent and decorrelated, their power gets spread.

Now suppose, there exists a transform or basis $\boldsymbol{\Phi} \neq \boldsymbol{U}$ such that $\boldsymbol{\Phi}(\boldsymbol{Z} \circ \overline{\boldsymbol{d}})$ is sparse but $\boldsymbol{\Phi}\boldsymbol{\mathcal{D}}$ is not. This is the essential requirement for dual-CS that allows both signals to be separated by identifying their individual support in their respective different bases. Hence, an appropriate sparse basis of the FMCW signal has to be identified. As illustrated in Section 5.1, the FMCW signal gets most compressed in the spectrogram. Moreover, both $\boldsymbol{Z}$ and $\boldsymbol{Z} \circ \overline{\boldsymbol{d}}$ are sparse with sparsity $\varsigma_{\text{int}} = p_{\text{theo}}^{f} \cdot MN_s$, whereas $\boldsymbol{\mathcal{D}}$ is flat and dense. On the other hand, as exploited in SOFDM, the measured OFDM signal is sparse in the discrete 2D Fourier basis, i.e. the radar image, where the interference signal is decorrelated and dense. Hence, both signals are separable using a dual-CS approach. The developed dual-2D-CAMP implementation [118] utilizes a 2D-CAMP as a basis. Eventually, the dual-2D-CAMP is given by the iterative algorithm

$$\tilde{\boldsymbol{X}}^{[k]} = \boldsymbol{U}\boldsymbol{E}^{[k-1]}\boldsymbol{U}^{\mathsf{H}} + \hat{\boldsymbol{X}}^{[k-1]} \tag{5.13a}$$

$$\tilde{\boldsymbol{X}}_{\text{int}}^{[k]} = \boldsymbol{\Phi}\boldsymbol{E}^{[k-1]} + \hat{\boldsymbol{X}}_{\text{int}}^{[k-1]} \tag{5.13b}$$

$$\hat{\boldsymbol{X}}^{[k]} = \text{soft}\left(\tilde{\boldsymbol{X}}^{[k]}; \Upsilon\hat{\boldsymbol{\sigma}}^{[k]}\right) \tag{5.13c}$$

$$\hat{\boldsymbol{X}}_{\text{int}}^{[k]} = \text{soft}\left(\tilde{\boldsymbol{X}}_{\text{int}}^{[k]}; \Upsilon_{\text{int}}\hat{\sigma}_{\text{int}}^{[k]}\right) \tag{5.13d}$$

$$\boldsymbol{E}^{[k]} = \tilde{\boldsymbol{\mathcal{D}}} - \boldsymbol{P} \circ \left(\boldsymbol{U}^{\mathsf{H}}\hat{\boldsymbol{X}}^{[k-1]}\boldsymbol{U} + \boldsymbol{\Phi}^{\mathsf{H}}\hat{\boldsymbol{X}}_{\text{int}}^{[k]}\right) + \frac{\|\hat{\boldsymbol{X}}^{[k]}\|_0}{MN_s}\boldsymbol{E}^{[k-1]}\,. \tag{5.13e}$$

It basically consist of two intertwined and partly merged instances of two 2D-CAMP ones. Similar to 2D-CAMP, the dual algorithm is initialized with the residual $\boldsymbol{E}^{[0]} = \tilde{\boldsymbol{\mathcal{D}}}$ and the initial sparse estimates $\hat{\boldsymbol{X}}^{[0]} = \hat{\boldsymbol{X}}_{\text{int}}^{[0]} = \boldsymbol{0}$, one for the desired signal and one for the interference. In each iteration, first, noisy estimates of the desired and interfered signals are determined in their respective sparse domains via (5.13a) and (5.13b). Note that this requires two distinct bases. Since in the considered application the spectrogram is the sparse basis of the FMCW signal, the transform $\boldsymbol{\Phi}$ equals an identity matrix and may be omitted in the above implementation. Next, in (5.13c) and (5.13d), the sparse

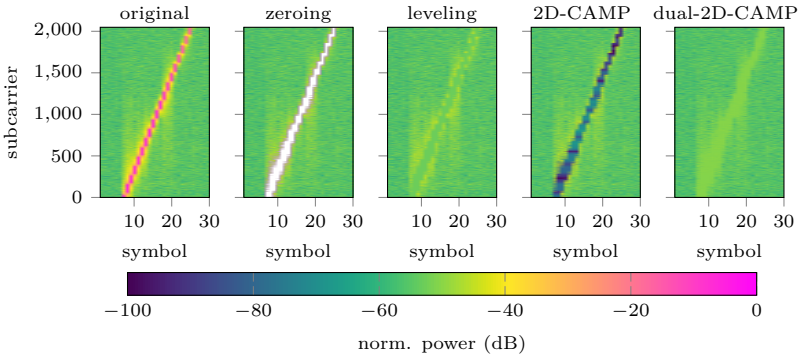


Fig. 5.8: Comparison of the different interference mitigation results in the spectrogram for the interfered dense OFDM measurement from Fig. 5.3 (a). The spectrogram of the original measurement without interference mitigation is shown in the left-most figure. The figures show a magnification of the first interference ramp. White spaces in the zeroing case indicate eliminated elements.

estimates are determined using soft-thresholding for both signals. For the desired part $\tilde{\boldsymbol{X}}^{[k]}$, the threshold step (5.13c) is identical to that in Section 3.2.1. On the other hand, the threshold step for the interference part $\tilde{\boldsymbol{X}}_{\text{int}}^{[k]}$ is derived from the detection in Section 5.3, and $\hat{\sigma}_{\text{int}}^{[k]}$ is obtained from the median estimate (5.4). It is recommended to use a small scaling factor $1 \leq \Upsilon_{\text{int}} \ll \Upsilon$ in order to capture the entire interference. Furthermore, it is not critical to collect small parts of the noise or the desired signal in the interference part in the dual approach. Finally, in step (5.13e), the two branches are brought together again in a common residual. After K iterations, both a noisy estimate of the desired signal $\boldsymbol{U}\boldsymbol{E}^{[K]}\boldsymbol{U}^{\mathsf{H}} + \hat{\boldsymbol{X}}^{[K]}$ and an estimate of the interference part $\hat{\boldsymbol{X}}_{\text{int}}^{[K]}$ are reached. The residual signal is solely counted towards the desired signal, since it is considered to contain the system noise and potentially missed weak signal. However, it may also be shared between both signal parts [118], but this leads to an artificial lowering of the pseudo PNR.

5.4.5 Evaluation and Comparison

In this section, the developed interference countermeasures are evaluated and compared. First, the spectrograms after applying zeroing, leveling, 2D-CAMP recovery, and dual-2D-CAMP recovery to an interfered dense OFDM are analyzed. The obtained results for the interfered dense OFDM measurement example of Fig. 5.3 (a) are shown in Fig. 5.8. For better visualization, only the first interfering ramp is depicted. Compared to the original spectrogram before mitigation, with zeroing, distinct gaps (white areas) are introduced. Moreover, the gaps approximate the shape of a ramp indicating that the detection has properly identified the disturbance. Applying leveling, the magnitudes of these elements are aligned with those of the non-interfered ones. In contrast, the 2D-CAMP fills the introduced gaps by the recovered signal, where it shows that the magnitude of the recovered and desired signal is notably lower than the noise in the spectrogram. Finally, in dual-2D-CAMP, only the interference gets separated and thereby removed from the spectrogram, but most of the noise contribution remains. While the two-stage approaches only change the elements of the spectrogram detected in the first stage, the dual-2D-CAMP approach also changes other elements, so that, for instance, the spectrogram is slightly smoothed, since noise artifacts are also removed. In addition, it is the only approach that achieves to remove the smearing of the interference along the frequency components. With the simple threshold-based detection, these elements are not detectable without significantly increasing the false detection rate.

The spectrograms of the SOFDM measurements from Fig. 5.5 (a) after 2D-CAMP and dual-2D-CAMP interference mitigation are shown in Fig. 5.9. Detection and mitigation via leveling is not considered, because there is no additional value in keeping few disturbed samples when 2D-CAMP recovery is applied anyway. In both the 2D-CAMP and dual-2D-CAMP results, the major part of the signal missing due to undersampling is recovered using the estimated signal support. In the spectrogram, the support translates into distinct sine waves that spread out in both the subcarriers and time dimension. The scene contains only static targets, therefore waves are only observable along the subcarriers and the Doppler dependent frequency along the time dimension is zero. Comparing the recovery results, a distinct difference of 2D-CAMP and dual-2D-CAMP is observable for the regions of the spectrogram where

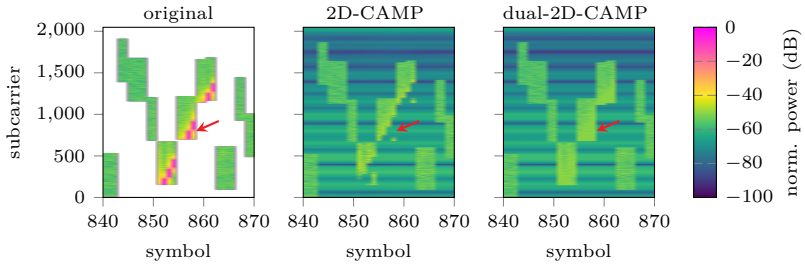


Fig. 5.9: Comparison of the 2D-CAMP and dual-2D-CAMP interference mitigation results in the spectrogram for the interfered SOFDM measurement from Fig. 5.5 (a). The figures show a magnification of one interference ramp from symbol 840 to symbol 870. The spectrogram of the original measurement without interference mitigation is shown in the left-most figure. The red arrow indicates a region where the results of the two approaches significantly differ.

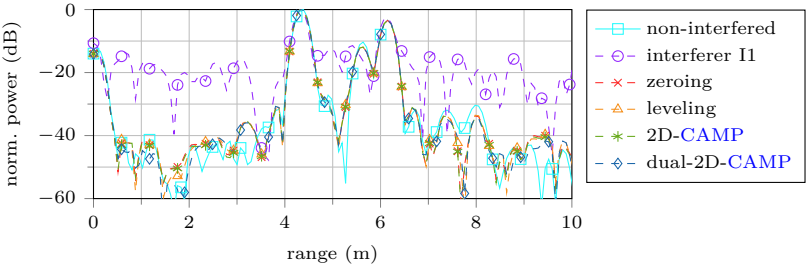
Tab. 5.2: Comparison of average achieved PNRs in the R-v-image of different mitigation approaches applied to several interfered measurements.

		OFDM	SOFDM ($\delta_{\text{cs}} = 1/4$)
	non-interfered	44.0 dB	55.6 dB†
interfered	without mitigation	22.0 dB	32.1 dB†
	zeroing	43.5 dB	–
	leveling	43.4 dB	54.2 dB†
	FBLP [149]	43.3 dB	54.0 dB†
	2D-CAMP	44.6 dB	54.7 dB†
	dual-2D-CAMP	44.3 dB	55.3 dB

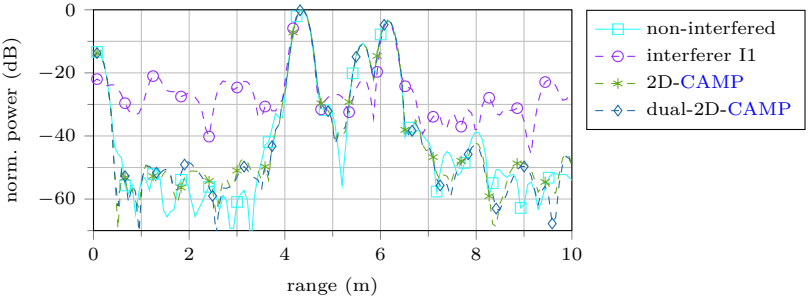
† with 2D-CAMP evaluation

interference emerges and is detected. In Fig. 5.9, such a region is exemplarily indicated by the red arrow. In 2D-CAMP, the elements of these regions are first eliminated and then recovered and are therefore noiseless. Whereas in dual-2D-CAMP, only their interference is removed.

Performing 2D-(I)DFT evaluation on the recovered (S)OFDM spectrograms finally gives the undisturbed R-v-images. The corresponding range profiles along the static zero-Doppler bins of the images are depicted in Fig. 5.10.



(a) Dense OFDM.



(b) SOFDM. Adapted from [118] © 2020 IEEE.

Fig. 5.10: Range profiles (v=0 m/s cut of the R-v-images) of (a) dense OFDM and (b) SOFDM measurements after interference mitigation.

It shows that all approaches succeed in eliminating the severe impact of the interference and are able to uncover the target reflections. Note in particular the middle target, which was not visible in the disturbed measurements at all, becomes clearly discernible after mitigation. In Table 5.2, the average achieved PNRs of non-interfered, interfered, and restored R-v-images are given. Since all mitigation methods succeed in interference mitigation, the differences in PNR are small. In the dense OFDM case, the achieved PNR after applying zeroing and leveling is about 0.5 dB less than the average of non-interfered measurements. The reason is that up to 6 % of the samples in the spectrogram are eliminated, which reduces the compression gain of the 2D-(I)DFT. The

same is observable for the leveling method, since the phases are also disturbed affecting the compression. In contrast, the opposite is observed with 2D-CAMP that achieves an improvement of about 0.5 dB. For each element detected, in a sense, only the noise and interference are removed, leaving only the recovered signal. This leads to an improvement similar in magnitude to the expected deterioration upon removal. Since in dual-2D-CAMP, the noise is only smoothed but not removed, the total improvement is smaller. In case of interference of SOFDM, 2D-CAMP and dual-2D-CAMP achieve the best PNR, which comes close to the non-interfered case. Leveling or FBLP, which do not include the interfered samples in the CS recovery, are about 1 dB worse.

To sum up, the developed mitigation methods achieve to eliminate the interference successfully and enable radar performance similar to the non-interfered case. Zeroing and leveling require less effort and are less complex than the CS-based approaches. In case of only few interfered elements in the spectrogram, for instance in case of a single FMCW interferer, these methods are appropriate. With increasing number of affected elements, the loss but also the recovery gain of the CS-based methods increase. For instance, with 30 % disturbed elements, the compression loss of zeroing is about 1.5 dB, whereas the recovery gain of 2D-CAMP is also about 1.5 dB compared to an equivalent non-interfered measurement. As a consequence, 2D-CAMP is about 3 dB better than zeroing in this case. Therefore, with increasing amount of interference, for instance in case of multiple FMCW interferers or other more broadband interferers, the additional effort of CS becomes worthwhile. Furthermore, instead of applying specific interference countermeasures in the event of interference, the signal evaluation itself may be adapted to be more robust in the first place. The dual-2D-CAMP approach enables signal evaluation that is robust against interfering FMCW radars. In case of SOFDM, the 2D-CAMP-based or dual-2D-CAMP recovery is recommended as they fit best in the existing CS-based evaluation. The additional computational effort for both methods is negligible.

5.5 Summary

Interference is an increasingly important topic in radar sensing, in particular in automotive and safety systems, where robust and reliable functionality is an

important factor. Therefore, the impact of a state-of-the-art fast-ramp FMCW radar signal on the (S)OFDM evaluation stages is analyzed. Since the interfering and the emitted (S)OFDM signals are independent and uncorrelated, the interference is most compressed in the spectrogram and spread in the R-v-image. An interference detection method that applies power detection in the spectrogram is developed. The method allows to reliably identify disturbed elements in the spectrogram, provided that at most half of them are affected. Moreover, four mitigation methods are developed. The two-stage methods zeroing, leveling, and 2D-CAMP recovery first utilize the developed detection. Afterwards, the identified elements are either set to zero, leveled in power, or eliminated and recovered. Additionally, a single-stage method called dual-2D-CAMP is developed that requires no detection step and allows to separate the desired (S)OFDM and the interfering FMCW signal.

In case of dense OFDM and only few disturbed elements in the spectrogram, the zeroing approach offers the best trade-off between mitigation effort and performance. With higher relative interferences, the additional performance improvement achievable with 2D-CAMP and dual-2D-CAMP mitigation becomes more relevant and increasingly justifies the additional effort. In this case, they are a reasonable alternative. In SOFDM, 2D-CAMP and dual-2D-CAMP are always superior to zeroing and leveling. Here, they do not require additional computational effort and at the same time achieve an improvement of PNR. Moreover, by replacing the usual evaluation by the dual-2D-CAMP approach allows unchanged and robust radar sensing regardless of whether signals from other radars with comparatively low instantaneous bandwidth and high narrowband power interfere.

6 Conclusion

Driven by recent advances in CMOS technology and ever-increasing digital processing power, novel digital radar concepts become viable and research interest in them continuous to grow. While with state-of-the-art radar systems such as FMCW radars, most of the signal processing is accomplished in the analog domain, in digital radar systems most of the signal generation and processing is performed in the digital domain. This opens up completely new possibilities regarding modulation, waveform design, and processing power. The OFDM modulation concept for digital radars has attracted increasing interest in radar research in the last two decades. Its characteristic discrete signal structure allows flexible waveform design and modulation, and enables new MIMO concepts that are yet unused or impractical in radars. Together with the growing processing power enabling high performance signal processing, digital OFDM concepts open up new perspectives and allow even more powerful radars.

This thesis is concerned with the waveform design and high-performance signal processing of MIMO OFDM radars. It aims to contribute to make OFDM radars more powerful, overcome limiting factors, and explore new possibilities for waveform design and digital processing. The main achievements of this work are the following:

- Break the close link between the attainable range resolution of OFDM and modulation bandwidth, which sets high demands on the sampling rate and is a major limiting factor in realizing high-resolution OFDM radars.
- Break new grounds in MIMO concepts by developing new multiplexing concepts that take advantage of the high waveform design flexibility OFDM is offering.
- Investigation of the interference impact of state-of-the-art FMCW radars on OFDM radars and develop countermeasures to make its operation

robust in non-cooperative multi-sensor environments.

In Chapter 3, the novel SOFDM waveform design and high-performance processing concept is developed that achieves high-resolution radar imaging with an instantaneously narrow baseband bandwidth. SOFDM allows to break the close relation between range resolution and modulation bandwidth of OFDM signals and thereby enables to realize high-resolution OFDM radar imaging at low sampling rates. In addition, a new high-performance digital signal evaluation concept using novel 2D CS methods is developed. The presented 2D-CAMP, 2D-HAMP, and 2D-SALSA algorithms are specially adapted to the SOFDM waveform and achieve high-resolution imaging comparable to an equivalent wideband dense OFDM measurement. With the proposed processing concept, an improvement of up to the factor of eight of the range resolution is achieved compared to a dense OFDM signal using the same baseband bandwidth. In other words, with SOFDM it is possible to achieve the performance of a wideband dense OFDM with up to eight times less baseband bandwidth. Furthermore, the processing improves the PNR by introducing pseudo PNR. If the bandwidth is reduced by the factor of $1/\delta_{\mathrm{cs}}$, an improvement of PNR of up to factor $1/\delta_{\mathrm{cs}}$ is achieved compared to an equivalent wideband dense OFDM signal that uses the same power per subcarrier. Therefore, with $1/\delta_{\mathrm{cs}} = 8$, an increase of PNR up to 9 dB is possible. This facilitates target detection. Another feature of SOFDM is that through the flexible Tx pattern design and spectrum allocation, it allows the wideband frequency spectrum to be shared by multiple radar nodes and therefore has the potential to actively avoid interference.

In Chapter 4, novel multiplexing strategies to realize multi-channel MIMO radar and spatial OFDM radar operation are developed. The goal was to explore the possibility of using the diversity of OFDM signals in the time, frequency, and code dimensions to enable MIMO operation using new multiplexing concepts. The RM concept combines TDM and FDM by randomly assigning each element of the spectrogram to the different transmitters. The random transmission pattern of each channel enables high-performance evaluation using CS algorithms. Therefore, an enhanced 2D-CAMP algorithm is developed that allows simultaneous multi-channel processing. Other than in the state-of-the-art interleaving FDM MIMO OFDM concept, it is shown that with the RM concept, no losses or restrictions in the unambiguous range or resolution is experienced compared to a dense single-channel measurement.

With CDM, a new possibility for MIMO OFDM radar waveform design was explored. The goal was to enable all transmitters to use all subcarriers simultaneously and continuously throughout the entire measurement without significantly interfering with each other. Although OFDM waveforms are ideally suited to realize CDM, a major challenge is the fact that perfect code and thus signal isolation and perfect autocorrelation properties cannot be achieved at the same time. Therefore, the three different developed coded MIMO waveform design strategies ZCZ, AC, and MRS-CDM each offer a good trade-off between channel isolation and radar imaging performance. Moreover, they only specify the design rules of the phases and amplitudes of the modulation symbols but do not require any modification to the usual MIMO OFDM signal processing and evaluation. The concepts may therefore be implemented on any existing digital OFDM radar hardware, and the MIMO concept may be changed during operation between measurements in order to adapt to changing conditions and environments. Moreover, the three methods offer the possibility to place constraints in different measurement dimensions and therefore enable a wide range of applications. By performing some additional processing steps, AC-CDM also allows to resolve emerging ambiguities and thereby overcome all limiting constraints in the range dimension. Through various measurements it was shown that all approaches are competitive to the standard FDM MIMO OFDM but with differing constraints and advantages. Therefore, in addition, hybrid MIMO concepts are developed that combine two MIMO concepts into a new one that enjoys the advantages of both. At the same time they have fewer constraints than either on its own. Finally, the application of RM to realize MIMO SOFDM was investigated. The approaches complement each other perfectly in their signal design and evaluation concepts. Furthermore, RM SOFDM achieves the maximum possible unambiguous ranges and improved PNR through the CS-based signal evaluation.

In Chapter 5, the impact of FMCW radars on OFDM measurements is investigated, and countermeasure that enable robust operation in coexistence with such sensors are developed. First, the interference impact of state-of-the-art FMCW radars on the various OFDM Rx signal processing stages was examined in detail. It was found that every processing stage is affected by the interference to different degrees. In the radar image, the interference is decorrelated and manifests itself as an increase of the noise level and therefore impairs the target detection

performance. On the other hand, the interference is most compressed in the spectrogram. Therefore, an interference detection method in the spectrogram is developed that allows to identify the interfered elements. In addition, four methods to mitigate or eliminate the interference are proposed. The zeroing method eliminates interfered elements in the spectrogram. With up to 30 % of interfered samples, it was found to provide a good trade-off between radar performance loss and complexity. If the number of interfered samples is about 20 % or more, signal recovery using the 2D-CAMP or the dual-2D-CAMP approach provides additional radar performance improvements. Furthermore, the dual-2D-CAMP approach enables unchanged and robust radar sensing regardless of whether FMCW or other signals with comparatively low instantaneous bandwidth and high narrowband power interfere. In case of interference of SOFDM signals, interference mitigation can be directly included in the existing 2D-CAMP signal evaluation or by replacing it with the dual-2D-CAMP approach. With both approaches it was shown that the interference can be entirely eliminated and the original radar performance regained.

In this thesis, it is demonstrated that by taking advantage of the high degree of flexibility and diversity provided by digital OFDM radars, new waveform designs and advanced signal processing methods can be realized. It is shown that through this, constraints can be overcome, new MIMO concepts become feasible, and robust sensing is achievable.

Appendix A Additional Notes on 2D CS

A.1 Mathematical Notations and Relations

The following mathematical transformations and notations are used in the following sections:

- $\mathrm{vec}(\boldsymbol{A})$: transforms the matrix $\boldsymbol{A}$ into a column vector by stacking its columns
- $\mathrm{diag}(\boldsymbol{a})$: diagonal matrix with main diagonal entries given by vector $\boldsymbol{a}$
- $\boldsymbol{A} \otimes \boldsymbol{B}$: Kronecker product of the matrices $\boldsymbol{A}$ and $\boldsymbol{B}$.

With these, the following relations hold: The vectorization of the matrix product $\boldsymbol{AXB}$ corresponds to

$$\mathrm{vec}(\boldsymbol{AXB}) = \boldsymbol{B} \otimes \boldsymbol{A}^{\mathsf{T}} \, \mathrm{vec}(\boldsymbol{X}) \,, \tag{A.1}$$

and the vectorization of the Hadamard product of two matrices $\boldsymbol{A}$ and $\boldsymbol{B}$ equals

$$\mathrm{vec}(\boldsymbol{A} \circ \boldsymbol{B}) = \mathrm{vec}(\boldsymbol{A}) \circ \mathrm{vec}(\boldsymbol{B}) = \mathrm{diag}\Big(\mathrm{vec}(\boldsymbol{A})\Big) \, \mathrm{vec}(\boldsymbol{B}) \,. \tag{A.2}$$

A.2 Kronecker CS for SOFDM

The 2D CS problem for SOFDM (3.11)

$$\boldsymbol{\mathcal{D}}^{\boxplus} = \boldsymbol{P} \circ \left(\boldsymbol{U}^{\mathsf{H}} \boldsymbol{X} \boldsymbol{U}\right) + \boldsymbol{P} \circ \boldsymbol{W}$$

may be transferred to an equivalent 1D problem similar to (2.56) using vectorization and the Kronecker product as defined in Section A.1. First, the 2D problem gets vectorized, which gives

$$\mathrm{vec}(\boldsymbol{\mathcal{D}}^{\boxplus}) = \mathrm{vec}\Big(\boldsymbol{P} \circ \left(\boldsymbol{U}^{\mathsf{H}} \boldsymbol{X} \boldsymbol{U}\right)\Big) + \mathrm{vec}(\boldsymbol{P} \circ \boldsymbol{W}) \,. \tag{A.3}$$

The equation may further by broken down using the vectorization of a Hadamard product (A.2), which yields

$$\operatorname{vec}(\boldsymbol{\mathcal{D}}^{\boxplus}) = \operatorname{diag}\big(\operatorname{vec}(\boldsymbol{P})\big)\operatorname{vec}(\boldsymbol{U}^{\mathsf{H}}\boldsymbol{X}\boldsymbol{U}) + \operatorname{diag}\big(\operatorname{vec}(\boldsymbol{P})\big)\operatorname{vec}(\boldsymbol{W})\,. \tag{A.4}$$

Define the square decimation matrix $\boldsymbol{\Xi}_{\boldsymbol{P}} = \operatorname{diag}(\operatorname{vec}(\boldsymbol{P}))$ containing zeros and ones on the diagonal according to $\operatorname{vec}(\boldsymbol{P})$. With this, the equation finally gives

$$\underbrace{\operatorname{vec}(\boldsymbol{\mathcal{D}}^{\boxplus})}_{\boldsymbol{y}} = \underbrace{\boldsymbol{\Xi}_{\boldsymbol{P}}\big(\boldsymbol{U}\otimes\boldsymbol{U}^{\mathsf{H}}\big)}_{\boldsymbol{A}}\cdot\underbrace{\operatorname{vec}(\boldsymbol{X})}_{\boldsymbol{x}} + \underbrace{\boldsymbol{\Xi}_{\boldsymbol{P}}\operatorname{vec}(\boldsymbol{W})}_{\boldsymbol{w}}\,. \tag{A.5, A.6}$$

Eventually, the sensing matrix $\boldsymbol{A} = \boldsymbol{\Xi}_{\boldsymbol{P}}\big(\boldsymbol{U}\otimes\boldsymbol{U}^{\mathsf{H}}\big)$ is of size $MN\times MN$ for SOFDM. However, this is prohibitive, considering for instance the radar R1 configuration with N=1024 and M=2048 and a precision of 12 bit, the complex valued matrix would require 13.2 TB storage. For comparison, both $\boldsymbol{U}$ and $\boldsymbol{U}^{\mathsf{H}}$ require only about 6.3 MB storage each, and moreover, they do not need to be stored at all if efficient implementations of FFT and IFFT are used. As in the 2D case, the observation and sensing matrices of the equivalent expression are not decimated as in the usual CS. In the 1D case, the decimation may be implemented by eliminating zeros in the observation and all-zero rows of the sensing matrix. To this end, the index set $\Omega=\{i \mid \operatorname{vec}(\boldsymbol{P})_i \neq 0\}$ of non-zero entries in the vectorized pattern is defined. Furthermore, define $\boldsymbol{A}_\Omega$ the decimated matrix of $\boldsymbol{A}$ composed of the rows of $\boldsymbol{A}$ indexed by Ω. Thus, the observation and sensing matrices may be replaced by $\boldsymbol{y}_\Omega$ and $\boldsymbol{A}_\Omega$, respectively. Thereby, the storage requirements of $\boldsymbol{A}_\Omega$ reduces by the factor δ_{cs}, e.g. for $\delta_{\text{cs}}=1/4$ to 3.3 TB, which is still huge.

A.3 Equivalence of 1D- and 2D-AMP

In this section, it is shown that 2D-CAMP and 2D-HAMP can be transformed into their 1D form of Section 2.4.1. Omitting the iteration counter, the first step of the 2D-CAMP and 2D-HAMP iteration is

$$\tilde{\boldsymbol{X}} = \boldsymbol{U}\boldsymbol{E}\boldsymbol{U}^{\mathsf{H}} + \hat{\boldsymbol{X}}\,. \tag{A.7}$$

Applying vectorization and using the Kronecker product properties from Section A.1 yields

$$\begin{aligned}
\operatorname{vec}(\tilde{\boldsymbol{X}}) &= \operatorname{vec}(\boldsymbol{U}\boldsymbol{E}\boldsymbol{U}^{\mathsf{H}}) + \operatorname{vec}(\hat{\boldsymbol{X}}) && \text{(A.8)}\\
&= (\boldsymbol{U}^{\mathsf{H}} \otimes \boldsymbol{U})\operatorname{vec}(\boldsymbol{E}) + \operatorname{vec}(\hat{\boldsymbol{X}}) && \text{(A.9)}\\
\underbrace{\qquad} &= \underbrace{(\boldsymbol{U}^{\mathsf{H}} \otimes \boldsymbol{U})\operatorname{diag}\big(\operatorname{vec}(\boldsymbol{P})\big)}\,\underbrace{\operatorname{vec}(\boldsymbol{E})} + \underbrace{\operatorname{vec}(\hat{\boldsymbol{X}})} && \text{(A.10)}\\
\tilde{\boldsymbol{x}} &= \boldsymbol{A}^{\mathsf{H}} \cdot \boldsymbol{e} + \hat{\boldsymbol{x}} && \text{(A.11)}
\end{aligned}$$

which gives an equivalent 1D expression as in (2.61a). The matrix $\boldsymbol{\Xi}_{\boldsymbol{P}} = \operatorname{diag}(\operatorname{vec}(\boldsymbol{P}))$ in (A.10) is a neutral element to $\operatorname{vec}(\boldsymbol{E})$, as it already inherently has the pattern structure. The equivalence of the element-wise threshold functions in the second step is straightforward for both hard- and soft-threshold.

The third step of the iteration is the residual

$$\boldsymbol{E} = \boldsymbol{\mathcal{D}}^{\boxplus} - \boldsymbol{P} \circ \big(\boldsymbol{U}^{\mathsf{H}}\hat{\boldsymbol{X}}\boldsymbol{U}\big) + \tfrac{\|\hat{\boldsymbol{X}}\|_0}{MN_s}\boldsymbol{E}\,. \tag{A.12}$$

Applying vectorization and using the Kronecker product property (A.2) yields

$$\begin{aligned}
\operatorname{vec}(\boldsymbol{E}) &= \operatorname{vec}(\boldsymbol{\mathcal{D}}^{\boxplus}) - \operatorname{vec}\Big(\boldsymbol{P} \circ \big(\boldsymbol{U}^{\mathsf{H}}\hat{\boldsymbol{X}}\boldsymbol{U}\big)\Big) + \tfrac{\|\operatorname{vec}(\hat{\boldsymbol{X}})\|_0}{MN_s}\operatorname{vec}(\boldsymbol{E}) && \text{(A.13)}\\
\underbrace{\qquad} &= \underbrace{\operatorname{vec}(\boldsymbol{\mathcal{D}}^{\boxplus})} - \underbrace{\boldsymbol{\Xi}_{\boldsymbol{P}}\big(\boldsymbol{U} \otimes \boldsymbol{U}^{\mathsf{H}}\big)}\,\underbrace{\operatorname{vec}(\hat{\boldsymbol{X}})} + \underbrace{\tfrac{\|\operatorname{vec}(\hat{\boldsymbol{X}})\|_0}{MN_s}}\,\underbrace{\operatorname{vec}(\boldsymbol{E})} && \text{(A.14)}\\
\boldsymbol{e} &= \boldsymbol{y} - \boldsymbol{A} \cdot \hat{\boldsymbol{x}} + \tfrac{\|\hat{\boldsymbol{x}}\|_0}{S}\,\boldsymbol{e} && \text{(A.15)}
\end{aligned}$$

which gives an equivalent 1D expression as in (2.61c). Since $\boldsymbol{\Xi}_{\boldsymbol{P}}$ is a diagonal matrix with real entries, it holds that $\boldsymbol{\Xi}_{\boldsymbol{P}}^{\mathsf{H}} = \boldsymbol{\Xi}_{\boldsymbol{P}}$. Finally, the Hermetian transpose of the sensing matrix becomes

$$\boldsymbol{A}^{\mathsf{H}} = \Big(\boldsymbol{\Xi}_{\boldsymbol{P}}\big(\boldsymbol{U} \otimes \boldsymbol{U}^{\mathsf{H}}\big)\Big)^{\mathsf{H}} = \big(\boldsymbol{U} \otimes \boldsymbol{U}^{\mathsf{H}}\big)^{\mathsf{H}}\boldsymbol{\Xi}_{\boldsymbol{P}}^{\mathsf{H}} = \big(\boldsymbol{U}^{\mathsf{H}} \otimes \boldsymbol{U}\big)\boldsymbol{\Xi}_{\boldsymbol{P}}$$

verifying the consistency of the projections in (A.10) and (A.14).

Similar to the 2D case, $\boldsymbol{y}$, $\boldsymbol{e}$, and $\boldsymbol{A}$ are not reduced in size compared to $\hat{\boldsymbol{x}}$ in both (A.10) and (A.14). However, $\boldsymbol{y}$, $\boldsymbol{e}$, $\boldsymbol{A}$ have $(N - N_s)$ rows containing only zeros. The indices of these rows are given by the index set $\Omega = \{i \mid \operatorname{vec}(\boldsymbol{P})_i \neq 0\}$. Therefore, (A.10) and (A.14) can be transformed to their compressed formulation

by replacing the residual, sensing matrix, and observation by their compact counterparts $\boldsymbol{e}_\Omega$, $\boldsymbol{A}_\Omega$, and $\boldsymbol{y}_\Omega$. Note that the resulting systems of equations remains the same.

A.4 Equivalence of 1D- and 2D-SALSA

The transformations of the first (3.19a) and third step (3.19c) of the 2D-SALSA algorithm to its 1D counterparts (2.64a) and (2.64c), respectively, is straightforward, since it involves only element-wise operations.

Omitting the iteration indices for simplicity, the second iteration step of 2D-SALSA (3.19b)

$$\boldsymbol{H} = \boldsymbol{U}\big(\boldsymbol{\mathcal{D}}^{\boxplus} - \boldsymbol{P} \circ (\boldsymbol{U}^{\mathsf{H}}\boldsymbol{G}\boldsymbol{U})\big)\boldsymbol{U}^{\mathsf{H}}$$

is first vectorized to

$$\operatorname{vec}(\boldsymbol{H}) = \operatorname{vec}\Big(\boldsymbol{U}\big(\boldsymbol{\mathcal{D}}^{\boxplus} - \boldsymbol{P} \circ (\boldsymbol{U}^{\mathsf{H}}\boldsymbol{G}\boldsymbol{U})\big)\boldsymbol{U}^{\mathsf{H}}\Big)\,. \tag{A.16}$$

Using the Kronecker relation (A.2), the equation is broken down to

$$\begin{aligned}
\operatorname{vec}(\boldsymbol{H}) &= \big(\boldsymbol{U}^{\mathsf{H}} \otimes \boldsymbol{U}\big) \cdot \big(\operatorname{vec}(\boldsymbol{\mathcal{D}}^{\boxplus}) - \operatorname{vec}(\boldsymbol{P} \circ (\boldsymbol{U}^{\mathsf{H}}\boldsymbol{G}\boldsymbol{U}))\big) && \text{(A.17)}\\
&= \big(\boldsymbol{U}^{\mathsf{H}} \otimes \boldsymbol{U}\big) \cdot \big(\operatorname{vec}(\boldsymbol{\mathcal{D}}^{\boxplus}) - \boldsymbol{\Xi}_{\boldsymbol{P}}\big(\boldsymbol{U} \otimes \boldsymbol{U}^{\mathsf{H}}\big)\operatorname{vec}(\boldsymbol{G})\big) && \text{(A.18)}\\
\underbrace{\phantom{\boldsymbol{h}}} &= \underbrace{\big(\boldsymbol{U}^{\mathsf{H}} \otimes \boldsymbol{U}\big)\boldsymbol{\Xi}_{\boldsymbol{P}}}\big(\underbrace{\operatorname{vec}(\boldsymbol{\mathcal{D}}^{\boxplus})} - \underbrace{\boldsymbol{\Xi}_{\boldsymbol{P}}\big(\boldsymbol{U} \otimes \boldsymbol{U}^{\mathsf{H}}\big)}\underbrace{\operatorname{vec}(\boldsymbol{G})}\big) && \text{(A.19)}\\
\boldsymbol{h} &= \quad \boldsymbol{A}^{\mathsf{H}} \quad \big(\quad \boldsymbol{y} \quad - \quad \boldsymbol{A} \quad \cdot \quad \boldsymbol{g} \quad \big)\,, && \text{(A.20)}
\end{aligned}$$

with the decimation matrix $\boldsymbol{\Xi}_{\boldsymbol{P}}$=diag(vec($\boldsymbol{P}$)) containing zeros and ones on the diagonal according to vec($\boldsymbol{P}$). In addition, inserting the first $\boldsymbol{\Xi}_{\boldsymbol{P}}$ in (A.19) is possible as it is a neutral element to the expression within the latter parentheses. On the one hand, the second term of the expression already gets multiplied with $\boldsymbol{\Xi}_{\boldsymbol{P}}$, and on the other hand, $\boldsymbol{\Xi}_{\boldsymbol{P}}$ is neutral in the multiplication with the spectrogram vec($\boldsymbol{\mathcal{D}}^{\boxplus}$)= $\boldsymbol{\Xi}_{\boldsymbol{P}}$vec($\boldsymbol{\mathcal{D}}^{\boxplus}$). Furthermore, it yields that the projections $\boldsymbol{A}^{\mathsf{H}}$ and $\boldsymbol{A}$ correspond to those obtained for the 1D equivalence of 2D-CAMP in Section A.3.

A.5 Coherence of the Range and Doppler Dimensions in SOFDM

Instead of solving the 2D problem (3.11), two independent 1D problems, one for R and one for v, may be solved instead. The coherence of these 1D problems is determined by the row- and column-wise structure of $\boldsymbol{P}$. The coherence of acquiring R, v, and both jointly is illustrated in Fig. A.1 for different δ_{cs}. Since for R, always only a contiguous block of subcarriers is available framed by large blocks of zeros, the problem exhibits a high coherence. Recovering R is similar to applying zero-padding prior to the IDFT. However, zero-padding thus refining the frequency resolution of equidistant Nyquist-rate samples severely impairs the coherence [183], as observable in the graph. On the other hand, the coherence of estimating v is much better than for R up to about δ_{cs}=1/8. The resason is that along the slow-time dimension of $\boldsymbol{P}$, zeros and ones are distributed approximately randomly. However, with a decreasing number of samples available in the frame, less ones are contained in each column of $\boldsymbol{P}$, and consequently, less samples of each subcarrier are collected. If too few samples are available, the coherence degrades. On the contrary, μ of the joint 2D recovery problem is always lower than the coherences of both 1D problems. This finding was proven in [76]. Therefore, a joint recovery is always superior to two separate 1D recoveries.

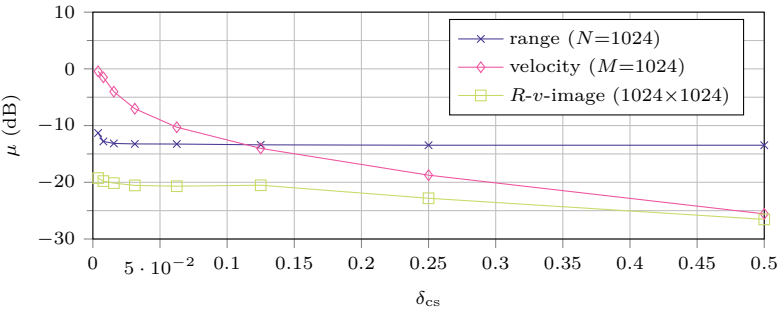


Fig. A.1: Coherence of acquiring and evaluating range and Doppler independently and jointly at different degrees of SOFDM undersampling.

Appendix B Derivation of the ITCT Part of the Range Evaluation

The IDFT of the undesired ITCT contribution in the spectrogram (4.10) due to the interfering transmitters in CDM MIMO OFDM operation yields

$$\breve{\mathcal{R}}_m^{[\hat{q},l]}[\rho] \propto \sum_{\substack{q=0 \\ q\neq\hat{q}}}^{N_{\mathrm{tx}}-1} \alpha^{[q,l]}\, \mathrm{e}^{\mathrm{j}\varphi_\theta[q,l]}\, \frac{1}{\sqrt{N}} \sum_{n=0}^{N-1} d_{mn}^{[q]} \left(d_{mn}^{[\hat{q}]}\right)^* \mathrm{e}^{-\mathrm{j}2\pi n \Delta f \frac{2R_0}{c}}\, \mathrm{e}^{\mathrm{j}2\pi \frac{n\rho}{N}} \ .$$

Using the discrete-time representation of the baseband Tx signal (2.3) yields

$$d_{mn}^{[q]} = \frac{1}{\sqrt{N}} \sum_{k=0}^{N-1} x_m^{[q]}[k]\, \mathrm{e}^{-\mathrm{j}2\pi \frac{nk}{N}} \tag{B.1}$$

and

$$\left(d_{mn}^{[q]}\right)^* = \frac{1}{\sqrt{N}} \sum_{\eta=0}^{N-1} \left(x_m^{[q]}[\eta]\right)^* \mathrm{e}^{\mathrm{j}2\pi \frac{n\eta}{N}} \ . \tag{B.2}$$

By substituting (B.1) and (B.2) into the original equation, and then rearranging the terms and sums gives the following result:

$$\begin{aligned} \breve{\mathcal{R}}_m^{[\hat{q},l]}[\rho] \propto \sum_{\substack{q=0 \\ q\neq\hat{q}}}^{N_{\mathrm{tx}}-1} \alpha^{[q,l]}\, \mathrm{e}^{\mathrm{j}\varphi_\theta[q,l]}\, \frac{1}{N\sqrt{N}} \sum_{k=0}^{N-1} \sum_{\eta=0}^{N-1} x_m^{[q]}[k] \left(x_m^{[\hat{q}]}[\eta]\right)^* \\ \times \sum_{n=0}^{N-1} \mathrm{e}^{\mathrm{j}2\pi \frac{n}{N}\left(\rho - \frac{R_0}{\Delta R} + \eta - k\right)} \ . \end{aligned} \tag{B.3}$$

The last sum becomes N if the phase becomes zero, for instance if

$$k = \left[\eta + \rho - \frac{R_0}{\Delta R}\right]_N .$$

Otherwise, the sum is zero. Therfore, the undesired range profile contribution becomes

$$\breve{\mathcal{R}}_m^{[\hat{q},l]}[\rho] \propto \sum_{\substack{q=0 \\ q\neq\hat{q}}}^{N_{\mathrm{tx}}-1} \alpha^{[q,l]}\, \mathrm{e}^{\mathrm{j}\varphi_\theta[q,l]}\, \frac{1}{\sqrt{N}} \sum_{\eta=0}^{N-1} x_m^{[q]}\left[\eta + \rho - \tfrac{R_0}{\Delta R}\right]_N \left(x_m^{[\hat{q}]}[\eta]\right)^* \tag{B.4}$$

$$\propto \sum_{\substack{q=0 \\ q\neq\hat{q}}}^{N_{\mathrm{tx}}-1} \alpha^{[q,l]}\, \mathrm{e}^{\mathrm{j}\varphi_\theta[q,l]}\, \frac{1}{\sqrt{N}} \chi^{\mathrm{cc}}_{x_m^{[q]} x_m^{[\hat{q}]}}\left[\rho - \tfrac{R_0}{\Delta R}\right], \tag{B.5}$$

which finally gives (4.12).

Appendix C Optimal Design Parameters to Construct Complex-Valued ZCZ Sequences

The construction of complex-valued QPSK-based ZCZ sequences from recursively interleaved Hadamard matrices in [155] requires two free design parameters: the initial order of the Hadamard matrices Q and the interleaving depth i. With this, sequences of $(\mathcal{L}, \mathcal{P}, \mathcal{Z})=(2^{i+2}Q, 4Q, 2^{i-2}3)$ can be generated. Since $\mathcal{Z}$ determines the maximum signal delay resulting in zero cross-correlation, for the purpose of radar operation, $\mathcal{Z}$ should be maximized given the signal parameters N and N_{tx}. Therefore, an optimal choice of the parameters Q and i for ZCZ-CDM is obtained by the following procedure. First, the DFT in (4.14) requires $\mathcal{L}=N=2^{i+2}Q=2^{i}\mathcal{P}$. Solving for the interleaving depth gives $i=\log_2(N/\mathcal{P})$. Since i must be an integer and N is usually chosen to be a power of two to achieve efficient computation of the involved DFTs and IDFTs of the OFDM processing chain, $\mathcal{P}$ must be a power of two as well. With this, the length of the ZCZ becomes $\mathcal{Z}=3N/(4\mathcal{P})$, which is approximately $3/4\mathcal{Z}_{\max}$. Therefore, in order to optimize ZCZ without changing the OFDM signal parameters, the member size $\mathcal{P}$ of the set should be as small as possible. Since, additionally, $\mathcal{P}$ has to be at least N_{tx} to provide a sufficient number of unique sequences, eventually, the initial order of the Hadamard matrix must be $Q=N'_{\mathrm{tx}}/4$ with $N'_{\mathrm{tx}}\geq 4$ the smallest power of two equal or larger than N_{tx}. In summary, the optimal parametrization proportional to N and N_{tx} is as follows:

$$Q=\left\lceil\frac{N_{\mathrm{tx}}}{4}\right\rceil=\frac{N'_{\mathrm{tx}}}{4},\quad i=\log_2\left(\frac{N}{\mathcal{P}}\right)=\log_2\left(\frac{N}{N'_{\mathrm{tx}}}\right),\quad \text{and}\quad \mathcal{Z}=\frac{3N}{4N'_{\mathrm{tx}}}. \tag{C.1}$$

Appendix D Derivation of the MRS Velocity Profile

Following the typical DFT-based velocity evaluation of Section 2.2.2, the DFT of the ITCT part of the spectrogram $\breve{\boldsymbol{\mathcal{D}}}^{[\hat{q},l]}$ yields

$$\breve{\mathcal{V}}_n^{[\hat{q},l]}[\nu] = \frac{1}{\sqrt{M}} \sum_{m=0}^{M-1} \breve{\boldsymbol{\mathcal{D}}}_{mn}^{[\hat{q},l]} \Psi_{mn}\, \mathrm{e}^{-\mathrm{j}2\pi \frac{m\nu}{M}} \quad . \tag{D.1}$$

Plugging in $\breve{\boldsymbol{\mathcal{D}}}^{[\hat{q},l]}$ (2.43) and omitting terms independent of m and q gives

$$\breve{\mathcal{V}}_n^{[\hat{q},l]}[\nu] \propto \frac{1}{\sqrt{M}} \sum_{m=0}^{M-1} \mathrm{e}^{\mathrm{j}2\pi \frac{m\hat{\nu}}{M}} \sum_{\substack{q=0 \\ q\neq\hat{q}}}^{N_{\mathrm{tx}}-1} \alpha^{[q,l]} d_{mn}^{[q]} \left(d_{mn}^{[\hat{q}]}\right)^* \mathrm{e}^{\mathrm{j}\varphi_\theta[q,l]}\, \Psi_{mn}\, \mathrm{e}^{-\mathrm{j}2\pi \frac{m\nu}{M}} \tag{D.2}$$

with $\hat{\nu}{=}f_d M T_{\mathrm{OFDM}}$. Rearranging terms and sums results in

$$\propto \sum_{\substack{q=0 \\ q\neq\hat{q}}}^{N_{\mathrm{tx}}-1} \alpha^{[q,l]}\, \mathrm{e}^{\mathrm{j}\varphi_\theta[q,l]} \frac{1}{\sqrt{M}} \sum_{m=0}^{M-1} d_{mn}^{[q]} \left(d_{mn}^{[\hat{q}]}\right)^* \Psi_{mn}\, \mathrm{e}^{-\mathrm{j}2\pi \frac{m}{M}(\nu-\hat{\nu})} \quad . \tag{D.3}$$

Without loss of generality, assume the non-permuted MRS modulation design ($\boldsymbol{\mathcal{S}}_1$) based on the non-permuted Hadamard matrix $\boldsymbol{\mathcal{H}}_{N_{\mathrm{tx}}}$, equation (D.3) becomes $d_{mn}^{[q]}{=}a_q h_{q\varpi}$ where $\varpi{=}(m \bmod N_{\mathrm{tx}})$. With this, the ITCT part of the velocity evaluation becomes

$$\propto \sum_{\substack{q=0 \\ q\neq\hat{q}}}^{N_{\mathrm{tx}}-1} \alpha^{[q,l]}\, \mathrm{e}^{\mathrm{j}\varphi_\theta[q,l]} \frac{1}{\sqrt{M}} \sum_{m=0}^{M-1} a_q h_{q\varpi} \left(a_{\hat{q}} h_{\hat{q}\varpi}\right)^* \Psi_{mn}\, \mathrm{e}^{-\mathrm{j}2\pi \frac{m}{M}(\nu-\hat{\nu})} \tag{D.4}$$

$$\propto \sum_{\substack{q=0\\q\neq\hat{q}}}^{N_{\mathrm{tx}}-1} \alpha^{[q,l]}\, \mathrm{e}^{\mathrm{j}\varphi_\theta[q,l]}\, a_q(a_{\hat{q}})^* \frac{1}{\sqrt{M}} \sum_{m=0}^{M-1} h_{q\varpi} h_{\hat{q}\varpi} \Psi_{mn}\, \mathrm{e}^{-\mathrm{j}2\pi\frac{m}{M}(\nu-\hat{\nu})} \,. \quad \text{(D.5)}$$

Resolving the modulo operation of ϖ by splitting the last sum up into a product of two sums gives

$$\begin{aligned} &\propto \sum_{\substack{q=0\\q\neq\hat{q}}}^{N_{\mathrm{tx}}-1} \alpha^{[q,l]}\, \mathrm{e}^{\mathrm{j}\varphi_\theta[q,l]}\, a_q(a_{\hat{q}})^* \\ &\quad\times \frac{1}{\sqrt{M}} \sum_{\mu=0}^{\frac{M}{N_{\mathrm{tx}}}-1} \sum_{u=0}^{N_{\mathrm{tx}}-1} h_{qu} h_{\hat{q}u} \Psi_n[u+\mu N_{\mathrm{tx}}]\, \mathrm{e}^{-\mathrm{j}2\pi\frac{u+\mu N_{\mathrm{tx}}}{M}(\nu-\hat{\nu})} \end{aligned} \quad \text{(D.6)}$$

with the original index $m{=}u+\mu N_{\mathrm{tx}}$. Usually, it holds that $N_{\mathrm{tx}}{\ll}M$. Thus, for common window functions, the following approximation can be assumed:

$$\Psi_n[\mu N_{\mathrm{tx}}] \approx \Psi_n[1+\mu N_{\mathrm{tx}}] \approx \cdots \approx \Psi_n[N_{\mathrm{tx}}-1+\mu N_{\mathrm{tx}}] \,.$$

With this, (D.6) becomes

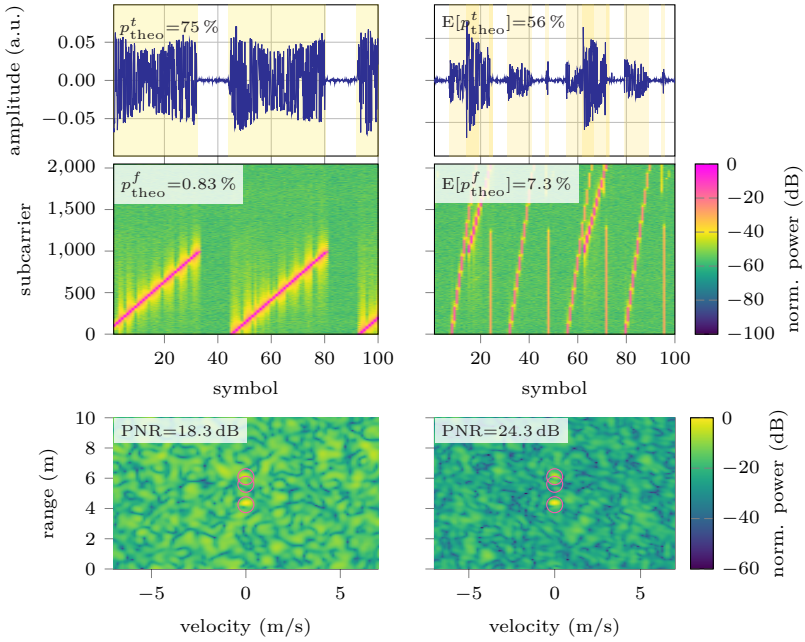
$$\breve{\mathcal{V}}_n^{[\hat{q},l]}[\nu] \propto \sum_{\substack{q=0\\q\neq\hat{q}}}^{N_{\mathrm{tx}}-1} \alpha^{[q,l]}\, \mathrm{e}^{\mathrm{j}\varphi_\theta[q,l]}\, a_q(a_{\hat{q}})^* \frac{1}{\sqrt{M}} \underbrace{\sum_{\mu=0}^{\frac{M}{N_{\mathrm{tx}}}-1} \Psi_n[\mu N_{\mathrm{tx}}]\, \mathrm{e}^{-\mathrm{j}2\pi\frac{\mu}{M/N_{\mathrm{tx}}}(\nu-\hat{\nu})}}_{\frac{M}{N_{\mathrm{tx}}}\psi_n[\nu-\hat{\nu}]_{\frac{M}{N_{\mathrm{tx}}}}} \quad \text{(D.7)}$$

$$\begin{aligned} &\quad\times \sum_{u=0}^{N_{\mathrm{tx}}-1} h_{qu} h_{\hat{q}u}\, \mathrm{e}^{-\mathrm{j}2\pi\frac{u}{M}(\nu-\hat{\nu})} \\ &\propto \frac{\sqrt{M}}{N_{\mathrm{tx}}} \psi_n[\nu-\hat{\nu}]_{\frac{M}{N_{\mathrm{tx}}}} \sum_{\substack{q=0\\q\neq\hat{q}}}^{N_{\mathrm{tx}}-1} \alpha^{[q,l]}\, \mathrm{e}^{\mathrm{j}\varphi_\theta[q,l]}\, a_q(a_{\hat{q}})^* \sum_{u=0}^{N_{\mathrm{tx}}-1} h_{qu} h_{\hat{q}u}\, \mathrm{e}^{-\mathrm{j}2\pi\frac{u}{M}(\nu-\hat{\nu})} \,, \end{aligned} \quad \text{(D.8)}$$

which finally gives (4.21).

Appendix E Additional Interference Measurement Results

In addition to measurements using the interference signal parameters in Table 5.1, measurements are performed with variations of the chirp bandwidth and carrier frequency of I1. Excerpts of such measurements are shown in Fig. E.1. In Fig. E.1 (a), I1 is active but its bandwidth is reduced to 500 MHz such that the entire interfering signal lies within the OFDM frame. As a consequence, p^t_{theo} in time domain doubles compared to the example in Fig. 5.3 (a). On the other hand, since the slope of the interference is smaller, the p^f_{theo} in the spectrogram decreases in comparison to Fig. 5.3 (a). In Fig. E.1 (b), a measurement with both I1 and I2 active within the measured frame is shown. The carrier frequency of I1 was increased to 76.5 GHz. In both the time signal (upper graph) and the spectrogram (middle graph), the power difference of the two interferer is visible. The relative interferences p^t_{theo} and p^f_{theo} cannot be determined by (5.1) and (5.3) anymore, but have to be determined either analytically or individually for each measurement, provided that the amount of overlap of the interfering chirps is known. Therefore, the expected value is given here. Worth highlighting here is that among all considered setups in this thesis, the measurement of I1 with reduced chirp bandwidth in Fig. E.1 (a) achieves with about 75 % the highest relative interference in the time domain. At the same time, due to its small total bandwidth, especially compared to the OFDM signal, it comprises the lowest relative interference in the spectrogram.



(a) Interfered by I1 with reduced $\mathcal{B}_{\text{chirp}}$=500 MHz.

(b) Interfered by I1 and I2 with I1 shifted to f_{chirp}=76.5 GHz.

Fig. E.1: Interference measurements using OFDM radar R2 and interfering FMCW radars (a) I1 with a reduced bandwidth of 500 MHz and (b) both I1 and I2 active at the same time with carrier frequency of I1 increased to 76.5 GHz. From top to bottom, the graphs show the time domain and spectrogram excerpts of the first 100 OFDM symbols and the *R*-*v*-images. In time domain, interference intervals are highlighted. The values for p^t_{theo} and p^f_{theo} give the maximum relative interference in time domain and spectrogram, respectively, if the interference persists for the entire frame.

Index of Symbols, Indices, and Acronyms

As far as possible, variable names and indices were chosen according to DIN 1304 in order to avoid double entries as far as possible. For all remaining double entries, the correct meaning can be gathered from the context. Common running indices and basic operators are not listed here. In accordance with DIN 1338 all symbols are displayed in italics. The page numbers state the page a certain variable is used for the first time.

Notations

$\mathbb{B}$	set of binary numbers $\{0, 1\}$	24
$\mathbb{C}$	set of complex numbers	9
$\mathbb{I}_{\mathcal{C}}$	indicator function $\mathbb{I}_{\mathcal{C}}$ is 1 (true) if condition $\mathcal{C}$ is fulfilled, 0 (false) if not.	25
$\mathbb{Z}_N$	set of integers, $\mathbb{Z}_N = \{0, 1, \ldots, N-1\}$	8
j	complex unit	9
$\mathbf{0}_{MN}$	zero matrix of size $M \times N$	25
$\boldsymbol{I}_N$	identity matrix of size $N \times N$	10
$\boldsymbol{A}^{\mathsf{H}}$	Hermetian or conjugate transpose $\boldsymbol{A}^{\mathsf{H}} = (\boldsymbol{A}^{\mathsf{T}})^*$	10
$\boldsymbol{A}^{\mathsf{T}}$	matrix transpose	41
$\boldsymbol{A} \circledast \boldsymbol{B}$	circular 2D convolution	43
$\boldsymbol{A} \circ \boldsymbol{B}$	Hadamard product, element-wise product	14
$\boldsymbol{A} \otimes \boldsymbol{B}$	Kronecker product	145
$\Gamma(X; \Upsilon)$	threshold function with threshold parameter Υ	31
$\mathrm{hard}(X; \Upsilon)$	hard-threshold function with threshold parameter Υ	32
$\mathrm{median}(X)$	median of samples or matrix X	49
$\mathrm{soft}(X; \Upsilon)$	soft-threshold function with threshold parameter Υ	32
$\mathcal{CN}$	complex normal distribution	29
$\mathcal{N}$	normal distribution	49
$\mathcal{O}$	complexity order of algorithms	58

Indices

h	target	11
k	iteration number	31
k	discrete time index	9
κ	virtual antenna element	20
l	receive element	21
m	OFDM symbol	8
n	(virtual) subcarrier	8
ν	velocity bin	17
$\hat{\nu}$	target velocity bin	17
q	transmit element	21
$\hat{q}$	specific transmit element	23
ρ	range bin	15
$\hat{\rho}$	target range bin	15
ϑ	azimuth angle index	27
$\hat{\vartheta}$	target azimuth angle index	27

Symbols

$\boldsymbol{A}$	sensing matrix of CS	29
$\mathcal{A}$	modulation alphabet	8
α	time and frequency-invariant complex amplitudes of the receive signal, proportional to the target RCS	11
a	fundamental modulation symbol in MRS-OFDM	91
B	OFDM signal bandwidth	8
$\boldsymbol{b}$, b_m	frequency hopping sequence with elements b_m	41
$\mathcal{B}_{\text{chirp}}$	FMCW bandwidth	118
β	scaling factor of Doppler safety margin	19
$\mathcal{B}_{\text{int}}$	interfered bandwidth of the OFDM signal	121
$\mathcal{B}_s$	baseband bandwidth of SOFDM	39
c	speed of light	11
$\boldsymbol{\mathcal{D}}$	demodulated Rx spectrogram	14
$\mathcal{D}_{mn}$	coefficient of the mth OFDM symbol and nth subcarrier of the demodulated Rx spectrogram $\boldsymbol{\mathcal{D}}$	15

$\hat{\boldsymbol{\mathcal{D}}}$	desired auto-correlation part of the Rx spectrogram ... 23
$\breve{\boldsymbol{\mathcal{D}}}$	inter-transmitter cross-talk (cross-correlation) contribution to the Rx spectrogram ... 23
$\boldsymbol{\mathcal{D}}^{\star}$	hybrid spectrogram after CS recovery in SOFDM ... 47
$\tilde{\boldsymbol{\mathcal{D}}}$	noisy and interfered demodulated Rx spectrogram ... 132
$\boldsymbol{\mathcal{D}}^{\boxplus}$	demodulated virtual wideband Rx spectrogram of SOFDM ... 42
δ_{cs}	indeterminacy of the system of equation in CS, $\delta_{\text{cs}}{=}S/L$ 29
Δf	subcarrier spacing, $\Delta f = 1/T$ ... 8
ΔR	range resolution ... 13
Δv	velocity resolution ... 18
D_λ	element spacing of the ULA ... 20
$\boldsymbol{d}$	modulation symbols ... 9
d_{mn}	modulation symbol of the mth OFDM symbol and nth subcarrier ... 8
$\boldsymbol{E}$	residual in the 2D-(H/C)AMP algorithm ... 49
$\boldsymbol{e}$	residual in the 1D-(H/C)AMP algorithm ... 31
f_c	carrier frequency / RF frequency ... 11
f_{chirp}	FMCW carrier frequency ... 118
f_d	Doppler frequency ... 11, 13
f_m	RF carrier frequency of the mth SOFDM symbol ... 41
$\boldsymbol{\Phi}$	basis matrix in CS ... 28
f_s	sampling frequency (Nyquist) ... 9
θ	azimuth angle ... 20
H	number of targets in the field of view ... 11
$\boldsymbol{\mathcal{H}}_k$	Hadamard matrix of order k ... 90
i	zero-correlation zone sequence construction interleaving depth ... 88
$\boldsymbol{\mathcal{I}}$	radar range-velocity image matrix ... 19
K	number of iterations ... 31
$\mathcal{L}$	code length ... 83
L	dimension of the sparse signal in its sparse basis in CS, large dimension ... 28
$\boldsymbol{\Lambda}$	matrix of element dependent threshold values ... 49
Λ	threshold value (scalar) ... 31

λ	wavelength 14
M	number of OFDM symbols in the frame 8
μ	coherence 30
N	number of subcarriers in the frame 8
N_{cp}	number of samples of the prefix, $N_{\mathrm{cp}} = T_{\mathrm{cp}} f_s$ 10
N_{guard}	number of guard samples in the AC-CDM design 97
N_{rx}	number of receivers 20
N_{virt}	number of virtual array elements 21
N_s	number of baseband subcarriers in SOFDM 39
N_{tx}	number of transmitters 20
Ω	set of indices and support set 77
$\mathcal{P}$	code set cardinality 83
$\boldsymbol{P}$, P_{mn}	pattern matrix; transmit pattern in SOFDM and MIMO 24
$\varphi_R, \varphi_v, \varphi_\theta$	target range, velocity, and angle dependent phase 13
PNR	peak-to-noise ratio of the strongest target in the radar image 54
p_{det}	detection rate 61
p_{far}	false alarm rate 51
$p^{f}_{\mathrm{theo/meas}}$	theoretical/measured relative number of interfered elements in the spectrogram 120
$p^{t}_{\mathrm{theo/meas}}$	theoretical/measured relative number of interfered samples in time domain 120
Q	initial Hadamard matrix order in zero-correlation zone sequence construction 88
R	target range 11
ϱ_{cs}	relative sparseness of a signal: ratio of support size and total number of acquired samples $\varrho_{\mathrm{cs}}{=}s/S$ 31
R_{max}	maximum range 17
$\boldsymbol{\mathcal{R}}$, $\mathcal{R}_m$, $\mathcal{R}_\nu$	matrix of radar range profiles and the range profile of the mth OFDM symbol or νth velocity index 15
$\hat{\mathcal{R}}_m$	desired range profile of the mth OFDM symbol (vector) 85
$\breve{\mathcal{R}}_m$	inter-transmitter cross-talk contribution to the range profile of the mth OFDM symbol (vector) 85
$\boldsymbol{r}$, r_m	OFDM baseband time domain receive signal matrix and signal of the mth OFDM symbol 11

R_{ua}	maximum unambiguous range 16
S	number of observations, dimension of the measured signal in CS, small dimension 29
ς	sparseness of a signal, cardinality of the true signal support 28
σ	standard deviation of a distribution or samples 29
$\hat{\boldsymbol{\sigma}}$	matrix of estimates of the standard deviation of a distribution or samples 50
$\hat{\sigma}$	estimate of the standard deviation of a distribution or samples (scalar) 49
$\boldsymbol{\mathcal{S}}$	modulation assignment set in MRS-OFDM 91
Υ	scaling of the threshold in the soft-threshold function .. 50
τ	signal time delay, time of flight in the channel 11
t	time (continuous) 9
τ_s	sample duration 95
Θ	azimuth angle profile 27
T	OFDM symbol duration without cyclic prefix, $T = 1/\Delta f$ 8
T_{cp}	duration of the cyclic prefix 10
T_{OFDM}	OFDM symbol duration with cyclic prefix 10
T_{down}	FMCW down-ramp duration 118
T_{r2r}	FMCW ramp repetition time 118
T_{up}	FMCW up-ramp duration 118
$\boldsymbol{U}$	unitary DFT matrix for CS 10
v	target velocity 11
$v_{\max}$	maximum velocity 19
$\boldsymbol{\mathcal{V}}$, $\mathcal{V}_n$, $\mathcal{V}_\rho$	matrix of radar velocity profiles and the velocity profile of the nth subcarrier or ρth range index 17
$\breve{\mathcal{V}}_n$	inter-transmitter cross-talk contribution to the velocity profile of the nth subcarrier (vector) 92
$\hat{\mathcal{V}}_n$	desired velocity profile of the nth subcarrier (vector) ... 92
v_{ua}	maximum unambiguous velocity 18
$\boldsymbol{W}$	noise matrix 45
$\boldsymbol{w}$	noise vector 29
$\boldsymbol{\mathcal{W}}$	noise image matrix, DFT of the noise matrix $\boldsymbol{W}$ 132
$\boldsymbol{X}$	sparse signal of interest in 2D CS 45

$\boldsymbol{x}$	sparse signal of interest in 1D CS ... 28
χ^{ac}, χ^{cc}	auto- and cross-correlation function ... 83
$\hat{\boldsymbol{x}}$	sparse estimate in 1D CS algorithms ... 29
$\hat{\boldsymbol{X}}$	noisy estimate in 2D CS algorithms ... 49
$\tilde{\boldsymbol{x}}$	noisy estimate in 1D CS algorithms ... 31
$\boldsymbol{\xi}$	sparse signal in CS (vector) ... 28
$\boldsymbol{\Xi}$	decimation matrix in CS ... 29
$\boldsymbol{x}$	baseband discrete-time transmit signal matrix ... 10
x_m	baseband time domain transmit signal of the mth OFDM symbol ... 8
$\boldsymbol{y}$	measurement/observation of the sparse signal in 1D CS 29
$\boldsymbol{y}$, y_{mn}	modulated OFDM receive spectrogram matrix with elements y_{mn} ... 14
$\boldsymbol{\Psi}$, Ψ_{mn}	window matrix with elements Ψ_{mn} ... 15
$\boldsymbol{\psi}$, $\psi_{\nu\rho}$	image of the window matrix $\boldsymbol{\Psi}$ with elements $\psi_{\nu\rho}$ ... 15
$\mathcal{Z}$	length of the zero-correlation zone ... 87
$\boldsymbol{z}_m$, $z_m[\eta]$	zero-correlation zone sequence of the mth OFDM symbol with elements $z_m[\eta]$ ... 87
ζ	relative mutual sample shift in AC-CDM ... 95

Acronyms

R-v-image	range-velocity image ... 19
AC	auto-correlation ... 86, 95
ACDC	all-cell Doppler correction ... 108
ACF	auto-correlation function ... 83
ADC	analog-to-digital converter ... 28
AL	artifact level ... 78
AMP	approximate message passing ... 31
BPDN	basis pursuit denoising ... 29
CAMP	complex approximate message passing ... 48
CCF	cross-correlation function ... 83
CDM	code-division multiplexing ... IV, VI, 4
CDMA	code-division multiple access ... 86
CFAR	constant false alarm rate ... 27

CIR	channel impulse response	10
CP	cyclic prefix	10
CS	compressed sensing	III, V, 4
CW	continuous-wave	126
DAC	digital-to-analog converter	39
DBF	digital beamforming	27
DFT	Discrete Fourier Transform	2
DoA	direction of arrival	19
FAR	false-alarm rate	46
FBLP	forward-backward linear prediction	117
FDM	frequency-division multiplexing	IV
FFT	Fast Fourier Transform	7
FMCW	frequency-modulated continuous-wave	IV, VI, 3
FoV	field of view	102
HAMP	hard-threshold approximate message passing	52
ICI	inter-carrier interference	10
IDFT	inverse Discrete Fourier Transform	2
IFFT	inverse Fast Fourier Transform	9
IOFDM	equidistant interleaving OFDM	24
IQ	in-phase/quadrature	1
ISI	inter-symbol interference	10
IST	iterative soft thresholding	31
ITCT	inter-transmitter cross-talk	23
LASSO	least absolute shrinkage and selection operator	29
LO	local oscillator	40
MIMO	multiple-input multiple-output	III, V, 1
MRS	modified repeated symbol	86, 90
MSE	mean-squared error	32
NCI	non-coherent integration	36
NEqI	non-equidistant interleaving	75
OFDM	orthogonal frequency-division multiplexing	III, V, 2
OMP	orthogonal matching pursuit	31
OS-CFAR	ordered statistics constant false alarm rate	36
PMCW	phase-modulated continuous-wave	86
PNR	peak-to-noise ratio	III, VI, 26

PSLR	peak-to-sidelobe ratio	43
QPSK	quadrature phase-shift keying	8
RCS	radar cross-section	60, 61
RF	radio frequency	1
RFSoC	RF system-on-chip	35
RM	random multiplexing	IV, VI, 73
RS-OFDM	repeated symbol OFDM	90
Rx	receive	1
SALSA	split augmented Lagrangian shrinkage algorithm	33
SIR	signal-to-interference ratio	118
SISO	single-input single-output	16
SOFDM	sparse OFDM	38
STC	space-time coding	90
STFT	Short-Time Fourier Transform	14
TDM	time-division multiplexing	IV
Tx	transmit	1
ULA	uniform linear array	20, 21
XAC	extended AC-CDM with target identification	101, 102
ZCZ	zero-correlation zone	86

Bibliography

[1] C. Waldschmidt, J. Hasch, and W. Menzel, "Automotive Radar — From First Efforts to Future Systems," *IEEE Journal of Microwaves*, vol. 1, no. 1, pp. 135–148, 2021 (cit. on pp. 1, 24, 117).

[2] F. Roos, P. Hügler, C. Knill, L. L. Tovar Torres, N. Appenrodt, J. Dickmann, and C. Waldschmidt, "Comparison of 2D and 3D Compressed Sensing for High-Resolution TDM-MIMO Radars," *European Radar Conference*, pp. 253–256, 2019 (cit. on pp. 1, 34, 46, 76).

[3] B. Schweizer, A. Grathwohl, G. Rossi, P. Hinz, C. Knill, S. Stephany, H. J. Ng, and C. Waldschmidt, "The Fairy Tale of Simple All-Digital Radars: How to Deal With 100 Gbit/s of a Digital Millimeter-Wave MIMO Radar on an FPGA [Application Notes]," *IEEE Microwave Magazine*, vol. 22, no. 7, pp. 66–76, Jul. 2021 (cit. on pp. 1, 3, 7, 28, 35, 37, 39).

[4] N. Levanon, "Multifrequency radar signals," in *International Radar Conference [Cat. No. 00CH37037]*, IEEE, 2000, pp. 683–688 (cit. on p. 2).

[5] N. Levanon, "Multifrequency complementary phase-coded radar signal," *IEE Proceedings - Radar, Sonar and Navigation*, vol. 147, no. 6, pp. 276–284, 2000 (cit. on pp. 2, 7).

[6] N. Levanon and E. Mozeson, "Multicarrier Radar Signal – Pulse Train and CW," *IEEE Transactions on Aerospace and Electronic Systems*, vol. 38, no. 2, pp. 707–720, April 2002 (cit. on p. 2).

[7] G. Franken, H. Nikookar, and P. Van Genderen, "Doppler Tolerance of OFDM-Coded Radar Signals," in *European Radar Conference*, vol. 9, 2006, pp. 108–111 (cit. on pp. 2, 18, 19, 107).

[8] B. J. Donnet and I. D. Longstaff, "Combining MIMO Radar with OFDM Communications," in *European Radar Conference*, IEEE, Sep. 2006, pp. 37–40 (cit. on pp. 2, 7).

[9] C. R. Berger, S. Zhou, P. Willett, B. Demissie, and J. Heckenbach, "Compressed Sensing for OFDM/MIMO Radar," in *Asilomar Conference on Signals, Systems and Computers*, IEEE, October 2008, pp. 213–217 (cit. on pp. 2, 14, 35).

[10] R. F. Tigrek, W. J. A. de Heij, and P. Van Genderen, "Multi-Carrier Radar Waveform Schemes for Range and Doppler Processing," in *IEEE Radar Conference*, IEEE, 2009, pp. 1–5 (cit. on pp. 2, 7, 15).

[11] C. Sturm, E. Pancera, T. Zwick, and W. Wiesbeck, "A Novel Approach to OFDM Radar Processing," in *IEEE Radar Conference*, IEEE, 2009, pp. 1–4 (cit. on pp. 2, 7, 10, 14).

[12] C. Sturm, T. Zwick, and W. Wiesbeck, "An OFDM System Concept for Joint Radar and Communications Operations," in *Vehicular Technology Conference*, IEEE, April 2009, pp. 1–5 (cit. on pp. 2, 8).

[13] C. Sturm and W. Wiesbeck, "Waveform Design and Signal Processing Aspects for Fusion of Wireless Communications and Radar Sensing," *Proceedings of the IEEE*, vol. 99, no. 7, pp. 1236–1259, 2011 (cit. on pp. 2, 7, 15, 19, 107, 117, 123).

[14] R. F. Tigrek, W. J. A. De Heij, and P. Van Genderen, "OFDM Signals as the Radar Waveform to Solve Doppler Ambiguity," *IEEE Transactions on Aerospace and Electronic Systems*, vol. 48, no. 1, pp. 130–143, January 2012 (cit. on pp. 2, 7).

[15] R. W. Chang, "Synthesis of Band-Limited Orthogonal Signals for Multichannel Data Transmission," *Bell System Technical Journal*, vol. 45, no. 10, pp. 1775–1796, December 1966 (cit. on p. 2).

[16] S. B. Weinstein and P. M. Ebert, "Data Transmission by Frequency-Division Multiplexing Using the Discrete Fourier Transform," *IEEE Transactions on Communication Technology*, vol. 19, no. 5, pp. 628–634, 1971 (cit. on pp. 2, 10).

[17] J. Bingham, "Multicarrier Modulation for Data Transmission: An Idea Whose Time Has Come," *IEEE Communications Magazine*, vol. 28, no. 5, pp. 5–14, May 1990 (cit. on pp. 2, 10).

[18] P. Banelli, "Theoretical Analysis and Performance of OFDM Signals in Nonlinear Fading Channels," *IEEE Transactions on Wireless Communications*, vol. 2, no. 2, pp. 284–293, March 2003 (cit. on p. 2).

[19] M. Jiang and L. Hanzo, "Multiuser MIMO-OFDM for Next-Generation Wireless Systems," *Proceedings of the IEEE*, vol. 95, no. 7, pp. 1430–1469, Jul. 2007 (cit. on p. 2).

[20] K. Fazel and S. Kaiser, *Multi-Carrier and Spread Spectrum Systems: From OFDM and MC-CDMA to LTE and WiMAX*, 2nd. Chichester, UK: John Wiley & Sons, Ltd, October 2008, p. 374 (cit. on pp. 2, 7).

[21] T. Hwang, C. Yang, G. Wu, S. Li, and G. Y. Li, "OFDM and Its Wireless Applications: A Survey," *IEEE Transactions on Vehicular Technology*, vol. 58, no. 4, pp. 1673–1694, May 2009 (cit. on pp. 2, 7, 24).

[22] F. Roos, J. Bechter, C. Knill, B. Schweizer, and C. Waldschmidt, "Radar Sensors for Autonomous Driving: Modulation Schemes and Interference Mitigation," *IEEE Microwave Magazine*, vol. 20, no. 9, pp. 58–72, Sep. 2019 (cit. on pp. 3, 48, 117, 120, 131).

[23] G. Hakobyan and B. Yang, "High-Performance Automotive Radar: A review of signal processing algorithms and modulation schemes," *IEEE Signal Processing Magazine*, vol. 36, no. 5, pp. 32–44, Sep. 2019 (cit. on pp. 3, 7, 24, 117).

[24] G. Hakobyan, K. Armanious, and B. Yang, "Interference-Aware Cognitive Radar: A Remedy to the Automotive Interference Problem," *IEEE Transactions on Aerospace and Electronic Systems*, vol. 56, no. 3, pp. 2326–2339, Jun. 2020 (cit. on pp. 3, 7, 72).

[25] D. Garmatyuk, J. Schuerger, Y. T. Morton, K. Binns, M. Durbin, and J. Kimani, "Feasibility Study of a Multi-Carrier Dual-Use Imaging Radar and Communication System," in *European Radar Conference*, IEEE, October 2007, pp. 194–197 (cit. on p. 7).

[26] D. Garmatyuk, J. Schuerger, and K. Kauffman, "Multifunctional Software-Defined Radar Sensor and Data Communication System," *IEEE Sensors Journal*, vol. 11, no. 1, pp. 99–106, January 2011 (cit. on p. 7).

[27] Y. L. Sit, L. Reichardt, C. Sturm, and T. Zwick, "Extension of the OFDM Joint Radar-Communication System for a Multipath, Multiuser Scenario," in *IEEE Radar Conference*, 2011, pp. 718–723 (cit. on pp. 7, 117).

[28] S. Sen and A. Nehorai, "Adaptive Design of OFDM Radar Signal With Improved Wideband Ambiguity Function," *IEEE Transactions on Signal Processing*, vol. 58, no. 2, pp. 928–933, February 2010 (cit. on p. 7).

[29] G. Lellouch, A. K. Mishra, and M. Inggs, "Stepped OFDM Radar Technique to Resolve Range and Doppler Simultaneously," *IEEE Transactions on Aerospace and Electronic Systems*, vol. 51, no. 2, pp. 937–950, 2015 (cit. on pp. 7, 37).

[30] G. Lellouch, A. K. Mishra, and M. Inggs, "Design of OFDM radar pulses using genetic algorithm based techniques," *IEEE Transactions on Aerospace and Electronic Systems*, vol. 52, no. 4, pp. 1953–1966, August 2016 (cit. on p. 7).

[31] B. Schweizer, C. Knill, D. Schindler, and C. Waldschmidt, "Stepped-Carrier OFDM-Radar Processing Scheme to Retrieve High-Resolution Range-Velocity Profile at Low Sampling Rate," *IEEE Transactions on Microwave Theory and Techniques*, vol. 66, no. 3, pp. 1610–1618, March 2018 (cit. on pp. 7, 35, 37, 38, 41, 57, 118).

[32] C. Knill, B. Schweizer, S. Sparrer, F. Roos, R. F. H. Fischer, and C. Waldschmidt, "High Range and Doppler Resolution by Application of Compressed Sensing Using Low Baseband Bandwidth OFDM Radar," *IEEE Transactions on Microwave Theory and Techniques*, vol. 66, no. 7, pp. 3535–3546, Jul. 2018 (cit. on pp. 7, 35, 38, 40, 41, 46, 53).

[33] D. Schindler, B. Schweizer, C. Knill, J. Hasch, and C. Waldschmidt, "An Integrated Stepped-Carrier OFDM MIMO Radar Utilizing a Novel Fast Frequency Step Generator for Automotive Applications," *IEEE Transactions on Microwave Theory and Techniques*, vol. 67, no. 11, pp. 4559–4569, November 2019 (cit. on pp. 7, 39).

[34] D. Werbunat, B. Meinecke, B. Schweizer, J. Hasch, and C. Waldschmidt, "OFDM-Based Radar Network Providing Phase Coherent DOA Estimation," *IEEE Transactions on Microwave Theory and Techniques*, vol. 69, no. 1, pp. 325–336, January 2021 (cit. on p. 7).

[35] D. Schindler, B. Schweizer, C. Knill, J. Hasch, and C. Waldschmidt, "Synthetization of Virtual Transmit Antennas for MIMO OFDM Radar by Space-Time Coding," *IEEE Transactions on Aerospace and Electronic Systems*, vol. 57, no. 3, pp. 1964–1971, Jun. 2021 (cit. on p. 7).

[36] C. Knill, F. Embacher, B. Schweizer, S. Stephany, and C. Waldschmidt, "Coded OFDM Waveforms for MIMO Radars," *IEEE Transactions on Vehicular Technology*, vol. 70, no. 9, pp. 8769–8780, Sep. 2021 (cit. on pp. 7, 73, 84, 86–88, 90, 95, 97–99, 101–104, 107).

[37] C. Sturm, Y. L. Sit, M. Braun, and T. Zwick, "Spectrally interleaved multi-carrier signals for radar network applications and multi-input multi-output radar," *IET Radar, Sonar & Navigation*, vol. 7, no. 3, pp. 261–269, 2013 (cit. on pp. 7, 19, 22, 24, 73, 107, 117).

[38] H. T. Davis and K. T. Thomson, *Linear Algebra and Linear Operators in Engineering - With Applications in Mathematica*, ser. Process Systems Engineering. London: Academic Press, 2000, vol. 3 (cit. on p. 10).

[39] A. Peled and A. Ruiz, "Frequency Domain Data Transmission using Reduced Computational Complexity algorithms," in *IEEE International Conference on Acoustics, Speech, and Signal Processing*, vol. 5, 1980, pp. 964–967 (cit. on p. 10).

[40] G. Hakobyan, "Orthogonal Frequency Division Multiplexing Multiple-Input Multiple-Output Automotive Radar with Novel Signal Processing Algorithms," PhD Thesis, Universität Stuttgart, 2018 (cit. on pp. 13, 46).

[41] C. R. Berger, B. Demissie, J. Heckenbach, P. Willett, and S. Zhou, "Signal Processing for Passive Radar Using OFDM Waveforms," *IEEE Journal of Selected Topics in Signal Processing*, vol. 4, no. 1, pp. 226–238, February 2010 (cit. on pp. 14, 35).

[42] R. F. Tigrek, W. J. De Heij, and P. Van Genderen, "Solving Doppler Ambiguity by Doppler Sensitive Pulse Compression Using Multi-Carrier Waveform," *European Radar Conference*, pp. 72–75, 2008 (cit. on pp. 15, 18).

[43] J. Li and P. Stoica, "MIMO Radar – Diversity means Superiority," in *MIMO Radar Signal Processing*, J. Li and P. Stoica, Eds., Hoboken, New Jersey: Wiley & Sons, 2009, ch. 1 (cit. on pp. 19, 20).

[44] J. Hasch, E. Topak, R. Schnabel, T. Zwick, R. Weigel, and C. Waldschmidt, "Millimeter-wave technology for automotive radar sensors in the 77 GHz frequency band," *IEEE Transactions on Microwave Theory and Techniques*, vol. 60, no. 3, pp. 845–860, 2012 (cit. on pp. 20, 117).

[45] J. Li and P. Stoica, "MIMO Radar with Colocated Antennas," *IEEE Signal Processing Magazine*, vol. 24, no. 5, pp. 106–114, Sep. 2007 (cit. on p. 20).

[46] D. W. Bliss and K. Forsythe, "Multiple-Input Multiple-Output (MIMO) Radar and Imaging: Degrees of Freedom and Resolution," in *Asilomar Conference on Signals, Systems & Computers*, vol. 1, IEEE, 2003, pp. 54–59 (cit. on p. 20).

[47] J. Li and P. Stoica, Eds., *MIMO Radar Signal Processing*. Hoboken, New Jersey: John Wiley & Sons, 2009 (cit. on p. 21).

[48] H. L. Van Trees, *Detection, Estimation and Modulation Theory: Optimum Array Processing*, 4th ed. New York, NQ, USA: Wiley, 2002 (cit. on p. 21).

[49] T. E. Tuncer and B. Friedlander, Eds., *Classical and Modern Direction-of-Arrival Estimation*. Amsterdam: Academic Press, 2009 (cit. on p. 21).

[50] E. Fishler, A. Haimovich, R. Blum, D. Chizhik, L. Cimini, and R. Valenzuela, "MIMO radar: an idea whose time has come," in *IEEE Radar Conference*, IEEE, 2004, pp. 71–78 (cit. on p. 21).

[51] Z. Wang, F. Tigrek, O. Krasnov, F. Van Der Zwan, P. Van Genderen, and A. Yarovoy, "Interleaved OFDM Radar Signals for Simultaneous Polarimetric Measurements," *IEEE Transactions on Aerospace and Electronic Systems*, vol. 48, no. 3, pp. 2085–2099, Jul. 2012 (cit. on pp. 22, 24).

[52] G. Hakobyan and B. Yang, "A Novel OFDM-MIMO Radar with Non-Equidistant Dynamic Subcarrier Interleaving," in *European Radar Conference (EuRAD)*, 2016, pp. 45–48 (cit. on pp. 24, 75).

[53] B. Nuss and T. Zwick, "A Novel Interference Mitigation Technique for MIMO OFDM Radar Using Compressed Sensing," in *European Radar Conference (EURAD)*, 2017, pp. 98–101 (cit. on pp. 24, 35, 117).

[54] Y. L. Sit, C. Sturm, J. Baier, and T. Zwick, "Direction of Arrival Estimation Using the MUSIC Algorithm for a MIMO OFDM Radar," in *IEEE Radar Conference*, IEEE, May 2012, pp. 0226–0229 (cit. on p. 24).

[55] C. Sturm, Y. L. Sit, M. Braun, and T. Zwick, "Spectrally interleaved multi-carrier signals for radar network applications and multi-input multi-output radar," *IET Radar, Sonar & Navigation*, vol. 7, no. 3, pp. 261–269, March 2013 (cit. on p. 24).

[56] T. Multerer, U. Prechtel, M. Vossiek, and V. Ziegler, "Systematic Phase Correction for Direction-of-Arrival Estimation in Spectrally Interleaved OFDM MIMO Radar," *IEEE Transactions on Microwave Theory and Techniques*, vol. 67, no. 11, pp. 4570–4577, November 2019 (cit. on p. 26).

[57] H. Krim and M. Viberg, "Two Decades of Array Signal Processing Research: The Parametric Approach," *IEEE Signal Processing Magazine*, vol. 13, no. 4, pp. 67–94, Jul. 1996 (cit. on p. 27).

[58] L. Anitori, W. L. van Rossum, and A. Huizing, "Array Aperture Extrapolation using Sparse Reconstruction," in *IEEE Radar Conference*, IEEE, May 2015, pp. 0237–0242 (cit. on pp. 27, 47).

[59] H. Rohling, "Radar CFAR Thresholding in Clutter and Multiple Target Situations," *IEEE Transactions on Aerospace and Electronic Systems*, vol. AES-19, no. 4, pp. 608–621, 1983 (cit. on pp. 27, 36).

[60] M. A. Davenport, M. F. Duarte, Y. C. Eldar, and G. Kutyniok, "Introduction to compressed sensing," in *Compressed Sensing*, Y. C. Eldar and G. Kutyniok, Eds., Cambridge: Cambridge University Press, 2012, pp. 1–64 (cit. on pp. 28–30, 33, 46).

[61] D. L. Donoho, "Compressed sensing," *IEEE Transactions on Information Theory*, vol. 52, no. 4, pp. 1289–1306, April 2006 (cit. on pp. 28–30).

[62] E. J. Candes, J. Romberg, and T. Tao, "Robust Uncertainty Principles: Exact Signal Reconstruction from Highly Incomplete Frequency Information," *IEEE Transactions on Information Theory*, vol. 52, no. 2, pp. 489–509, February 2006 (cit. on pp. 28–30).

[63] E. J. Candes, J. K. Romberg, and T. Tao, "Stable Signal Recovery from Incomplete and Inaccurate Measurements," *Communications on Pure and Applied Mathematics*, vol. 59, no. 8, pp. 1207–1223, August 2006 (cit. on p. 28).

[64] E. J. Candes and T. Tao, "Near-Optimal Signal Recovery From Random Projections: Universal Encoding Strategies?" *IEEE Transactions on Information Theory*, vol. 52, no. 12, pp. 5406–5425, December 2006 (cit. on pp. 28, 30).

[65] Y. C. Eldar and G. Kutyniok, *Compressed Sensing: Theory and Applications*, Y. C. Eldar and G. Kutyniok, Eds. Cambridge, UK: Cambridge University Press, 2012 (cit. on pp. 28, 30).

[66] J. A. Tropp and S. J. Wright, "Computational Methods for Sparse Solution of Linear Inverse Problems," *Proceedings of the IEEE*, vol. 98, no. 6, pp. 948–958, Jun. 2010 (cit. on pp. 28–30).

[67] D. L. Donoho, A. Maleki, and A. Montanari, "Message Passing Algorithms for Compressed Sensing: I. Motivation and Construction," in *IEEE Information Theory Workshop*, IEEE, January 2010, pp. 1–5 (cit. on pp. 29, 31).

[68] E. Candes and M. Wakin, "An Introduction To Compressive Sampling," *IEEE Signal Processing Magazine*, vol. 25, no. 2, pp. 21–30, March 2008 (cit. on p. 29).

[69] J. A. Tropp, "Just Relax: Convex Programming Methods for Identifying Sparse Signals in Noise," *IEEE Transactions on Information Theory*, vol. 52, no. 3, pp. 1030–1051, March 2006 (cit. on p. 29).

[70] I. N. Bronštejn, K. A. Semendjaev, G. Musiol, and H. Mühlig, *Taschenbuch der Mathematik*, 10., ser. Edition Harri Deutsch. Haan-Gruiten: Verlag Europa-Lehrmittel - Nourney, Vollmer GmbH & Co. KG, 2016, pp. XLI, 1233 (cit. on pp. 29, 96).

[71] R. Tibshirani, "Regression Shrinkage and Selection via the Lasso," *Journal of the Royal Statistical Society. Series B (Methodological)*, vol. 58, no. 1, pp. 267–288, 1996 (cit. on p. 29).

[72] S. S. Chen, D. L. Donoho, and M. A. Saunders, "Atomic Decomposition by Basis Pursuit," *SIAM Rev.*, vol. 43, no. 1, pp. 129–159, 2001 (cit. on pp. 29, 30).

[73] Z. Zhang, Y. Xu, J. Yang, X. Li, and D. Zhang, "A Survey of Sparse Representation: Algorithms and Applications," *IEEE Access*, vol. 3, pp. 490–530, 2015 (cit. on p. 30).

[74] D. Donoho and X. Huo, "Uncertainty Principles and Ideal Atomic Decomposition," *IEEE Transactions on Information Theory*, vol. 47, no. 7, pp. 2845–2862, 2001 (cit. on p. 30).

[75] W. U. Bajwa, M. F. Duarte, and R. Calderbank, "Conditioning of Random Block Subdictionaries With Applications to Block-Sparse Recovery and Regression," *IEEE Transactions on Information Theory*, vol. 61, no. 7, pp. 4060–4079, Jul. 2015 (cit. on pp. 30, 46).

[76] M. F. Duarte and Y. C. Eldar, "Structured Compressed Sensing: From Theory to Applications," *IEEE Transactions on Signal Processing*, vol. 59, no. 9, pp. 4053–4085, Sep. 2011 (cit. on pp. 30, 46, 52, 149).

[77] D. Donoho, M. Elad, and V. Temlyakov, "Stable Recovery of Sparse Overcomplete Representations in the Presence of Noise," *IEEE Transactions on Information Theory*, vol. 52, no. 1, pp. 6–18, January 2006 (cit. on p. 30).

[78] L. Welch, "Lower Bounds on the Maximum Cross Correlation of Signals (Corresp.)," *IEEE Transactions on Information Theory*, vol. 20, no. 3, pp. 397–399, May 1974 (cit. on pp. 30, 83).

[79] E. Candes and T. Tao, "Decoding by Linear Programming," *IEEE Transactions on Information Theory*, vol. 51, no. 12, pp. 4203–4215, December 2005 (cit. on p. 30).

[80] A. Maleki and A. Montanari, "Analysis of approximate message passing algorithm," in *2010 44th Annual Conference on Information Sciences and Systems (CISS)*, IEEE, March 2010, pp. 1–7 (cit. on pp. 30, 32, 49, 53).

[81] T. Huang, Y. Liu, X. Xu, Y. C. Eldar, and X. Wang, "Analysis of Frequency Agile Radar via Compressed Sensing," *IEEE Transactions on Signal Processing*, vol. 66, no. 23, pp. 6228–6240, December 2018 (cit. on pp. 30, 46).

[82] D. L. Donoho and J. Tanner, "Neighborliness of randomly projected simplices in high dimensions," *Proceedings of the National Academy of Sciences*, vol. 102, no. 27, pp. 9452–9457, Jul. 2005 (cit. on p. 31).

[83] D. L. Donoho, A. Maleki, and A. Montanari, "Message Passing Algorithms for Compressed Sensing," *Proceedings of the National Academy of Sciences of the United States of America*, Jul. 2009 (cit. on pp. 31, 32, 48, 49).

[84] A. Maleki and D. Donoho, "Optimally Tuned Iterative Reconstruction Algorithms for Compressed Sensing," *IEEE Journal of Selected Topics in Signal Processing*, vol. 4, no. 2, pp. 330–341, April 2010 (cit. on pp. 31, 32).

[85] I. Daubechies, M. Defrise, and C. De Mol, "An Iterative Thresholding Algorithm for Linear Inverse Problems with a Sparsity Constraint," *Communications on Pure and Applied Mathematics*, vol. 57, no. 11, pp. 1413–1457, November 2004 (cit. on p. 31).

[86] Y. Pati, R. Rezaiifar, and P. Krishnaprasad, "Orthogonal Matching Pursuit: Recursive Function Approximation with Applications to Wavelet Decomposition," in *Asilomar Conference on Signals, Systems and Computers*, vol. 1, IEEE Comput. Soc. Press, 1993, pp. 40–44 (cit. on p. 31).

[87] J. A. Tropp and A. C. Gilbert, "Signal Recovery From Random Measurements Via Orthogonal Matching Pursuit," *IEEE Transactions on Information Theory*, vol. 53, no. 12, pp. 4655–4666, December 2007 (cit. on p. 31).

[88] D. L. Donoho, A. Maleki, and A. Montanari, "Message Passing Algorithms for Compressed Sensing: II. Analysis and Validation," in *IEEE Information Theory Workshop*, IEEE, January 2010, pp. 1–5 (cit. on p. 31).

[89] P. Schniter, "Turbo Reconstruction of Structured Sparse Signals," in *Annual Conference on Information Sciences and Systems (CISS)*, IEEE, March 2010, pp. 1–6 (cit. on p. 32).

[90] C. A. Metzler, A. Maleki, and R. G. Baraniuk, "From Denoising to Compressed Sensing," *IEEE Transactions on Information Theory*, vol. 62, no. 9, pp. 5117–5144, Sep. 2016 (cit. on p. 32).

[91] Y. Ma, J. Zhu, and D. Baron, "Approximate Message Passing Algorithm With Universal Denoising and Gaussian Mixture Learning," *IEEE Transactions on Signal Processing*, vol. 64, no. 21, pp. 5611–5622, November 2016 (cit. on p. 32).

[92] M. Bayati and A. Montanari, "The Dynamics of Message Passing on Dense Graphs, with Applications to Compressed Sensing," *IEEE Transactions on Information Theory*, vol. 57, no. 2, pp. 764–785, February 2011 (cit. on pp. 32, 48).

[93] A. Montanari, "Graphical models concepts in compressed sensing," in *Compressed Sensing*, Y. C. Eldar and G. Kutyniok, Eds., Cambridge: Cambridge University Press, 2012, pp. 394–438 (cit. on p. 32).

[94] T. Blumensath and M. E. Davies, "Iterative Hard Thresholding for Compressed Sensing," *Applied and Computational Harmonic Analysis*, vol. 27, no. 3, pp. 265–274, November 2009 (cit. on p. 32).

[95] M. V. Afonso, J. M. Bioucas-Dias, and M. A. T. Figueiredo, "Fast Image Recovery Using Variable Splitting and Constrained Optimization," *IEEE Transactions on Image Processing*, vol. 19, no. 9, pp. 2345–2356, Sep. 2010 (cit. on pp. 32, 33).

[96] A. Maleki, L. Anitori, Z. Yang, and R. G. Baraniuk, "Asymptotic Analysis of Complex LASSO via Complex Approximate Message Passing (CAMP)," *IEEE Transactions on Information Theory*, vol. 59, no. 7, pp. 4290–4308, Jul. 2013 (cit. on pp. 32, 48).

[97] A. Hirabayashi, J. Sugimoto, and K. Mimura, "Approximate Message Passing Algorithm for Complex Separable Compressed Imaging," in *Asia-Pacific Signal and Information Processing Association Annual Summit and Conference*, IEEE, October 2013, pp. 1–5 (cit. on pp. 32, 46).

[98] M. V. Afonso, J. M. Bioucas-Dias, and M. A. T. Figueiredo, "A fast algorithm for the constrained formulation of compressive image reconstruction and other linear inverse problems," in *IEEE International Conference on Acoustics, Speech and Signal Processing*, IEEE, March 2010, pp. 4034–4037 (cit. on p. 33).

[99] I. Selesnick. "L1-norm penalized least squares with SALSA," OpenStax CNX. (2014), [Online]. Available: http://cnx.org/contents/e980d3cd-f201-4ef6-8992-d712bf0a88a3@5 (cit. on p. 33).

[100] M. A. T. Figueiredo, J. M. Bioucas-Dias, and M. V. Afonso, "Fast frame-based image deconvolution using variable splitting and constrained optimization," in *IEEE/SP 15th Workshop on Statistical Signal Processing*, IEEE, August 2009, pp. 109–112 (cit. on p. 34).

[101] R. G. Baraniuk and P. Steeghs, "Compressive Radar Imaging," in *IEEE Radar Conference*, IEEE, April 2007, pp. 128–133 (cit. on p. 34).

[102] M. A. Herman and T. Strohmer, "High-Resolution Radar via Compressed Sensing," *IEEE Transactions on Signal Processing*, vol. 57, no. 6, pp. 2275–2284, Jun. 2009 (cit. on p. 34).

[103] A. Gurbuz, J. McClellan, and W. Scott, "A Compressive Sensing Data Acquisition and Imaging Method for Stepped Frequency GPRs," *IEEE Transactions on Signal Processing*, vol. 57, no. 7, pp. 2640–2650, Jul. 2009 (cit. on p. 34).

[104] Y. Yu, A. P. Petropulu, and H. V. Poor, "MIMO Radar Using Compressive Sampling," *IEEE Journal of Selected Topics in Signal Processing*, vol. 4, no. 1, pp. 146–163, February 2010 (cit. on p. 34).

[105] J. H. Ender, "On compressive sensing applied to radar," *Signal Processing*, vol. 90, no. 5, pp. 1402–1414, May 2010 (cit. on p. 34).

[106] J. H. Ender, "A Brief Review of Compressive Sensing Applied to Radar," in *International Radar Symposium (IRS)*, 2013, pp. 3–16 (cit. on p. 34).

[107] A. De Maio, Y. C. Eldar, and A. M. Haimovich, Eds., *Compressed Sensing in Radar Signal Processing*. Cambridge, UK: Cambridge University Press, 2020 (cit. on p. 34).

[108] M. A. Hadi, S. Alshebeili, K. Jamil, and F. E. A. El-Samie, "Compressive sensing applied to radar systems: an overview," *Signal, Image and Video Processing*, vol. 9, no. S1, pp. 25–39, December 2015 (cit. on p. 34).

[109] M. Rossi, A. M. Haimovich, and Y. C. Eldar, "Spatial Compressive Sensing for MIMO Radar," *IEEE Transactions on Signal Processing*, vol. 62, no. 2, pp. 419–430, January 2014 (cit. on pp. 34, 46, 56).

[110] F. Roos, P. Hugler, L. L. T. Torres, C. Knill, J. Schlichenmaier, C. Vasanelli, N. Appenrodt, J. Dickmann, and C. Waldschmidt, "Compressed Sensing based Single Snapshot DoA Estimation for Sparse MIMO Radar Arrays," in *German Microwave Conference (GeMiC)*, IEEE, March 2019, pp. 75–78 (cit. on p. 34).

[111] A. Correas-Serrano and M. A. Gonzalez-Huici, "Experimental Evaluation of Compressive Sensing for DoA Estimation in Automotive Radar," in *International Radar Symposium (IRS)*, IEEE, Jun. 2018, pp. 1–10 (cit. on p. 34).

[112] R. Heckel, "Super-Resolution Radar Imaging via Convex Optimization," in *Compressed Sensing in Radar Signal Processing*, A. De Maio, Y. Eldar, and A. Haimovich, Eds., Cambridge, UK: Cambridge University Press, 2019, pp. 193–224 (cit. on p. 34).

[113] C. R. Berger, S. Zhou, and P. Willett, "Signal Extraction Using Compressed Sensing for Passive Radar with OFDM Signals," in *International Conference on Information Fusion*, 2008, pp. 1–6 (cit. on p. 35).

[114] G. Lellouch, R. Pribic, and P. Van Genderen, "Merging Frequency Agile OFDM Waveforms and Compressive Sensing into a Novel Radar Concept," in *European Radar Conference (EuRAD)*, 2009, pp. 137–140 (cit. on p. 35).

[115] G. Hakobyan, M. Ulrich, and B. Yang, "OFDM-MIMO Radar With Optimized Nonequidistant Subcarrier Interleaving," *IEEE Transactions on Aerospace and Electronic Systems*, vol. 56, no. 1, pp. 572–584, February 2020 (cit. on p. 35).

[116] C. Knill, F. Roos, B. Schweizer, D. Schindler, and C. Waldschmidt, "Random Multiplexing for an MIMO-OFDM Radar With Compressed Sensing-Based Reconstruction," *IEEE Microwave and Wireless Components Letters*, vol. 29, no. 4, pp. 300–302, April 2019 (cit. on pp. 35, 46, 73, 76).

[117] D. Werbunat, F. Sgroi, C. Knill, B. Schweizer, B. Meinecke, R. Michev, J. Hasch, and C. Waldschmidt, "Multiplexing of OFDM-Based Radar Networks," in *IEEE Radar Conference*, IEEE, May 2021, pp. 1–6 (cit. on p. 35).

[118] C. Knill, B. Schweizer, and C. Waldschmidt, "Interference-Robust Processing of OFDM Radar Signals Using Compressed Sensing," *IEEE Sensors Letters*, vol. 4, no. 4, pp. 1–4, April 2020 (cit. on pp. 35, 46, 85, 117, 118, 130, 132–134, 137).

[119] C. Knill, B. Schweizer, S. Stephany, D. Werbunat, and C. Waldschmidt, "FMCW-Interference of Frequency Agile OFDM Radars," in *European Radar Conference*, 2021, pp. 160–163 (cit. on pp. 35, 117, 118, 121, 124, 126, 129–131).

[120] B. Farley, J. McGrath, and C. Erdmann, "An All-Programmable 16-nm RFSoC for Digital-RF Communications," *IEEE Micro*, vol. 38, no. 2, pp. 61–71, March 2018 (cit. on p. 35).

[121] D. Schindler, B. Schweizer, C. Knill, J. Hasch, and C. Waldschmidt, "MIMO-OFDM Radar Using a Linear Frequency Modulated Carrier to Reduce Sampling Requirements," *IEEE Transactions on Microwave Theory and Techniques*, vol. 66, no. 7, pp. 3511–3520, Jul. 2018 (cit. on pp. 37, 38).

[122] G. Lellouch, R. Pribic, and P. van Genderen, "Frequency Agile Stepped OFDM Waveform for HRR," in *International Waveform Diversity and Design Conference*, IEEE, February 2009, pp. 90–93 (cit. on p. 37).

[123] K. Huo, B. Deng, Y. Liu, W. Jiang, and J. Mao, "The Principle of Synthesizing HRRP Based on a New OFDM Phase-coded Stepped-frequency Radar Signal," in *IEEE International Conference on Signal Processing (ICSP)*, IEEE, October 2010, pp. 1994–1998 (cit. on p. 37).

[124] C. Pfeffer, R. Feger, and A. Stelzer, "A Stepped-Carrier 77-GHz OFDM MIMO Radar System with 4 GHz Bandwidth," in *European Radar Conference (EuRAD)*, IEEE, Sep. 2015, pp. 97–100 (cit. on pp. 37, 38).

[125] B. Schweizer, D. Schindler, C. Knill, J. Hasch, and C. Waldschmidt, "Expanding the Unambiguous Velocity Limitation of the Stepped-Carrier OFDM Radar Scheme," in *European Radar Conference (EuRAD)*, IEEE, Sep. 2018, pp. 22–25 (cit. on pp. 37, 38, 102).

[126] B. Schweizer, D. Schindler, C. Knill, J. Hasch, and C. Waldschmidt, "On Hardware Implementations of Stepped-Carrier OFDM Radars," in *IEEE/MTT-S International Microwave Symposium*, IEEE, Jun. 2018, pp. 891–894 (cit. on pp. 37–39).

[127] B. Nuss, J. Mayer, S. Marahrens, and T. Zwick, "Frequency Comb OFDM Radar System With High Range Resolution and Low Sampling Rate," *IEEE Transactions on Microwave Theory and Techniques*, vol. 68, no. 9, pp. 3861–3871, Sep. 2020 (cit. on pp. 37, 38).

[128] B. Schweizer, C. Knill, D. Schindler, and C. Waldschmidt, "IQ-Imbalance Compensation for Wideband OFDM-Radar," in *European Conference on Antennas and Propagation (EuCAP)*, IEEE, March 2020, pp. 1–5 (cit. on pp. 39, 88).

[129] C. Steffens, Y. Yang, and M. Pesavento, "Multidimensional sparse recovery for MIMO channel parameter estimation," in *European Signal Processing Conference*, IEEE, August 2016, pp. 66–70 (cit. on p. 45).

[130] D. Cohen, A. Dikopoltsev, and Y. C. Eldar, "Extensions of sub-Nyquist Radar: Reduced Rime-on-Rarget and Cognitive Radar," in *International Workshop on Compressed Sensing Theory and its Applications to Radar, Sonar and Remote Sensing (CoSeRa)*, IEEE, Jun. 2015, pp. 31–35 (cit. on pp. 45, 46).

[131] C.-Y. Chen and P. P. Vaidyanathan, "Compressed Sensing in MIMO Radar," in *Asilomar Conference on Signals, Systems and Computers*, IEEE, October 2008, pp. 41–44 (cit. on p. 46).

[132] M. F. Duarte and R. G. Baraniuk, "Kronecker Compressive Sensing," *IEEE Transactions on Image Processing*, vol. 21, no. 2, pp. 494–504, February 2012 (cit. on p. 46).

[133] T. Wimalajeewa, Y. C. Eldar, and P. K. Varshney, "Recovery of Sparse Matrices via Matrix Sketching," pp. 1–5, November 2013 (cit. on pp. 46, 47).

[134] A. Ghaffari, M. Babaie-Zadeh, and C. Jutten, "Sparse decomposition of two dimensional signals," in *IEEE International Conference on Acoustics, Speech and Signal Processing*, IEEE, April 2009, pp. 3157–3160 (cit. on p. 46).

[135] Y. Rivenson and A. Stern, "Compressed Imaging With a Separable Sensing Operator," *IEEE Signal Processing Letters*, vol. 16, no. 6, pp. 449–452, Jun. 2009 (cit. on p. 46).

[136] Y. Fang, J. Wu, and B. Huang, "2D sparse signal recovery via 2D orthogonal matching pursuit," *Science China Information Sciences*, vol. 55, no. 4, pp. 889–897, April 2012 (cit. on p. 46).

[137] Y. Wang, H. Wang, and Y. Fu, "Modified Two-Dimensional Compressed Sensing Scheme for Massive MIMO Channel Estimation," in *International Conference on Wireless Communications & Signal Processing (WCSP)*, IEEE, October 2016, pp. 1–5 (cit. on p. 46).

[138] F. Roos, "Optimierte Signalverarbeitung für Chirp-Sequence-modulierte Kfz-Radarsensoren," PhD Thesis, Universität Ulm, 2019 (cit. on pp. 46, 102).

[139] L. Anitori, A. Maleki, M. Otten, R. G. Baraniuk, and P. Hoogeboom, "Design and Analysis of Compressed Sensing Radar Detectors," *IEEE Transactions on Signal Processing*, vol. 61, no. 4, pp. 813–827, February 2013 (cit. on pp. 46–52).

[140] F. Uysal and S. Sanka, "Mitigation of Automotive Radar Interference," in *IEEE Radar Conference (RadarConf18)*, IEEE, April 2018, pp. 0405–0410 (cit. on pp. 48, 132).

[141] F. Uysal, "Synchronous and Asynchronous Radar Interference Mitigation," *IEEE Access*, vol. 7, pp. 5846–5852, 2019 (cit. on pp. 48, 132).

[142] D. L. Donoho, A. Maleki, and A. Montanari, "The Noise-Sensitivity Phase Transition in Compressed Sensing," *IEEE Transactions on Information Theory*, vol. 57, no. 10, pp. 6920–6941, October 2011 (cit. on pp. 48, 49).

[143] L. Anitori and A. Maleki, "Compressed CFAR Techniques," in *Compressed Sensing in Radar Signal Processing*, A. De Maio, Y. C. Eldar, and A. M. Haimovich, Eds., Cambridge, UK: Cambridge University Press, Sep. 2020, ch. 4, pp. 105–134 (cit. on p. 48).

[144] L. Anitori, M. Otten, W. L. van Rossum, A. Maleki, and R. G. Baraniuk, "Compressive CFAR Radar Detection," in *IEEE Radar Conference*, IEEE, May 2012, pp. 0320–0325 (cit. on p. 49).

[145] A. Grami, "The Gaussian Distribution," in *Probability, Random Variables, Statistics, and Random Processes*, Hoboken, NJ, USA: John Wiley & Sons, Inc., March 2019, pp. 201–238 (cit. on p. 49).

[146] D. Needell and J. Tropp, "CoSaMP: Iterative signal recovery from incomplete and inaccurate samples," *Applied and Computational Harmonic Analysis*, vol. 26, no. 3, pp. 301–321, May 2009 (cit. on p. 52).

[147] P. Stoica and Y. Selen, "Model-Order Selection: A review of information criterion rules," *IEEE Signal Processing Magazine*, vol. 21, no. 4, pp. 36–47, Jul. 2004 (cit. on p. 53).

[148] M. Mitzenmacher and E. Upfal, *Probability and Computing: Randomization and Probabilistic Techniques in Algorithms and Data Analysis*, 2nd ed. Cambridge University Press, 2017, p. 484 (cit. on p. 59).

[149] G. Hakobyan and B. Yang, "A Novel OFDM-MIMO Radar with Non-equidistant Subcarrier Interleaving and Compressed Sensing," in *International Radar Symposium (IRS)*, 2016 (cit. on pp. 75, 136).

[150] K. Fazel and S. Kaiser, *Multi-Carrier and Spread Spectrum Systems*. Chichester, UK: John Wiley & Sons, Ltd, Sep. 2003 (cit. on pp. 82, 83).

[151] T. Frey and M. Bossert, *Signal- und Systemtheorie*. Wiesbaden: Vieweg+ Teubner, 2009 (cit. on p. 83).

[152] J. Overdevest, F. Jansen, F. Uysal, and A. Yarovoy, "Doppler Influence on Waveform Orthogonality in 79 GHz MIMO Phase-Coded Automotive Radar," *IEEE Transactions on Vehicular Technology*, vol. 69, no. 1, pp. 16–25, January 2020 (cit. on pp. 85, 86, 90).

[153] P. Fan, N. Suehiro, N. Kuroyanagi, and X. Deng, "Class of binary sequences with zero correlation zone," *Electronics Letters*, vol. 35, no. 10, p. 777, 1999 (cit. on pp. 86, 88).

[154] X. Tang and W. H. Mow, "A New Systematic Construction of Zero Correlation Zone Sequences Based on Interleaved Perfect Sequences," *IEEE Transactions on Information Theory*, vol. 54, no. 12, pp. 5729–5734, December 2008 (cit. on pp. 86–88).

[155] T. Hayashi, Y. Watanabe, A. Pham, T. Miyazaki, S. Matsufuji, and T. Maeda, "A Novel Class of QPSK Zero-Correlation Zone Sequence Sets," in *International Workshop on Signal Design and its Applications in Communications (IWSDA)*, IEEE, Sep. 2015, pp. 205–208 (cit. on pp. 86, 88, 108, 153).

[156] H. Haderer, R. Feger, C. Pfeffer, and A. Stelzer, "Millimeter-Wave Phase-Coded CW MIMO Radar Using Zero- and Low-Correlation-Zone Sequence Sets," *IEEE Transactions on Microwave Theory and Techniques*, vol. 64, no. 12, pp. 4312–4323, December 2016 (cit. on p. 86).

[157] H. Torii, M. Satoh, T. Matsumoto, and M. Nakamura, "Generalized Mutually Orthogonal ZCZ Sequence Sets Based on Perfect Sequences and Orthogonal Codes," *International Conference on Advanced Communication Technology*, pp. 894–899, 2013 (cit. on p. 88).

[158] L. Wang, X. Zheng, H. Wen, and G. Zhang, "Novel Asymmetric Zero Correlation Zone Sequence Sets for Code Division Multiple Access," in *IEEE Vehicular Technology Conference (VTC-Fall)*, IEEE, Sep. 2017, pp. 1–5 (cit. on p. 88).

[159] G. Hakobyan, M. Girma, X. Li, N. Tammireddy, and B. Yang, "Repeated Symbols OFDM-MIMO Radar at 24 GHz," in *Proceedings of the 13th European Radar Conference*, 2016 (cit. on p. 90).

[160] X. Song, S. Zhou, and P. Willett, "Reducing the Waveform Cross Correlation of MIMO Radar With Space-Time Coding," *IEEE Transactions on Signal Processing*, vol. 58, no. 8, pp. 4213–4224, August 2010 (cit. on p. 90).

[161] H. Sun, F. Brigui, and M. Lesturgie, "Analysis and comparison of MIMO radar waveforms," in *International Radar Conference*, IEEE, October 2014, pp. 1–6 (cit. on pp. 90, 95).

[162] W. L. van Rossum and L. Anitori, "Doppler Ambiguity Resolution using Random Slow-Time Code Division Multiple Access MIMO Radar with Sparse Signal Processing," in *IEEE Radar Conference (RadarConf18)*, IEEE, April 2018, pp. 0441–0446 (cit. on p. 90).

[163] A. Bourdoux, U. Ahmad, D. Guermandi, S. Brebels, A. Dewilde, and W. Van Thillo, "PMCW Waveform and MIMO Technique for a 79 GHz CMOS Automotive Radar," *IEEE Radar Conference (RadarConf)*, 2016 (cit. on p. 95).

[164] F. Roos, J. Bechter, N. Appenrodt, J. Dickmann, and C. Waldschmidt, "Enhancement of Doppler Unambiguity for Chirp-Sequence Modulated TDM-MIMO Radars," in *IEEE MTT-S International Conference on Microwaves for Intelligent Mobility (ICMIM)*, IEEE, April 2018, pp. 1–4 (cit. on p. 102).

[165] G. Hakobyan and B. Yang, "A Novel Intercarrier-Interference Free Signal Processing Scheme for OFDM Radar," *IEEE Transactions on Vehicular Technology*, vol. 67, no. 6, pp. 5158–5167, Jun. 2018 (cit. on p. 108).

[166] B.-E. Tullsson, "Topics in FMCW radar disturbance suppression," in *Radar Systems (RADAR 97)*, IEE, 1997, pp. 1–5 (cit. on pp. 117, 130, 131).

[167] G. Brooker, "Mutual Interference of Millimeter-Wave Radar Systems," *IEEE Transactions on Electromagnetic Compatibility*, vol. 49, no. 1, pp. 170–181, February 2007 (cit. on p. 117).

[168] M. Goppelt, H.-L. Blöcher, and W. Menzel, "Automotive radar – investigation of mutual interference mechanisms," *Advances in Radio Science*, vol. 8, pp. 55–60, Sep. 2010 (cit. on p. 117).

[169] C. Fischer, M. Goppelt, H.-L. Blöcher, and J. Dickmann, "Minimizing interference in automotive radar using digital beamforming," *Advances in Radio Science*, vol. 9, pp. 45–48, Jul. 2011 (cit. on p. 117).

[170] M. Barjenbruch, D. Kellner, K. Dietmayer, J. Klappstein, and J. Dickmann, "A Method for Interference Cancellation in Automotive Radar," *International Conference on Microwaves for Intelligent Mobility*, pp. 1–4, 2015 (cit. on pp. 117, 130).

[171] J. Bechter, "Eigenschaften und Unterdrückung von Interferenzen zwischen Kfz-Radarsensoren," PhD Thesis, Ulm University, 2019 (cit. on p. 117).

[172] C. Aydogdu, M. F. Keskin, G. K. Carvajal, O. Eriksson, H. Hellsten, H. Herbertsson, E. Nilsson, M. Rydstrom, K. Vanas, and H. Wymeersch, "Radar Interference Mitigation for Automated Driving: Exploring Proactive Strategies," *IEEE Signal Processing Magazine*, vol. 37, no. 4, pp. 72–84, 2020 (cit. on p. 117).

[173] C. Knill, B. Schweizer, P. Hügler, and C. Waldschmidt, "Impact of an Automotive Chirp-Sequence Interferer on a Wideband OFDM Radar," *European Radar Conference (EuRAD)*, pp. 8–11, 2018 (cit. on pp. 117, 118, 126, 129, 130).

[174] J. Fink, M. Braun, and F. K. Jondral, "Effects of Arbitrarily Spaced Subcarriers on Detection Performance in OFDM Radar," *IEEE Vehicular Technology Conference*, no. 4, pp. 5–9, 2012 (cit. on p. 117).

[175] Y. L. Sit and T. Zwick, "MIMO OFDM Radar with Communication and Interference Cancellation Features," *IEEE National Radar Conference*, pp. 265–268, 2014 (cit. on p. 117).

[176] Y. L. Sit and T. Zwick, "Automotive MIMO Radar using Spectrally-Interleaved OFDM Signals for Multiple-User Access," in *German Microwave Conference*, 2014 (cit. on p. 117).

[177] Y. L. Sit and T. Zwick, "MIMO OFDM Radar Networks: Inter- & Intra-System Interference Handling," in *Asia-Pacific Microwave Conference*, November 2014, pp. 1318–1320 (cit. on p. 117).

[178] G. Hakobyan and B. Yang, "A Novel Narrowband Interference Suppression Method for OFDM Radar," in *European Signal Processing Conference (EUSIPCO)*, IEEE, August 2016, pp. 2230–2234 (cit. on pp. 117, 126, 131).

[179] X. Wang, G. Zhang, Y. Zhang, H. Leung, and F. Wen, "Method to suppress narrowband interference for OFDM radar," *The Journal of Engineering*, vol. 2019, no. 21, pp. 8170–8174, November 2019 (cit. on pp. 117, 131).

[180] C. Fischer, H. L. Blöcher, J. Dickmann, and W. Menzel, "Robust Detection and Mitigation of Mutual Interference in Automotive Radar," in *International Radar Symposium*, 2015, pp. 143–148 (cit. on p. 130).

[181] J. Bechter, K. D. Biswas, and C. Waldschmidt, "Estimation and Cancellation of Interferences in Automotive Radar Signals," in *International Radar Symposium (IRS)*, IEEE, Jun. 2017, pp. 1–10 (cit. on p. 130).

[182] J. Bechter, F. Roos, M. Rahman, and C. Waldschmidt, "Automotive Radar Interference Mitigation using a Sparse Sampling Approach," in *European Radar Conference (EURAD)*, IEEE, October 2017, pp. 90–93 (cit. on p. 131).

[183] M. F. Duarte and R. G. Baraniuk, "Recovery of Frequency-Sparse Signals from Compressive Measurements," in *Annual Allerton Conference on Communication, Control, and Computing (Allerton)*, Allerton: IEEE, Sep. 2010, pp. 599–606 (cit. on p. 149).

Index of own Publications

Parts of this thesis have already been published by the author. This section lists the author's publications.

Articles in Peer-Reviewed Scientific Journals

[1] B. Schweizer, A. Grathwohl, G. Rossi, P. Hinz, C. Knill, S. Stephany, H. J. Ng, and C. Waldschmidt, "The Fairy Tale of Simple All-Digital Radars: How to Deal With 100 Gbit/s of a Digital Millimeter-Wave MIMO Radar on an FPGA [Application Notes]," *IEEE Microwave Magazine*, vol. 22, no. 7, pp. 66–76, Jul. 2021.

[2] B. Schweizer, C. Knill, D. Werbunat, S. Stephany, and C. Waldschmidt, "Mutual Interference of Automotive OFDM Radars—Analysis and Countermeasures," *IEEE Journal of Microwaves*, vol. 1, no. 4, pp. 950–961, October 2021.

[3] C. Knill, F. Embacher, B. Schweizer, S. Stephany, and C. Waldschmidt, "Coded OFDM Waveforms for MIMO Radars," *IEEE Transactions on Vehicular Technology*, vol. 70, no. 9, pp. 8769–8780, Sep. 2021.

[4] D. Schindler, B. Schweizer, C. Knill, J. Hasch, and C. Waldschmidt, "Synthetization of Virtual Transmit Antennas for MIMO OFDM Radar by Space-Time Coding," *IEEE Transactions on Aerospace and Electronic Systems*, vol. 57, no. 3, pp. 1964–1971, Jun. 2021.

[5] P. Hügler, T. Grebner, C. Knill, and C. Waldschmidt, "UAV-Borne 2-D and 3-D Radar-Based Grid Mapping," *IEEE Geoscience and Remote Sensing Letters*, pp. 1–5, 2020.

[6] C. Knill, B. Schweizer, and C. Waldschmidt, "Interference-Robust Processing of OFDM Radar Signals Using Compressed Sensing," *IEEE Sensors Letters*, vol. 4, no. 4, pp. 1–4, April 2020.

[7] F. Roos, J. Bechter, C. Knill, B. Schweizer, and C. Waldschmidt, "Radar Sensors for Autonomous Driving: Modulation Schemes and Interference Mitigation," *IEEE Microwave Magazine*, vol. 20, no. 9, pp. 58–72, Sep. 2019.

[8] D. Schindler, B. Schweizer, C. Knill, J. Hasch, and C. Waldschmidt, "An Integrated Stepped-Carrier OFDM MIMO Radar Utilizing a Novel Fast Frequency Step Generator for Automotive Applications," *IEEE Transactions on Microwave Theory and Techniques*, vol. 67, no. 11, pp. 4559–4569, November 2019.

[9] C. Knill, F. Roos, B. Schweizer, D. Schindler, and C. Waldschmidt, "Random Multiplexing for an MIMO-OFDM Radar With Compressed Sensing-Based Reconstruction," *IEEE Microwave and Wireless Components Letters*, vol. 29, no. 4, pp. 300–302, April 2019.

[10] C. Knill, B. Schweizer, S. Sparrer, F. Roos, R. F. H. Fischer, and C. Waldschmidt, "High Range and Doppler Resolution by Application of Compressed Sensing Using Low Baseband Bandwidth OFDM Radar," *IEEE Transactions on Microwave Theory and Techniques*, vol. 66, no. 7, pp. 3535–3546, Jul. 2018.

[11] D. Schindler, B. Schweizer, C. Knill, J. Hasch, and C. Waldschmidt, "MIMO-OFDM Radar Using a Linear Frequency Modulated Carrier to Reduce Sampling Requirements," *IEEE Transactions on Microwave Theory and Techniques*, vol. 66, no. 7, pp. 3511–3520, Jul. 2018.

[12] B. Schweizer, C. Knill, D. Schindler, and C. Waldschmidt, "Stepped-Carrier OFDM-Radar Processing Scheme to Retrieve High-Resolution Range-Velocity Profile at Low Sampling Rate," *IEEE Transactions on Microwave Theory and Techniques*, vol. 66, no. 3, pp. 1610–1618, March 2018.

Articles in Conference Proceedings with Peer-Review Process

[1] C. Knill, B. Schweizer, S. Stephany, D. Werbunat, and C. Waldschmidt, "FMCW-Interference of Frequency Agile OFDM Radars," in *European Radar Conference*, 2021, pp. 160–163.

[2] D. Werbunat, F. Sgroi, C. Knill, B. Schweizer, B. Meinecke, R. Michev, J. Hasch, and C. Waldschmidt, "Multiplexing of OFDM-Based Radar Networks," in *IEEE Radar Conference*, IEEE, May 2021, pp. 1–6.

[3] B. Schweizer, C. Knill, D. Schindler, and C. Waldschmidt, "IQ-Imbalance Compensation for Wideband OFDM-Radar," in *European Conference on Antennas and Propagation (EuCAP)*, IEEE, March 2020, pp. 1–5.

[4] S. Stephany, B. Schweizer, C. Knill, and C. Waldschmidt, "Impact of an Automotive Chirp-Sequence Interferer on a Wideband Pseudo-Noise Radar," in *International Conference on Electromagnetics in Advanced Applications (ICEAA)*, IEEE, Sep. 2019, pp. 0859–0862.

[5] B. Schweizer, D. Schindler, C. Knill, and C. Waldschmidt, "A Doppler-Tolerant Stepped-Carrier OFDM-Radar Scheme Based on All-Cell-Doppler-Correction," in *International Radar Symposium (IRS)*, IEEE, Jun. 2019, pp. 1–9.

[6] F. Roos, P. Hügler, J. Bechter, M. A. Razzaq, C. Knill, N. Appenrodt, J. Dickmann, and C. Waldschmidt, "Effort Considerations of Compressed Sensing for Automotive Radar," in *IEEE Radio and Wireless Symposium (RWS)*, IEEE, January 2019, pp. 1–3.

[7] F. Roos, P. Hugler, L. L. T. Torres, C. Knill, J. Schlichenmaier, C. Vasanelli, N. Appenrodt, J. Dickmann, and C. Waldschmidt, "Compressed Sensing based Single Snapshot DoA Estimation for Sparse MIMO Radar Arrays," in *German Microwave Conference (GeMiC)*, IEEE, March 2019, pp. 75–78.

[8] F. Roos, P. Hügler, C. Knill, L. L. Tovar Torres, N. Appenrodt, J. Dickmann, and C. Waldschmidt, "Comparison of 2D and 3D Compressed Sensing for High-Resolution TDM-MIMO Radars," *European Radar Conference*, pp. 253–256, 2019.

[9] H. Iqbal, C. Knill, M. Z. Khan, T. Chaloun, and C. Waldschmidt, "Polarimetric SAR for Automotive Applications," in *European Radar Conference (EuRAD)*, IEEE, Sep. 2018, pp. 30–33.

[10] C. Knill, B. Schweizer, P. Hügler, and C. Waldschmidt, "Impact of an Automotive Chirp-Sequence Interferer on a Wideband OFDM Radar," *European Radar Conference (EuRAD)*, pp. 8–11, 2018.

[11] B. Schweizer, D. Schindler, C. Knill, J. Hasch, and C. Waldschmidt, "Expanding the Unambiguous Velocity Limitation of the Stepped-Carrier OFDM Radar Scheme," in *European Radar Conference (EuRAD)*, IEEE, Sep. 2018, pp. 22–25.

[12] B. Schweizer, D. Schindler, C. Knill, J. Hasch, and C. Waldschmidt, "On Hardware Implementations of Stepped-Carrier OFDM Radars," in *IEEE/MTT-S International Microwave Symposium*, IEEE, Jun. 2018, pp. 891–894.

[13] F. Roos, P. Hügler, C. Knill, N. Appenrodt, J. Dickmann, and C. Waldschmidt, "Data Rate Reduction for Chirp-Sequence based Automotive Radars using Compressed Sensing," in *2018 11th German Microwave Conference (GeMiC)*, IEEE, March 2018, pp. 347–350.

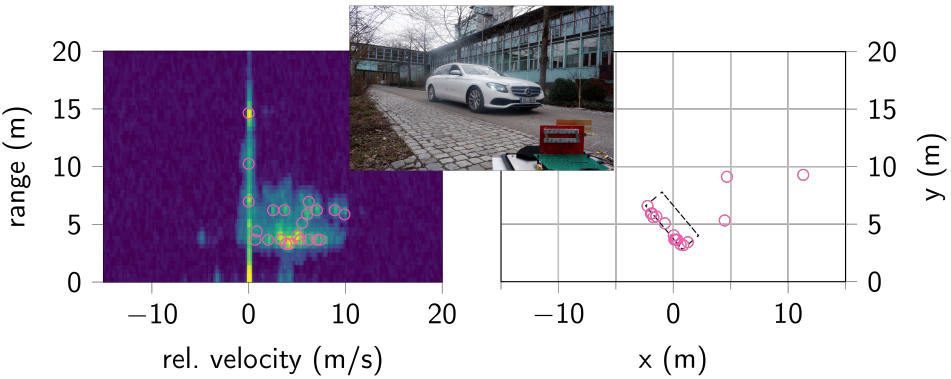
[14] C. Knill, J. Bechter, and C. Waldschmidt, "Interference of Chirp Sequence Radars by OFDM Radars at 77 GHz," in *IEEE MTT-S International Conference on Microwaves for Intelligent Mobility (ICMIM)*, IEEE, March 2017, pp. 147–150.

[15] A. Scheel, C. Knill, S. Reuter, and K. Dietmayer, "Multi-Sensor Multi-Object Tracking of Vehicles Using High-Resolution Radars," in *IEEE Intelligent Vehicles Symposium, Proceedings*, IEEE, Jun. 2016, pp. 558–565.

[16] C. Knill, A. Scheel, and K. Dietmayer, "A Direct Scattering Model for Tracking Vehicles with High-Resolution Radars," in *IEEE Intelligent Vehicles Symposium (IV)*, IEEE, Jun. 2016, pp. 298–303.

Herausgeber:
Prof. Dr.-Ing. Christian Waldschmidt

universität ulm



Recent advances in digital hardware and processing power have enabled the realization of novel digital radars that are superior to radars commercially available today in flexibility and performance. This opens up new opportunities in radar waveform design, modulation, and high-performance signal processing that were previously unfeasible. Probably the most known digital radar modulation concept is OFDM, which has attracted much interest in radar research in the last two decades.

The goal of this thesis is to explore new possibilities for OFDM radar waveform design and high-performance digital processing to make future digital radars even more powerful and robust. To this end, the developed novel waveform and signal processing concepts take advantage of the high degree of flexibility and diversity provided by OFDM to overcome previous limitations in radar performance, to enable new MIMO concepts, to enhance radar imaging performance, and to enable robust radar sensing in coexistence with other radars.

ISBN: 978-3-948303-25-9 ISBN: 978-3-948303-26-6 (E-Book)